

514  
✓  
10

41 0622362 X



ProQuest Number: 10183047

All rights reserved

INFORMATION TO ALL USERS

The quality of this reproduction is dependent upon the quality of the copy submitted.

In the unlikely event that the author did not send a complete manuscript and there are missing pages, these will be noted. Also, if material had to be removed, a note will indicate the deletion.



ProQuest 10183047

Published by ProQuest LLC (2017). Copyright of the Dissertation is held by the Author.

All rights reserved.

This work is protected against unauthorized copying under Title 17, United States Code  
Microform Edition © ProQuest LLC.

ProQuest LLC.  
789 East Eisenhower Parkway  
P.O. Box 1346  
Ann Arbor, MI 48106 – 1346

# **Acoustic Wave Interactions with Viscous Liquids Spreading in the Acoustic Path of a Surface Acoustic Wave Sensor**

**Markus K. Banerjee**

A thesis submitted in partial fulfilment of the requirements of The Nottingham  
Trent University for the degree of Doctor of Philosophy.

September 1999

**ABSTRACT**

This thesis introduces a novel sensor system based on surface acoustic waves (SAW's) to investigate the wetting dynamics of partially localised stripes of highly viscous polydimethylsiloxane (PDMS) oil spreading directly in the acoustic path of a surface acoustic wave sensor. SAW's have their energy confined to within one wavelength of the surface and are extremely sensitive and can detect sub-monolayer surface coverages. Therefore SAW's have the potential to study film dynamics in addition to the dynamics of the macroscopic spreading of a liquid. PDMS oils of four different viscosities (100,000 cSt, 30,000 cSt, 10,000 cSt and 1,000 cSt) have been deposited on the substrate surface of a 169 MHz Rayleigh wave sensor operating in pulse mode, to control the characteristic velocity,  $v^* = \gamma / \eta$ , and thus adjust the timescale for the spreading over several orders of magnitude. Simultaneous measurements of SAW transmission and reflection signals and optical interferometry have been conducted directly in the acoustic path of the sensor. The time evolution of the shape of the stripe was followed over a period of up to eight hours. Image processing algorithms and programs have been created and applied to extract the dynamic changes of geometric parameters. The profile of the liquid has been reconstructed and the changes in geometric parameters (contact width, cylindrical cap radius, cylindrical cap height and contact angle) are found to follow well defined power laws. As the stripe spreads across the acoustic path, with an accompanying decrease in cylindrical cap height to conserve volume, the acoustic signals are reflected and transmitted. The acoustic reflection from the stripe of PDMS is found to show a distinct pattern of resonances. The reflection oscillates in amplitude as the advancing front of the fluid reduces the acoustic path length. The transmitted signals, propagating along the solid-liquid interface, are found to be progressively attenuated as the fluid spreads and show asymmetric shaped attenuation resonances in the transmission coefficient. To model the acoustic attenuation, an approach treating the liquids using a Maxwell model of viscoelastic fluids with a single relaxation time has been developed. Mechanisms for the transmission and reflection resonances are discussed. Resonances in the transmission coefficient occur cyclically and approximately correspond to the stripe height matching  $n\lambda_s/4$ , where  $n$  is odd and  $\lambda_s$  is the shear wavelength of the fluid. The periodic structure of resonance peaks in the reflection signal is discussed using step and triangular shape approximate forms for the stripe geometry.

*Wir müssen aber den Bereich der Dinge erweitern und wissen, daß die Welt und alles, was wir in ihrem Umkreis sehen und greifen, nur die eine Hälfte der Welt ist.*

PARACELSIUS (1493 – 1541)

*Science is the attempt to make the chaotic diversity of our sense-experience correspond to a logically uniform system of thought.*

ALBERT EINSTEIN (1879–1955)

# ACKNOWLEDGEMENT

This is an opportunity to think about the years I have spent in Nottingham. In these years I have learned a lot about myself. In general people are not reflecting back about their past. If I reflect back about my past I can truly and honestly say that the people in England have altered the way how I should think about the things which are personally important for me in my life and how to reflect about the past, which tremendously altered my entire life. This is not trivial since the focus of my life in the past was only directed towards myself. The chance to break out of this circle is an incredible gift that one receives only once in a lifetime. The chance to experience a different culture and its people was the best that could ever have happened to me. This is not an achievement of my own, this is also an achievement of the people who were carrying about my progress and helped me to break out of this mentality and to start to experience a new aspect of myself, the true me. This should give everyone the courage to do the things that are the priority to their personal development and success, whatever these goals are.

I would like to speak out my gratitude to the Supervisors, Dr. Glen McHale and Dr. Michael Ian Newton who had the faith in me to get through the entire programme. Their support and understanding is invaluable to me. Furthermore I would like to thank the entire thin film and interfaces group, Peter, Thomas, Nhan and John for lively discussions, a superb atmosphere and a great time in Nottingham. I also would like to thank my best friend at Nottingham University, Victor, who gave the whole years that touch of spice from Spain. Kevin and Chris who made me aware about the really important things in life. The French connection, who gave me the feeling that France is definitely a place to visit. My house mates, who made me really feel at home even though home was always far away. Caroline, Sue Yee, Bruno, Reinhold, Roland, Jason, Severine, Sandrine and so many more who dragged me out of my everyday Ph.D. live to show me that there is more to life than only research.

## *ACKNOWLEDGEMENT*

---

However this all would not have been possible without the aid of some people that are closest to me. My parents and my family. Without their faith their understanding and their tremendous support and love I would not have been able to finish this enormous task. It made all the difference. I will never forget what you have done for me.

*Thank you all!*

# TABLE OF CONTENTS

ABSTRACT	ii
WORDS OF WISDOM	iii
ACKNOWLEDGEMENT	iv
TABLE OF CONTENTS	vi
LIST OF FIGURES	ix
LIST OF TABLES	xiii
<b>CHAPTER 1 INTRODUCTION</b>	<b>1</b>
1.1. Introduction	2
1.2. Spreading of a Viscous Liquid on a Horizontal Surface	8
1.2.1. Contact Angle and Interface Energy	9
1.2.2. High-Energy and Low-Energy Surfaces	14
1.3. Standard Methods of Measuring Wetting Phenomena	15
1.3.1. Static Equilibrium Measurement Methods	15
1.3.2. Methods of Measuring the Dynamics of Liquid Spreading	16
1.4. Acoustic Sensors and Devices	21
1.4.1. Thickness Shear Mode (TSM) Resonator	22
1.4.2. Rayleigh Wave - Surface Acoustic Wave Device (SAW)	26
1.4.3. Principle of Operation of a SAW Device	28
1.4.4. Other Classes of Acoustic Sensors for Liquid Sensing	32
1.5. Motivation and Objectives	38
<b>CHAPTER 2 THEORY</b>	<b>46</b>
2.1. Introduction	47
2.2. The Dynamics of Liquid Spreading	50
2.2.1. Spreading of a Droplet	53
2.2.2. Surface Free Energy	53
2.2.3. Viscous Dissipation	56
2.2.4. Dissipation in a Wedge	57
2.2.5. Dissipation in a Cone	58
2.2.6. Spreading of a Stripe of Oil	59
2.2.7. Small Angle Limit	60
2.3. Rayleigh Surface Waves in Elastic Media	61
2.3.1. Rayleigh Waves in Non-Piezoelectric Solids	62
2.3.2. Equation of Motion	64
2.3.3. The Wave Equation	65
2.3.4. Rayleigh Waves in Piezoelectric Solids	66
2.4. Rayleigh Wave Interaction with Partially Localised Viscous Liquid	70
2.4.1. SAW Transmission Resonances Model	71

<b>CHAPTER 3</b>	<b><i>EXPERIMENTAL DEVELOPMENT</i></b>	<b>82</b>
3.1.	Introduction	83
3.2.	System Configuration	84
3.2.1.	Description of the Electronic Components	86
3.3.	The Interdigital Transducer (IDT)	90
3.3.1.	Uniform IDT	90
3.3.2.	SAW Device Description	97
3.4.	Signal Generation and Set-up Configuration	101
3.5.	Interfacing using GPIB BUS (IEEE-488) and Controller Program for PM 3365	103
3.6.	Optical System Development – Interferometry	109
3.6.1.	Configuration and Set-up of the Optics	111
3.6.2.	Interferometry	113
3.6.3.	Image Processing and Analysis	115
3.7.	Calibration Procedure to Estimate Acoustic Losses	123
3.8.	The influence of the Diode Detector Threshold for the Transmission Signal Losses	125
3.9.	Deposition Method for Stripes of Liquid	131
<b>CHAPTER 4</b>	<b><i>RESULTS</i></b>	<b>135</b>
4.1.	Introduction	136
4.2.	Trends in Acoustic Signals	137
4.3.	Signal Response of Different SAW Devices	143
4.4.	Optical Analysis	146
4.4.1.	Theoretical Time Dependence of the Stripe Geometry	146
4.4.2.	Trends in Acoustic Signals as a Function of Dynamic Changes in Stripe Geometry	154
4.5.	Fluid Viscosity Dependence on SAW-Liquid Interaction	159
4.6.	High Degree of Similarity in Acoustic Signals	169
4.6.1.	Comparison of Signal Trends of Two Different Double Transits and Two Reflection Signals	169
4.6.2.	The Influence of the Stripe Geometry on the Signal Structure	172
4.7.	Summary	180
<b>CHAPTER 5</b>	<b><i>ANALYSIS AND DISCUSSION</i></b>	<b>182</b>
5.1.	Introduction	183
5.2.	Influence of the $\omega\tau$ Limits on the Resonance Structure	185
5.3.	Area Approximation of the Cross-Section of the Cylindrical Cap	188
5.4.	Transmission Resonances in the SAW Transit Signals	191
5.4.1.	Starting Conditions and the Influence of Relaxation Rate $\tau^{-1}$ and the Parameter $\xi$	191
5.4.2.	Transmission Resonances with Asymmetric Shape	192
5.4.3.	Viscosity Dependence of the Relaxation Rate $\tau^{-1}$	199

**TABLE OF CONTENTS**

---

5.5. Resonances in the Reflection Coefficient of SAW's	204
5.5.1. The Step Model	204
5.5.2. Dispersion	209
5.5.3. Triangle Model Approximation	212
<b>CHAPTER 6 CONCLUSION</b>	<b>216</b>
6.1. Conclusion	217
6.2. Further Development	220
<b>APPENDIX</b>	<b>225</b>
Appendix	226
<b>REFERENCES</b>	<b>235</b>

# LIST OF FIGURES

## CHAPTER 1 INTRODUCTION

<i>Fig. 1.1</i>	A typical simple bulk-wave delay line.	5
<i>Fig. 1.2</i>	A small droplet in equilibrium on a horizontal surface.	10
<i>Fig. 1.3</i>	Young's force balance giving the static contact angle.	11
<i>Fig. 1.4</i>	A surface wave delay line.	29
<i>Fig. 1.5</i>	Bi-directional surface wave transducer.	31

## CHAPTER 2 THEORY

<i>Fig. 2.1</i>	The cross-sectional shape of a thin stripe of oil.	48
<i>Fig. 2.2</i>	The spherical cap shape of a droplet with constant volume.	52
<i>Fig. 2.3</i>	The Maxwell Model for viscoelasticity.	75

## CHAPTER 3 EXPERIMENTAL DEVELOPMENT

<i>Fig. 3.1</i>	The SAW-circuit with instrumentation arranged in pulsed transmission/reflection mode.	85
<i>Fig. 3.2</i>	Operation of the double balanced mixer.	88
<i>Fig. 3.3</i>	A four port 180° hybrid junction as a circulator.	88
<i>Fig. 3.4</i>	Uniform periodic interdigital transducer (IDT) with single electrode configuration.	91
<i>Fig. 3.5</i>	A surface acoustic wave delay line device showing the configuration of the interdigital transducers along the free surface.	94
<i>Fig. 3.6</i>	The SAW device using the simplest type of transducer layout.	98
<i>Fig. 3.7</i>	The single transit signal, double transit signal and the reflection change in peak height if phase detection occurs.	104
<i>Fig. 3.8</i>	The three acoustic signals measured for each surface wave pulse.	106
<i>Fig. 3.9</i>	The loop direction and displacement of the cursors when measuring peak-to-peak values.	107
<i>Fig. 3.10</i>	An improved algorithm using the mean function rather than the peak-to-peak measurement.	108
<i>Fig. 3.11</i>	The flow chart of the DSO controller program.	110
<i>Fig. 3.12</i>	The optical set-up of the system.	112
<i>Fig. 3.13</i>	Image showing interference pattern produced by a stripe of viscous liquid.	117

## LIST OF FIGURES

<b>Fig. 3.14</b>	A full intensity line profile of one image.	119
<b>Fig. 3.15</b>	A full line profile of dark and bright fringes.	120
<b>Fig. 3.16</b>	The extracted contact width of 30 images and the fitted $1/7^{\text{th}}$ power law.	121
<b>Fig. 3.17</b>	The decrease in contact angle with time.	122
<b>Fig. 3.18</b>	The calibration process for the single transit signal in the transmission path.	124
<b>Fig. 3.19</b>	The calibration process for the double transit signal in the reflection path.	124
<b>Fig. 3.20</b>	The calibration converting the measured mean value into acoustic attenuation caused by the spreading liquid.	126
<b>Fig. 3.21</b>	Estimation of the attenuation coefficient for the single transit and the double transit signals.	128
<b>Fig. 3.22</b>	Comparison between single and double transit attenuation.	129

## CHAPTER 4 RESULTS

<b>Fig. 4.1</b>	The full oscilloscope screen, showing the single transit signal, the double transit signal and the reflection.	138
<b>Fig. 4.2</b>	The signal response of the three observed signals when a deposited stripe of oil progressively wets the surface.	139
<b>Fig. 4.3</b>	The response of the three signals, single transit signal ( <u>ST</u> ), double transit signal ( <u>DT</u> ) and the reflection ( <u>REFLECTION</u> ) plotted on a logarithmic time axis.	141
<b>Fig. 4.4</b>	The single transit showing an overall attenuation, but with a rich oscillatory structure (A-D and A'-D') and some subsidiary peaks (X and Y).	144
<b>Fig. 4.5</b>	The geometrical cross-section parameters contact width, $d_0$ , ( <u>a(Y1)</u> ), cylindrical cap radius, $R$ , ( <u>b(Y1)</u> ), contact angle, $\theta$ , ( <u>a(Y2)</u> ), and height, $h_0$ , ( <u>b(Y2)</u> ).	147
<b>Fig. 4.6</b>	The acoustic signals as a function of contact width.	148
<b>Fig. 4.7</b>	The acoustic signals as a function of cylindrical cap radius.	149
<b>Fig. 4.8</b>	The acoustic signals as a function of contact angle.	151
<b>Fig. 4.9</b>	The acoustic signals as a function of height.	152
<b>Fig. 4.10</b>	The reflection from the stripe (lower curve) showing significant oscillations as the oil spreads in comparison with Fig. 4.6.	155
<b>Fig. 4.11</b>	Fits of contact width, and cylindrical cap radius.	157
<b>Fig. 4.12</b>	The acoustic signal trends during the spreading of a 100,000 cSt oil.	160
<b>Fig. 4.13</b>	The acoustic signal trends during the spreading of a 30,000 cSt oil.	163
<b>Fig. 4.14</b>	The acoustic signal trends during the spreading of a 10,000 cSt oil.	165
<b>Fig. 4.15</b>	The acoustic signal trends during the spreading of a 1,000 cSt oil.	168
<b>Fig. 4.16</b>	Comparison of two double transit signal trends from two experiments with 100,000 cSt oils.	171
<b>Fig. 4.17</b>	Comparison of reflection data from two experiments with 100,000 cSt oils.	173

<b>Fig. 4.18</b>	The course of the double transit curves for two 100,000 cSt experiments.	175
<b>Fig. 4.19</b>	The overlap of the five consecutive reflection peaks from two separate experiments.	177

## **CHAPTER 5 ANALYSIS AND DISCUSSION**

<b>Fig. 5.1</b>	Predictions of attenuation for uniform viscoelastic films of variable depth.	186
<b>Fig. 5.2</b>	Predictions of frequency for uniform viscoelastic films of variable depth.	187
<b>Fig. 5.3</b>	Numerical fit of the theoretical model to the acoustic attenuation for a 100,000 cSt stripe of oil of cross-sectional area of $1.23 \times 10^{-9} \text{ m}^2$ .	195
<b>Fig. 5.4</b>	Numerical fit of the theoretical model to the acoustic attenuation for a 100,000 cSt stripe of oil of cross-sectional area of $1.28 \times 10^{-9} \text{ m}^2$ .	196
<b>Fig. 5.5</b>	Numerical fit of the theoretical model to the acoustic attenuation for a 100,000 cSt stripe of oil of cross-sectional area of $1.39 \times 10^{-9} \text{ m}^2$ .	197
<b>Fig. 5.6</b>	Numerical fit of the theoretical model to the acoustic attenuation for a 100,000 cSt stripe of oil of cross-sectional area of $1.31 \times 10^{-9} \text{ m}^2$ .	198
<b>Fig. 5.7</b>	Numerical fit of the theoretical model to the acoustic attenuation for a 30,000 cSt stripe of oil of cross-sectional area of $1.50 \times 10^{-9} \text{ m}^2$ .	201
<b>Fig. 5.8</b>	Numerical fit of the theoretical model to the acoustic attenuation for a 100,000 cSt stripe of oil of cross-sectional area of $1.23 \times 10^{-9} \text{ m}^2$ .	202
<b>Fig. 5.9</b>	Resonant reflections from a 100,000 cSt oil showing an average separation of approximately one SAW wavelength.	205
<b>Fig. 5.10</b>	A solid abrupt step model for reflections.	207
<b>Fig. 5.11</b>	Possible effects of dispersion on acoustic signals.	211
<b>Fig. 5.12</b>	A triangular solid model for reflections.	213
<b>Fig. 5.13</b>	Distributed reflections from the edges of the triangular shape.	214

## **APPENDIX**

<b>Fig. A1</b>	The contact width, $d_0$ , (top chart) for experiment Fig. 4.12 using 39 stripe images (Table A1). Conversion of acoustic losses of the double transit measured in mV (mean value) into attenuation (dB), Table A2.	228
<b>Fig. A2</b>	Contact width, $d_0$ , (top chart) for experiment Fig. 4.13 using 25 stripe images (Table A1). Conversion of acoustic losses of the double transit and single transit measured in mV (mean value) into attenuation (dB), Table A2.	229
<b>Fig. A3</b>	Contact width, $d_0$ , (top chart) for experiment Fig. 4.14 using 24 stripe images (Table A1). Conversion of acoustic losses of the double transit and single transit measured in mV (mean value) into attenuation (dB), Table A2.	230
<b>Fig. A4</b>	Contact width, $d_0$ , (top chart) for experiment Fig. 4.15 using 18 stripe images (Table A1). Conversion of acoustic losses of the double transit and single	231

**LIST OF FIGURES**

---

	transit measured in mV (mean value) into attenuation (dB), Table A2.	
<b>Fig. A5</b>	Contact width, $d_0$ , (top chart) for experiment Figs. 4.16 (a) and 4.18 (b) using 41 stripe images (Table A1). Conversion of acoustic losses of the double transit measured in mV (mean value) into attenuation (dB), Table A2.	232
<b>Fig. A6</b>	Contact width, $d_0$ , (top chart) for experiment Figs. 4.16 (b) using 45 stripe images (Table A1). Conversion of acoustic losses of the double transit measured in mV (mean value) into attenuation (dB), Table A2.	233
<b>Fig. A7</b>	Contact width, $d_0$ , (top chart) for experiment Figs. 4.18 (a) using 41 stripe images (Table A1). Conversion of acoustic losses of the double transit measured in mV (mean value) into attenuation (dB), Table A2.	234

# LIST OF TABLES

## CHAPTER 3 *EXPERIMENTAL DEVELOPMENT*

<b>Table 3.1</b>	A summary of the design parameters and device parameters according to the mask design are presented.	100
<b>Table 3.2</b>	The manufacturer's data sheet for 128° Y-X Lithium Niobate (LiNbO <sub>3</sub> ).	101
<b>Table 3.3</b>	The characteristic velocity for the spreading dynamics of PDMS oils and the capillary length, $\kappa^{-1}$ , are listed.	134

## CHAPTER 4 *RESULTS*

<b>Table 4.1 (a)</b>	Geometrical relation for reflection resonances in dependence of viscosity and changes of height and contact width of the stripe between attenuation resonances.	178
<b>Table 4.1 (b)</b>	Geometrical relations for reflection resonances.	179
<b>Table 4.1 (c)</b>	Geometrical fits for the contact width, $d_0$ and cylindrical cap radius, $R$ , obtained from the optical measurements for PDMS oils spreading on lithium niobate.	179

## CHAPTER 5 *ANALYSIS AND DISCUSSION*

<b>Table 5.1</b>	Geometrical fits for the contact width, $d_0$ and cylindrical cap radius, $R$ , obtained from the optical measurements for PDMS oils spreading on lithium niobate.	193
<b>Table 5.2</b>	Starting conditions for the computational model to match the fluid width after deposition and the other geometrical dependent parameter for a 100,000 cSt PDMS oil on a 168.8 MHz SAW device.	193
<b>Table 5.3</b>	Geometrical fits for the contact width, $d_0$ and cylindrical cap radius, $R$ , obtained from the optical measurements for PDMS oils spreading on lithium niobate.	203
<b>Table 5.4</b>	Starting conditions for the computational model to match correctly the fluid width after deposition and the other geometrical dependent parameter for 30,000 cSt PDMS and 10,000 cSt PDMS on a 168.8 MHz SAW-device.	203

**APPENDIX**

<b>Table A1</b>	Geometrical fits for the contact width, $d_0$ from the optical measurements for PDMS oils spreading on lithium niobate.	226
<b>Table A2</b>	The coefficient, $A_1 - A_8$ and the constant, $C$ for the logarithmic power series to determine the conversion function for the amplitude magnitude of the single and double transit to convert the mean value into attenuation in dB.	227

# CHAPTER 1

# *INTRODUCTION*

## 1.1. Introduction

Wetting of solid surfaces at macroscopic and microscopic length scales are of fundamental and growing importance to the scientific community in understanding microscopic solid-liquid interactions. It is important to many industries, such as the agrochemical, manufacturing and the electronics industries. In the agrochemical industry, wetting controls the film formation properties in pesticide formulations and the drainage properties of containers to ensure little residue remains and therefore minimises environmental pollution. In the manufacturing industry the understanding of wetting processes and their physical meaning is necessary due to the use of lubrication and surface treatments for manufacturing composite materials. In process control of printed circuit boards (PCB's) the comprehension of wetting ensures film homogeneity and film stability across the board, when coated with protective films or in photolithography where photoresist films require a highly clean surface to prevent film discontinuity imposed by surface heterogeneities. The process of the liquid, wetting a solid surface can be found in a number of other practical situations such as textile dyeing, gluing, paints and metal and glass anticorrosives [1]. Surface treatment to change the short-range interactions of the substrate with liquid and vapour molecules are important to ensure both the stability of films and the dewetting of surfaces. The degree of wetting at the solid-liquid interface can be investigated by measuring the contact angle of various fluids on the surface and hence determine properties, such as adhesion strength.

At the same time sensors are important to the scientific community and industry and regarded as a precise and cost effective measurement tool. Sensors produce an output signal in response to some input quantity. The input quantity can be either a physical quantity such as the mechanical properties of a thin film or fluid or chemical and biological quantities such as the concentration and identities of unknown species in air or liquid media. The process of transduction converts the input event into an electrical signal. The input event perturbs the sensing part of the sensor and causes a change at the output signal. More importantly such devices are widely used in chemical and

biological process monitoring to warn if toxic vapours or hazardous substances are present in the environment. Another area where sensors are gaining more and more importance is in the clinical diagnostics and surveillance of patients where they provide a physician or surgeon with the vital status or condition of the patient on which to base a medical decision. Sensors have to fulfil a variety of tasks such as sensitivity, resolution and selectivity. Sensitivity is a measure of the magnitude of the output signal produced in response to an input quantity of given magnitude. Resolution characterises minimum changes of an input quantity to which a sensor can respond and selectivity indicates the ability of the sensor to which degree it is possible to distinguish one input quantity from another [2].

Strong efforts in the past dedicated to the development of integrated circuits has led to a reduction in costs of storing and computing information and transmitting information from one location to another. This progress made it possible to create and construct sophisticated systems to process complex sensor signals. However, sensors themselves have evolved more slowly and have remained relatively large and expensive, until recently. The realisation that sensor development is still lagging behind that of integrated circuits [3] has attracted the attention of many scientists to develop inexpensive microsensors. In recent years the availability of a growing number of microsensors with a large diversity in sensing characteristics has found its way outside the research laboratories into development and commercialisation [4]. Their small size, ruggedness and low power consumption [5, 6] encouraged researchers worldwide to pursue further research into their potentials to sense physical or chemical and biological quantities. The scale of interest in the interaction of microsensors with physico-chemical quantities has resulted in more than 3000 references to "chemical sensors" alone between 1985 and 1989 [2].

An extensive role in the investigation of chemical interaction was the use of miniaturised potentiometric and amperometric chemical sensors [7]. Optical sensors provide chemical, physical or biological information via changes in refractive index, amount of absorbance, or intensity in photoluminescence. Whereas these are well established methods of sensing physico-chemical quantities, high frequency acoustics, as a method of sensing and detecting

physical, chemical and/or biological quantities has only been introduced relatively recently [2].

Acoustic microsensors, previously assumed to be acting as simple mass detectors, have been found to respond to a combination of other factors. A variety of properties of solid or liquid media have been identified such as liquid density, liquid viscosity, polymer modulus, and electrical conductivity [8]. Different substrate materials have been used to create acoustic microsensors. These materials can be characterised as isotropic solids or anisotropic piezoelectric crystals with a large variety of different cuts of the crystallographic orientation which allows surface waves and elastic bulk waves [9, 10] to propagate in any direction in the solid. The crystallographic orientation and thickness of the piezoelectric material, influences the propagation, shape and properties of the wave. The variety of different types of wave generation has led to an increasing availability of acoustic wave devices and recent advances in understanding the mechanisms of sensor response. One remarkable feature of acoustic microsensors is that their analyte does not necessarily require any special properties such as optical, electrochemical or enzymic activity [11].

Bulk acoustic waves propagating inside solids have played an important role in electronics [12]. Devices using a delay line geometry as shown in Fig. 1.1 convert an electromagnetic signal into a bulk acoustic wave via a transducer. Such a device uses a solid propagation medium with transducers mounted at each end. One transducer generates an acoustic wave when an oscillatory voltage is applied to it. The acoustic wave traverses the length of the crystal, a path many wavelengths long (the signal is delayed), and the acoustic wave is then transduced back at the other end into an outgoing electromagnetic wave. The output waveform is a delayed replica of the input waveform. Due to the low propagation speed within the solid large delays can be obtained, typically a few microseconds for each cm of the propagation path [13]. However, the wave is present in the interior of the crystal and it is difficult to obtain access to the wave in order to modify it (Fig. 1.1) thus inhibiting its use as a sensor.

It had been known since Lord Rayleigh's [14] investigation in 1885 that elastic waves could also propagate along the boundary surfaces of solids. In the years since his pioneering study, properties of surface waves have

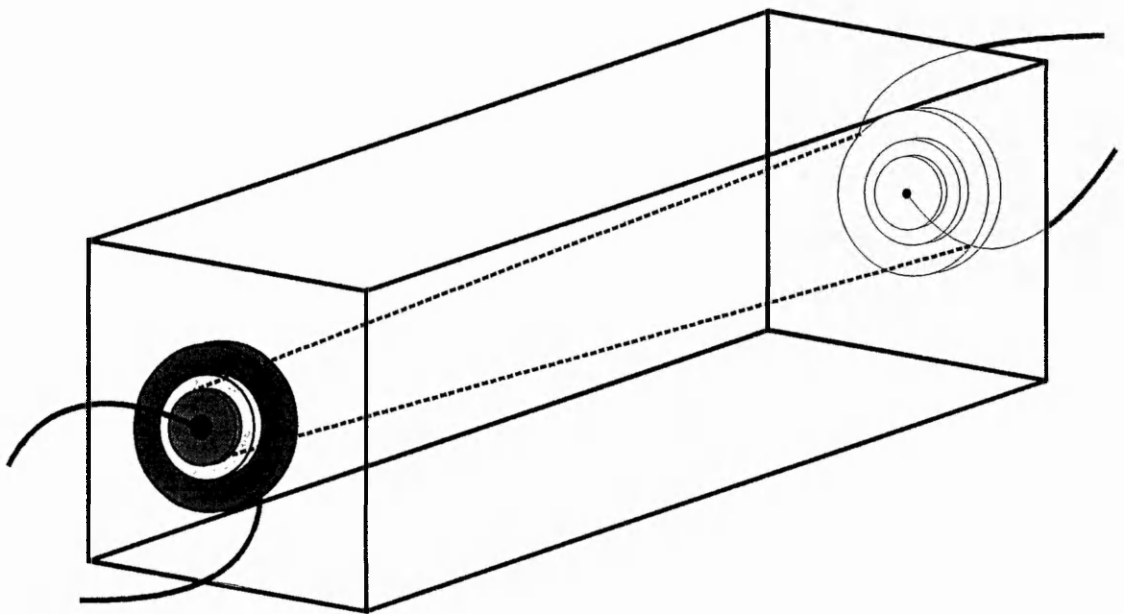


**Fig. 1.1** A typical simple bulk-wave delay line. A bulk wave beam propagates within the solid medium between the transducers.

gradually been discovered [12]. A SAW is a coupled elastic and electric field disturbance and can therefore be generated by distorting the surface of a piezoelectric material in a periodic manner [15]. The wave travels along the stress-free surface of the solid giving one significant advantage over bulk acoustic waves. The surface wave is always accessible as the wave travels, allowing a free and unrestricted access to the surface. Consequently it is possible to generate or detect surface waves with surface structures such as interdigital transducers on piezoelectric materials. Access to the wave at the surface allows a modification of the wave velocity due to surface manipulations of chemical or physical origin involving deposited layers of solid or liquid quantity. In order to use such devices as chemical transducers a chemically sensitive layer is often added to the device surface to recognise and bind the analyte of interest. The binding process means that the analyte attaches to the surface of the sensor where it alters one or more physical properties to which the acoustic wave responds. These effects have been described by many authors. A typical example is the absorption of vapour from the gas phase into chemical active materials of both organic and inorganic compounds. Caliendo et al. [16, 17, 18] deposited or spin coated various organic chemical interactive substances, such as polyphenylacetylene (PPA), poly-(distibutylphosphine)-palladium-diethylnylbi-phenyl (Pt-DEBP) etc. and an inorganic compound such as titanium oxide ( $\text{TiO}_2$ ), on surface acoustic wave (SAW) devices designed as relative humidity (RH) sensors, for different orientations of both, quartz and lithium niobate substrates. They exposed the chemically modified devices to water vapour of different concentrations and a variety of hydroxylated molecules such as acetone and ethanol and compared their results with a standard RH sensor as reference element. Tom-Moy et al. [19] developed a new kind of chemical sensor based on surface transverse waves (STW's) operating at a frequency of 250 MHz. They used a 500 Å thick  $\text{SiO}_2$  film as the sensing layer. Their bioanalytical sensor detected atrazine in the range of 0.06 ppb to 10 ppm. Welsch et al. [20, 21] coated a surface acoustic wave (SAW) dual delay line lithium tantalate ( $\text{LiTaO}_3$ ) (SAW) device to build an immunosensor operating at a frequency of 345 MHz with a sputtered chromium/gold layer as the coating for the protein binding process. The coating also eliminates the evanescent electric field travelling with the SAW. They

investigated the binding of immunoglobins of type G in phosphate buffer by depositing small droplets of liquid onto the substrate surface, or using a flow-through cell. The experimental results gave a device sensitivity of  $112.5 \text{ ngmm}^{-2}$  and indicated a quadratic frequency dependence of the sensor signal demonstrating that a mass-loading effect existed. Gizeli et al [22] used an immunosensor based on an acoustic waveguide geometry that supports a Love wave. The binding surface was attached to a gold layer and fabricated of a biotinylated supported lipid layer which binds specifically the protein streptavidin. They could show that rabbit anti-goat IgG in low concentration could be detected and identified by the sensor and reference measurements proved that the immunosensor response can be entirely related to the mass density of the protein layer.

In order to investigate the physical properties of microsensors interacting with liquid quantities, interest has focused on sensing liquid density, liquid viscosity and electrical conductivity. These types of measurements do not necessarily require a chemically sensitive layer that can recognise or bind the analyte. A cause of physical changes (interaction mechanisms) of the sensor can be attributed to a perturbation in wave-propagation characteristics at the piezoelectric substrate-liquid interface. Nomura and Yasuda [23] used a leaky surface acoustic wave (SAW) sensor immersed in a liquid pool to determine the acoustic properties (changes of the surface wave velocity and acoustic losses due to damping of the acoustic wave amplitude) of water/glycerol mixtures. The shear horizontal displacement of the wave propagation makes the sensor less susceptible to energy losses than Rayleigh wave devices. The shear wave propagating in the plane of the substrate coupled viscously to the adjacent liquid. Perturbation theory [24] was used to model the attenuation as a function of the viscosity/density product. Martin et al. [25] used a two-port shear-horizontal (SH) acoustic plate mode (APM) sensor to probe the solid-liquid interface of thinned quartz plates in contact with glycerol/water mixtures. The sensor response was a result of the physical interaction with the analyte such as mass loading, viscous entrainment of the contacting liquid and acoustoelectric effects by coupling between the evanescent plate mode electric field and ions and dipoles in solution. Kondoh and Shiokawa [26] presented a

taste sensor based on a shear horizontal displacement SH-SAW sensor using an uncoated 36YX-LiTaO<sub>3</sub> piezoelectric substrate. The sensor was used to identify 11 kinds of fruit juices by classification in principal-component analysis and discriminate analysis. The electric-field associated with the SAW propagation interacted with the electric properties of the juice and affected the velocity and/or attenuation of the surface wave amplitude of the SH-SAW. The SH-SAW liquid sensor has been shown to detect viscosity and mass loading effects as the mechanical perturbation, and permittivity and conductivity as the acoustoelectric interaction [27, 28, 29, 30]. Within the study of liquids the acoustoelectric effect offers the possibility to monitor in real-time the changes in interfacial charges in solution.

Most studies of physical or chemical interactions with liquids using the acoustic technique especially acoustic microsensors, have been limited to fixed pools of liquid in contact with the device surface. Studies concerning the dynamic evolution of spatially localised fluids spreading across the solid surface of an acoustic sensor investigating acoustic wave-liquid interaction have been rarely reported in the literature. However, the use of the acoustic technique to probe the wetting dynamics of the liquid partially localised on the device surface enables one to investigate solid-liquid interactions directly at the solid-liquid interface and provides the ability to study extensively the dynamic evolution of the fluid in-situ and in real time.

## 1.2. Spreading of a Viscous Liquid on a Horizontal Surface

Spreading of liquids across a solid surface has been studied since the early nineteenth century by famous physicists, such as Young (1805), Laplace (1806, 1807), Plateau (1869) and Gibbs (1875-1878) [1]. They were the forerunners for the understanding of a thermodynamic and mechanical description of capillarity. This enabled other researchers to interpret a wide range of solid-liquid interfacial effects occurring at the macroscopic scale e.g.

capillary rise, the shape of sessile or pendant drops and the shape of a meniscus in a glass cylinder.

### 1.2.1. Contact Angle and Interface Energy

Classical capillarity involves the notion of interfacial tension,  $\gamma_{ij}$ .  $\gamma$  is a force per unit length of the triple line and  $i$  and  $j$  are two different phases characterised by the existing three aggregate states, vapour V, liquid L and solid S. Consider a small drop of fluid deposited on a flat surface. The drop shape will evolve and adopt a spherical cap cross-section with a finite contact angle [31]. At this stage the three interfaces come into play and their interfacial tensions drive the spreading of the drop until it reaches an equilibrium shape. If the drop is able to balance the interfacial energies, partial wetting occurs as can be seen in Fig. 1.2 (a) and 1.2 (b) and a finite contact angle,  $\theta_e$  exists. Here,  $\theta_e$  denotes the equilibrium contact angle. In the situation where complete wetting occurs as demonstrated in Fig. 1.2 (c) the equilibrium contact angle vanishes to  $\theta_e = 0$ . In the case of partial wetting, the wetted portion of the surface is delimited by the contact line, which for a droplet is a circle.

When we look at the interaction between the solid, the liquid and the vapour the three interfacial tensions involved are  $\gamma_{SL}$ ,  $\gamma_{SV}$ ,  $\gamma_{LV}$ , respectively the solid-liquid (SL) interfacial tension, solid-vapour (SV) interfacial tension, and the liquid-vapour (LV) interfacial tension. The interfacial tensions,  $\gamma_{ij}$  form the region where the three phases merge exactly at the triple line as shown in Fig. 1.3. Alternatively, it can be viewed as the energy per unit area of the interfacial surface.

Considering partial wetting under ideal conditions, when the solid surface has no roughness and is homogenous, the spreading parameter (coefficient),  $S = \gamma_{SV} - (\gamma_{SL} + \gamma_{LV})$ , is negative ( $S < 0$ ) and the drop does not spread, it retains a spherical cap cross-sectional shape and thus the drop reaches an equilibrium condition characterised by the contact angle (Fig. 1.3). The equilibrium contact angle is determined by the values of the  $\gamma_{ij}$  interfacial tensions between the three phases [32, 33]. The interfacial tensions are acting tangential to the

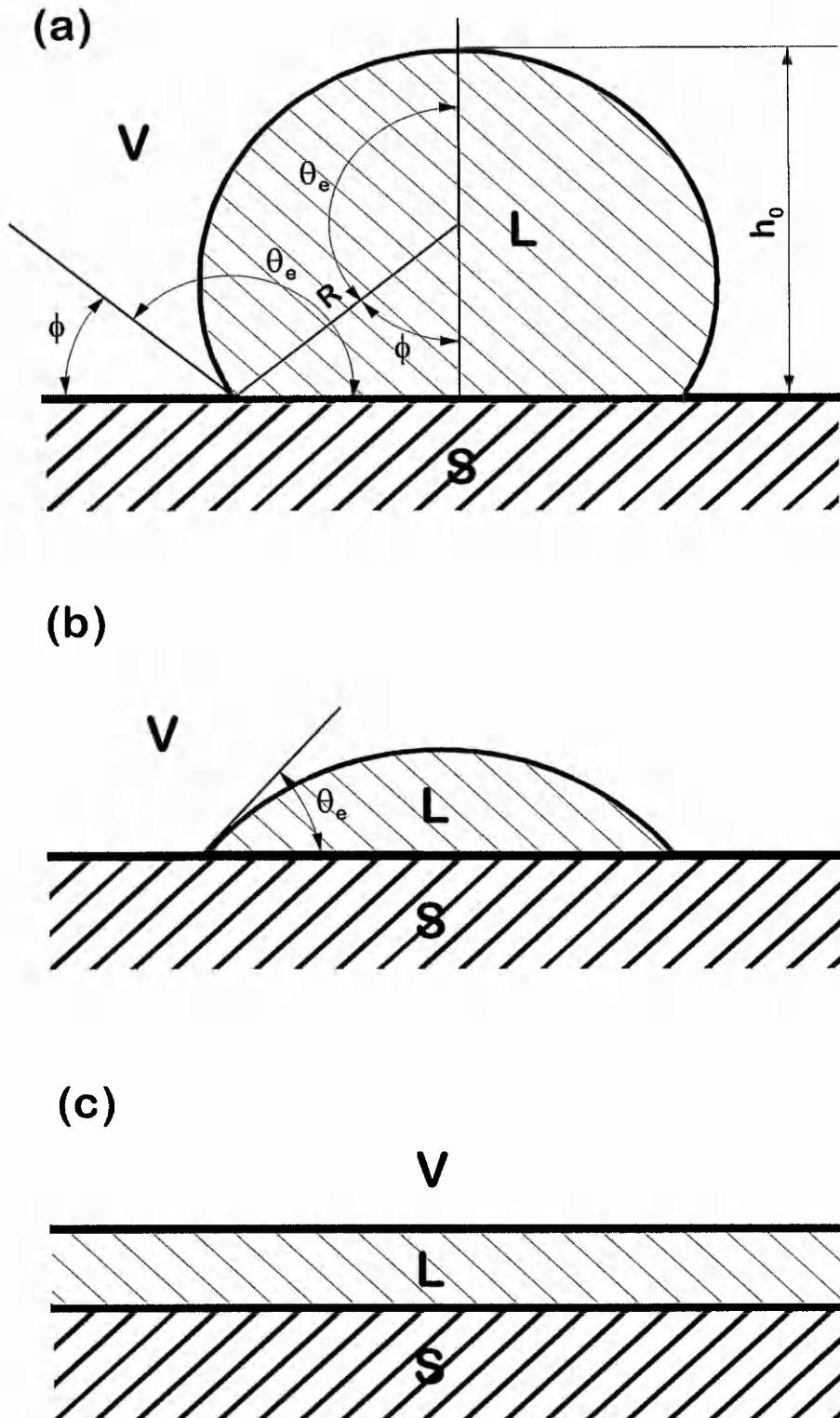


**Fig. 1.2** A small droplet in equilibrium over a horizontal surface: (a) and (b) correspond to partial wetting, the trend towards wetting being stronger in (b) than in (a). (c) corresponds to complete wetting ( $\theta_e = 0$ ).

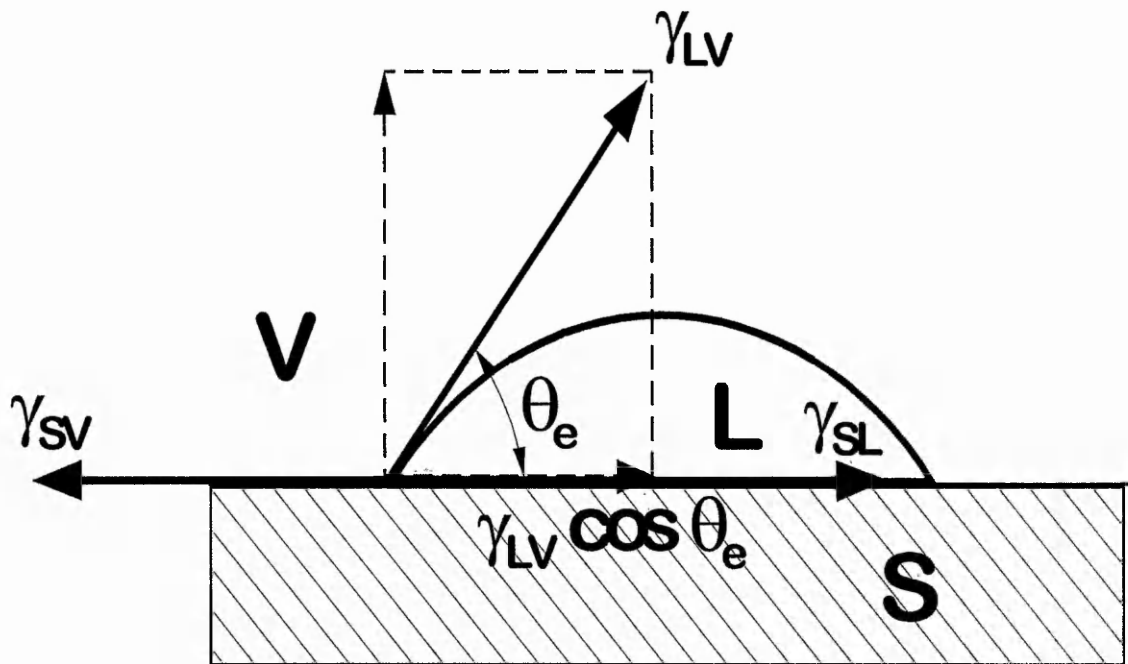


**Fig. 1.3** Young's force balance giving the static contact angle.

contact line where the three phases merge. At mechanical equilibrium, the horizontal components of the interfacial forces balance (Fig. 1.3):

$$\gamma_{SV} - \gamma_{SL} = \gamma_{LV} \cos \theta_e \quad (1.1)$$

or in terms of the spreading coefficient  $S$ ,

$$\cos \theta_e = (\gamma_{SV} - \gamma_{SL}) / \gamma_{LV} = 1 + S / \gamma_{LV} \quad (1.2)$$

where  $\theta_e$  is the equilibrium contact angle. This relation has been proposed by Young in 1805 [34] and is the fundamental law of classical capillarity. The last term in equation (1.1) is the projection of the vector  $\gamma_{LV}$  on the plane of the surface (see Fig. 1.3).

In a situation where complete wetting occurs the spreading parameter  $S$  is positive ( $S > 0$ ); the drop spontaneously spreads across the surface and tends to cover the entire surface. Equation (1.1) expresses  $\cos \theta_e$  as a function of the interfacial energies. The case,  $\gamma_{LV} = \gamma_{SV} - \gamma_{SL}$  leads then to  $\cos \theta_e = 1$  if  $\theta_e = 0$  (complete wetting). This situation appears rather exceptional. In fact, it is not, because  $\gamma_{SV} + \gamma_{LV}$  can never be larger than  $\gamma_{SL}$  (in thermodynamic equilibrium). If it was larger, this would imply that the free energy of the solid-vapour interface ( $\gamma_{SV}$ ) could be lowered, by intercalating a liquid film of macroscopic thickness to ( $\gamma_{SL} + \gamma_{LV}$ ). The equilibrium solid-vapour interface then automatically comprises such a film, and the true  $\gamma_{SV}$  is identical to  $\gamma_{SL} + \gamma_{LV}$ , i.e. we have complete wetting in this regime.

In the other case, where one deals with non-equilibrium situations, one may have a solid-vapour interfacial energy,  $\gamma_{SO}$  that is larger than  $\gamma_{SL} + \gamma_{LV}$ . The difference

$$S = \gamma_{SO} - \gamma_{SL} - \gamma_{LV}, \quad (1.3)$$

is called the spreading coefficient. In order to distinguish between two variations in the surface conditions, physically,  $\gamma_{SO}$  is associated with a "dry" solid surface,

while  $\gamma_{SV}$  is associated with a “moist” surface [35]. The rate at which the spreading occurs is controlled by the surface tension and viscous dissipation, and for a viscous liquids, such as polydimethylsiloxane oils spreading on a solid surface, the spreading kinetics are independent of the spreading coefficient,  $S$  of the surface [31, 36]. An investigation of the macroscopic scale of the drop, spreading on a “dry” solid surface reveals a discrepancy. With a vanishing equilibrium angle,  $\theta_e = 0$  there exists no clear distinction whether  $S = 0$  or  $S > 0$ . De Gennes [35] explained the phenomena in such a manner that for a “moist” surface ( $\gamma_{SV}$ ) the wetting system “locks in” at an equilibrium angle,  $\theta_e = 0$ , but for the “dry” case ( $\gamma_{SO}$ ) such a “lock in” process does not happen and one would expect  $S$  to be positive.

It is also important to notice that Young's law stems from a mechanical equilibrium condition on the contact line which is a region of liquid with a vanishingly small volume. The effect of body forces such as gravity on the contact line is also vanishingly small and Young's law as given by equation (1.1) is valid even in the presence of gravity or of any other body force. Gravity affects the circular shape of the cross section of liquid drops in their central region where they become flattened by the drag of the gravitational force and this results in a distortion of the spherical cap. However, in a small region close to the contact line, (significantly smaller than the capillary length beyond which gravity becomes important) the liquid-vapour and the solid-liquid interfaces form an angle given by Young's law [1].

Another problem with the formation of contact angles is the existence of contact angle hysteresis. A phenomenon in which the contact angle formed between the solid-liquid and the liquid-vapour interface by the liquid is advancing across a “dry” or unwetted surface is generally larger than the angle of the same liquid as it recedes across a previously wetted “moist” surface. Models which predict the existence of metastable states or contact angle hysteresis arising from heterogeneity and roughness have been reviewed in detail by Léger et al. [1], and de Gennes [35].

## 1.2.2. High-Energy and Low-Energy Surfaces

There are two main types of solids,

- (a) hard solids (covalent, ionic, or metallic)
- (b) weak molecular crystals (bound by van der Waals forces, or in some special cases by hydrogen bonds).

Hard solids are generally classified as "high-energy surfaces" ( $\gamma_{SO} \sim 500 \cdot 10^{-7}$  to  $5000 \cdot 10^{-7}$  J/cm<sup>2</sup>), while molecular solids (and also molecular liquids) belong to the class of "low-energy surfaces" ( $\gamma_{SO} \sim 50 \cdot 10^{-7}$  J/cm<sup>2</sup>).

Most molecular liquids in contact with high energy surfaces completely wet the surface ( $S \geq 0$ ) (complete wetting), assuming that hard bonds control  $\gamma_{SO}$ , while van der Waals interactions control the solid-liquid energies (no chemical binding between liquid and solid). The solid-liquid energy can be expressed as:

$$\gamma_{SL} = \gamma_{SO} + \gamma_{LV} - V_{SL} \quad (V_{SL} > 0). \quad (1.4)$$

Here the term  $-V_{SL}$  describes the relation of van der Waals forces interacting between solid and liquid near the surface. Equation (1.4) represents the condition when the solid and liquid regions are progressively brought into contact. When they are well separated, the energy is  $\gamma_{SO} + \gamma_{LV}$ ; when contact is established between the solid and the liquid, the energy which is recovered can be expressed as  $-V_{SL}$ . High-energy surfaces are wetted by molecular liquids, not because  $\gamma_{SO}$  is high, but rather because the underlying solid usually has a polarizability much higher than the polarizability of the liquid [35].

Low-energy surfaces can give rise to partial or complete wetting, dependent on the liquid chosen. In some cases we find complete wetting by a whole series of liquids. In other cases we find a finite contact angle,  $\theta_e$ , varying within the series. In practice many forces contribute to the solid-liquid interactions - dipoles, hydrogen bonds, etc., with each force giving its contribution to  $V_{SL}$  [35].

## 1.3. Standard Methods of Measuring Wetting Phenomena

### 1.3.1. Static Equilibrium Measurement Methods

One of the most established methods to obtain the static equilibrium is to measure the contact angle of a drop of liquid resting on a solid surface. The equilibrium contact angle is measured using direct visual observation such as a microscope with an eyepiece. Zisman et al [37, 38] investigated receding contact angles,  $\theta_r$  and advancing contact angles,  $\theta_a$ , using a tip of fine platinum wire. The receding angle is determined by a shrinking contact area of the solid-liquid interface while the advancing contact angle can be measured when the contact area increases [35]. The measurement was performed by adding more liquid to the droplet from the wire and measuring  $\theta$  after each addition of liquid. They conducted the measurement by using a comparator microscope with a goniometer scale.

Good et al [39, 40] used a micrometer syringe with a fine needle to deposit the drop. The advantage of this technique is to keep the drop captive while additional liquid is added until a steady value of  $\theta_a$  is obtained, and the addition of liquid can be stopped. To obtain a receding angle, liquid can be withdrawn from the drop by sucking the liquid into the syringe.

Another method to deduce the contact angle is the use of a photograph of the drop profile where a direct measurement from the image can be obtained [41]. A light reflection method has also been used [42]. A vertical illuminator emits a light beam through a microscope tube. The light is only reflected back into the microscope when the tube direction is perpendicular to the liquid surface. The contact angle is equal to the angle which the microscope tube forms with the vertical when the liquid appears bright. Another method uses the liquid as a convex lens with refractive index  $n$ . A parallel beam is reflected into a cone of aperture range  $2\theta$  [43]. This allows a simultaneous test of the whole

periphery of the drop. Size and thickness can be deduced from direct observation from the microscope.

In the tilting plate method a several centimetre wide polymer plate or polymer cylinder is immersed into a liquid pool and tilted to an angle until the liquid surface at the liquid-vapour interface appears to remain perfectly flat and forms a horizontal line when the liquid is in contact with the polymer surface. This method can be used when large amounts of liquid are available and the measurement is not affected by gravitational distortion [44]. Tilted plates are also used to observe both advancing and receding contact angles. The horizontal plate is tilted in the horizontal plane at an angle,  $\theta$  and a drop resting on the surface in equilibrium forms two distinct angles, the receding and the advancing contact angle, due to gravitational drag.

The idea of the Wilhelmy plate method proposed by Wilhelmy (1863) [45] is to use a thin plate, such as a microscope slide or a polymeric material using an automated Wilhelmy balance, and partially immerse the plate into the testing liquid. The slide is suspended from the beam of an electrobalance. When the slide immerses into the liquid and is held stationary a meniscus rises to a definite height if  $\theta$  is finite. When connecting the balance to a computer measurements of both static and dynamic contact angles are possible. When the platform assembly is held stationary (static mode) the variation of the electrobalance force with time is measured [46].

### 1.3.2. Methods of Measuring the Dynamics of Liquid Spreading

The dynamics of a moving contact line is related to the approach of the equilibrium and its relationship with the interfacial energies in the system at the triple line. The spreading rate of a viscous liquid such as polydimethylsiloxane (PDMS) oil, is determined by a balance between the change of surface free energy and viscous dissipation [47].

Most of the research in the past has focused on the traditional investigation of equilibrium properties of solid-liquid interaction. Over the last

decade interest in the dynamics of wetting and dewetting processes have increased. Prior to 1985 dynamic wetting was the subject of steady, but unspectacular, research activity. Theory did not accord well with experimental data. The only exception was given by Tanner's (1979) hydrodynamic theory [48], related to the complete spreading of non-volatile, viscous oils on high energy surfaces. Tanner demonstrated that the edge speed of macroscopic droplets on high-energy surfaces is related to the cube of the dynamic contact angle. De Gennes and co-workers [35, 49] extended Tanner's hydrodynamic model. They reviewed dry wetting of non-volatile liquid, spreading on a solid surface until the liquid reached equilibrium shape or until the liquid formed a thick liquid film. De Gennes and co-workers gave a clear exposition of the role of interfacial energies and energy dissipation in determining the rate of spreading and quasi-equilibrium shapes of micro-droplets. Léger and Joanny [1] recently reviewed the wetting and spreading properties of simple liquids in respect of the heterogeneities of the solid surface and of the spreading kinetics. A special aspect of their review was the formation of contact angle hysteresis due to the heterogeneities of the solid surface and the investigation of a mesoscopic precursor film which spreads ahead of the body of the fluid.

Fundamental aspects of solid-liquid surface interactions have been elucidated such as, the investigation of polymer slippage on semi-ideal surfaces with an associated transition effect between a low-velocity non-slipping regime and a high-velocity, slipping regime [50]. The phenomenon of surface-induced self-assembly, observed as ethyloxylated siloxane surfactants with different composition spreading at the solid-vapour interface [51] to extract information about molecular properties is critical for spreading. The shape evolution of microdroplets of pure surfactants put on high- and low-energy solid surfaces has been monitored by ellipsometry. The shape, structure and the degree of intrinsic order of a spreading layer precursor varies strongly with the characteristics of the surface and shows that atmospheric water can significantly enhance the rate of spreading. The transition from partial wetting to high-energy-type complete wetting has led to the identification of a new regime, between the two distinct wetting regimes, where the whole spreading is highly sensitive to the layer polarisability [52]. The dynamics and stability of fluid interfaces has provided a new interpretation of the thickness of surface-tension-

gradient-driven spreading films [53]. The relationship between apparent and real contact angles [54, 55, 56], slip boundary conditions [57, 58], and precursor films spreading in advance of the macroscopic cap of a droplet which is to be believed, has a molecular thickness [36, 51] has also been extensively studied. This has motivated researchers to find other techniques to investigate the complex microscopic interface shapes near the moving contact line.

Traditional methods for quantitatively examining macroscopic droplets draining into microscopic films are based on profile or plan views [59]. The evaluation of the side profile allows one to determine the cross-section and with the aid of video imaging systems, digitised image analysis can provide a complete picture of the spreading dynamics. However, there may be a limitation associated with this method. The spatial resolution of the cross-section may not hold the shape of a whole droplet, due to surface heterogeneity such as single defects on the surface, surface roughness, or surface contamination, causing a depinning effect of the contact line [1, 35]. On the other hand a plan view observation using interferometry provides the entire periphery of a droplet. The use of digital image analysis after processing the images offers a possibility to reconstruct the profile by investigating the interference pattern. The introduction of video observation techniques using a CCD-Camera enables timed video analysis and dynamic information of the evolution of the liquid to be extracted [60]. In the situation where the microscopic part of the droplet, such as the film thickness, is of importance rather than the macroscopic profile, laser interferometry, X-ray reflectivity, ellipsocontrast and ellipsometry, present an extension to the one used in static equilibrium studies.

### 1.3.2.1. Laser Light Interference

Chen and Wada [55] reported in one of their previous papers [61] the use of time-sequence photographs to investigate the silhouette of a non-volatile liquid drop spreading on a smooth horizontal surface. They obtained the drop diameter, apex height and contact angle and found that the photographs in reference [61] are limited in resolution and that an angle measured in this way

is apparent and its dependence on the distance cannot be studied. As a consequence they focused on the edge of a spreading drop using laser light interference to study the meniscus shape as a function of distance and characteristic velocity of the spreading liquid. The technique uses a parallel laser beam illuminating the edge of a droplet. The droplet is deposited on a clean glass surface. The image is transferred into a microscope object lens and is recorded onto a video tape by a video camera mounted on top of the microscope. The vertical resolution is dependent on the laser beam wavelength  $\lambda$ , and the outmost destructive interference fringe is measured by the relationship  $\lambda/4n$ , where  $n$  is the refractive index of the liquid in order to determine the film thickness at the edge of the drop. The difference in thickness from one bright fringe to the next bright fringe is  $\lambda/2n$ .

### 1.3.2.2. X-Ray Reflectivity

X-ray reflectivity enables one to study and investigate the final stages of spreading [62] and is to be considered as a sensitive and powerful tool to investigate very thin wetting films involving complex density profiles. A highly collimated x-ray beam is targeted at an incidence angle,  $\theta$  just below the critical angle,  $\theta_c$ ; total external reflection takes place and an evanescent wave propagates parallel to the surface and is diffracted by planes normal to the surface. Penetration, which is a function of the incident angle, is small and thus is highly selective for the first layers near the surface [63]. X-ray reflectivity provides a vertical resolution down to 1 Å, but only at the expense of an average lateral resolution of minimum of 50  $\mu\text{m}$ .

### 1.3.2.3. Ellipsocontrast

Ausserré et al. [36] investigated the spreading behaviour of non-volatile liquid on a smooth horizontal surface to observe the existence of a thin precursor film and the universality of the spreading kinetics, followed by means

of simultaneous size and contact angle measurements. They used for their investigation reflection polarising microscopy where a thin film of molecular thickness (precursor film) is placed between two crossed polarisers. For an incidence angle,  $\theta$  and a given angle,  $\phi$  between the plane of incidence and the first polariser axis, the reflection coefficient of the polarised beam depends on the direction of the polarisation with respect to the plane of incidence. In the measurement the contrast due to cross polarisation is a function of the film thickness. Ellipsocontrast shows good vertical resolution up to 50 Å but allows only a qualitative observation of the moving contact line.

#### 1.3.2.4. Ellipsometry

Heslot et al. [64] studied the profile evolution of very small drops of non-volatile liquids. They investigated the profile at its molecular thickness using the technique of ellipsometry. In ellipsometry the behaviour of monochromatic light (for example a laser beam) passing through or reflected by an interface allows the determination of the film thickness, its refractive index and the absorption coefficient. The refractive index and the absorption coefficient are both a function of the wavelength of the light source. When plane polarised light strikes the film surface from a certain angle, the light is resolved into two components, a) the parallel component and b) the component perpendicular to the plane. The components are reflected back differently and as a consequence the beam is elliptically polarised. In the special case where the light hits the surface at the Brewster angle only the perpendicular component will be reflected back, this is under the condition, that the surface between the film and air is absolutely sharp [45]. The vertical resolution of the ellipsometry technique can be obtained up to the Angstrom level whilst still maintaining a good lateral resolution of ca. 20  $\mu\text{m}$ .

## 1.4. Acoustic Sensors and Devices

All the previously mentioned methods, investigating solid-liquid interactions and the dynamics of the moving contact line of the spreading liquid, consider only optical observation and are extensions of ones used in static equilibrium studies and all use plan or profile views of the spreading liquid. The choice of the individual method is linked with the specific aspect of the solid-liquid interaction. The consideration is based either on the time evolution of the macroscopic body of the fluid as the focus of interest or whether the microscopic effects near the contact line is the cause of investigation. However, none of these methods work directly in the spreading plane [65]. One exception represents the work by Ghiradella et al. [66]. They used an in-plane technique to observe the conductance between HCl as conducting substance and an electrode attached to a vertically orientated solid plate. The experiment showed a significant rise in conductivity well before the visible bulk of the liquid came in contact with the electrode showing the possible existence of a precursor film spreading in advance of the moving contact line.

Acoustic wave-liquid interactions have been primarily investigated for the detection of thin uniform gas/fluid surface loading and almost entirely limited to the study of fixed pools of liquids in contact with the device surface. Little work has been performed on surfaces covered with spatially localised thin and thick films of fluid. In particular, the use of surface acoustic wave (SAW) devices using a Rayleigh wave propagation which can be described as elliptical motion of particles on the surface, propagating along the solid-vapour interface, and having their energy confined within one acoustic wavelength of the solid-vapour interface [67] presents a new and elegant way to investigate the interaction mechanism and dynamics of a spreading liquid directly in the spreading plane of the solid-liquid interface and are therefore excellent probes of this interface.

A typical acoustic microsensor consists of a polished and clean piezoelectric material to give a flat and smooth surface of optical quality free of extraneous particles or grease. One or more metal transducers in the form of a thin metal film of thickness of 0.1 to 0.3  $\mu\text{m}$  are usually applied onto the substrate surface by sputter techniques or thermal vacuum evaporation. These

metal structures launch acoustic waves into the material at ultrasonic frequencies ranging from one up to several hundred megahertz. The choice of metal for the transducer is usually selected either for its chemical inertness such as gold or for its acoustic match to the piezoelectric material (e.g. aluminium on lithium niobate). The geometry of the metal transducer and the properties of the substrate determine the acoustic wave type and propagation direction as well as the device resonant frequency. A wave may propagate through the bulk of a plate material or be guided by one surface such as the surface wave or by multiple reflections from multiple surfaces such as a plate wave [8].

### 1.4.1. Thickness Shear Mode (TSM) Resonator

The first of the acoustic sensors used in acoustic wave-liquid interaction studies was the thickness-shear mode (TSM) resonator also sometimes referred as quartz crystal microbalance (QCM) as it has been known by chemists. The TSM was first employed as an active part in radio frequency circuits to stabilise the frequency of radio transmitters. From this, TSM's have found their way into watches, TV apparatus, video recorders, CD-players, computers and mobile phones as frequency control element [68]. The device consists of a thin disk of AT-cut quartz with circular electrodes deposited as thin metal films on both sides of the crystal surface. The electrodes form a single port. If an oscillatory voltage is applied to the port a bulk transverse wave having opposite polarities travels in a direction perpendicular to the crystal surface (the two faces of the crystal resonator). The bulk wave has a particle displacement parallel to the crystal surface a, so called, in-plane motion or standing acoustic shear wave. The waves are only generated at the electrodes because those are the only regions in the crystal where the piezoelectric source term  $e_{ijk}E$  varies spatially.  $e_{ijk}$  denotes the piezoelectric stress constants and  $E$  is the electric field. The fundamental resonant frequency, ( $n = 1$ , where  $n$  determines the resonant mode) of the transverse wave and its harmonics ( $n = 3, 5, 7, \dots$ ), is dependent of the plate thickness  $h_q$  and determines the

acoustic wavelength to  $\lambda = 2 h_q/n$  of the bulk wave [69]. The resonant frequency is typically of the order of 5 to 10 MHz, and an increase in frequency is only achieved with a decrease in plate thickness making the device very fragile when higher frequencies are required.

The TSM's chemical sensing ability can only be achieved by modifying the crystals surface by applying a sorptive film. When the device's sorptive layer is exposed to a chemical substance such as a gaseous or liquid media, this causes a drop in the resonant frequency of the crystal ( $\Delta f$ ), due to a mass increase ( $\Delta m$ ) in the sorptive film [70, 71, 72, 73]. Sauerbrey [74] first investigated the sensitivity of the TSM by studying its response to a thin solid overlayer rigidly attached to the crystal surface. He discovered that there is a proportional relation between the overlayer and the associated fractional frequency shift of the crystal. This could be attributed to an equivalent mass change of the quartz crystal itself [75]. The change in frequency is associated with changes in surface areal density and the square of frequency. That was the first time that a TSM was used as a microbalance also sometimes referred as microgravimetric sensor [76]. Sauerbrey found in his investigation that a weighing sensitivity of  $\pm 4 \times 10^{-9} \text{ g cm}^{-2}$  could be achieved and with special care in designing and assembling the circuit and arranging the mechanical set-up a further increase of sensitivity to  $10^{-10} \text{ g cm}^{-2}$  could be achieved [74]. The shear vibration amplitude of the quartz crystals follows closely the Gaussian distribution curve [77]. Furthermore he could show that the sensitive area of the TSM resonator is mainly restricted to the electrode area showing maximum sensitivity at the centre of the electrode [78, 79, 80] indicating a restricted use of the TSM confined to its electrode area. The decrease of the resonant frequency of a thickness shear vibrating quartz crystal in dependence of the added mass of the overlayer is:

$$\Delta f = - \frac{f_q^2}{N_{cc} \rho_q} \varphi \quad \text{with} \quad \varphi = \frac{\Delta m}{A_{el}}$$

where  $f_q$  is the fundamental resonance frequency of the quartz,  $N_{cc}$  is the frequency constant of the specific crystal cut;  $N_{cc} = f_q h_q$  with  $h_q$  representing the

thickness of the quartz,  $\rho_q$  is the quartz density and  $\varphi$  is the mass sensitivity expressed as a change in mass,  $\Delta m$  by the overlayer in relation to the piezoelectrically active electrode area,  $A_{el}$ . Sauerbrey's findings and the use of the quartz crystal microbalance as a microgravimetric sensor has since been used for real time monitoring of changes at the solid-vapour interface in routine applications such as film thickness monitors and in intricate studies requiring high sensitivity such as the investigation of molecular slip [81, 82, 83].

At the beginning of the '80's researchers recognised that the device is not only capable of detecting the mass changes caused by a solid deposited on the surface of the crystal, but also can be efficiently used to sense liquids. For example Konash and Bastiaans [84] studied the quartz crystal resonator in a flow cell arrangement observing changes in the resonance frequency of the crystal when different liquids passed through the cell and they ascribed the observed changes to the liquid density. Glassford [85] investigated the response factor of a liquid loaded quartz-crystal resonator. Before, it was argued that the TSM could not efficiently work in a liquid environment since unstable oscillation of the shear vibrating quartz crystal due to viscous damping [86] was anticipated resulting in large frequency shifts and intense losses in the quality factor,  $Q$ , leading even to a cessation of the oscillations [87, 88]. In reality, this is not the case because the TSM exhibits an elastic shear wave into the liquid which is viscously coupled to the oscillatory motion of the TSM surface. Coupling occurs because of the zero-slip condition; the molecules of the liquid must follow the motion of the solid [89]. The viscous shear wave, propagating into the liquid, is damped and decays within a penetration depth,  $\delta = \sqrt{2\eta/\omega\rho}$  [87, 90] of the interface, where  $\eta$  is the dynamic viscosity,  $\omega$  the angular frequency and  $\rho$  represents the fluid density. The envelope of the penetration depth is the propagation function  $1/k$  where  $k$  is the propagation constant.

Mainly the TSM device has been used as an active element in an oscillator set-up to investigate the frequency response in the form of a shift in resonance frequency [91, 92, 93, 94]. The frequency change is a result of the analyte properties interacting with the device surface. Moreover, the oscillator gain (amplification) which compensates the analytes perturbation effects such

as viscous energy losses, can be used to provide a means of fluid characterisation [95, 96]. The relationship of losses due to liquid entrainment as a function of the penetration depth has allowed the TSM technique (QCM) to be used for real time in-situ studies of chemical processes [97]. Fluid loaded quartz-crystal resonators (QCR's) exhibit both frequency shifts and energy losses and these changes are associated with limitations in using oscillator circuits with an actively driven quartz crystal resonator. The reason for this is that the quartz is placed in the feedback loop of an RF amplifier. The gain of the amplifier must exceed the insertion losses in order to sustain oscillation. With increasing viscosity the impedance of the quartz increases, thus leading to a decrease in current. The more the quartz is damped the less power it obtains from the driver circuit and thus the output frequency becomes less stable.

One way to overcome these limitations of the oscillator method is to estimate the effect of liquid loading on the electrical equivalent parameter circuit, which describes the unloaded TSM device as an electrical equivalent circuit model [98]. This has encouraged several scientists to utilise the admittance-impedance measurement method of a liquid loaded TSM. The device is no longer the active element in the measurement circuit. It is passively driven by an alternating reference voltage at resonance and any changes in resonant frequency and the resistance related to the equivalent circuit model of the TSM can be measured. Impedance measurements use an impedance analyser [99] and measure the voltage applied across the crystal and the current flowing through it. The ratio of voltage and current can be easily computed and is by definition the impedance. As a result the series resonant frequency obtained from the impedance measurement is the same as in the oscillator method. Martin et al. [100] investigated the effects of viscous coupling and mass loading of a liquid on a TSM by monitoring the electrical admittance. The method enabled them to clearly distinguish between these two properties and allowed them to study the response of the TSM when the contacting surface is rough [101, 102].

Network analysers are therefore capable of measuring for a one port sensor (two-terminals) the voltage incident on and reflected from the load (the sensor) as a function of the frequency. From here all electrical quantities that determine the load can be found, including series resonant frequency and

impedance. Kipling and Thompson [88] and Yang and Thompson [103] used a network analyser to characterise the TSM-liquid interaction. The attention has focused on the response of the series resonant frequency in contact with liquids under various conditions such as surface roughness.

### **1.4.2. Rayleigh Wave - Surface Acoustic Wave Device (SAW)**

The understanding of surface acoustic waves is related to the properties of elastic waves of very high frequency that can be guided along the interface between two media, at least one of them being a solid. The solid medium is usually piezoelectric, so that interactions with electromagnetic fields become possible, and the second medium is usually air.

It was White and Voltmer [104] who achieved a remarkable breakthrough in the development of surface acoustic wave (SAW) devices by inventing the interdigital transducer which made it possible to generate surface waves in piezoelectric solids. SAW's, originally developed for the purpose of high-performance signal processing and radio-frequency signal processing in the form of SAW filters, delay lines and convolvers have been the asset of many practical applications [13, 105]. Their field is diverse and include non-destructive evaluation (NDE), seismology, and signal processing in electronic systems. Devices exhibiting exceptional performance have been used in systems such as pulse compression filters for FM signals used in radar systems, and they are being incorporated into new systems such as matched filters for phase-coded applications in spread spectrum communications systems [15].

The invention by White and Voltmer had also tremendous impact in the use of SAW devices in sensor applications such as gas or liquid sensing. Their device geometry and structure allowed a direct access to the surface wave, propagating along the solid-vapour interface and hence allowed modification and modulation of the surface wave. SAW devices offer an easy integration and production due to their compatibility with planar integrated circuit

technology. The availability of a wide frequency range made the SAW device a high sensitivity sensor for sensing chemical and physical perturbations such as mass loading effects and gaseous or vapour quantities. This had special implications in the field of measurement techniques, where high performance sensors for the detection of specific chemical compounds required cost effective, small in size and easy to design sensor compounds such as the interdigital transducer (IDT). The first approach of using a SAW device as a chemical sensor was based on vapour detection in a delay-line configuration on ST-quartz and lithium niobate,  $\text{LiNbO}_3$ , a strong piezoelectric material, and appeared in a series of papers by Wohltjen and Dessy [106] in 1979. They placed the sensor in the feedback loop of an amplifier to form an oscillator. The delay line consisted of two uniform transducers using one of the transducers to launch the surface wave and the other transducer to detect the incoming signal. The delay was achieved by a separation of the transducers along the surface and producing a time dependent travelling surface wave. An evaluation of the device's characteristics and performance as a detector in a gas chromatograph system when coated with sensitising organic films was examined. A direct comparison of the mass loading sensitivity between a 15 MHz TSM (QCM) oscillator and a 300 MHz SAW oscillator revealed in an investigation by Wohltjen [107] that the SAW device produced a frequency shift of the order of 200 times greater than the TSM under identical mass loading conditions. Martin et al. [108] used for the first time a gas sensor based on a SAW resonator, an extremely narrow-band filter generally used in accurate frequency control circuits as the oscillator element. In this arrangement a SAW emitting transducer is located between two arrays of metal strips on the substrate surface or grooves in the substrate surface. This causes an effect of standing waves due to a matched distance allowing constructive interference of successive reflections to occur.

Chemical or biochemical interfaces can be used to measure the concentration of a specific gas in a mixture of different gases. Herein changes in the gas concentration results in a mass loading effect perturbing the acoustic field of the SAW and a change in the electrical conductivity, interacting with the electric field associated with the SAW's at the chemical interface. This affects the SAW amplitude and phase velocity. As a consequence, selectivity and

reversibility is very important. It has been established in gas sensing that silanisation can be used to control the surface properties of SAW-devices [109]. This is of particular importance in wetting applications since silanisation alters the surface energy and hence the formation of the equilibrium contact angle. The chemical treatments which have been established for sensing applications should also allow the full range of contact angles and spreading regimes on the surface of a SAW device to be obtained.

### 1.4.3. Principle of Operation of a SAW Device

SAW's are micro-miniaturised bandpass filters with a frequency range of 10 MHz up to several GHz, hence their wavelength is in the range between  $<1...100 \mu\text{m}$ , respectively. They consist of a planar electrode structure deposited on a piezoelectric substrate. The wavelength is dependent on the electrode spacing [110].

The first, and most important property of these devices is their low velocity, compared to that of electromagnetic waves. The phase velocity typically is in the range of  $1500 - 4000 \text{ ms}^{-1}$  [111] and is independent of the frequency of operation. This property makes acoustic waves ideal for long delay lines. Acoustic waves also possess a small wavelength when compared with electromagnetic waves of the same frequency. The reduction is of the order of  $10^{-5}$ , the precise value depends on the material used [15].

The surface structure (delay-line geometry) shown in Fig. 1.4 employs two interdigital transducers to excite a Rayleigh surface wave that travels along the free surface of an elastic solid. The particle displacement of Rayleigh surface waves consists of a longitudinal component moving backwards and forwards parallel to the plane and a vertical shear component having a displacement direction up and down normal to the surface when propagating along the crystalline axis. The superposition of these two components results effectively in a retrograde elliptical motion. The wave is non-dispersive and has displacements which decay exponentially away from the surface so that most of the energy (usually more than 95%) is confined to within a depth of

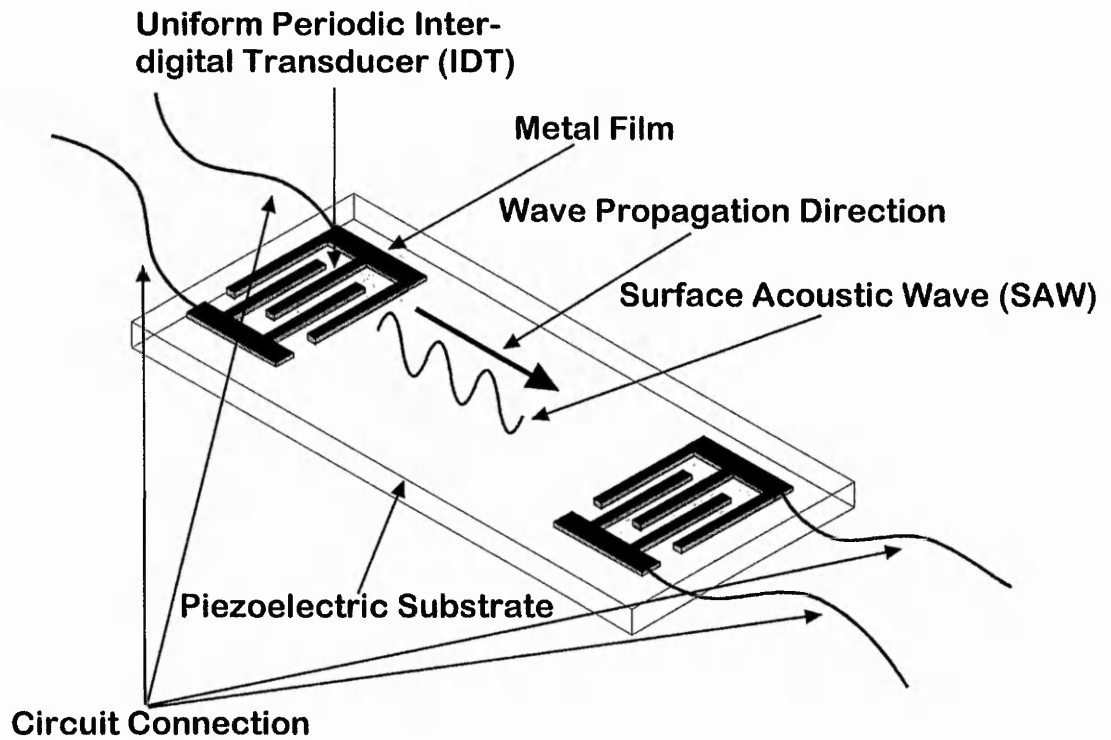


**Fig. 1.4** A surface wave delay line, which employs interdigital transducers on the surface of a piezoelectric crystal. A surface wave propagates between the transducers.

approximately one wavelength. The vertical particle displacement leads to a significant interaction with any medium adjacent to the surface. An evanescent electric field is associated with the SAW propagation when piezoelectric material is used. To generate this type of surface waves a time-varying electrical signal is applied to the planar electrode structure which consists of pairs of interleaved comb structure metal electrodes microlithographically fabricated from a thin film of thickness of 100 to 200 nm by vacuum evaporation or sputtering. The signal introduces into the piezoelectric substrate an electrical field which causes a deformation-wave at the top of the surface propagating in both directions along the crystalline axis and perpendicularly away from the adjacent fingers. As a consequence of the bilateral symmetry, the elastic strains produced by the electrical input signal leave the transducer symmetrically, as demonstrated in Fig. 1.5. A surface wave filter is then created when a second transducer is used to detect the piezoelectric wave emanating from one end of the first transducer. Detection occurs by means of inverse piezoelectric coupling [15].

The choice of crystalline material is dependent on the surface wave characteristic and the associated application. Crystalline materials such as lithium niobate -  $\text{LiNbO}_3$ , quartz -  $\text{SiO}_2$ , lithium tantalate -  $\text{LiTaO}_3$ , etc. (see also the review by Morgan [112]) have been found to have low acoustic losses and are suitable for the operation of interdigital transducers because of their piezoelectric characteristic. It is necessary in surface acoustic wave filter applications and some sensor applications to use single crystal structures in order to reduce high-frequency attenuation characteristics of polycrystalline materials and sometimes to permit piezoelectric effects for electromechanical coupling to the surface wave or to introduce specific propagation properties. The material and orientation is normally chosen in such a manner that only one surface mode can be excited. Usually piezoelectric materials show anisotropic behaviour and therefore elastic waves can still exist. However, anisotropy can induce changes in properties of elastic waves, e.g. the phase velocity depends on the direction of propagation, and generally the direction of energy flow is not parallel to the wave vector. The plane of elliptical polarisation of the particle displacement is not necessarily in the sagittal plane. Furthermore the decay with depth of each displacement component (longitudinal component and shear

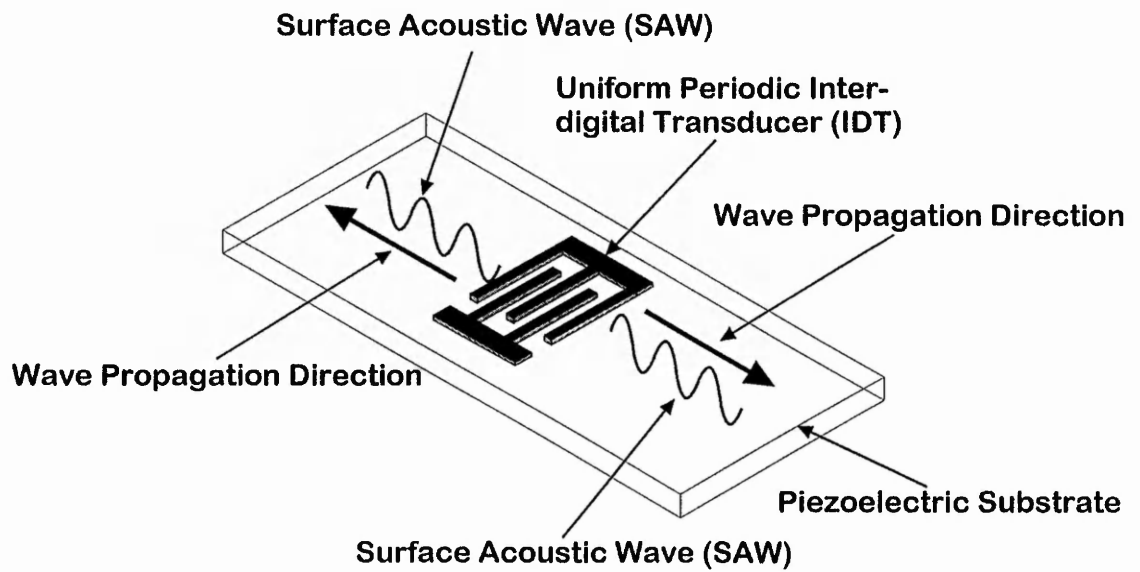


**Fig. 1.5** As a consequence of the bilateral symmetry of the transducer, surface waves leave the transducer in both directions along the crystalline axis and perpendicular away from the adjacent fingers.

vertical component) in anisotropic material is the sum of exponentially damped sinusoids [113].

It should be mentioned that an excited IDT can also generate bulk acoustic waves. While these bulk waves are desired in "conventional" solid state circuits (such as sonar transducers or crystal oscillator circuits), their presence in SAW filter design is a highly undesirable one, which can cause serious degradation of the desired filter response. Unlike surface acoustic waves (SAW's), bulk waves can propagate in any direction within the body of the substrate material. The bulk wave components that arrive at the output IDT induce an output voltage that is additional to those induced by the surface wave. A bulk wave generation at the input transducer can reduce the energy transfer into a surface wave. Also a coupling between bulk modes and surface modes is possible modifying the surface wave radiation. Bulk wave generation is a particular serious problem for broad bandwidth transducers.

#### **1.4.4. Other Classes of Acoustic Sensors for Liquid Sensing**

The TSM has been one of the most widely used piezoelectric detectors for the detection of physical or chemical quantities of a broad class of acoustic wave devices which have now been started to be exploited for solid-liquid interactions [114]. The class of other acoustic wave devices can be divided in horizontally polarised surface acoustic wave devices also called shear horizontal surface acoustic wave (SH-SAW) devices, acoustic plate mode (APM) devices, and Love-wave devices. All of them using different propagation modes of acoustic waves and differ in their physical interaction with the analyte. Another distinction can be found in their driving characteristic. TSM are of the class of one-acoustic port devices, whereas the SH-SAW, APM, and the Love wave devices are categorised as two port devices. One-port acoustic wave devices can only use a single port to serve as both the input and the output port. An input signal generates an acoustic mode that, in turn produces charges at the input electrode; combining these signals produces an impedance

variation that constitutes the TSM response. Two port devices use one port usually assigned as input port for the excitation of acoustic waves, which can propagate across a given distance to a receiving transducer, which regenerates a signal on the output port.

Different acoustic wave propagation modes can be generated when different substrate materials are used and this produces a specific particle displacement within the substrate relative to the direction of wave propagation. Depending on their physical properties these other classes of acoustic sensors can either operate in gas or liquid media. The sensing characteristics is dependent on physical or chemical perturbations such as pressure, temperature, mass loading effects and chemical or biological interaction with an analyte. This generally affects the propagation characteristics of the acoustic waves on the surface. A brief overview of the functionality of each device, and an explanation of the different interaction mechanism when operated in liquid media is given in the next section.

#### **1.4.4.1. Shear Horizontal Surface Acoustic Waves (SH-SAW)**

These devices utilise interdigital transducers (IDT's) that are fabricated onto the substrate surface to generate shear horizontal surface waves. The selection of a different crystal cut yields shear horizontal waves rather than Rayleigh waves. Two pairs of interdigital transducers on each end of the substrate launch and receive the shear waves. "Shear" describes the motion of the acoustic wave relative to the direction of wave propagation. Shear horizontal modes have in general a particle displacement parallel to the plane of the surface; the predominant SH displacement component and transverse to the wave propagation of the surface wave; a longitudinal in-plane component (P). The absence of a surface normal component [115] makes the device suitable to operate in liquid media where propagation at the solid-liquid interface is possible with minimal energy losses [116]. No excessive coupling of acoustic energy into the surrounding liquid is anticipated as this is the case with the Rayleigh SAW based devices. Comparing this with a TSM, the shear

motion of the SH-SAW shears the liquid transverse to the wave propagation (considering a no-slip condition). Their physical appearance is very similar to standard Rayleigh SAW devices. Resonant frequency conditions are determined by the transducer geometry: the IDT finger spacing and the wave velocity of the particular substrate material. One possible substrate material is lithium tantalate ( $\text{LiTaO}_3$ ). The dominant crystal lattice is  $36^\circ$ -rotated Y-cut, X-propagating  $\text{LiTaO}_3$  also referred as 36XY-LT [26, 27, 28, 29, 30].

#### 1.4.4.2. Acoustic Plate Modes (APM)

Acoustic plate modes APM's can be subdivided into two different main categories according to the vibration plate polarisation. They are classified in shear horizontal acoustic plate modes SH-APM's and Lamb waves. The SH-APM has a particle displacement parallel to the device surface and perpendicular to the direction of mode propagation. The SH-APM is generated and detected by a set of interdigital transducers placed on opposite ends of the device surface. The transducers are generally positioned on one face of the substrate. If an alternating electrical potential is applied to one of the transducers, this causes an alternating strain in the piezoelectric material launching a bulk wave into the substrate. Multiple reflection on the lower and the upper face of the piezoelectric material confines the wave and the material, also called plate, acts as acoustic waveguide. This results in an SH plate mode having a sinusoidal shear displacement along the substrate surface with maxima at the upper and the lower face of the material. The detected signal at the receiving transducer is transduced back into an electrical signal which conveys information about attenuation and phase delay experienced by the bulk propagation along the plate. This allows APM's to be used on either side of the device face, since both sides have similar particle displacements [25].

In contact with a liquid the shear displacement causes a penetration into the liquid, causing viscous damping of the APM's. In situations where the contacting medium solidifies from the liquid state (a change from viscous to elastic behaviour) the APM will instead radiate shear waves into the bulk of the

contacting solid. This will cause substantial attenuation of the APM due to energy losses into the solidified liquid [117]. These sensors are ideal to sense liquid loading since the shear displacement on the surface causes minor attenuation, but suffers substantial attenuation when a phase transition from a liquid to a solid occurs. However, the APM device is very well suited for monitoring in-situ the solidification process of liquids e.g. the phase transition of freezing and melting of liquid substances [118] or detect the changes in shear modulus which accompanies the photocross-linking of negative photoresist polymer film [117]. Niemczyk et al. [119] used a quartz APM to sense acoustoelectric interaction with a conducting solution. They found that the evanescent RF electric field generated by APM's propagating in the piezoelectric crystal extends into the liquid and couples to nearby ions and dipoles in solution causing a perturbation in the propagation velocity of the plate mode. Josse et al. [120] used an acoustic plate mode (APM) sensor using ZX-LiNbO<sub>3</sub>. The sensing wave (APM), was exposed to dilute electrolyte and to various metal-ion solutions causing a measurable perturbation in the wave-propagation characteristics when the electrolyte was loaded on the free surface. They carried out various experiments based on different frequencies and various aqueous solutions of electrolytes such as Mg(NO<sub>3</sub>)<sub>2</sub>, Fe(NO<sub>3</sub>)<sub>3</sub>, Cu(NO<sub>3</sub>)<sub>2</sub> and CaCl<sub>2</sub> and measured the changes in wave characteristics (phase and attenuation). Josse and his co-workers concluded that the detection mechanism involves the bonding of specific metal ions in solution to a ligand-coated silica on LiNbO<sub>3</sub> support. Detailed description of APM device characteristics and device performance can be obtained from Martin et al. [25].

Lamb wave devices also referred to as flexural plate wave devices (FPW) are characterised by a vibration of the plate either in symmetric mode, normally indicated by S<sub>0</sub>, S<sub>1</sub>,..., whose particle displacement is symmetric about the middle axis of the plate substrate, or an antisymmetrical mode referred to as A<sub>0</sub>, A<sub>1</sub>,..., whose particle displacement has an uneven symmetry to the middle axis. These modes can be generated in thin piezoelectric plates [121]. The plate can support a number of these waves depending on the thickness to wavelength ratio  $h/\lambda$  where  $h$  defines the plate thickness and  $\lambda$  is the wavelength of the acoustic bulk transverse wave. The wave propagation characteristics are found

to be similar to the characteristics of a surface acoustic wave device. However, the phase velocity of the device decreases as the ratio of plate thickness to wavelength decreases. This means that the FPW typically operates in the low MHz region and the phase velocity can be as low as a few hundred  $\text{ms}^{-1}$ . Choosing a very thin plate (the thickness to wavelength ratio is  $< 1/4$ ), only two waves exist; the lowest order symmetric mode  $S_0$  and the lowest order antisymmetric mode  $A_0$ . With increasing plate thickness the phase velocity of the FPW approaches that of surface waves and  $A_0$  and  $S_0$  are almost equally generated [122, 123]. The surface wave is a result of the superposition of antisymmetric and symmetric plate waves [2]. The motion of particles is an elliptical motion normal to the plate predominately for the lowest order antisymmetric mode and elliptical motion tangential to the plate predominately for the lowest order symmetric mode. The Lamb wave is launched and detected by the same type of transducer geometry as can be found for Rayleigh wave surface acoustic wave devices [124]. Particular materials for the design of FPW membranes include silicon nitride, an amorphous glasslike substance. It is normally deposited on a silicon wafer by low-pressure chemical-vapour deposition [2]. Using Lamb wave sensors, two quantities; the phase velocity and the amplitude are monitored simultaneously [125].

#### 1.4.4.3. Love-Wave Acoustic Sensors

Love waves exist in the half-space between a solid substrate and a guiding layer. This is called a bilayer geometry [22]. The acoustic energy of the wave is mainly confined to the thin layer deposited on the substrate. The layer serves as a so called waveguide and is very sensitive to surface perturbations such as mass loading effects. Horizontal polarised shear wave devices (SH-SAW) of the same sensitivity compared to Love wave devices are more fragile because of a thinner substrate thickness [126]. In principle a shear horizontal (SH) wave with displacement parallel to the surface couples a shear bulk wave into the guiding layer if the velocity of the shear wave in the waveguide is less than the shear wave velocity in the substrate [127]. The mass sensitivity is not

only a measure of the resonant frequency but can be enhanced by the thickness of the wave guiding layer and by the excitation and propagation differences of the phase velocity of the above shear horizontal wave in comparison to the phase velocity of the bottom shear horizontal wave. This allows a good design flexibility, since the energy confinement is purely determined by the acoustic properties and the thickness of the guiding layer and can be regarded as independent from the characteristics of the substrate material [22]. In general Love wave devices resemble a very similar geometry to that of Rayleigh surface acoustic wave delay-line devices. Two interdigital transducers (IDT's) are located at opposite ends of the substrate and are normally deposited at the interface between substrate and elastic overlayer. Both transducers can either launch or receive shear horizontal waves. In order to achieve maximum sensitivity to mass loading an optimum layer thickness of the waveguide has to be measured to ensure maximum energy density close to the surface otherwise acoustic absorption increases with increasing layer thickness limiting the sensors sensitivity [128]. Theoretical calculations by Kovacs et al. [129], Enderlein et al. [130] and Wang et al. [131] have shown that the thickness of the guiding layer determines the sensitivity of the Love mode and its coupling into the layer. Harding and Du [132] tried to evaluate the effects of the guiding layer on ST-cut quartz. Their investigation involved silicon dioxide films sputtered onto the surface and spin coated polymethylmethacrylate (PMMA) films and a multiple layer sandwich structure consisting of PMMA/SiO<sub>2</sub>. The use of a SSBW (surface skimming bulk waves) device has been proposed by Gizeli [133] as biosensor, which utilises a shear horizontal wave propagating just below the surface of the device. A deposited overlayer converts the SSBW into a guided SH wave coupled predominately into the overlayer close to the interface. This is called a composite waveguide geometry. The device uses a single crystal Y-cut, Z-propagating lattice. Two different guiding layers; an elastic silica and an inelastic PMMA have been studied and acoustic properties compared. The investigation revealed for the PMMA waveguide structure a high sensitivity, due to its low-shear-acoustic-velocity and therefore a more effective coupling of Love waves into the material but also more effective viscoelastic and acoustoelectric interaction with the analyte.

There have been other ways of building wave guiding sensors. A surface transverse wave (STW) device utilising a corrugating guiding layer. The grating provides a better guiding layer because it can be matched to the structure of the transducer and therefore gives a stronger guiding. The STW device uses the periodic grating deposited on the surface of the substrate to slow down the phase velocity of the transverse wave and to prevent energy being radiated into the bulk of the crystal. The grating structure is also required to confine the STW to the surface. The surface particle motion of the STW device is pure shear horizontal (normal to the propagation direction and in plane of the surface), and the STW motion does not include the shear vertical component, therefore STW's may be propagated under liquids with low attenuation. Furthermore a STW device is demonstrated to be relatively insensitive to environmental factors such as temperature [19].

## 1.5. Motivation and Objectives

Generally, the application of acoustic sensors involves either a gaseous or vacuum environment, or applications are limited to fixed pools of liquids in contact with the device surface. To investigate the interaction of surface acoustic waves with partially localised liquids spreading across the free surface of a Rayleigh wave SAW sensor has found little attention in the literature. One reason maybe that it has been argued for quite some time that surface acoustic waves (SAW's) using a Rayleigh wave excitation with a substantial surface-normal displacement component, which is believed to radiate compressional waves into the liquid, suffer excessive damping. Calabrese et al. [134] investigated the role of Rayleigh wave propagation on liquid loaded ST-cut quartz surface acoustic wave delay line devices at various design frequencies using a delay line oscillator circuit. Experiments with extensive liquid drops (water) deposited on the top surface within the Rayleigh excitation path, or deposited at the devices edges to investigate pass-band ripples, or deposited on the back surface of the device, suggested that the dominant mode of energy propagation is not due to Rayleigh waves in thin substrate devices (thickness

<5 wavelength). Thicker substrate devices showed a behaviour according to an expected Rayleigh wave propagation at the resonant frequency (design frequency) but have been found to be insufficient upon massive liquid loading due to severe signal attenuation and therefore not to be useful as a liquid sensor. Campbell and Jones [135] presented in a theoretical investigation of Rayleigh waves propagating at the boundary between a piezoelectric crystal and a liquid medium, that the energy losses experienced by a SAW device loaded with water should be of the order of 2 dB/(MHz cm). Theoretically a Rayleigh wave SAW device operating at a resonant frequency of around 20 MHz having a 1 cm acoustic path distance covered with water should experience an energy loss of  $\sim 40$  dB. The two theoretical methods used in the studies did not include the effect of viscous losses of the acoustic wave due to fluid loading. This led to erroneously low estimates of the power loss caused by the fluid medium. However, even their low estimates showed for a high frequency Rayleigh wave device very severe energy losses that would lead to a complete attenuation of the Rayleigh wave amplitude. On the other hand, Wohltjen and Dessy [136] performed thermomechanical analysis of polymer films using Rayleigh wave surface acoustic wave devices. Their experimental set-up measured acoustic losses in wave amplitude of the propagating surface wave. They employed a delay line configuration as sensor. The SAW device was driven by an external power source directly connected to the taps of the source transducer. The arrangement permitted a direct transmission of surface waves. However, the system was limited and allowed only one transducer to launch surface waves and therefore only operate as source transducer whereas the other transducer were used as the receiver. The source transducer was fed by the external power source with a continuous alternating voltage (RF power level). Due to anticipated excessive damping of the surface wave, a set of cascaded amplifiers were directly connected to the taps of the receiving transducer. The surface wave undergoes a severe damping in amplitude if the device surface is partially covered with a liquid. In addition the wave experiences a change in phase velocity. A diode detector was used to rectify the signal into a DC voltage. Wohltjen and Dessy used this technique to investigate the glass transition temperature of polymer films clamped to the surface and attributed the attenuation as a result of surface contact between

the polymer film and the SAW device when the elastic modulus of the polymer decreases. Another aspect of their investigation was the solvent evaporation rate of KPR photoresist droplets during baking. The effect of a droplet placed in the acoustic path of the sensor showed "wild oscillations". Their interpretation of the behaviour was attributed to interference due to compressional waves dissipating into the liquid and partly reflected back from the liquid-vapour boundary causing destructive and constructive interference as the film thickness changed (boundary distance changes). After the solvent fully evaporated from the KPR photoresist, the visual observation of the photoresist being dry coincided with the end of the wild oscillation. The amplitude shift in their study approached a constant value. They were only able to give an qualitative explanation of their observation and stated further work would be necessary to understand the nature of the observed behaviour of surface wave-liquid interactions. However, Wohltjen and Dessy concluded that the SAW technique could present a convenient way of studying the effects of photoresist cross-linking. This was the first time such observations have been made using a Rayleigh surface acoustic wave sensor in direct contact with a liquid covering a fractional part of the SAW device. Roederer and Bastiaans [137] used a SAW device in an oscillator circuit configuration at considerably low frequencies to minimise excessive signal losses as was previously predicted by Campbell and Jones [135]. Their investigations were focused on the interactions of immobilised goat anti-human IgG with human IgG at the surface of a quartz piezoelectric crystal. A specific adsorption of human IgG occurs and can be detected. Detection was based on surface mass changes caused by adsorption; measured as shifts in resonant frequency of the crystal. They showed that a SAW delay-line oscillator was capable of detecting mass changes on the substrate surface. Stable oscillation was achieved even upon liquid loading. However, it was possible to show that this so called SAW sensor actually employed a shear-horizontal acoustic plate mode (APM) [134]. A rare attempt to measure the SAW attenuation upon liquid loading has been performed by Košťál et al. [138, 139]. A YZ-cut LiNbO<sub>3</sub> SAW sensor has been partially immersed into liquids with a relatively high evaporation rate and a linear SAW attenuation versus time has been observed. They attributed their observation to two energy loss mechanisms when the liquid is in contact with

the device surface. One mechanism was the conversion of energy into a volume wave which from the authors' point of view would penetrate perpendicular to the crystal surface into the liquid and a second mechanism was identified as phase velocity differences between crystal and liquid, respectively. Their investigation focused on the loss mechanism caused by a reflection of SAW energy at the liquid-vapour boundary and mainly at the crystal edge immersed into the fluid dependent on sensor immersion into the liquid. The results showed linear attenuation of the reflection during evaporation versus time with a small "zig-zag" modulation superimposed on the overall attenuation of the SAW reflection signal. Košťál et al. deduced a high sensitivity of 250 dB/g and established a dependency of the evaporation rate as a function of molecular mass showing the high mass sensitivity of the SAW device. This is the only experiment known to the author using a SAW-device to measure a reflection signal from a liquid-vapour boundary.

This review has shown that most of the studies investigating acoustic sensors interacting with liquids have mainly concentrated on liquid pools contacting the sensor surface. Mainly TSM devices have been used for the investigation of liquid properties. However, the idea of studying dynamically evolving liquids which are confined to a part of the sensor's detection path have been rarely considered. Partially localised fluids spreading on acoustic sensors have only recently been considered by some scientists. Ward et al. [140, 141, 142] used a thickness shear mode resonator TSM (QCM) to measure the wetting rates of aqueous dispersion of trisiloxane surfactant exhibiting "superspreading" behaviour. The interest was focused on the rate at which a droplet advances across the TSM and a relation from the frequency transient accompanying radial spreading from the centre of the quartz to the periphery has been investigated. The mass sensitivity of this device allowed an examination of whether condensation to create a thin precursor film of water was necessary for the superspreading. A suggestion was made to use the QCM to deduce the dynamic contact angle of liquid drops [143]. The only attempt to use SAW's for the investigation of contact angles has been recently proposed by Shiokawa et al. [144]. The influence of the contact angle on the reflection coefficient of pseudo-Rayleigh waves has been demonstrated by De Billy et al. [145, 146]. They immersed a semi-infinite elastic plane solid, partially

into a liquid. The existence of two interface waves could be demonstrated; a generalised Rayleigh wave, or leaky Rayleigh wave and a pseudo-Stonely wave. The experimental observation of the contact angle presented in their study an oscillating behaviour of the acoustic wave amplitude rather than a monotonic change and could be attributed to the superposition of the pseudo-Stonely wave and the generalised Rayleigh wave. The only investigation of the dynamic wetting stages of a partially localised liquid using Rayleigh surface acoustic waves (SAW's) and a highly viscous liquid has been studied by McHale et al. [47, 65, 147, 148, 149]. In this work highly viscous polydimethylsiloxane oils (PDMS) have been deposited locally on a Rayleigh surface acoustic wave device. A systematic series of experiments have been carried out to observe the spreading behaviour of a liquid stripe dynamically evolving during an extensive period of time. The investigation showed a resonance structure on three observed signals interacting with the liquid phase. A model was provided to explain the resonance structure of the transmission signals.

The intrinsic speed of the surface acoustic wave SAW method and its extreme sensitivity to mass loading provides a unique detection method which will complement other techniques and extend the use of acoustic waves. In addition to their remarkable properties in sensing small quantities of mass accumulations in their vicinity, they offer a unique possibility to observe the spreading behaviour of the advancing edge of a fluid directly and continuously in the spreading plane and this represents a novel in-plane technique and allows one to monitor the process in real time [149]. The sensing surface of the SAW sensor is accessible and can be chemically modified, and this provides a rapid in-situ method for studying dynamic chemical and bio-chemical changes.

Insufficient understanding currently exists on the nature of acoustic wave-liquid interactions. This thesis reviews the progress of this project in building a surface acoustic wave SAW-system combined with an optical observation technique. The simultaneous character of this system using SAW's and interferometry enables a new look into the macroscopic changes of a spreading fluid by monitoring the dynamic changes of localised small stripes of viscous oil spreading across the surface of the acoustic sensor. When the surface wave impinges on fluid loading the existence of resonant reflections of SAW's are

observed for particular geometrical parameters of the stripe of oil and the acoustic signals transmitting through the stripe along the solid-liquid interface, do not decrease steadily but show strong local and asymmetric attenuation resonance peaks.

A theoretical description of the dynamics of liquid spreading is given in Chapter 2. This is based on the dynamic evolution of a small liquid drop. Later in the chapter an extension for the dynamic changes of a thin stripe of fluid to take geometrical changes of the fluid shape into account, is presented. Here the theoretical treatment of the spreading of two different shapes using a cut-off is given. The theory is based on Frenkel's method [150] of balancing the change in surface free energy to viscous dissipation. Providing a Poiseuille type flow field is chosen, the dissipation in a wedge does give the de Gennes type [35] result. A velocity-edge angle relation for the wider angular range is derived and the dissipation in a cone inscribed within the spherical cap formed by the interfacial tension acting at three interfaces is modelled. The second section describes Rayleigh surface waves in elastic media. Herein, the excitation of Rayleigh waves in non-piezoelectric material is described and leads to the equation of motion. From the equation of motion and the elastic constitutive equation the wave equation is derived, which describes the propagation of a plane acoustic wave in a non-piezoelectric solid. Building on this foundation, Rayleigh waves in piezoelectric material are described. The last section presents a theoretical model to explain changes observed in transmission coefficient of pulses of high frequency (170 MHz) Rayleigh surface acoustic waves. The model considers a damped harmonic oscillator, with the main damping assumed due to shear motion induced in the fluid overlayer of thickness  $t_f$  (stripe of liquid) on the device surface. The theory assumes that the fluid is viscoelastic and obeys the Maxwell model.

In Chapter 3 the SAW-system and the optics are described in detail. A delay-line configuration which employs both sets of interdigital transducers (IDT's) is used for detecting pulses of Rayleigh surface acoustic waves. One set of transducers is assigned for both transmitting and receiving Rayleigh surface acoustic waves (SAW's), whereas the second transducer is responsible for detecting transmission signals and therefore works only as a receiver. A detailed description of system components is given and a full explanation of the

system operation is presented. Furthermore, an overview of the data acquisition system and interfacing with a PC is given. An optical system using an interference technique has been designed aside the SAW system to simultaneously follow the dynamic evolution of the profile of the viscous stripe of oil directly at the location of interaction of surface waves with the fluid. The deposition technique for the stripe of oil is described.

Chapter 4 presents a selection of experimental results, showing the spreading of a series of thin stripes of oil of different viscosities such as 100,000 cSt, 30,000 cSt, 10,000 cSt and 1,000 cSt polydimethylsiloxane (PDMS) oils wetting the lithium niobate ( $\text{LiNbO}_3$ ) substrate surface of the Rayleigh SAW sensor. The presence of three different signals: a single transit signal which propagates in one direction on the liquid loaded surface of the SAW sensor; a double transit signal which passes twice through the liquid along the solid-liquid interface and a reflection signal, due to the advancing front edge of the stripe of fluid are presented in the data. The double transit and the reflection signal are detected at the same set of interdigital transducers. Optical observations confirm that the time evolution of the geometrical parameters of the spreading stripe geometry follow well defined power laws. The results show the effect of the dynamically changing stripe located in the SAW path on the amplitude response of transmitted and reflected SAW pulses. Finally a comparison is performed of experimental results showing identical signal trends in all three signals.

Analysis of the SAW data is given in Chapter 5, and the existence of transmission resonances in the two transmission signals are interpreted within an approximate single relaxation time Maxwell model for viscoelasticity. A first attempt to interpret the reflection resonances using a combination of a triangular shape model to approximate the fluid geometry based on the idea of a step model and the influence of dispersion is discussed. A summary of surface wave-liquid interaction mechanisms; discussed in Chapter 5 are presented in Chapter 6. An outlook of future activities and a possible direction

of a further development of the project is provided to indicate the potential for the acoustic technique in investigating the dynamics of localised liquids.

# CHAPTER 2

# *THEORY*

## 2.1. Introduction

The theoretical treatment of the dynamic evolution of a thin stripe of fluid on the surface of a Rayleigh surface acoustic wave sensor involves the understanding of dynamic wetting processes and the knowledge of surface waves in an elastic medium. Moreover, the coalescence of these two individual subjects has led to the development of a new theoretical model to describe the interaction processes of surface acoustic waves with localised liquids. The interaction mechanisms for localised liquids interacting with surface waves has only found little attention in the scientific community. One approach to study these interactions mechanisms in greater detail has been carried out by McHale et al. [31, 65, 47, 147, 148, 149]. However, still insufficient understanding currently exists of the nature of the interaction mechanisms. Transmission signals are progressively attenuated by the spreading of a thin stripe of viscous oil, but also show a resonance structure present in the acoustic signals when transmitting through the stripe along the solid-liquid interface. The use of simultaneous optical and surface wave observations of the wetting dynamics require a theoretical examination of optical changes in stripe geometry and changes in SAW signals. In order to correlate geometric changes in the profile of the advancing stripe shown in Fig. 2.1 with changes in the SAW signals, the time evolution of the contact width,  $d_0$ , contact angle,  $\theta$ , height,  $h_0$ , and cylindrical cap radius,  $R$ , have been theoretically described by power law relationships [65]. This is based on the hydrodynamic theory given by Tanner [48] related to the complete spreading of non-volatile, viscous oils on high energy surfaces. McHale et al [151] applied Frenkel's method [150] in a manner that recovered the generalised Tanner's law [48]. The theory based on Frenkel's method balances the change in surface free energy to viscous dissipation and presents a straightforward extension to the dynamic evolution of a spherical cap geometry of a liquid drop. The power law described in this chapter is a wide angle version of Tanner's law and is valid for low-energy surfaces where finite equilibrium contact angles can exist as well as high-energy surfaces where complete spreading occurs.

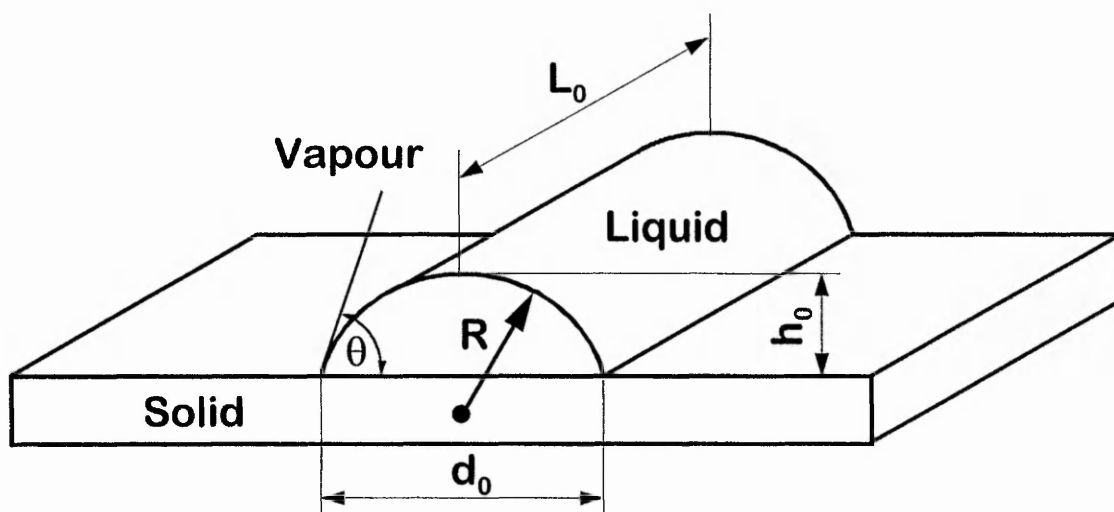


**Fig. 2.1** A thin stripe of oil and the cross-sectional shape assumed to be a portion of a circle with a time dependent radius,  $R$ .

To model approximately the effect of Rayleigh wave-viscous liquid interactions, it is necessary to know that a Rayleigh surface wave undergoes an elliptical motion and so has an in-plane motion, in the direction of wave propagation, and a vertical displacement. The energy of the wave is confined to within one SAW wavelength. Consequently the elliptical motion occurs only within a thin surface layer. To model surface wave-liquid interactions the model proposed in this chapter considers, for reasons of simplicity, the in-plane motion of the wave and treats the system (substrate plus liquid overlayer) as a damped harmonic oscillator. As a consequence, the damping is assumed to arise from the viscous force that the viscous overlayer enforces on the surface during oscillation. To describe exactly the behaviour of the fluid overlayer the liquid is taken to be viscoelastic and shows therefore two significant physical behaviours. If the relaxation time of the liquid is small, it can be regarded as a Newtonian fluid and if the relaxation time is large the fluid has the physical behaviour of an amorphous solid [25, 152]. Considering these conditions, it is possible to obtain an expression for the damping of the SAW related to its in-plane motion, due to surface loading by a viscoelastic overlayer of arbitrary thickness.

The first section of this chapter reviews Frenkel's method to calculate the surface free energy of a spherical cap of fluid of constant volume (droplet geometry) which is balanced with the viscous dissipation in a wedge. This is extended to a cone geometry to introduce the macroscopic contact angle into the viscous dissipation. Afterwards, a theoretical examination of the dynamic evolution of a thin stripe of viscous and non-volatile oil is outlined. A revision of Rayleigh surface waves in elastic medium is provided in the second section. An explanation of Rayleigh wave motion is given. The displacement vector for the motion of an infinitesimal small elastic solid in non-piezoelectric material is described and an expression for the wave equation is derived from the equation of motion. Finally, Rayleigh wave motion in piezoelectric material, which represents the actual physical behaviour of the sensor is discussed. In the last section we look at the development of a theoretical model capable of describing attenuation resonances present in the acoustic transmission signals, when traversing through a thin stripe of viscous, non-volatile oil. To model the

acoustic attenuation, the fluid overlayer is treated as a viscoelastic fluid with a single relaxation time (Maxwell model of viscoelasticity).

## 2.2. The Dynamics of Liquid Spreading

In the case where an oil wets the solid surface of a surface acoustic wave (SAW) device complete wetting may occur. The device surface is a high-energy surface and if the spreading parameter,  $S$  is positive and large a liquid, in the form of a drop, spreads spontaneously. During the course of spreading two distinct regimes may occur. These regimes can be identified as a) a macroscopic regime which characterises the periphery of the drop such as the spherical cap geometry of the drop which is not affected by molecular interactions and b) a microscopic regime at the very edge of the drop where a very thin liquid film of molecular thickness may exist, a so called precursor film. In the complete wetting situation the free energy favours a uniform coverage of the surface by the thin film whose ultimate thickness is then determined by van der Waal's forces. For moderately low molecular weights polydimethylsiloxane (PDMS) droplets, it has been observed that, on a chemically treated surface of crystalline structure, a flat, dense liquid film forms at long times, with a thickness of  $\sim 9 \text{ \AA}$ , comparable to the diameter of one monomer [62]. The important point is that the spreading appears to stop, provided the volume of the deposited drop is chosen small enough to ensure that this molecularly thin film is not able to cover the whole surface. The periphery of the surface remains dry even over periods as long as six months; the edge of the wetted area is well defined and immobile. This is in good qualitative agreement with the pancake structure suggested by Joanny and de Gennes [153]. The thickness,  $e$  of the film, sometimes called the pancake film, is determined by the capillary forces (the spreading coefficient,  $S$ ) that tends to spread the film and thus decreases its thickness.

We will focus here entirely on the macroscopic aspects of the dynamic evolution of a non-volatile liquid on a solid surface. Such spreading is referred to as "dry wetting" in which the spreading only takes place through liquid flow

[35]. In addition, the lack of volatility of the liquid (there is no transport of matter via the vapour phase), as this is the case with polydimethylsiloxane oils, means that mass and volume are conserved, thus simplifying the theoretical analysis.

Tanner demonstrated in 1979 [48], from the equation for viscous flow in two dimensions, that for complete spreading the edge speed,  $v_E$  could be related to the cube of the contact angle; this is referred to as Tanner's law. A remarkable feature of this law is its universality and an investigation of the dynamic contact angle shows that the angle does not depend on the spreading coefficient,  $S$ . The macroscopic spreading process is thus independent of the wettability of the solid surface if we consider complete wetting [1]. An important implication of Tanner's law is that the dynamic contact angle is only weakly affected by surface heterogeneities. Later de Gennes [35] derived a modified Tanner's law for small angles. This modified law takes into account finite equilibrium contact angles by considering the interfacial forces at the edge of the fluid. Balancing the various forces by the rate of viscous dissipation within the leading edge resulted in a modified Tanner's law with the edge speed,  $v_E$  proportional to  $\theta(\theta^2 - \theta_e^2)$  where  $\theta_e$  is the equilibrium contact angle and  $\theta$  is the dynamic contact angle [31, 151].

Experimental investigation for small droplets where gravity can be ignored and a spherical cap shape is assumed at all times during the spreading allows Tanner's law to be converted into a contact angle proportional to  $t^{-3/10}$ . One consequence is that the radius,  $R$  of the macroscopic cap of the spreading droplet can be deduced. If the profile of the drop, given in Fig. 2.2, is known,  $R$  and  $\theta$  are coupled, because the volume of liquid is fixed. There exists a well established systematic series of experimental data investigating the time evolution of the spherical cap radius, or equivalently the maximum thickness of a spreading liquid drop as well as the evolution of the contact angle. The data follow Tanner's law, at least for such experiments with large enough time domains so that the spherical cap radius is much larger than the initial radius at the beginning of the measurements. A number of results can be found in Ausserré et al's work [36], in Silberzan and Léger's work [52] or McHale et al's work [31, 151] in addition to the original work of Tanner [48].

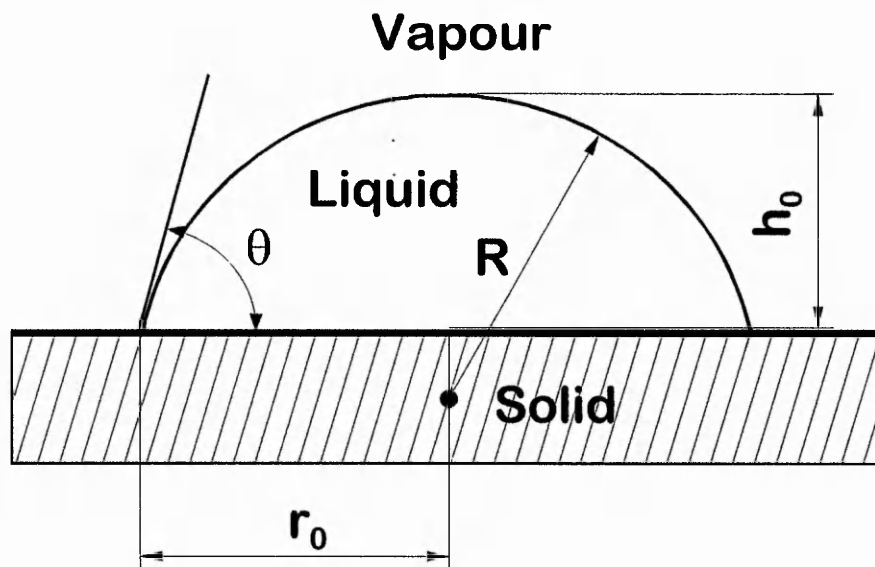
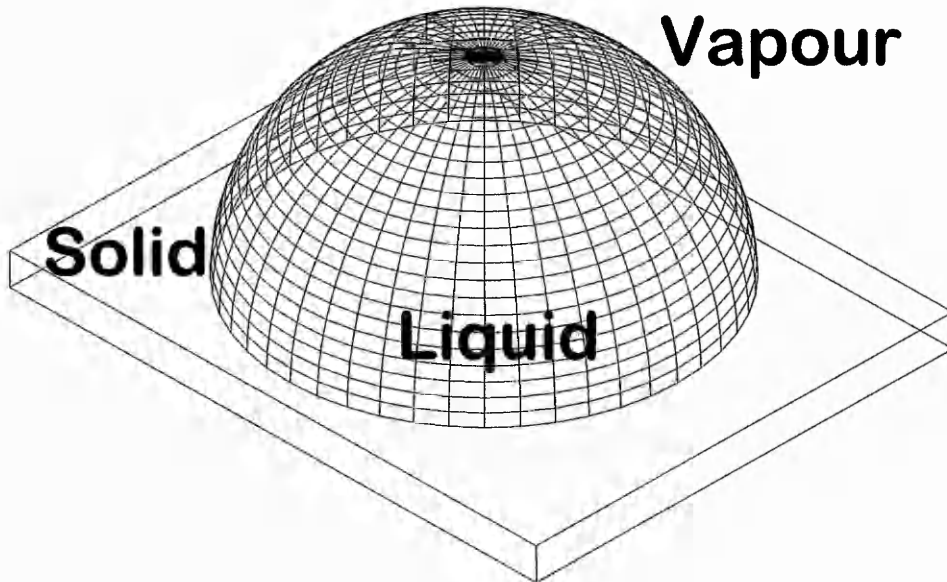


**Fig. 2.2** The spherical cap of a droplet with constant volume can be defined by any two parameters such as contact radius,  $r_0$ , the cap height,  $h_0$ , the spherical cap radius,  $R$  and the edge angle,  $\theta$ .

The primary purpose of this section is to give a foundation of the macroscopic evolution of a small stripe of non-volatile viscous oil spreading on the surface of a Rayleigh wave surface acoustic wave device. Such stripes are used in the acoustic experiments because they provide an advancing front edge which can act as a plane reflector for surface acoustic waves. The theoretical analysis based on Frenkel's method [150] recovers the generalised Tanner's law. A wide angle version of this law for both low- and high-energy surfaces is obtained. The extended power law relationship is valid for the complete wetting situation where in general a vanishing contact angle ( $\theta_e = 0$ ) exists as well as for equilibrium contact angles ( $\theta_e \neq 0$ ) which can be found in partial wetting. Furthermore, on lithium niobate ( $\text{LiNbO}_3$ ), which has been confirmed is a suitable high-energy surface [31] for the dynamic evolution of polydimethylsiloxane (PDMS) stripes of oil, the equilibrium contact angle,  $\theta_e$  vanishes.

### 2.2.1. Spreading of a Droplet

We review in this section the dynamic evolution of a droplet with characteristic dimensions less than the capillary length,  $\kappa^{-1} = (\gamma_{LV}/\rho g)$ , where  $\gamma_{LV}$  defines the liquid-vapour surface tension,  $\rho$  is the density of the fluid and  $g$  is the acceleration due to gravity. Thus gravitational forces do not affect the spherical shape of the droplet and the spreading is dominated by capillarity. If the characteristic size of a drop exceeds this natural length scale, gravitation will lead to a flattening of the spherical cap in the central region and distort the shape. Moreover this so called body force can accelerate the spreading [1].

### 2.2.2. Surface Free Energy

The derivation of the rate at which the spreading of a droplet of viscous and non-volatile fluid occurs finds its origin in Frenkel's method [150]. Frenkel predicted the equilibrium contact angle based on the changes in surface free

energy as the shape of the droplet evolves. Later Strella [154] extended this to the time dependence of the coalescence of spherical drops by including a viscous dissipation term based on a rod under uniaxial compression. McHale et al. [151] modified this model by equating the changes of the surface free energy to the viscous dissipation derived by assuming a more realistic Poiseuille type flow field. This approach is outlined in the equations given below. In the regime where gravity is negligible, the macroscopic shape of the droplet is a spherical cap as defined in Fig. 2.2. The spherical cap radius,  $R$ , the contact angle,  $\theta$ , the contact radius,  $r_0$ , and the cap height,  $h_0$  are related by

$$R^3 = \frac{3V}{\pi\beta} \quad (2.1)$$

$$r_0 = R \sin \theta \quad (2.2)$$

$$h_0 = R (1 - \cos \theta) \quad (2.3)$$

where

$$\beta = 2 - 3 \cos \theta + \cos^3 \theta \quad (2.4)$$

and  $V$  is the volume of the fluid in the spherical cap which is assumed to be constant. The relation between the spherical cap height and the contact radius is expressed as

$$\tan \left( \frac{\theta}{2} \right) = \frac{h_0}{r_0} \quad (2.5)$$

and the total surface free energy,  $F_s$  is found by considering the three surfaces separating the liquid, vapour and solid,

$$F_s = F_0 + \gamma_{LV} A_{LV} - (\gamma_{SV} - \gamma_{SL}) A_{SL}, \quad (2.6)$$

where  $F_0$  is a constant and  $\gamma_{ij}$  are the various interfacial energies.  $A_{ij}$  are the various surface areas defined by the solid-vapour, solid-liquid and liquid-vapour interface and are,

$$A_{SL} = \pi r_0^2 \quad \text{and} \quad A_{LV} = 2\pi R^2 (1 - \cos \theta). \quad (2.7)$$

The edge speed,  $v_E$  is the rate of change of the cap radius,  $r_0$ , and using equations (2.1 - 2.3) and (2.4), we find it is related to the dynamic contact angle,  $\theta$  by

$$v_E = \frac{-(3V/\pi)^{1/3} d\theta/dt}{(1 - \cos \theta)^{2/3} (2 + \cos \theta)^{4/3}}. \quad (2.8)$$

Equation (2.8) can be used to express the rate of change of surface free energy which is found by differentiating equation (2.6), subject to conservation of volume (equation (2.1)). After algebraic manipulation this gives

$$\frac{dF_s}{dt} = \frac{2\pi\gamma_{LV}(3V/\pi)^{1/3} \sin \theta (\cos \theta - I) v_E}{(1 - \cos \theta)^{2/3} (2 + \cos \theta)^{1/3}} \quad (2.9)$$

where  $I$  is defined as

$$I \equiv \frac{\gamma_{SV} - \gamma_{SL}}{\gamma_{LV}}. \quad (2.10)$$

Equation (2.9) is suitable for comparison to Tanner's law. To see more clearly the structure of the equation in terms of the equilibrium factor, equation (2.9) can be rearranged by using equations (2.1 - 2.3) and this gives

$$\frac{dF_s}{dt} = 2\pi\gamma_{LV} (\cos \theta - I) r_0 v_E. \quad (2.11)$$

If no dissipation occurs, the equilibrium contact angle,  $\theta_e$ , is given by a stationary free energy. Equation (2.11) then shows that  $I = \cos \theta_e$ , which recovers Young's law [151].

### 2.2.3. Viscous Dissipation

If dissipation occurs the rate of energy loss in the fluid, using cylindrical co-ordinates centred on the base of the spherical cap is given by [155]

$$\frac{dE_d}{dt} = \eta \int_{\text{liquid}} \phi_v dV, \quad (2.12)$$

where  $\eta$  is the viscosity and  $\phi_v$  is the cylindrical velocity field. In terms of the radial component,  $v_r$  and  $z$  component,  $v_z$  of the velocity,  $\phi_v$  is

$$\phi_v = 2 \left[ \left( \frac{\partial v_r}{\partial r} \right)^2 + \left( \frac{v_r}{r} \right)^2 + \left( \frac{\partial v_z}{\partial z} \right)^2 \right] + \left( \frac{\partial v_r}{\partial z} + \frac{\partial v_z}{\partial r} \right)^2. \quad (2.13)$$

Here it is assumed that the fluid is incompressible so that the divergence of the velocity field vanishes. Knowledge of the velocity field can now be used to obtain the viscous dissipation and from balancing this with the rate of change of surface free energy, an expression determining the rate of spreading can be obtained. With equation (2.5) which expresses the ratio of cap height to radius to  $\tan(\theta/2)$ , we can anticipate from a dimensional analysis of equations (2.12) and (2.13), a viscous dissipation, i.e. the rate of entropy production, of the form

$$\frac{dE_d}{dt} = T \frac{dS}{dt} = \frac{k \eta v_E^2 r_0}{\tan(\theta/2)} \quad (2.14)$$

where  $k$  is a constant. However, the exact form of dissipation will depend on the choice of the velocity field and the geometry over which dissipation occurs [151].

### 2.2.4. Dissipation in a Wedge

De Gennes [35] examined the flow pattern in a simple “wedge” using a force balance argument with the viscous force estimated by a velocity profile of the Poiseuille type. The wedge shaped edge extends from  $r_{min}$  to  $r_{max}$ . In order to get a simplified view of the viscous dissipation he used a small angle limit [151]. In this case the velocity field is one dimensional and is given by

$$v_r = v_A g[z / h(r)] \quad g(z) = \frac{3}{2}(-z^2 + 2z) \quad (2.15)$$

where  $v_A$  is the velocity averaged over the height of fluid and is equal to  $2 v_E / 3$ . The choice of  $g(z)$  ensures the radial velocity vanishes at the solid surface and its gradient vanishes at the free surface. Using equation (2.15) in equations (2.12) and (2.13) and assuming that only the vertical gradient in the radial velocity,  $v_r$  is important gives a viscous dissipation

$$T \frac{dS_w}{dt} = \frac{8 \pi \eta v_E^2 r_0 J_W}{3 \tan \theta} \quad (2.16)$$

where  $J_W$  is a cut-off integral. The limitation of this integral explained in [151] when extending it over the full radius of the macroscopic cap is in defining the relation of the wedge angle to the dynamic contact angle. In the small angle limit and with the integration restricted to the edge, the wedge angle can be linearly related to the macroscopic angle to obtain a functional form for the angle-edge velocity relation.

### 2.2.5. Dissipation in a Cone

McHale et al. [151] suggested a cone inscribed within the spherical cap of the drop, in order to extend the idea of a wedge geometry. The evolution of the viscous dissipation is then identical to the wedge with the only exception that the angle of the inscribed triangle (the cross section of a cone) at the fluid edge is one half of the angle used in the wedge calculation

$$T \frac{dS_c}{dt} = \frac{8 \pi \eta v_E^2 r_0 J_W}{3 \tan(\theta/2)}. \quad (2.17)$$

The approximation to the cut-off integral is then

$$J_W \approx \log_e \left( \frac{1}{\varepsilon} \right) - 1 \quad \text{with} \quad \varepsilon = \frac{z_0 r_0}{h_0} = z_0 \cot(\theta/2) \quad (2.18)$$

where  $\varepsilon$  is the horizontal distance from the contact line and  $z_0$  can be regarded as some finite height at which the macroscopic cap passes over into a film.

From balancing equation (2.17) with the rate of change of surface free energy (equation (2.9)), an expression determining the rate of spreading can be obtained. For small angles and vanishing equilibrium contact angles, we then find

$$\theta = \frac{A}{(t+c)^{3/10}}, \quad (2.18)$$

where  $A$  and  $c$  are constants. Equation (2.18) is valid for small spherical droplets spreading on high-energy surfaces.

Experimentally it is found that  $r_0$  increases rapidly at the early stages, and then very slowly. The evolution time for drops reaching their equilibrium contact angle,  $\theta_e$  can be from as short as  $10^{-5}$  s to several hours when the contact angle is small. Then the process stops and no further evolution of the drop can be

detected, its volume remains constant over periods as long as six months [52]. The data can often be represented by the power law

$$\theta \sim (t + c)^{-n}, \quad (2.19)$$

with  $c$  representing a constant of integration and  $\theta$  as the dynamic contact angle. The value of  $n$  was determined in a study by Tanner [48] on silicone oils, and gave  $n = 0.3$  which is in agreement with the theoretical prediction (equation (2.18)).

### 2.2.6. Spreading of a Stripe of Oil

The derivation of a law for the rate at which a thin stripe of oil spreads, follows the same approach as used for Frenkel's method for small droplets [31, 150]. The rate of change of the surface free energy is equated to the viscous dissipation derived by assuming the Poiseuille type flow field. The stripe cross-section is of the form of a spherical cap cross-section, so that  $r_0 = d_0/2$  (equation (2.2)), where  $d_0$  is the contact width of the cross-section. Equation (2.1) and  $h_0$  remains the same as derived for a spherical cap geometry (Fig. 2.2). However, conservation of volume alters the relationship between the contact angle,  $\theta$ , the volume of fluid,  $V$  and the cylindrical cap radius,  $R$ , to

$$R = \left( \frac{V}{L_0 \zeta} \right) \quad \text{where} \quad \zeta = \theta - \sin \theta \cos \theta. \quad (2.20)$$

For the stripe geometry the solid-liquid and liquid-vapour surface areas are given by

$$A_{LS} = d_0 L_0 \quad \text{and} \quad A_{LV} = 2 L_0 R \theta. \quad (2.21)$$

Differentiating equation (2.10) then gives a rate of change of energy

$$\frac{dF_s}{dt} = 2\gamma_{LV} L_0 v_E (\cos \theta - 1). \quad (2.22)$$

The edge speed,  $v_E$  in equation (2.22) is defined as the rate of change of contact width,  $d_0$  and is related to the dynamic contact angle by

$$v_E = \left( \frac{V}{L_0} \right)^{1/2} \frac{(\theta \cos \theta - \sin \theta) d\theta / dt}{(\theta - \sin \theta \cos \theta)^{3/2}}. \quad (2.23)$$

Equation (2.22) is similar in form to the rate of change of surface free energy of a spherical cap, but with the contact perimeter,  $2L_0$  replacing the spherical cap perimeter,  $2\pi r_0$ .

The viscous dissipation

$$T \frac{dS_T}{dt} = \frac{8 L_0 \eta v_E^2 J_W}{3 \tan(\theta / 2)} \quad (2.24)$$

follows exactly equation (2.17) for a cone inscribed within the spherical cap of a drop, but altering the circular contact area of a drop to a rectangular area of a liquid stripe. The spherical cross-section remains the same as for a drop, but instead of using a cone, the periphery of the cross-section of the stripe uses an inscribed triangle (essentially the geometrical cross-section of a cone) to determine the contact angle. Also the contact circle perimeter has been replaced by  $2L_0$  and the edge speed,  $v_E$  has been re-defined.

### 2.2.7. Small Angle Limit

To obtain a relation between Tanner's power law equation (2.19) and the contact diameter,  $d_0$ , the geometry of a spreading stripe on a high energy surface requires to have a small angle,  $\theta$ . The small angle limit is given as

$$\frac{d\theta}{dt} \approx \frac{\gamma_{LV}}{\eta J_W} \left( \frac{3L}{32V} \right)^{1/2} \theta^{9/2} (1 - \theta_e^2 / \theta^2). \quad (2.25)$$

The modified equation for Tanner's power law for a high energy surface ( $\theta_e = 0$ ), is then

$$\theta = \frac{A}{(t+c)^{2/7}} \quad (2.26)$$

where  $c$  is a constant of integration. The corresponding time dependence of the contact width is given by

$$d_0 = A(t+c)^{1/7} \quad (2.27)$$

where  $d_0$  is the width of the stripe and  $A$  is a constant.

### 2.3. Rayleigh Surface Waves in Elastic Media

To understand the nature of Rayleigh surface wave motion it is important to know that bulk elastic waves in comparison to surface elastic waves can propagate in any direction in a solid, whether the solid is elastically isotropic or anisotropic [9, 10]. Bulk waves can exist in elastic solids in the form of three independent waves and all of them can propagate in a given direction. One of them has a particle motion along the direction of propagation; this is the longitudinal bulk wave similar to pressure waves in fluids. The other two waves have transverse particle displacement which is transverse to the direction of wave propagation, such as the wave motion along a stretched string. The phase velocities of such bulk waves are independent of frequency (at least at the low frequency range and in the microwave range).

Surface elastic waves of the Rayleigh wave type, are surface confined waves and propagate along a stress-free surface of a solid and decay into the depth of the solid within a distance of the order of a wavelength [67, 156]. Their particle motion is in general described as an elliptical motion. If we analyse the elliptical wave motion we find that two orthogonal components exist in the direction of propagation coupled together in a fixed ratio. One is transverse to the wave propagation and is the normal component introducing a transverse stress into the material. The other one propagates within the surface plane in the direction of wave motion and introduces a longitudinal stress into the material sometimes referred as compressional component. The reason why the two wave motion components are coupled together is that at the surface there is no restraining force perpendicular to the surface and a compression of the material in the direction of wave propagation produces motion into the transverse direction perpendicular to the surface. There exist alternate regions of compression and dilation within the surface plane where regions of compression tend to bend down, whereas regions of dilation bulge up. This can be compared with the model of a bending rod. On bending the outer surface (top surface) of the rod is stretched and the inner surface (bottom surface) is compressed. The symmetry line which represents the intermediate plane of the cross section of the rod remains unrestrained. The phase velocity is of the same form as for bulk elastic waves, but the particles at the free surface are less restrained than the ones deep in the interior of the bulk material which are surrounded on all sides by the solid. This means for the surface wave a lower phase velocity exists than for bulk elastic waves. The low propagation velocity of the wave means the wave cannot propagate into the interior of the bulk and therefore remains mainly confined to the surface [12].

### 2.3.1. Rayleigh Waves in Non-Piezoelectric Solids

Application of force to a solid puts the solid under stress and stress results in strain. An elastic wave propagating in a solid displaces an infinitesimal small element of elastic solid defined by the Cartesian co-ordinates  $(x_1, x_2, x_3)$  from its

equilibrium position due to the exerted stress. The displacement causes the element to vary harmonically in the direction of wave propagation. The displacement vector,  $u(x_1, x_2, x_3, t)$ , that gives the departure from its unperturbed position, has three components,  $u_1$ ,  $u_2$ , and  $u_3$  representing the particle displacements, parallel to the respective Cartesian axes. If this is the  $x_1$  direction, for example, it may be presented as [157]

$$u(x_1, x_2, x_3, t) = (u_1 x_1 + u_2 x_2 + u_3 x_3) e^{i(\omega t - k x_1)} \quad (2.28)$$

where  $\omega$  is the angular frequency of the wave ( $\omega = 2\pi f$ , where  $f$  represents the fundamental frequency of the wave),  $i = \sqrt{-1}$ ,  $k$  is the wave vector  $k = \omega/v = 2\pi/\lambda$  (where  $\lambda$  is the wavelength and  $v$  is the phase velocity of the wave), and each of these components  $u_1$ ,  $u_2$ , and  $u_3$  is a function of time. The deformation of the volume element is given by the symmetric strain tensor,  $P$  [157]

$$P_{ij} = \frac{1}{2} \left( \frac{\partial u_i}{\partial x_j} + \frac{\partial u_j}{\partial x_i} \right) \quad (2.29)$$

where  $i, j, k$ , separately take on the values 1, 2, and 3, which correspond to the three axis  $x_1$ ,  $x_2$ , and  $x_3$ . Strain is the change in length per (unstrained) unit length in the solid as a result of applied stress. The diagonal elements in the strain tensor,  $P_{ij}$  represents for  $P_{11}$  strain in the  $x_1$  direction ( $P_{11} = iku_1$ ), while  $P_{22}$  and  $P_{33}$  represents strain in the  $x_2$  and  $x_3$  direction, respectively. These diagonal elements  $P_{ii}$  are the longitudinal or compressional strains, while the two off-diagonal elements ( $P_{ij}$  with  $i \neq j$ )

$$P_{13} = P_{31} = \frac{1}{2} iku_3, \quad (2.30)$$

are shear strains and deform the infinitesimal small element (cross section is a square) normal to the plane with sides parallel to the  $x_1$  and  $x_3$  axes periodically

into a rhombus elongated alternately along one diagonal, and then the other diagonal.

To represent completely the state of stress at each point in a solid requires the use of a stress tensor,  $T$ . Each element of the stress tensor,  $T_{ij}$  represents the  $i^{\text{th}}$  component of force per unit area acting on the positive side of the  $i^{\text{th}}$  face of an infinitesimal cube located at  $(x_1, x_2, x_3)$ . This second-rank stress tensor is symmetric

$$T_{ij} = T_{ji}. \quad (2.31)$$

$T$  allows the determination of the stress in any direction on any plane interior to the solid [2].

### 2.3.2. Equation of Motion

The definition of the stress and the strain permits derivation of the equation of motion for elastic deformation of a solid, in particular the wave motion. If there are no body forces acting on the material within the cube, and if  $\rho$  is the mass density of the solid, Newton's third law gives the equation of motion of the cube which can be generalised to all three co-ordinates:

$$\sum_{j=1}^3 \frac{\partial T_{ij}}{\partial x_j} = \rho \frac{\partial^2 u_i}{\partial t^2} \quad (2.32)$$

with  $i = 1, 2, 3$ , corresponding to the Cartesian co-ordinates  $x_1, x_2$ , and  $x_3$ . Equation (2.32) relates inertial forces to the stress gradient.

It can be shown that for small deformations, the strain in a body is linearly proportional to the stress. In one dimension this is known as Hooke's Law, relating the elongation of a spring or elastic material to the tensile force. A principle which relates stress to strain, is known as a constitutive relation [157]

$$T_{ij} = \sum_{k,l=1}^3 c_{ijkl} P_{kl} \quad (2.33)$$

where  $c_{ijkl}$  is the elastic stiffness constant, which can be characterised as “microscopic spring constant” in describing what strain results from a given stress. This provides a complete characterisation of the elastic behaviour of a solid in the small deformation limit [113].

### 2.3.3. The Wave Equation

From the equation of motion (equation (2.32)) and the elastic constitutive equation (equation (2.33)) it is possible to derive the wave equation, which describes the propagation of a plane acoustic wave in a non-piezoelectric solid. Differentiating equation (2.33) with respect to  $x_j$  gives

$$\sum_{j=1}^3 \frac{\partial T_{ij}}{\partial x_j} = \sum_{j,k,l=1}^3 c_{ijkl} \frac{\partial^2 u_k}{\partial x_j \partial x_l} \quad (2.34)$$

Equating the right hand side of equations (2.33) and (2.34) results in the wave equation for non-piezoelectric, elastic solids [158]

$$\rho \frac{\partial^2 u_i}{\partial t^2} = \sum_{j,k,l=1}^3 c_{ijkl} \frac{\partial^2 u_k}{\partial x_j \partial x_l} \quad (2.35)$$

which represents a set of three equations in the particle displacement direction  $u_1$ ,  $u_2$ , and  $u_3$  with summation over the indices,  $j$ ,  $k$ , and  $l$ . The polarisation of a wave refers to the direction of particle displacement. These three equations represent three propagating wave classes; a compressional or longitudinal wave with polarisation in the  $x_1$  direction only, propagating in direction  $x_1$ , and

two shear or transverse waves which have polarisation perpendicular to the propagation direction  $x_1$ .

Equation (2.35) has three solutions representing acoustic waves with displacements along the directions,  $x_1$ ,  $x_2$ , and  $x_3$ . This leads to the generalised wave equation

$$u_i(x, t) = u_{i0} e^{i(\omega t - kx_i)} \quad (2.36)$$

representing wave propagation in the positive direction of  $x_1$ .  $u_i$  is the displacement in the  $i^{\text{th}}$  direction and  $u_{i0}$  is the displacement amplitude. The components of the displacement are characterised for a Rayleigh wave in a non-piezoelectric solid by,

$$u_1 = u_{10} e^{i(\omega t - kx_1)}, \quad (2.37)$$

representing compressional strain ( $P_{ii}$ ) in the  $x_1$  direction. If we then consider the second displacement component, the transverse component  $x_3$  as the normal component to the uniform compressional wave propagating along  $x_1$  the displacement would be

$$u_3 = u_{30} e^{i(\omega t - kx_1)} \quad (2.38)$$

which is the transverse (shear) wave component and  $u_{30}$  is the displacement amplitude in the vertical direction to the plane.

### 2.3.4. Rayleigh Waves in Piezoelectric Solids

The use of piezoelectric anisotropic materials (crystals) allows the excitation of Rayleigh surface acoustic waves. However, an arbitrary anisotropic piezoelectric crystal allows a surface wave to propagate in any direction of the crystal. Another problem arises with the possibility that upon generation not

only one wave mode may exist in the crystal interior. In order to restrict these effects, single crystals are used as the propagation medium to introduce specific propagation of surface waves and to minimise high frequency attenuation that are normally the characteristics of polycrystalline material. The choice of crystal cut is dictated in large part by a desire to have a beam of elastic energy, created by an electromechanical transducer, propagating parallel to the wave vector and, in the case of Rayleigh wave propagation, to have confinement of energy to the surface. This makes such waves extremely sensitive to surface perturbations. In addition to the isotropic case of wave propagation, in anisotropic piezoelectric materials there is an electrical potential propagating along with the three components of mechanical displacement. The velocity of propagation of the wave is independent of the electrical conditions at or near the surface [113].

In piezoelectric crystals the mechanical strain produces a proportional electric polarisation and, conversely, an applied electric field produces a proportional mechanical strain. This effect can only be achieved if the crystal does not belong to a class that has inversion symmetry. A crystal structure with a centre of inversion symmetry has the property that a straight line drawn from any point in the lattice through the centre of inversion will meet an equivalent point at equal distance from the centre. The separate constitutive relations of the elastic behaviour,  $T_{ij} = c_{ijkl} P_{kl}$ , and of the electromagnetic behaviour,  $D_i = \varepsilon_{ij} E_j$ , where  $D$  is the electric displacement and  $E$  the electric field, become the coupled set

$$T_{ij} = c_{ijkl}^E P_{kl} - e_{ijk} E_k \quad (2.39a)$$

and

$$D_i = \varepsilon_{ij}^S E_j + e_{ijk} P_{jk} \quad (2.39b)$$

in which  $e_{ijk}$  are the piezoelectric stress constants, having units of charge/(length)<sup>2</sup> and  $\varepsilon_{ij}^S$  are the permittivity constants measured at constant

strain. Equations (2.39a and 2.39b), normally referred as piezoelectric constitutive relations, completely describe the interplay of stress, strain and electric field in the piezoelectric solid. In these equations summations over the repeated indices is assumed so that in the most general case, 18 piezoelectric constants are necessary to characterise a piezoelectric material [159].

The piezoelectric constitutive relations allow the derivation of the wave equation for piezoelectric media having displacements in the  $u_i$  direction coupled with an electrical potential,  $\phi$ , rather than coupled with the electric field components,  $E_j$ . The condition that  $E_k = -\partial\phi/\partial x_k$  can be used since the velocity of sound is small in comparison with light, we can write equation (2.39a) as

$$T_{ij} = \sum_{k,l=1}^3 c_{ijkl} \frac{\partial u_l}{\partial x_k} + \sum_{k=1}^3 e_{ijk} \frac{\partial \phi}{\partial x_k}. \quad (2.40)$$

Combining equation (2.39a) with the equation of motion (equation (2.32)) yields to

$$\sum_{j,k,l=1}^3 c_{ijkl} \frac{\partial^2 u_l}{\partial x_k \partial x_j} + \sum_{j,k=1}^3 e_{ijk} \frac{\partial^2 \phi}{\partial x_k \partial x_j} = \rho \frac{\partial^2 u_i}{\partial t^2}. \quad (2.41)$$

Equation (2.41) represents three equations in four unknowns,  $u_1$ ,  $u_2$ ,  $u_3$ , and  $\phi$ . In a region with no free charges, the electrical displacement of the Maxwell equation can be expressed as  $\nabla \cdot \underline{D} = 0$ . This implies that  $\partial D_i / \partial x_i = 0$ , so that equation (2.41) can be rewritten as

$$\sum_{i,k,l=1}^3 e_{ikl} \frac{\partial^2 u_l}{\partial x_k \partial x_i} - \sum_{i,k=1}^3 \varepsilon_{ik} \frac{\partial^2 \phi}{\partial x_k \partial x_i} = 0 \quad (2.42)$$

and the solution of this system of four equations is a linear combination of components of the partial waves given by the elastic displacement component,  $u_i$  and the electric potential component,  $\phi$  in form of

$$\begin{aligned} u_i &= \alpha_i \exp[-\beta_c kx_3] \exp[i(\omega t - kx_1)], \\ \phi &= \alpha_4 \exp[-\beta_c kx_3] \exp[i(\omega t - kx_1)], \end{aligned} \quad (2.43)$$

(the wave is propagating along the axis  $x_1$ , and the axis  $x_3$  ( $x_3 > 0$ ) is perpendicular to the acoustic wave propagation) where  $\beta_c$  is the decay factor, characterising the velocity of oscillations into the crystal ( $\text{Re} [\alpha] > 0$ ) and  $\alpha_i$  is the relative amplitude factor for the individual partial wave, determined by boundary conditions, and  $\alpha_4$  is the amplitude factor for the electric potential. The solution of equation (2.43) substituted in equations (2.41) and (2.42) leads to a system of four equations to determine the amplitudes  $\alpha_i$  and  $\alpha_4$  which can be expressed in a determinant of polynomial of degree 8 with both real and imaginary coefficients. The solution of this determinant is given by Campbell and Jones [135].

Considering equation (2.43) for a Rayleigh surface acoustic wave device, the particles displacement for the compressional wave,  $u_1$  and the shear wave,  $u_3$  and the electric potential,  $\phi$  are decoupled and are assumed to have the form

$$\begin{aligned} u_1 &= \sigma_1 \exp[-\beta_s kx_3] \exp[i(\omega t - kx_1)], \\ u_3 &= \sigma_3 \exp[-\beta_s kx_3] \exp[i(\omega t - kx_1)], \\ \phi &= C \exp[kx_3] \exp[i(\omega t - kx_1)] \end{aligned} \quad (2.44)$$

where  $\sigma_1$  and  $\sigma_3$  are the relative amplitudes of the particle displacements and  $\beta_s$  is the decay factor classifying the velocity of oscillations into the solid substrate and  $C$  is the amplitude for the electric potential. Here  $\alpha_i$  has been substituted by  $\sigma_i$  and  $\alpha_4$  by  $C$  in order to describe especially the particle motion of Rayleigh waves in piezoelectric material. Equation (2.43) can be regarded as the general form of particle displacement in piezoelectric materials. The wave is propagating in the  $x_1$  direction with  $x_3$  normal to the surface. The amplitude for the mechanical particles displacement,  $u_2$  in the substrate is negligible compared to  $u_1$  and  $u_3$  [135] and therefore has been ignored.

## 2.4. Rayleigh Wave Interaction with Partially Localised Viscous Liquid

To investigate the effect of Rayleigh wave-viscous liquid interaction a model has been recently proposed, which considers the in-plane component of the in  $x_1$  direction propagating wave [148]. Since the wave components are decoupled from each other this allows a separate consideration of the liquid interaction with the wave components. The longitudinal component of the surface wave interacts with the liquid overlayer by coupling a shear wave into the liquid. To investigate the damping effect caused by the viscous forces due to the liquid acting on the surface during wave propagation the system can be treated as damped harmonic oscillator (substrate plus liquid overlayer). Theoretical prediction of the amplitude attenuation and the frequency shift of the shear wave penetrating into the liquid are from there obtained. The model reviewed here assumes a no-slip condition, so that the longitudinal component of the wave which viscously couples the shear wave into the liquid causes motion of the overlayer with a distance dependent, exponentially decaying behaviour of the wave. The penetration of the shear wave into the liquid is determined by the relation of the viscosity of the liquid overlayer and the speed of shear wave in the fluid and is called the shear wave penetration depth,  $\delta$ . Effectively the fluid is dragged along by the oscillating surface causing a plane-parallel laminar flow. The model used, is based on a model approach used by Rodahl and Kasemo [160] which considers the changes in resonance frequency and the dissipation factor for a quartz-crystal microbalance (QCM) coated with a viscous film. Their model considers only the physical characteristics of a Newtonian fluid. A detailed review of Newtonian fluid dynamics is given by Bird et al. [161].

Polymer melts such as polydimethylsiloxane (PDMS) oils of high viscosity, also referred as polymeric liquids, are classed as amorphous polymers and show viscoelastic properties. This leads to a change in fluid classification when a transition in relaxation time appears. A small relaxation time classifies the liquid as ideal Newtonian liquid since its behaviour follows exactly Newtonian behaviour. In the case of long relaxation times the fluid can be more accurately

described as a creeping amorphous solid. Taking this consideration into account, an expression for the attenuation of SAW amplitude, related to the longitudinal (in-plane) motion of the surface wave caused by surface loading of a viscoelastic oil of arbitrary thickness, can be accomplished. With a numerical analysis the damping of the SAW can be obtained considering that the fluid has a variable thickness  $t_f(x)$  with time.

## 2.4.1. SAW Transmission Resonances Model

### 2.4.1.1. Damped Harmonic Oscillator

A damped harmonic oscillator,

$$m\ddot{q} + r\dot{q} + sq = 0, \quad (2.45)$$

has a solution  $q = Ce^{-\alpha t} e^{i\omega t}$ , where  $\alpha = r/2m$  is the damping coefficient and  $\omega = \sqrt{(sm - r^2/4m^2)} = \sqrt{(\omega_0^2 - \alpha^2)}$  is the angular frequency of the damped harmonic oscillation [148]. In general, both  $\alpha$  and  $\omega$  can be complex, although for small damping it is the changes in  $\alpha$  which dominate. For a small measured shift in frequency the first order shift in angular frequency,  $\Delta\omega$ , is

$$\Delta\omega = -\text{Im}(r/2m). \quad (2.46)$$

The attenuation of a wave after travelling  $d$  metres, at a speed,  $v$  is,

$$L = -10 \log_{10} e^{\text{Re}(dr/mv)} \quad (2.47)$$

where  $L$  is in decibels.

Rodahl and Kasemo [162] used an assumption based on a simple harmonic oscillator covered with a uniform film, to simulate the behaviour of the

QCM surface in contact with a fluid. Their equation considered the driving force per unit surface area,  $F$  of the harmonic oscillator with the deposited film and was expressed as

$$F = \frac{1}{2} \rho_s t_s (\ddot{q} + \gamma_d \dot{q} + \omega_0^2 q) - F_f \quad (2.48)$$

where  $q = A_0 \exp(i\omega t)$  is the (in-plane) displacement of the oscillator at time  $t$ .  $F_f$  is the force exerted by the fluid on the substrate per unit surface area,  $\gamma_d$  and  $\omega_0$  are the damping and resonant frequency of the unloaded substrate, respectively,  $\rho_s$  is the density of the substrate and  $t_s$  is the thickness of oscillating substrate. The particle displacement,  $u_1$  for the longitudinal wave propagating along the  $x_1$  direction in the SAW device is the dominant factor for the Rayleigh wave motion;  $t_s$  is then a characteristic thickness given approximately by one SAW wavelength,  $\lambda_R$ . It will be shown later (equation (2.66)), that the force acting on the substrate, including a single relaxation time,  $\tau$ , to account for the viscoelastic properties of the fluid, is of the form,

$$F_f = \frac{\beta \dot{q}}{1 + i\omega\tau}. \quad (2.49)$$

Substituting equation (2.49) into equation (2.46) and (2.47) we obtain from additional damping due to the fluid loading, and considering equation (2.48), the following expressions for the changes in the attenuation and angular frequency,

$$L \approx -20 \log_{10} e^{-\frac{d}{\rho_s t_s v_R} \operatorname{Re} \left[ \frac{\beta}{1 + i\omega\tau} \right]} \quad (2.50)$$

$$\Delta\omega \approx -\frac{1}{\rho_s t_s} \operatorname{Im} \left[ \frac{\beta}{1 + i\omega\tau} \right]. \quad (2.51)$$

where  $v_R$  is the speed of the Rayleigh surface acoustic wave. Equation (2.51) accounts in general for a frequency shift of a harmonic oscillator. To adopt this to a surface wave a translation of the shift in frequency,  $\Delta\omega/\omega$  into a shift in surface wave speed,  $\Delta v/v_R$  ( $\Delta\omega/\omega = \Delta v/v_R$ ) is necessary.

### 2.4.1.2. Viscoelasticity

Viscoelasticity describes the response of a polymer to applied stress in terms of deformation. The expression "elasticity" refers to the ability of the polymer to return to its original shape after it has been stressed. Here the process is dominated by Hooke's Law which determines the behaviour in small deformations and defines a relation between stress and strain. Stress is in this condition directly proportional to strain but it is independent of the rate of strain [163]. On the other hand viscosity is characterised by the resistance of a polymer or polymer solution to flow. Viscous behaviour is a linear relationship between shear stress,  $\sigma$ , and the rate of strain,  $\dot{\gamma}_V$  ( $\sigma \propto \partial\dot{\gamma}_V / \partial t$ ). In many polymers a combination of elastic and viscous response arises as a direct consequence of the chain structure, hence the term viscoelastic behaviour. When a fluid of viscoelastic behaviour is subjected to sinusoidally oscillating stress, the strain may neither exactly be in phase with the stress (as it would be for a perfectly elastic solid) nor  $90^\circ$  out of phase (as this would be for a perfectly viscous liquid) but can be somewhere in between. This can be best explained by their characteristic relaxation times. In the situation where the relaxation time,  $\tau$  is larger than the time period,  $T_s$  where stress is applied to the polymer ( $\tau \gg T_s$ ), polymer chains do not have time to move with respect to each other and this leads to an elastic solid behaviour. Whereas in the situation where  $\tau$  decreases until  $\tau \ll T_s$  polymer chains now can move with respect to each other and the polymer behaves as a viscous liquid.

### 2.4.1.3. Maxwell Model

The Maxwell model for viscoelasticity shown in Fig. 2.3 has been introduced as an aid in visualising viscoelastic response. It uses two linear mechanical elements to represent the extremes of the mechanical response spectrum. The model is therefore able to describe the viscoelastic nature of the stripe of fluid used in the experiments. The first element in the model is the spring which represents a linear elastic or Hookean solid and this can be related to the shear stress,  $\sigma$ . The second element is a dashpot and accounts for a linear viscous or Newtonian fluid and is related to the rate of strain,  $\dot{\gamma}$ . The dashpot in the model has a piston moving in a cylinder of Newtonian fluid. The elements are connected in series to form the Maxwell element and the total strain (extension) of the element is the sum of the strains in the spring and the dashpot:

$$\gamma = \gamma_{spring} + \gamma_{dashpot} \quad (2.52)$$

Differentiating equation (2.52) with respect to time gives

$$\dot{\gamma} = \dot{\gamma}_{spring} + \dot{\gamma}_{dashpot} \quad (2.53)$$

here the total rate of strain is the sum of the rate of strain for the elastic part or the spring,  $\dot{\gamma}_{spring} = \dot{\sigma} / \mu$  and the viscous part or the dashpot,  $\dot{\gamma}_{dashpot} = \sigma / \eta$ , so that equation (2.53) leads to

$$\dot{\gamma} = \frac{\dot{\sigma}}{\mu} + \frac{\sigma}{\eta} \quad (2.54)$$

where  $\mu$  is the fluid's shear modulus and  $\eta$  is the fluid's viscosity. Using the  $e^{i\omega t}$  time dependence and defining a relaxation time,

# Maxwell Model for Viscoelasticity

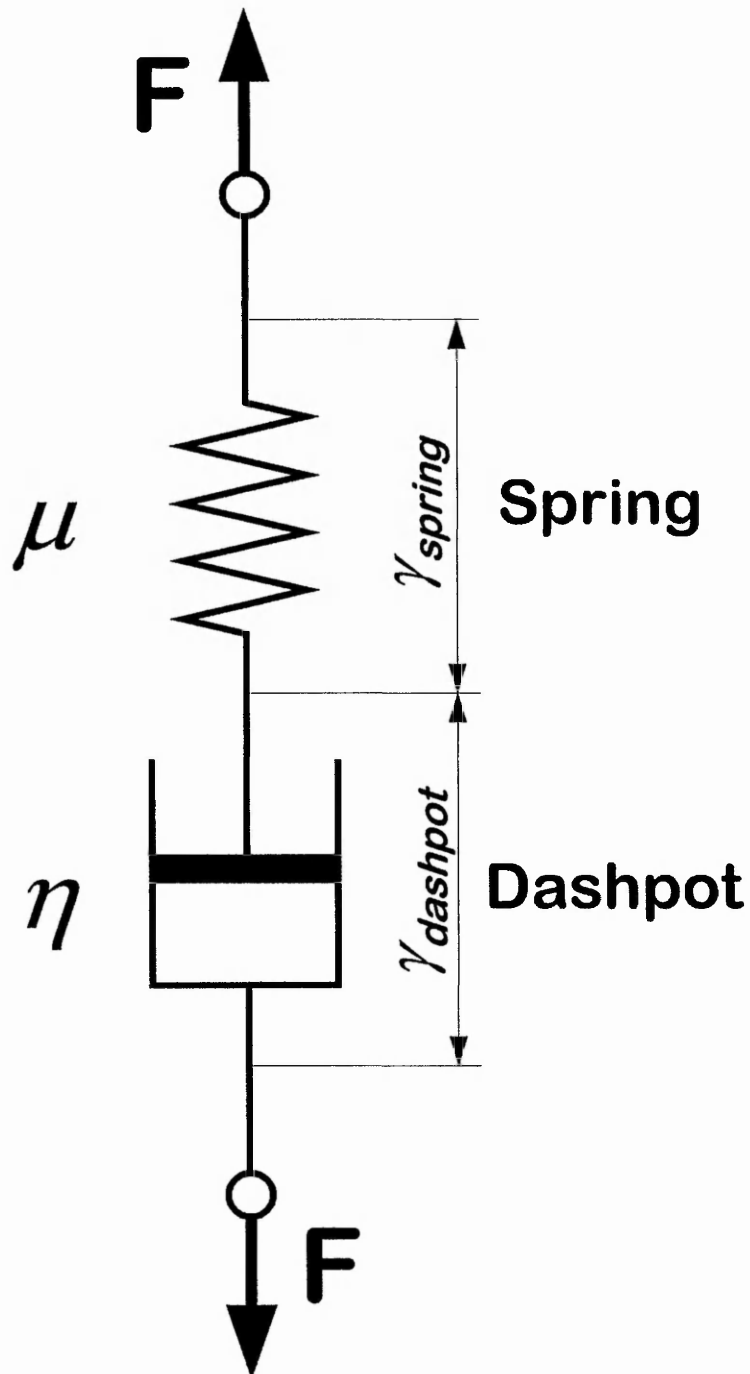


**Fig. 2.3** The Maxwell Model for viscoelasticity models the viscoelastic response of a viscoelastic medium such as a polymer fluid.

$$\tau = \frac{\eta}{\mu} \quad (2.55)$$

we obtain

$$\sigma + \tau \dot{\sigma} = \eta \dot{\gamma}. \quad (2.56)$$

We can rewrite equation (2.56), following the constitutive relation given for the small deformation of a solid body which has a linear dependence for the stress (equation (2.33)), to

$$(1 + i\omega\tau)\sigma = \eta\dot{\gamma}, \quad (2.57)$$

expressing a complex shear stress in dependence of the rate of strain. Thus

$$\sigma = \frac{\eta}{1 + i\omega\tau} \dot{\gamma} \quad (2.58)$$

and this gives for the relation  $\omega\tau$  the two extreme limits,

- i)  $\omega\tau \rightarrow 0$  characterising the above mentioned Newtonian liquid and
- ii) an amorphous solid when  $\omega\tau \rightarrow \infty$ .

#### 2.4.1.4. Navier-Stokes Equation and Boundary Conditions

Since the force that the liquid is exerting on the SAW device surface is opposite to the shear force in the liquid at  $x_3 = 0$ , we have the relation

$$F_f = -\eta \left[ \frac{\partial v_f^{x_1}}{\partial x_3} + \frac{\partial v_f^{x_3}}{\partial x_1} \right] \Bigg|_{x_3=0} \quad (2.59)$$

where  $v_f^{x_{1,3}}$  are the  $x_1$  and  $x_3$  components of the fluid velocity. The inclusion of the relaxation time means a rescaling of the viscosity to,

$$F_f = \frac{-\eta}{1+i\omega\tau} \left[ \frac{\partial v_f^{x_1}}{\partial x_3} + \frac{\partial v_f^{x_3}}{\partial x_1} \right] \Bigg|_{x_3=0} \quad (2.60)$$

The motion of the fluid overlayer can be described by the Navier-Stokes equation reducing the problem of determining the attenuation of the surface wave for an arbitrary thickness of viscoelastic fluid covering the device surface, to that of determining the fluid flow. The Navier-Stokes equation, that must therefore be solved is

$$\frac{\partial \underline{v}_f}{\partial t} + (\underline{v}_f \cdot \underline{\nabla}) \underline{v}_f = \frac{1}{\rho_f} \underline{\nabla} p + \frac{\eta}{\rho_f} \underline{\nabla}^2 \underline{v}_f \quad (2.61)$$

The fluid is considered to be viscous and incompressible, so that  $\underline{v}_f \cdot \underline{\nabla} = 0$ , and the pressure gradient in the fluid is neglected, so that  $\underline{\nabla} p = 0$ , We then obtain from equation (2.61)

$$i\omega \underline{v}_f = \frac{\eta / \rho_f}{1+i\omega\tau} \underline{\nabla}^2 \underline{v}_f \quad (2.62)$$

assuming a  $e^{i\omega t}$  time dependence and using the complex rescaling factor for the viscosity accounting for the single relaxation time,  $\tau$ . Solving equation (2.62) leads to the general solution of the fluid velocity given as

$$v_f = Ae^{x_3(\sqrt{2i}/\delta)} + Be^{-x_3(\sqrt{2i}/\delta)} \quad (2.63)$$

where  $A$  and  $B$  are the characteristic coefficients for the fluid velocity  $v_f$  for the shear wave penetrating into the liquid. In order to solve equation (2.62) subject to the first boundary condition the speed of fluid must match the substrate speed,  $v_0$  at  $x_3 = 0$  (since a no-slip consideration will couple the shear motion into the liquid). The shear wave's decay length is defined by the shear wave penetration depth,  $\delta = \sqrt{(2\pi/\omega\rho_f)}$ . The second boundary condition requires the shear stress [164] to vanish at the free surface of the liquid,  $x_3 = t_f$ . Thus the fluid velocity must satisfy,

$$v_f(x_3 = 0) = v_0 = \dot{q}(x_3 = 0) \quad (2.64)$$

and,

$$\left[ \frac{\partial v_f^{x_1}}{\partial x_3} + \frac{\partial v_f^{x_3}}{\partial x_1} \right]_{x_3=t_f} = 0 \quad (2.65)$$

where  $t_f$  is the fluid thickness.

#### 2.4.1.5. Fluid Velocity - Rayleigh Wave

To obtain the fluid velocity the Navier-Stokes equation must be solved, subject to the boundary conditions equations (2.64) and (2.65) and continuity. A suitable form for the solution is,

$$\underline{v}_f = (v_f(x_3)e^{i(\omega t - kx_1)}, 0, u_f(x_3)e^{i(\omega t - kx_1)}), \quad (2.66)$$

where  $v_f(x_3)$  is of the form given in equation (2.63). In the approximation considered in equation (2.66), this requires a non-vanishing  $x_3$  component of the fluid velocity in order to satisfy the continuity conditions and so maintain the incompressibility of the fluid. The fluid velocities for the  $x_1$  and  $x_3$  directions taking into account the boundary conditions are,

$$v_f = v_0 \left\{ \frac{\cosh[\sqrt{2i}(x_3 - t_f)/\alpha]}{\cosh[\sqrt{2i}t_f/\alpha]} \right\} \quad (2.67)$$

and

$$u_f = \frac{v_0 \alpha i k}{\sqrt{2i}} \left\{ \frac{\sinh[\sqrt{2i}(x_3 - t_f)/\alpha]}{\cosh[\sqrt{2i}t_f/\alpha]} \right\} \quad (2.68)$$

where

$$\alpha = \frac{\delta}{\sqrt{1 + i\omega\tau - i\delta^2 k^2 / 2}}. \quad (2.69)$$

With regard to the cosh and sinh term in equations (2.67) and (2.68) the complex argument for both terms contains for the fluid velocity both a damping and an oscillatory term. The force per unit surface area due to shearing stress of the liquid (equation (2.60)) can then be evaluated and is,

$$F_f = \frac{\beta v_0}{1 + i\omega\tau} \quad (2.70)$$

where  $\beta$  is

$$\beta = \left( \frac{\eta\sqrt{2i}}{\alpha} \right) \left( \frac{1 - ik^2\alpha^2}{2} \right) \tanh\left( \frac{\sqrt{2i}t_f}{\alpha} \right), \quad (2.71)$$

and defines the  $\beta$  used in equation (2.49). This gives for a Rayleigh wave propagation, a shearing force into the liquid of

$$F_f = \frac{\eta v_0 \sqrt{2i(1-ik^2\alpha^2/2)} \tanh(\sqrt{2i}t_f/\alpha)}{\alpha(1+i\omega\tau)}. \quad (2.72)$$

Since additional damping, arising from the fluid, is proportional to the substrate velocity,  $v_0$  we are now able to determine the acoustic losses in (dB) given in equation (2.50),

$$L \approx -20 \log_{10} e \frac{d}{\rho_s \xi \lambda_R v_R} \operatorname{Re} \left[ \frac{\beta}{1+i\omega\tau} \right], \quad (2.73)$$

similarly the shift in angular frequency (equation (2.51)) becomes

$$\Delta\omega \approx -\frac{1}{\rho_s \xi \lambda_R} \operatorname{Im} \left[ \frac{\beta}{1+i\omega\tau} \right], \quad (2.74)$$

where  $t_s = \xi \lambda_R$  and  $\xi$  represents the effective depth characterised by the elliptical motion of the Rayleigh surface wave penetrating into the solid substrate which is approximately equal to one SAW wavelength.

In the approximate model developed here, the fluid height acts as a resonant cavity for shear waves with a node at the liquid-vapour interface and an antinode at the solid-liquid interface. At the high viscosity limit, when the liquid acts as an amorphous solid, the maximum effectiveness of resonances occur. Thus the model predicts periodic variations in losses due to shear waves. The changes within the relaxation time represents a significant transition in fluid properties from liquid to effectively solid and the shear wave resonances occur when the fluid height matches the condition,

$$t_f = n \lambda_s / 4 \quad (2.75)$$

where  $n = 1, 3, 5, \dots$ .

Similar solutions given in equation (2.73) and equation (2.74) can be obtained from two other acoustic device families, the thickness shear mode (TSM) devices and shear horizontal surface acoustic wave (SH-SAW) devices. An extensive case study with respect to equations (2.50) and (2.51) considering various analytical limits is provided by McHale et al. [148, 149].

**CHAPTER 3**

***EXPERIMENTAL  
DEVELOPMENT***

### 3.1. Introduction

The aim of finding a new method of observing the dynamic wetting process of a liquid of non-volatile viscous oil has led to the development of an in-plane technique using a sensor based on surface acoustic waves (SAW's). The system monitors the dynamic evolution of a small stripe of viscous oil directly in the spreading plane. When a surface wave propagates along the solid-liquid interface on a liquid loaded surface, the wave may be reflected due to the advancing edge of the liquid stripe which can act as a plane reflector for surface acoustic waves or the wave travels along the solid-liquid interface. While transmitting along the interface, the surface wave experiences an increased attenuation of the signal amplitude with a distinct pattern of resonances. In principle a SAW sensor is able to detect changes in the spreading process in the early stages, when reflected and transmitted signals both exist and later on when the fluid spreads to a very small angle where only mass loading effects are significant [63].

On the other hand optical experiments are only capable of observing at the plan-view or the cross-section of an advancing liquid front. The most direct method of optical observation is to measure the contact angle, which involves direct visual observation of a droplet using either the profile or a plan view method [57]. Other methods for examining the changes of macroscopic droplets draining into microscopic films have been optical profiling, laser interferometry, X-ray reflectivity, ellipsocontrast and ellipsometry, (see the review presented in Chapter 1). However, none of these techniques monitors the dynamic changes in the spreading plane. Moreover these methods are only offering optical observations of the wetting dynamics. The accessibility to the surface of the SAW sensor, allows the use of optical observation to simultaneously monitor the spreading process in addition to the acoustic response produced by the sensor. Merging the two techniques to a new unique system allows the observer to obtain information of the dynamic evolution of liquids and possibly of the structure of the liquid.

This chapter introduces this novel system presenting the efforts of combining the optical interferometry system with the Rayleigh surface acoustic

wave sensor. The system monitors changes of the fluid within the acoustic path of the sensor. A CCD camera records images directly at the point where the SAW impinges on fluid loading. This allows the observer to directly correlate changes in fluid geometry with changes in signal amplitude of transmitted and reflected signals. The system components and system configuration is presented in the first section. A short technical description of SAW sensors used for the experiments is provided. Later the data acquisition process is outlined. The optical system with its technical features is explained and the method of image processing to process a sequence of images using interference pattern analysis to extract geometrical details from the dynamically evolving stripe are described. Finally a deposition technique for stripes of oil is presented.

## 3.2. System Configuration

A description of how the components are connected is shown in Fig. 3.1. The system was set-up using the following components.

- 1 Controller Unit PC Epson with 80286 Processor.
- 1 Philips/Fluke Digital Storage Oscilloscope (DSO) PM 3365A.
- 3 Double Balanced Mixers (DBM's) ZFM 4, Mini Circuit.
- 1 Hybrid Junction HH-107, MA-COM Inc.
- 4 RF-Amplifiers AMC-182, MA-COM Inc.
- 2 Diode Detectors HP 8471D, Hewlett and Packard.
- 2 TG 105 Pulse Generator, Thurlby Thandar Instruments.
- 1 2022D AM/FM Signal Generator, Marconi Instruments.
- 4 50  $\Omega$  Terminators.
- Various SAW-Devices, designs for 170 and 250 MHz.

To understand the operation of the circuitry it is necessary to give a brief introduction to several components.

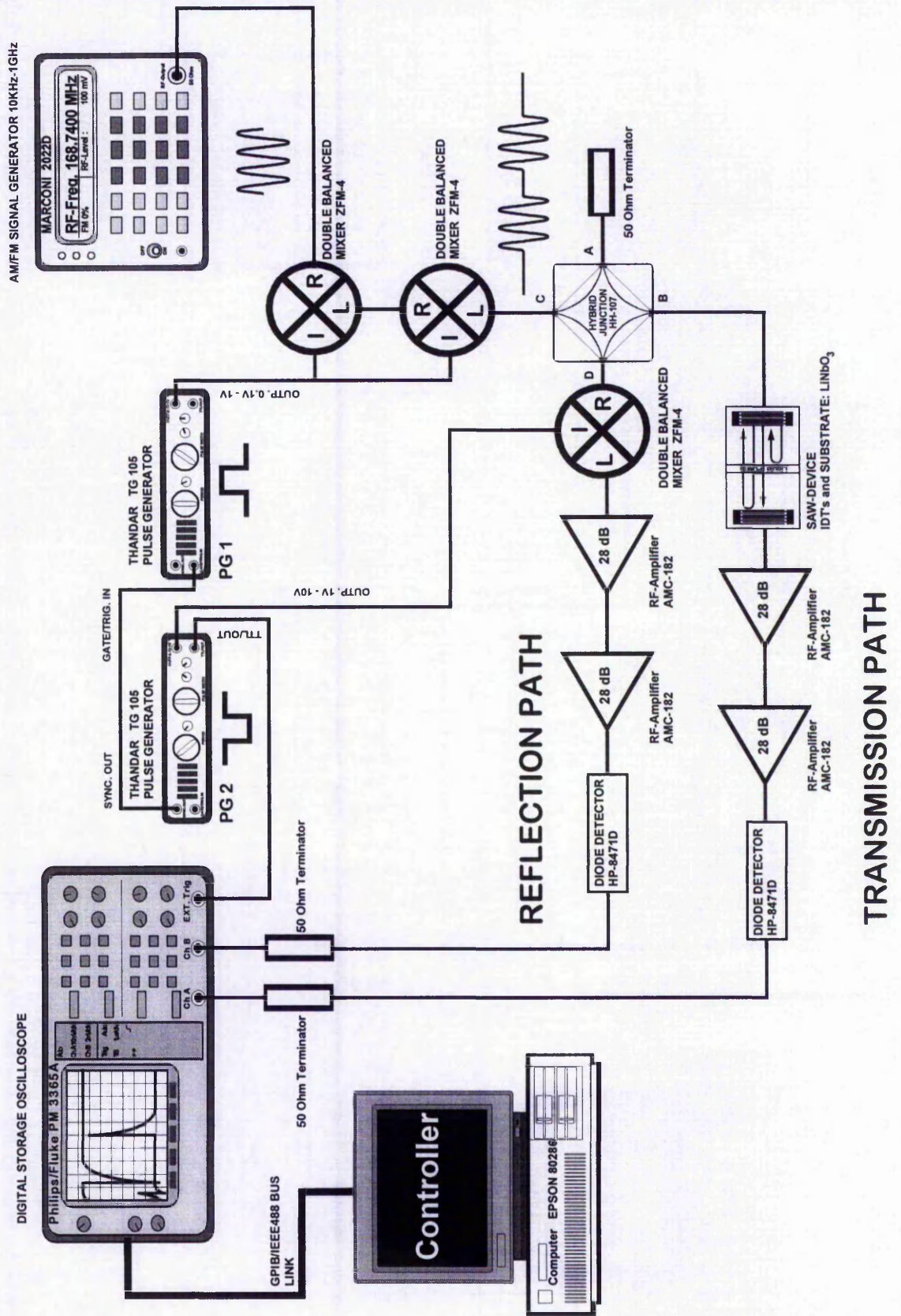


Fig. 3.1 The SAW-circuit with instrumentation arranged in pulsed transmission/reflection mode.

### 3.2.1. Description of the Electronic Components

#### 3.2.1.1. TG 105 Pulse Generator

The TG 105 is a mains operated, 5 Hz to 5 MHz pulse generator with independent TTL and 50  $\Omega$  variable outputs. Period and pulse width are each selected by a six position range switch, plus a vernier control. A special feature of the TG 105 is an internal inhibit circuit that blanks the output when the pulse is set greater than the period. The variable 50  $\Omega$  output is controlled by the third vernier which switches between ranges of 0.1 V to 1.0 V and 1 V to 10 V (from 50  $\Omega$ ) giving an overall range of 50 mV to 5 V into a 50  $\Omega$  load [165].

#### 3.2.1.2. Marconi 2022D 10 kHz-1 GHz Signal Generator

The Marconi 2022D is a synthesised signal generator having a frequency range of 10 kHz to 1 GHz and providing comprehensive amplitude, frequency and phase modulation facilities with an RF output level of -127 dBm to +13 dBm. Microprocessor control allows programming by the General Purpose Interface Bus (GPIB, GPIB in accordance with the IEEE-488 standard) [166].

#### 3.2.1.3. Digital Storage Oscilloscope (DSO) PM 3365A

The digital storage oscilloscope (DSO) is a two channel, six digital memory oscilloscope, with a frequency range up to 100 MHz. It also has a cursor function for time and amplitude measurements in the digital memory mode, a reference memory and a non-volatile storage of all wave forms. The oscilloscope is adapted to communicate with other GPIB bus measuring devices. This allows the user to control the oscilloscope by an external controller with independent processor unit. This includes reading and controlling

the oscilloscope settings, reading and writing into the oscilloscope's display memory, and reading and writing the screen or cursor positions or parameter sets into the controller [167].

#### 3.2.1.4. Double Balanced Mixer (DBM) ZFM-4

The DBM ZFM-4 is a 3 port device operating within a frequency range of 5 MHz to 1250 MHz. The function of a mixer is to convert radio-frequency (RF) energy at one frequency to a second frequency. The most popular application of balanced mixer modules is to convert an incoming RF signal to a lower intermediate frequency (IF) output. This is related to a single balanced mixer performance. In a double balanced mixer, the incoming RF signal (R) is combined with a high-level oscillator signal LO (L) and the desired IF side band is selected at the output (I). The RF signal (input signal) is multiplied with the higher local oscillator signal to produce the sum and difference frequencies at the output. In most models the RF and LO signal are transformer coupled, while the IF output is DC coupled, and this is used in the SAW-system (Fig. 3.1). All three ports are isolated from each other. Fig. 3.2 shows the actual operational mode used for the pulse configuration of the system [168].

#### 3.2.1.5. Hybrid Junction HH-107

The Hybrid Junction HH-107 is a 180° hybrid device, designed to operate at a frequency range of 2 - 200 MHz. This is a reciprocal four port device which provides two equal amplitudes in-phase signals when fed from its sum port and two equal amplitude 180° out-of-phase signals when fed from its difference port. Opposite ports of the hybrid are isolated. In Fig. 3.3 port B can be considered the sum port with port A as the difference port. Ports A and B and C and D are isolated ports. The total power dissipation in the hybrid under matched conditions is determined from the insertion loss and the known input power by, Insertion Loss (dB) =  $10 \log (P_{in}/P_{out})$ . Most of the power will be

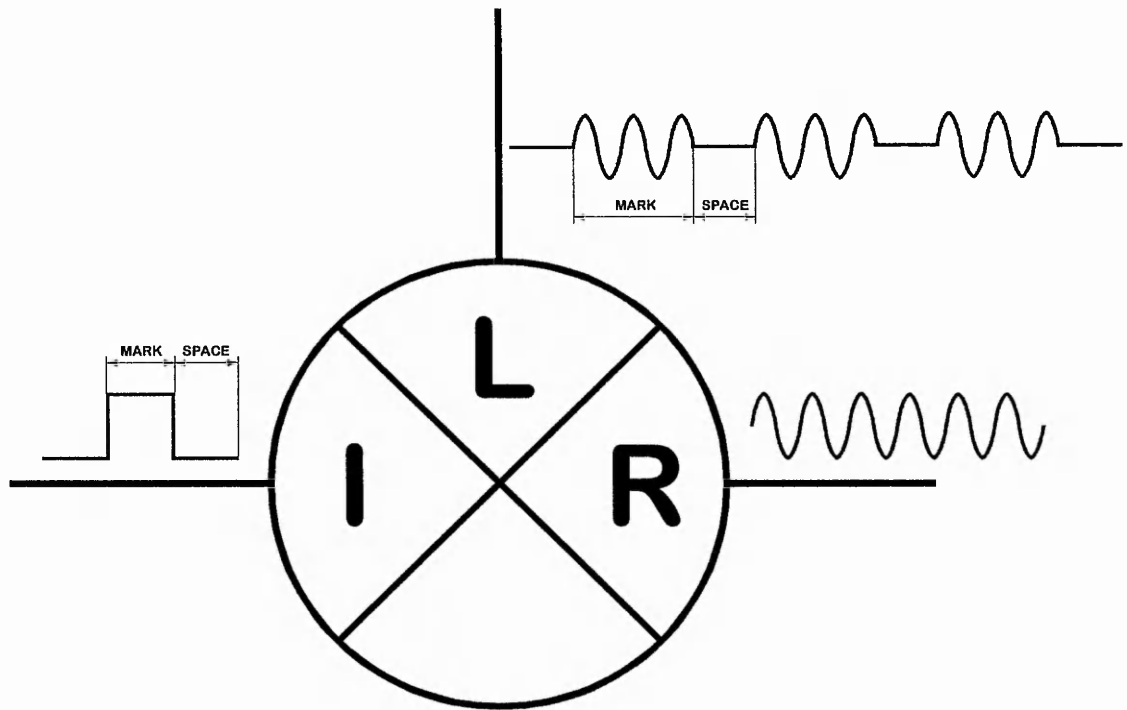


**Fig. 3.2** The double balanced mixer combines the incoming RF-signal (input signal) and a 400 ns pulse with a 1 kHz repetition rate, resulting in a pulsed RF-signal at the high level oscillator output port L.

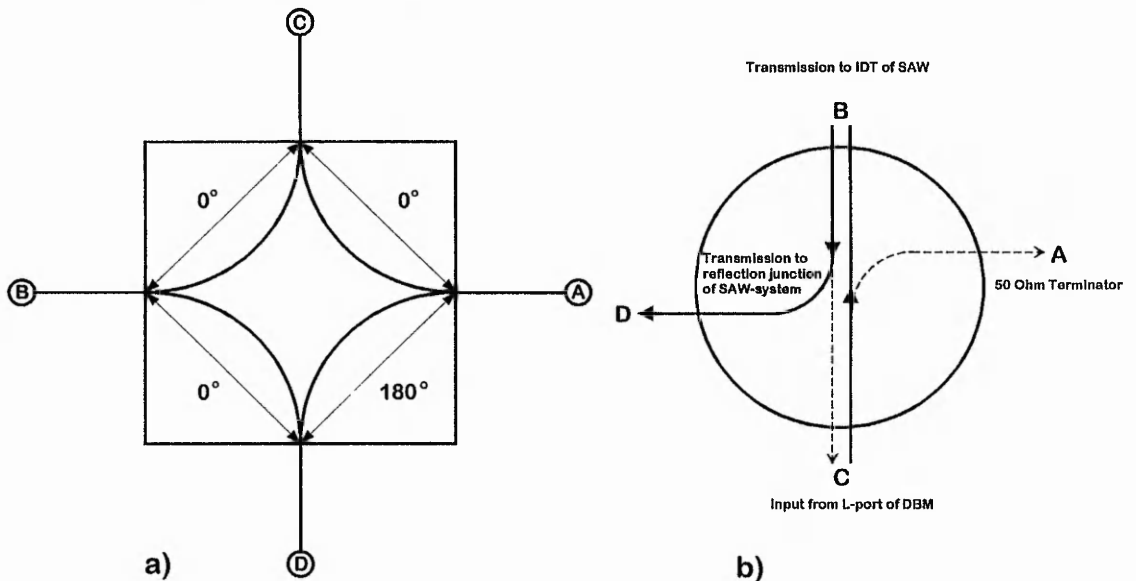


**Fig. 3.3** A four port 180° hybrid junction. In a) the principle of the circuit diagram with the 180° out-of-phase link between port A and D can be seen, b) represents the actual signal flow when operating together with the system.

dissipated in the wire and ferrite cores making up the transformer circuits and not in the internal load. There are two possibilities to drive this device:

- 1. Operation as a power divider - One source operating at ports A, B, C, or D.
- 2. Operation as power summer - Two sources operating at ports A and B, or C and D.

In the configuration of Fig 3.1 the hybrid is driven as a circulator (Fig. 3.3(b)) operating the device as a power divider respectively, enabling the SAW-device's source transducer to be used both to transmit and to detect surface waves [169].

#### **3.2.1.6. Diode Detector HP 8471D**

The HP 8471D diode (video) detector is the simplest type of microwave receiver available. It consists of a single Schottky-barrier, or point contact, microwave diode. The circuit has a microwave input port and a video output port. The function performed by the diode is simple rectification. The diode uses low resistance semiconductors and hence provides at small power levels a low impedance rectification. The frequency range of the detector for rectifying RF-signals is between 100 kHz and 2 GHz. A measure of the threshold sensitivity of a detector is called its tangential sensitivity (TTS). The tangential sensitivity of the detector is defined as the amount of signal required to raise the baseline level of a received pulsed signal to the peak noise amplitude when the signal is absent [170]. The threshold sensitivity of the HP 8471D for a nominal 50  $\Omega$  matching impedance is 7.1 mV  $\pm$  0.5 mV (- 30 dBm) input Voltage, fed from a RF input source, giving a transfer characteristic of minimum measurable output of 50  $\mu$ V [171].

### 3.3. The Interdigital Transducer (IDT)

Interdigital transducers (IDT's) are the building blocks of surface wave sensors. Generally IDT's consist of a series of interleaved electrodes made from a metal film, with each set extending from a common contact pad, as shown in Fig. 3.4. The IDT's are photodeposited on the highly polished surface of the precisely orientated piezoelectric crystal. The width of the electrodes is equal to the width of the interelectrode gaps. The distance of a pair of adjacent fingers is placed at half a wavelength when compared to the wavelength of a surface wave. Hence three neighbouring fingers represents the complete wavelength of an electro-mechanically excited surface wave. An applied voltage to the contact pads will cause, due to the piezoelectric effect, a strain pattern of periodicity  $L$ , in the structure. The electric field distribution having the spatial period of the electrodes is established between the electrodes. By means of piezoelectric coupling, these surface-concentrated fields produce a corresponding elastic strain distribution, the deformation-wave. With the field localised at the free surface, the coupling to surface acoustic waves can be made quite strong. It also follows that the transducer efficiency is a maximum at the RF excitation frequency for which the surface wave propagates one transducer period in one RF period. This frequency is called the synchronous frequency and is dependent on the Rayleigh wave phase velocity  $v_R$  and the electrode spacing constant  $L_N$  of one section, see Fig. 3.5.

One of the transducers acts as the device input and converts signal voltage variations into mechanical surface acoustic waves (SAW's). The other IDT is employed as an output receiver to convert mechanical SAW vibrations back into an output voltage. As a result, signal voltages can be applied to either IDT with the same end result.

#### 3.3.1. Uniform IDT

The comb structure of the transducer is of the form of a uniform periodic interdigital (IDT) transducer with single electrodes, a so called unapodised

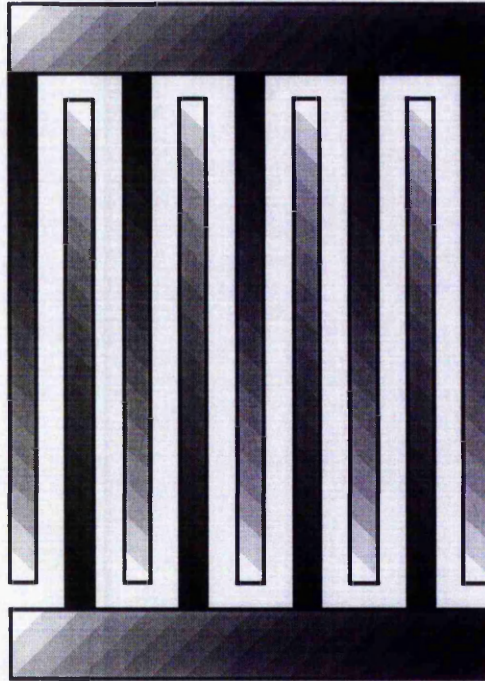


**Fig. 3.4** Uniform periodic interdigital transducer (IDT) with single electrode configuration, extending from a common contact pad and equal gap, electrodes spacing.

transducer. Its bandwidth is determined by the range of electrode spacing. The transducer is considered to have  $N$  sections, each of the length  $L_N$  as in Fig. 3.5 indicated, so that the total number of electrodes is  $2N+1$ . The adjacent and interleaved arrangement of the electrode structure give equal but opposite potentials. The IDT behaves as a sequence of ultrasonic sources. For an applied sinusoidal voltage, all vibrations interfere constructively only if the distance  $L_N/2$  between two adjacent fingers is equal to half the wavelength. If the frequency,  $f_0 = v_R/L_N$  departs from this value, the interference between the elastic signals is no longer constructive and the overall vibration is weaker. Here  $f_0$  represents the resonant frequency,  $v_R$  is the speed of the Rayleigh wave propagating along the free surface under resonance condition and  $L_N$  is the distance of three adjacent fingers representing the length of one entire wavelength at resonance. Thus, the bandwidth of an IDT is narrower when there are more fingers. The acoustic aperture,  $W$  defines the effective region of transduction between two adjacent electrodes and is defined as  $W = M \lambda_R$  where  $M$  represents a multiple integer of the wavelength,  $\lambda_R$ . The IDT is uniform if a constant aperture is obtained. Size restriction and impedance requirements limit the extent to which the acoustic aperture,  $W$  can be increased to reduce overall device loss. The aperture determines the width of the radiated beam and is typically of the order of 10-100 wavelengths in magnitude. The finite aperture of the emitting IDT causes diffraction and a consequent is signal loss because of the spreading of the beam and the departure of the transverse phase from a constant value. The magnitude of the electrical output signal of the receiving IDT depends on the fraction and profile of the beam intercepted, the IDT design, and matching of the IDT to the load.

Flexibility in SAW component design is obtained by the application of an equivalent circuit model [30]. It requires the knowledge of the piezoelectric coupling coefficient,  $k^2$  of the material, the synchronous frequency,  $f_0$  and the static capacitance,  $C_T$ . The piezoelectric coupling coefficient is a measure of the efficiency of the conversion of electrical energy into acoustic energy and vice versa. It is constant in the case of homogeneous substrates. Matching networks between the input and the output transducer and the source and load, respectively, allow for the optimum transfer of signal energy.

The total capacity,  $C_T$  of the transducer is given by:

$$C_T = NC_S \quad (3.1)$$

where  $C_S$  represents the static capacity and is proportional to the acoustic aperture,  $W$  and is independent of the periodicity,  $L_N$ . The magnitude of the transducer impedance at synchronous frequency,  $f_0$  is proportional to  $1/2\pi f_0 C_S$  and therefore proportional to  $L_N / 2\pi f_0$ . For a given synchronous frequency,  $f_0$  and surface wave velocity,  $v_R$ , the periodic length,  $L_N$  is fixed, but the width of acoustic beam set by the acoustic aperture,  $W$  can be adjusted to obtain a convenient impedance and keep the ratio  $L_N / W$  constant. In general this is chosen to be  $50 \Omega$  at the synchronous frequency to match the device to the driving circuit. The periodic length,  $L_N$  is inversely proportional to the synchronous frequency,  $f_0$ .

The piezoelectric coupling coefficient is determined generally from the changes in phase velocity,  $v_R$  caused by depositing a highly conducting thin metal film onto the substrate surface. The conducting film causes a velocity shift for the surface wave and this change of velocity  $\Delta v$  is related to the coupling coefficient,  $k^2$  by

$$k^2 \cong \frac{2|\Delta v|}{v_R} \quad (3.2)$$

The impedance of the transducer as seen at the electrical port  $Z(f)$  is represented by a series resonance circuit model [111]. The impedance  $Z(f)$  is given by:

$$Z_f = R_a(f) + jX_a(f) + (j2\pi f C_T)^{-1} = [G_a(f) + jB_a(f) + j2\pi f C_T]^{-1} \quad (3.3)$$

where  $X_a(f)$  is the reactance and  $R_a(f)$  is the radiation resistance, while  $B_a(f)$  is the susceptance and  $G_a(f)$  is the conductance. From the crossed-field model,  $B_a(f)$  is given by

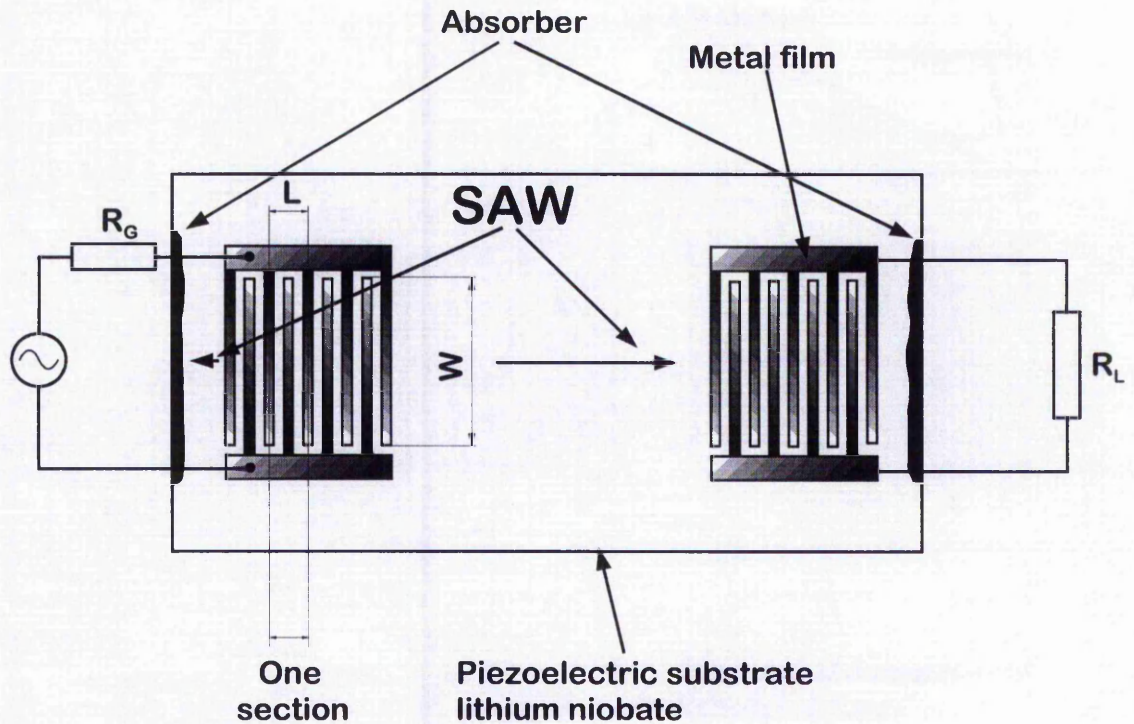


**Fig. 3.5** A surface acoustic wave delay line device showing the configuration of the interdigital transducers along the free surface. The excitation direction of the surface waves is indicated and on the opposite ends the absorbers can be seen.

$$B_a(f) = f_0 C_S k^2 \tan \frac{\theta}{4} \left[ 4N + \tan \frac{\theta}{4} \sin(N\theta) \right] \quad (3.4)$$

and the conductance  $G_a(f)$  is given by

$$G_a(f) = 2f_0 C_S k^2 \left( \tan \frac{\theta}{4} \sin \frac{N\theta}{2} \right)^2 \quad (3.5)$$

where  $\theta = 2\pi f / f_0$ . At synchronous frequency  $G_a(f)$  has a maximum ( $f = f_0$ ) given by

$$\hat{G}_a \equiv G_a(f_0) = 2\pi f_0 C_T \left( \frac{4k^2 N}{\pi} \right), \quad (3.6)$$

thus  $\hat{G}_a$  is proportional to  $N^2$  and to the acoustic aperture,  $W$ , considering equation (3.1). The static capacity,  $C_S$  is proportional to  $W$  and hence the total capacity,  $C_T$  is proportional to  $NW$ .  $\hat{G}_a$  is usually much smaller than  $2\pi f_0 C_T$ .

In the case where ohmic losses can be ignored, the acoustic power radiated away from the transducer is given by the power dissipation in the resistive part of the series resonance circuit model. For a transducer connected directly to a source, the conversion loss is in general reduced if  $k^2$  or  $N$  is increased, since this increases  $\hat{G}_a$  in relation to the total susceptance (equation (3.6)). The operating bandwidth is limited by the fact that both  $G_a(f)$  and  $R_a(f)$  have zeros at values of  $f$  given by

$$\frac{f - f_0}{f_0} = \pm \frac{1}{N}. \quad (3.7)$$

The conversion loss must necessarily be infinite at these points. For  $k^2 N \ll 1$  equations (3.3) - (3.5) give:

$$R_a(f_0) \approx \hat{R}_a \quad \text{where} \quad \hat{R}_a \equiv \frac{2k^2}{\pi^2 f_0 C_S} = \frac{\hat{G}_a}{(2\pi f_0 C_T)^2} \quad (3.8)$$

and  $\hat{R}_a$  is independent of  $N$  and proportional to  $1/W$ . At frequency  $f_0$  all the available electrical energy is converted to acoustic energy. The transducer radiates acoustic energy bi-directionally thus only half of the energy is radiated in the desired direction giving a minimum of loss of 3 dB. For an ideal designed delay line this would give a minimum conversion loss of 6 dB for each transducer.

If  $N$  is relatively large the bandwidth,  $\Delta f$  is governed by the frequency variation of  $R_a(f)$  and is approximately

$$\frac{\Delta f}{f_0} \approx \frac{1}{N}. \quad (3.9)$$

For small values of  $N$ ,  $\Delta f$  is governed by the electrical  $Q$ -factor (see ref. [112]) of the series resonance circuit, giving

$$\frac{\Delta f}{f_0} \approx \omega_0 C_T \hat{R}_a = 2\pi f_0 N C_S \hat{R}_a. \quad (3.10)$$

Considering the coupling coefficient,  $k^2$ , we obtain,

$$\frac{\Delta f}{f_0} \approx \frac{4}{\pi} k^2 N. \quad (3.11)$$

Balancing equation (3.9) with equation (3.11), the number of sections  $N$  for the transducer array can be expressed as,

$$N^2 \equiv \frac{1}{\omega_0 C_S \hat{R}_a} = \frac{\pi}{4} \frac{1}{k^2}. \quad (3.12)$$

The circuit theory herein described and originally discussed by Morgan [111] accounts for reflection and transmission coefficients for an incident wave. If the transducers are matched to the requirements of a  $50 \Omega$  circuit the power reflection coefficient is - 6 dB. However, an emitted surface wave in a delay-line device can cause a spurious signal called a triple transit echo, with a suppression level of 12 dB below the main output signal. The triple transit signal is travelling three times between the transducers along the acoustic path. A better suppression can only be achieved if insertion losses are increased.

### 3.3.2. SAW Device Description

The experiments used SAW devices designed to operate at frequencies of 170 MHz and 250 MHz. Preliminary experiments used SAW devices supplied by the University of Nottingham. These devices operated at 250 MHz. The mask design had been composed for GaAs and were finally fabricated on lithium niobate. These devices were mismatched as the mask design was for GaAs substrates but lithium niobate was used as a substrate. A second type of device working at a frequency of approximately 170 MHz was therefore fabricated from a mask, designed by Dr. G. McHale at Nottingham Trent University and produced at the EPSRC Central Microstructure Facility. The 170 MHz devices were designed so that maximum conversion of electromagnetic waves into mechanical Rayleigh waves and vice versa was established. The impedance of the transducers ( $50 \Omega$  matching network) was matched to the rest of the electronics. Consequently this minimises losses during conversion. The preliminary experiments also did not include either optical observation nor simultaneous measurements of the reflection and the single transit signal. A detailed description of the transducer parameters of the 250 MHz SAW device and the results from preliminary experiments have been described elsewhere [65]. The majority of experiments described in this thesis were performed using the 170 MHz devices. These devices used the simplest type of transducer layout which can generate SAW's; uniform periodic interdigital transducers

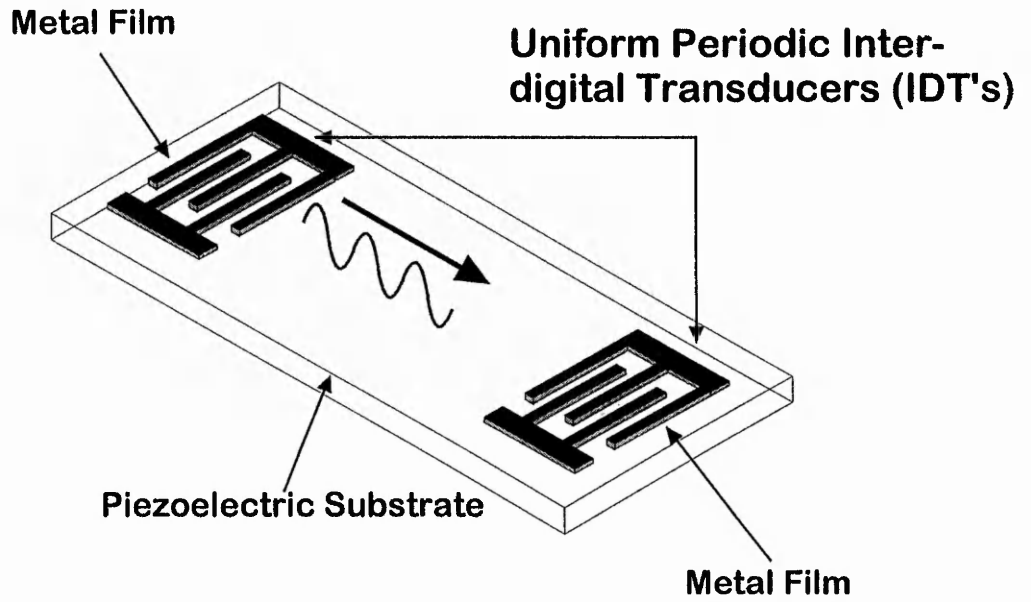


**Fig. 3.6** The SAW device used the simplest type of transducer layout; uniform periodic interdigital transducers (IDT's) with a single electrode structure.

(IDT's) with single electrodes as demonstrated in Fig. 3.6.

The transducers were simple parallel interdigital electrodes, with an equal mark-space ratio. The transducer array had 12 pairs of fingers with an equal mark-space ratio of  $5.5 \mu\text{m}$ . Since the mark-space ratio is identical, the wavelength,  $\lambda_R$  of the SAW device, which is defined by the geometrical dimensions of the fingers was  $22 \mu\text{m}$ . The total periodic length,  $L_N$  of the transducer was defined by the number of pairs of fingers times the wavelength,  $\lambda_R$  to  $264 \mu\text{m}$ . The transducer had a total width of  $390 \mu\text{m}$ . The aperture constant,  $M$  was chosen to be 13 full wavelength so that the aperture width,  $W$  would give a total length of  $286 \mu\text{m}$ . All geometrical dimensions were measured using a standard optical light microscope with a calibrated eyepiece ( $6.4 \mu\text{m}$  per optical division). The device had a resonant frequency of  $170 \text{ MHz}$  giving a surface wave speed,  $v_R$  calculated from the resonant frequency relationship,  $f_0 = v_R / \lambda_R$  of  $3740 \text{ ms}^{-1}$ . The choice of structure represents a compromise between a short acoustic wavelength and a high frequency (Table 3.2). A short acoustic wavelength is desirable, since  $\lambda_R$  provides a horizontal length scale. The wavelength sets the length scale for changes induced by a liquid spreading on the free surface within the acoustic path. A shorter wavelength produces in general a higher operation of frequency of a SAW device but puts greater constraints on both electronics and the accuracy of the photolithography. The choice of  $170 \text{ MHz}$  ( $\lambda_R = 22 \mu\text{m}$ ) is therefore a compromise between a short length scale and practical problems of device production and operation. For other devices fabricated from the same mask slightly different resonant frequencies ( $168 - 171 \text{ MHz}$ ) were observed. The acoustic bandwidth, as defined in equation (3.9)  $\Delta f / f_0 \approx 1 / N$ , gave an estimated value of  $14.2 \text{ MHz}$  bandwidth. The transducers were separated by approximately  $13.5 \text{ mm}$  on the lithium niobate surface, and with the estimated surface speed, the double transit time of the double transit pulse was calculated to be  $7.22 \mu\text{s}$  and the single transit time of the single transit pulse to be  $3.61 \mu\text{s}$ . The measured value for  $C_T$  was estimated to be  $2.54 \text{ pF}$  and this suggests a radiation impedance of  $31 \Omega$ . A complete summary of device dimensions and electrical transducer characteristics is given in Table 3.1. Table 3.2 provides a detailed list of

parameters for characterising lithium niobate substrate taken from the manufacturer's data sheet.

**Table 3.1** A summary of the design parameters and device parameters according to the mask design are presented.

<b>Design parameter</b>	<b>measured</b>	<b>Calculated</b>
<b>resonant frequency</b> $f_0$	168.8 MHz $\pm$ 0.5 MHz	170 MHz
<b>acoustic bandwidth</b> $\Delta f$	14.1 MHz	14.2 MHz
<b>radiation impedance</b> $\hat{R}_a$	31 $\Omega$	50 $\Omega$
<b>wavelength</b> $\lambda_R$	21.76 $\mu\text{m} \pm$ 0.5 $\mu\text{m}$	22 $\mu\text{m}$
<b>acoustic path distance</b> $l_p$	13.5 mm	13.5 mm
<b>aperture constant</b> $M$	13.14	13
<b>periodicity</b> $N$	12	12
<b>single transit time</b> $t_{st}$	3.45 $\mu\text{s} \pm$ 0.05 $\mu\text{s}$	3.61 $\mu\text{s}$
<b>double transit time</b> $t_{dt}$	6.95 $\mu\text{s} \pm$ 0.05 $\mu\text{s}$	7.22 $\mu\text{s}$
<b>surface wave velocity</b> $v_R$	3913 $\text{ms}^{-1}$	3740 $\text{ms}^{-1}$
<b>total capacity</b> $C_T$	2.54 pF $\pm$ 0.02 pF	1.56 pF
<b>total length</b> $L$	259.2 $\mu\text{m} \pm$ 3 $\mu\text{m}$	264 $\mu\text{m}$
<b>aperture width</b> $W$	284.8 $\mu\text{m} \pm$ 3 $\mu\text{m}$	286 $\mu\text{m}$

**Table 3.2\*** The manufacturer's data sheet for 128° Y-X lithium niobate (LiNbO<sub>3</sub>).

<i>substrate parameter</i>	<i>LiNbO<sub>3</sub></i>
<i>orientation</i>	128° Y-cut
<i>reference flat perpetuation to</i>	X
<i>thickness (mm)</i>	0.50 ± 0.05
<i>surface finish</i>	mirror polish
<i>main application</i>	SAW filter
<i>surface wave velocity <math>v_R</math> (ms<sup>-1</sup>)</i>	3980
<i>coupling coefficient <math>k^2</math> (%)</i>	5.6
<i>melting point</i>	1253
<i>crystal system</i>	trigonal
<i>dielectric constant <math>\epsilon_{11}^T</math></i>	84.6
<i>total length <math>\epsilon_{33}^T</math></i>	29.1
<i>surface permittivity <math>\epsilon_s</math> (pFm<sup>-1</sup>)</i>	437.82

\*[172]

### 3.4. Signal Generation and Set-up Configuration

Most experiments were performed using the system configuration as sketched in Fig. 3.1. However, a number of alternative configurations were used to test system performance. These arrangements included:

1. Pulse modulated sine waves excitation (RF-signal) with one double balanced mixer in the signal generation path.
2. Pulse modulated sine waves excitation (RF-signal) with no circulator (Hybrid Junction) in the signal generation/detection path.

3. Continuous sine waves excitation (RF-signal) directly fed to the transducer pads. No modulation of the sine wave occurred.

The configurations 1 to 3 where mainly substitutes of the set-up presented in Fig. 3.1 to investigate and evaluate signal response of the sensor in contact with the spreading liquid. This thesis will concentrate on the most complex set-up (Fig. 3.1) that allows both pulsed transit and reflection signals to be measured simultaneously. This section will focus on device operation of the Rayleigh wave SAW sensor without liquid loading.

In the experimental set-up presented in Fig. 3.1, a pulsed sine wave is launched at the source transducer rather than a continuous sine wave to enable the transducer to either generate or detect SAW's. The second transducer located at the opposite end of the substrate of the sensor (13.5 mm separated from the source transducer) is utilised as a detector and reflector. The set-up, uses the first pulse generator (PG 1) to produce a positive train of pulses. The period and pulse width controls set the pulse train parameters. The pulses are generated with a repetition rate of 1 kHz which represents a pulse period of 1 ms, respectively. The pulse width can be set variably from 150 ns to 400 ns. The signal generator (SG) produces a continuous sine wave (CW) radiofrequency (RF) signal of a given amplitude and frequency. In the set-up a 169 MHz continuous sine wave (CW) is then combined with the pulses supplied by the pulse generator PG 1, using double balanced mixers (DBM's) (see Fig. 3.2). The DBM's, act as switches. These switches are controlled by the sequence of pulses provided by the pulse generator. The combination of both signals produces on the output port of the second DBM (Fig. 3.1) a pulse modulated sine wave. The modulated radio-frequency pulses (RF-pulses) pass through the hybrid and create at the source transducer (IDT) a surface wave due to piezoelectric coupling. The wave propagates along the substrate surface and is detected and partly reflected by the second transducer. The transmitted part of the signal is amplified in the transmission path and immediately fed into the diode detector which is directly attached to one channel of the digital storage oscilloscope (DSO). The reflected part of the surface wave propagates back to the source transducer. Because of the pulsed character of the signal the source transducer can also work as a detector for surface waves. The

hybrid acts as a circulator (see Fig 3.3). The hybrid transfers the signal straight to the reflection path of the system where a pair of cascaded RF amplifiers with a gain of 28dB for each amplifier, amplifies the incoming signal by 56 dB. The transmission path uses a second set of cascade RF amplifiers with an additional amplification of 56 dB. The diode detectors rectify the signals and convert them from the given pulse into a peak. The transmitted pulse travelling once along the acoustic path of the sensor represents the single transit signal and occurs at the single transit time. The pulse, reflected back from the opposite end transducer is the double transit pulse occurring after travelling twice the path length of the acoustic path at the double transit time. The diode detectors are used because the bandwidth of the oscilloscope is limited to 100 MHz. The resolution of the electronic beam is limited by the time base minimum. The minimum range of the time base is 20 ns per division.

The system used two cascaded double balanced mixers in the signal path to ensure suppression of the continuously operating RF signal outside of the pulse duration. If only one DBM is used some leakage of continuous waves (CW) will occur, which will operate outside the pulse and this causes a non-zero baseline on the oscilloscope screen when directly fed into the diode detectors. Moreover, when a stripe of oil is spreading in the SAW path the presence of a continuous wave may give rise to an undesirable mixing of any reflected/transmitted signal and the unwanted continuous wave leakage. An example of this effect is demonstrated in Fig. 3.7. The second DBM completely removes this danger. The reflection path is gated out during the generation of SAW pulses by using a second pulse generator PG2 triggered by PG1. The DBM in the reflection path driven by PG2 simply switches the RF signal off [65].

### **3.5. Interfacing using GPIB BUS (IEEE-488) and Controller Program for PM 3365**

A program was created using C/C++ language to control the Digital Storage Oscilloscope (DSO) via the GPIB Bus. When a stripe of oil is

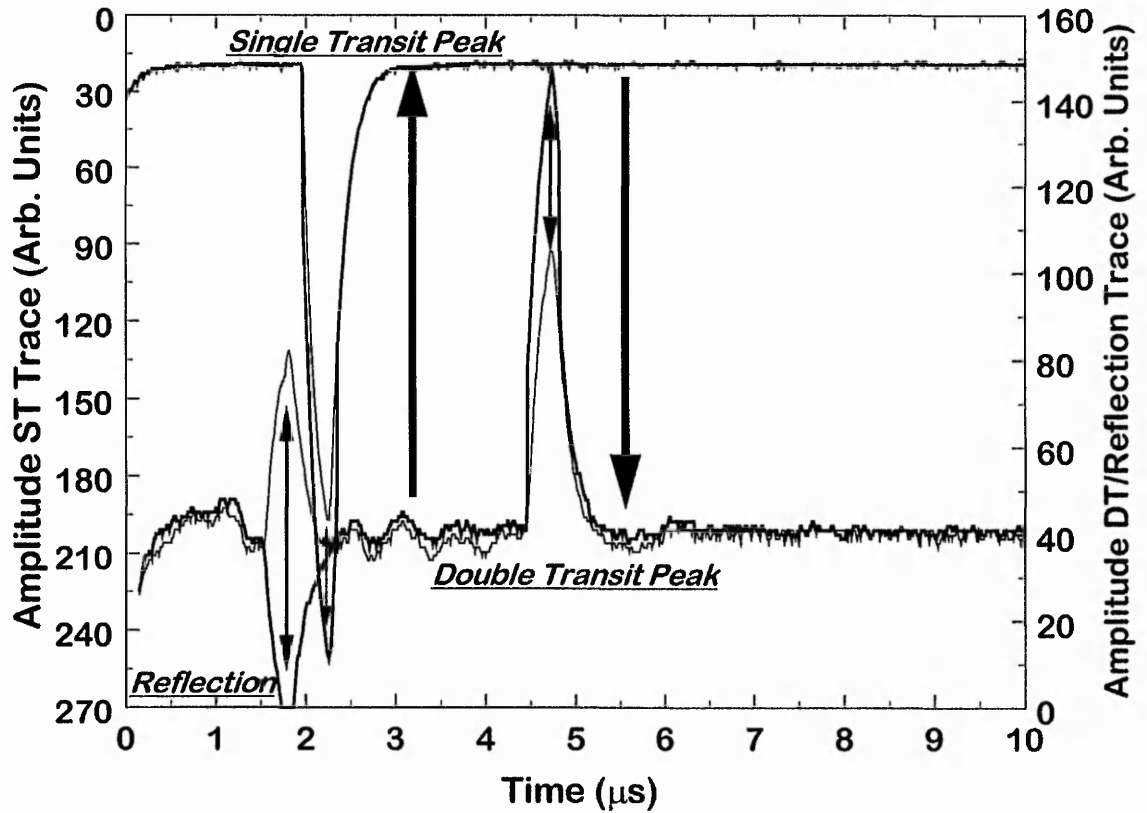


**Fig. 3.7** The single transit signal, double transit signal and the reflection change in peak height if phase detection occurs. The reflection changes the sign relative to the baseline due to the mixing with a continuous wave reference signal when the oil spreads. The large arrows indicate the overall attenuation behaviour of the single transit and the double transit. The small arrows show how all three peaks changes amplitude during the spreading process.

deposited on the surface of the sensor and spreads in the acoustic path three pulse modulated sine wave signals are observed rather than one which correspond to a single transit, a double transit and a reflection from the solid-liquid interface. These paths are indicated in Fig. 3.8. Set in the digital storage mode, the DSO can be programmed in such a manner that it either obtains the RMS value of these three signals using the RMS function, or the mean value when selecting the mean value function, or when the Voltage peak-to-peak mode is required to measure the peak-to-peak value. This is initiated by using a pair of cursors that are only active when the digital mode is activated. However, the oscilloscope is only equipped with one set of cursors, but measurements of at least two different peaks were required so that the pair of cursors had to be cycled between the peaks and the signal traces, when two input channels were used for the experiments. At the start of an experiment the positions of the cursors were located manually using the soft-keys and the program then stored their positions. During subsequent measurements these stored locations were automatically used to cycle the cursors through the peaks, as demonstrated in Fig. 3.9 and Fig. 3.10. Reading the values of three peaks, obtaining the time from the system clock and writing to a data file normally took around nine and a half seconds. In an experiment the choice of oil significantly altered the number of data points taken. The higher viscous oils (100,000 cSt and 30,000 cSt PDMS) were monitored during a full video tape length allowing a recording time of up to eight hours. In this period, approximately 4200 data points were recorded for each individual peak. The lower viscous oils (10,000 cSt and 1,000 cSt PDMS) tended to spread sufficiently far and fast enough with a vanishing contact angle of 1 to 2° within 2 to 4 hours corresponding to a maximum of 1500 - 2000 data points. In early experiments, the amplitude was recorded using the peak-to-peak function of the DSO. However, when the peak amplitude approached the baseline the position of the small cursors significantly affected the sign of the amplitude magnitude reading due to noise produced by the amplifier feedback. The peak-to-peak function was subsequently replaced by the mean value function on the DSO. This algorithm is not dependent on the position of the accompanied small cursors and simply determines the area below the peak (see Fig. 3.10) defined by the two main

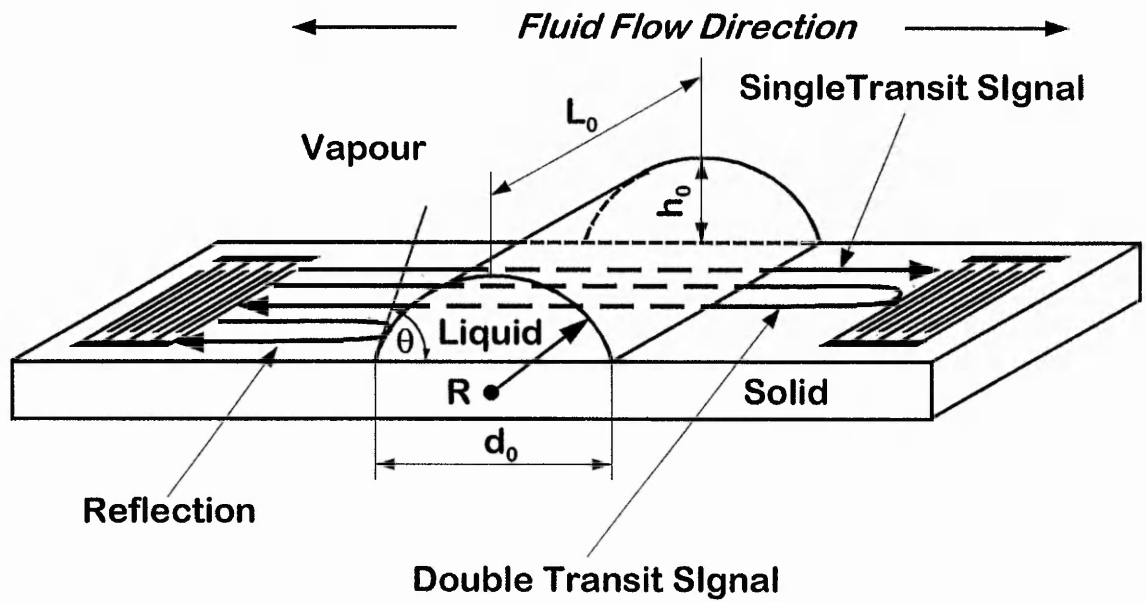


**Fig. 3.8** Three acoustic signals are measured for each surface wave pulse. The single transit signal travels once in the acoustic path of the sensor. The double transit signal is reflected from the opposite transducer and travels twice along the acoustic path passing the fluid loaded interface. The reflection is due to the dynamically advancing edge of the liquid stripe.

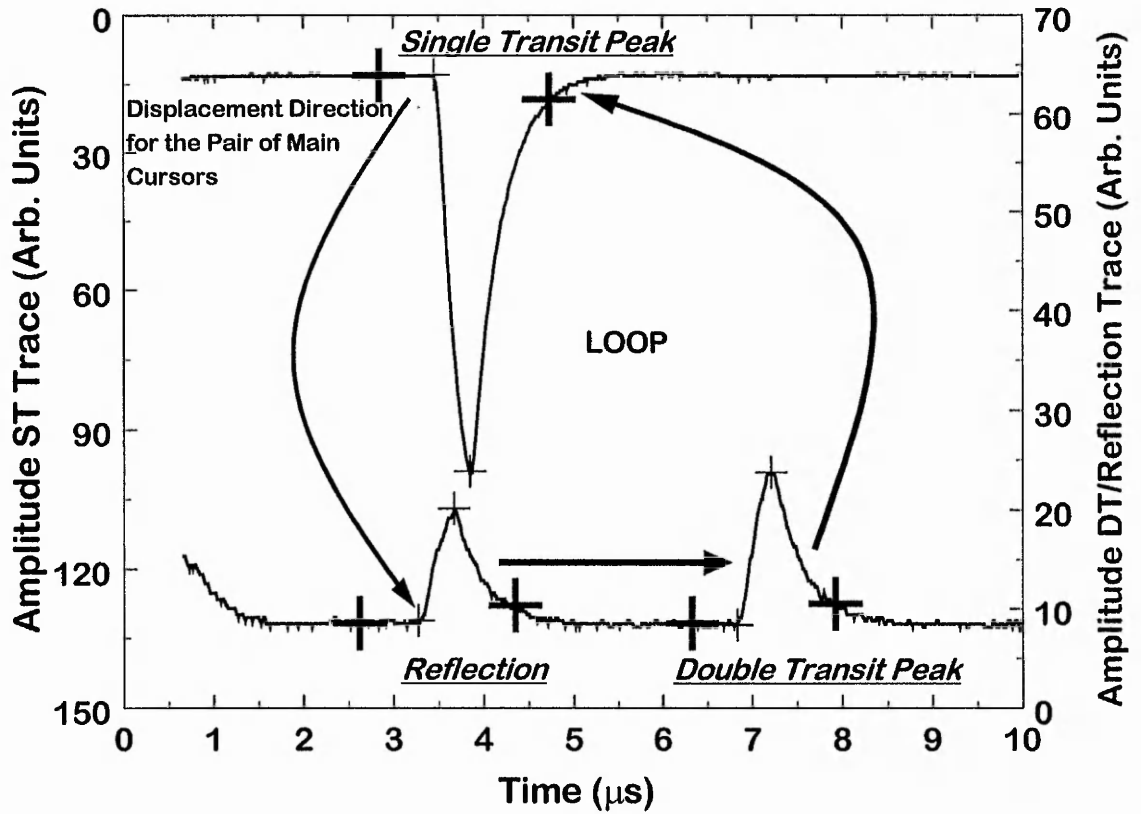


**Fig. 3.9** The loop direction and displacement of the cursors when measuring peak-to-peak values is presented. Each displacement of the large main cursors is followed by the small accompanied cursors. Noise superimposed on the trace produces a change in sign of the peak-to-peak amplitude when the signal reaches the baseline.

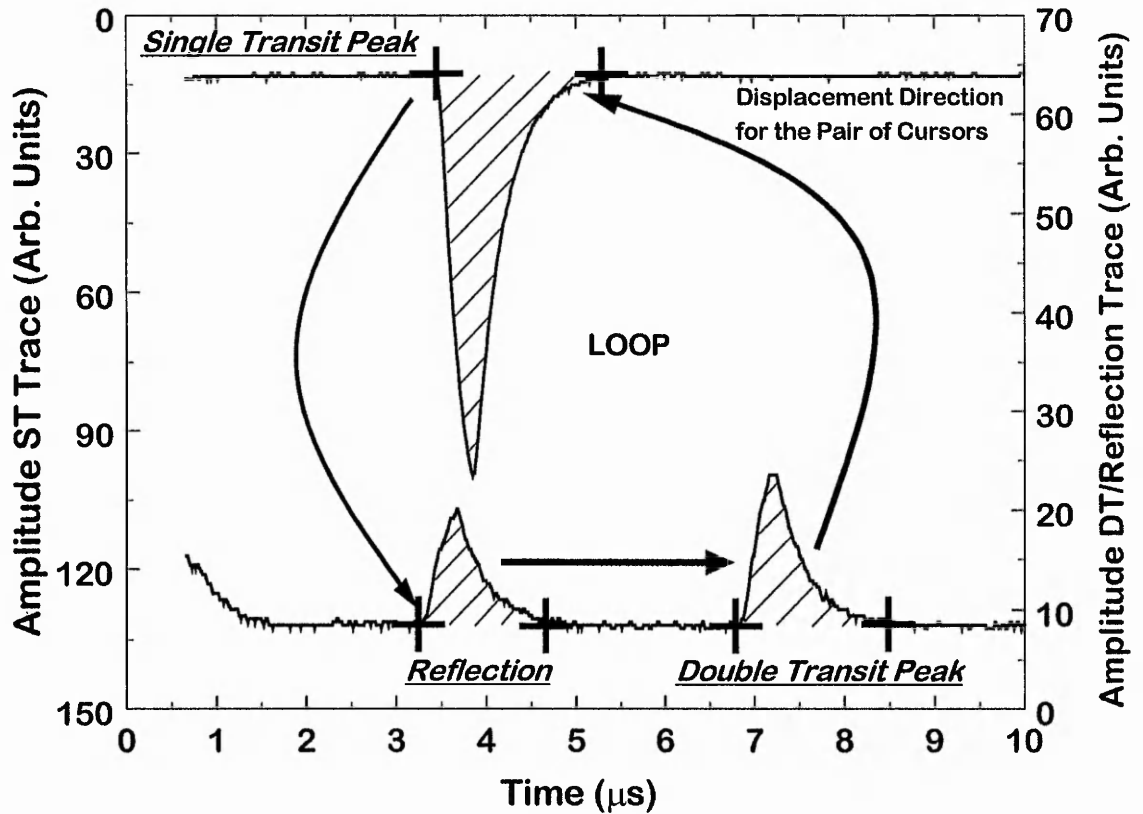


**Fig. 3.10** An improved algorithm using the mean function rather than the peak-to-peak measurement was introduced. The mean algorithm calculates the area under the curve and is less influenced by noise on the trace.

ursors. The algorithm uses the equation,

$$\overline{y(t)} = \frac{2}{T} \int_0^T y(t) dt$$

where  $\overline{y(t)}$  represents the mean.

The program also allowed the use of the "Running Average Mode" function. This function is carried out by the DSO and averages several consecutive traces. Hence with a 1 kHz repetition rate of the pulsed signal, averaging over about 1 to 2 ms occurs. Together with the time obtained from the system clock, the values of the various peaks at the different cursor position were recorded and arranged in a data table. Each new complete reading of data were appended to the last set in the table. The program was designed in a way, that an abrupt ending of the program cycle would not lead to the complete loss of the data sets. Additional information such as the time base settings, the input sensitivity of each channel, the date when the experiment was performed and the position of the baseline of each trace before and after the experiment were recorded. In Fig. 3.11 a flow chart of the controller program shows the set-up of the bus communication, preparation of the various parameters and how the initialisation of the settings take place and how the data are transferred to the controller.

### 3.6. Optical System Development - Interferometry

The set-up of the entire system is sub-divided into two systems; the SAW-circuit enabling the acoustic monitoring of the spreading liquid and the optical system set-up which provides a plan view observation of the geometrical changes of the liquid. Interferometry is used to obtain parameters such as the height,  $h_0$ , the cylindrical cap radius,  $R$ , contact width,  $d_0$ , and the dynamic contact angle,  $\theta$ , of the fluid. The dynamic evolution of the stripe is followed by

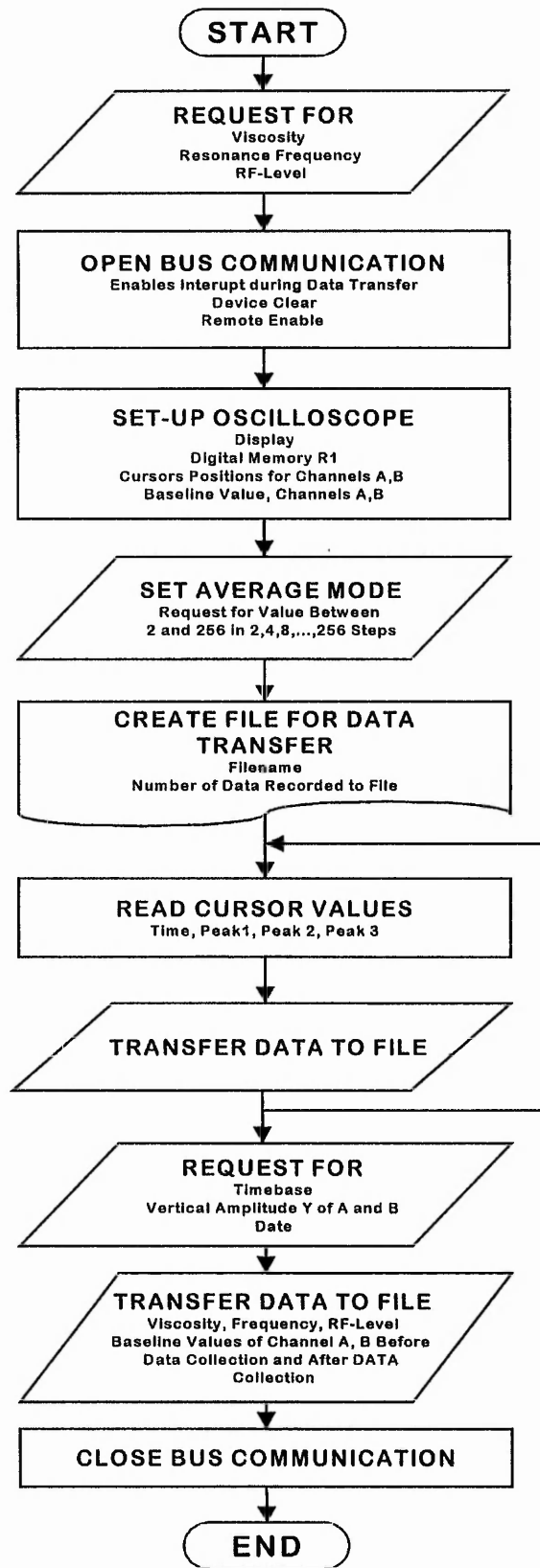


Fig. 3.11 The flow chart of the DSO controller program.

the interferometry set-up (camera on x-y-z stage and attached half mirror) at the location where the acoustic beam of the surface wave impinges on the advancing edge of the stripe. This allows a direct correlation of SAW-liquid interactions with the geometric changes of the fluid profile.

### 3.6.1. Configuration and Set-up of the Optics

To achieve a good precision in the optical measurements and to be able to have a good alignment of the optical components, the optics was installed on an optical bench located in a clean room. To monitor the wetting a CCD-camera was mounted on a three axis X-Y-Z stage, as shown in Fig. 3.12, allowing an adjustment of all three direction with a total adjustable distance of 15 mm for each axis. The X or Y micrometer adjustments moved the camera either in X or Y direction as desired. The Z direction allowed an easy adjustment of the focus of the camera and could also be used to lift the camera out of the experimental area. The stage was placed on a metal rod allowing a rotation of 360° along the Z-axis and to pan out the camera in either direction to allow a free and unrestricted access to the sample surface. A second X-Y-Z stage acted as a sample holder for the SAW-device (see also Fig. 3.12).

The CCD-camera was fitted with an objective tube, equipped with an adjustable positioner for focusing. The objective was a standard microscope objective with a magnification M10/0.22/240. To obtain not only the contact width,  $d_0$  of the liquid, but also the variation in height of the fluid surface and hence its curvature, interferometry was used. Sodium light ( $\lambda = 589 \text{ nm}$ ), was shone onto a microscope slide placed at a 45° angle above the SAW-sample. The microscope slide acted as a half mirror allowing light to be directed down to the fluid loaded sample and the reflected light from the sample surface to pass the mirror and to be transferred to the objective. The interaction between light reflected from the top surface of the liquid and the reflection from the substrate surface of the SAW-sample caused interference. This was seen as dark and bright fringes on the camera image. These fringes allowed the determination of

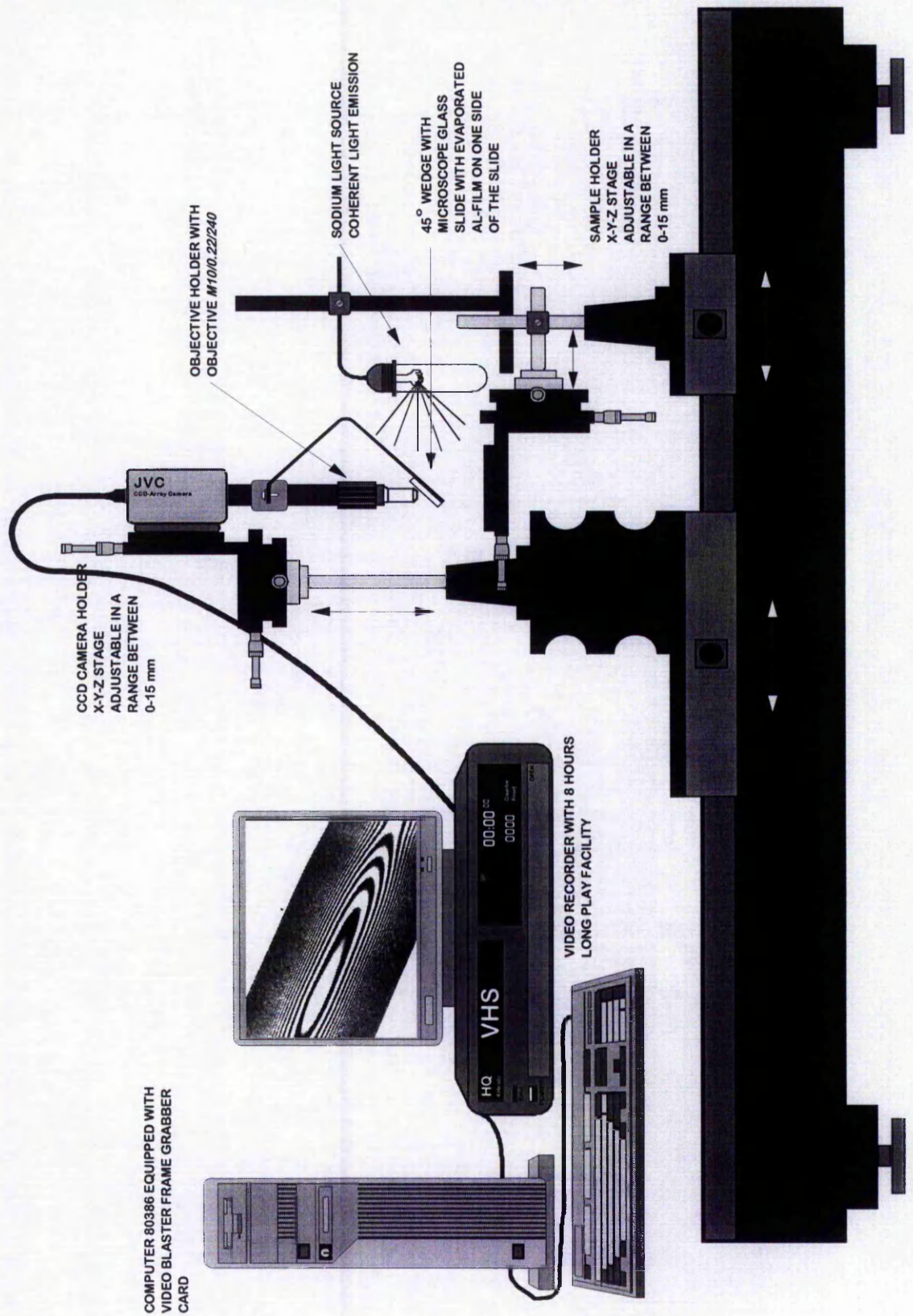


**Fig. 3.12** The optical set up of the system. The optical bench houses the two X-Y-Z stages with the CCD-camera and the sample holder.

the contact angle formed by the fluid edge and the substrate surface as well as a complete determination of the profile of the liquid. To enhance the contrast the microscope slide was evaporatively coated with a fine translucent film of aluminium.

During the initial stages of an experiment the interference fringes could only be resolved across the central part of the stripe, since a strong curvature of the fluid cap made it impossible for the optics to resolve the fringes close to the fluid edges. However this was sufficient to calculate the cylindrical cap radius,  $R$ . At any time during an experiment it was possible to directly measure the contact width,  $d_0$ . The assumption of a cylindrical cap shape then allowed the height,  $h_0$ , and contact angle,  $\theta$ , to be estimated. In all cases the fit of a set of interference fringes to the cylindrical shape was excellent. The full profile using a full set of interference fringes was taken in the later stages of the spreading process when the curvature of the stripe was flat enough and the formation of interference fringes were well separated to provide confirmation of the cylindrical cap. An image of the transducer orientation was taken prior to each start of an experiment to compare parallelism in orientation of the deposited stripe with the orientation of the transducer.

The camera was connected via a scart cable to a video recorder which took images constantly during a period of at least four hours. After recording the experiment, a standard video frame-grabber card was used to capture single frames at any desired position on the time scale. In general a sequence of 30 to 50 images was capture after the experiment was conducted. The capture sequence was chosen to focus on key events in the reflection and transmission signals, such as maxima or minima in the amplitude response of the SAW's.

### 3.6.2. Interferometry

Interference of light is an extremely powerful tool for e.g. metrology and spectroscopy. A wide variety of measurements can be performed, ranging from determining the shape of a surface to an accuracy of less than a millionth of an

inch (25 nanometers) to determine the separation, by millions of miles, of binary stars. In spectroscopy, interferometry can be used to determine the hyperfine structures of spectrum lines [173]. Two light rays from a coherent light source arriving at a point in phase agreement will reinforce each other, i.e. constructive interference. The final product is the summation of the amplitude of the interfering rays. If the light rays arrive completely out of phase, so that their amplitudes are shifted against each other then the summation results in a destructive interference. They cancel each other out so that the resulting amplitude is zero, depending on the phase shift between the two light rays.

In thin films a reflection from a denser medium back into a rarer medium generates an abrupt half-wavelength shift when the ray hits the surface of the film. It occurs at those interfaces where the light approaches from the lower refractive index. If we consider a macroscopic film such as the spherical shape of a droplet or the geometry of a stripe of fluid, the ray which approaches the liquid transmits directly through the medium and a reflection occurs at the surface of the substrate on which the liquid spreads. The distance travelled by the ray in the liquid interface is twice the thickness of the medium at the particular point where the ray strikes the meniscus of the fluid at the liquid-vapour interface. On reflection from the denser medium having a low refractive index, the ray will undergo a half-wavelength shift upon reflection at the substrate surface and at the free oil surface. Maximum reinforcement or constructive interference occurs when:

$$2\Delta y_{const} = \frac{m\lambda_{vac}}{n_{medium}}, \quad (m = 1, 2, \dots) \quad (3.13)$$

where  $\lambda_{vac}$  represents the wavelength in vacuum and  $\Delta y_{const}$  is the thickness of the medium at that point where the light ray hits the surface. The factor two indicates twice the path length (distance) the light ray has to travel in the denser medium.  $n_{medium}$  represents the refractive index of the denser medium here the fluid. Destructive interference appears when,

$$\Delta y_{dest} = \frac{(2m + 1)\lambda_{vac}}{4n_{medium}} \quad (m = 0, 1, 2, \dots). \quad (3.14)$$

The phase difference between bright fringes and dark fringes is given by  $\Delta y = \lambda_{vac} / 4n_{medium}$  of the wavelength.

With equation (3.13) and (3.14) it is possible to obtain the contact angle,  $\theta$  with the surface. With the use of image analysis it is possible to determine the distance between adjacent bright and dark fringes and correlate this to the contact angle,  $\theta$ .

### 3.6.3. Image Processing and Analysis

In order to analyse the dynamics of the wetting process, image processing was used to achieve a high precision in the analysis procedure and to reduce the time needed to analyse an experiment. Digitising the images allows image manipulation and image analysis to enhance noisy images, although this was not necessary for processing the images obtained by the optics. The main advantage lies in setting accurate line profiles of image intensity and so obtaining the position of fringes across the cylindrical cap cross-section of the oil. The automation of this process is essential to enable analysis of the optical information in a reasonably short period of time.

The video capture card used in the optical system had a resolution of 640 x 480 pixels at the highest resolution modulus. With the aid of a microscope scale, which is generally used to measure objects of microscopic dimension, one pixel was determined to be approximately 1  $\mu\text{m}$ .

The optical system had a non-square aspect ratio and a calibration factor was therefore needed. To achieve such a calibration factor, reference images were used. For this system a factor of 0.9129 was determined to correct the horizontal aspect ratio and one pixel horizontally corresponded to 1.083  $\mu\text{m}$ . This allowed a transformation of a pixel image into dimensions expressed in SI units. Image Tool, (public domain software from the Department of Dental

Diagnostic Science at The University of Texas Health Science Centre, San Antonio, Texas), was used to provide pixel-intensity line profiles from captured images. Programs were written in "C" to then convert these pixel-intensity line profiles to a distance and intensity format, identifying stripe width and maxima and minima intensities (distance, max/min intensity) and hence construct physical profiles of distance and height expressed in SI units. A separate "C" program was used to fit a circle through the points and extract various geometric parameters.

The only processing on images was to improve image contrast in order to enhance the separation between adjacent dark and bright fringes. A simple 3x3 median average mask was then applied to the image and the profiles (x, y, grey-level) obtained. Fig. 3.13 shows a typical image of a spreading stripe of a 100,000 cSt viscous oil from which a line profile could be obtained. The formation of the fringes along the periphery of the stripe can be seen. The contrast between dark and bright fringes is good and allows the construction of a complete line profile. The alignment of the two transducers located on each opposite end was used to ensure that the image captured was at that particular fraction of the liquid where the SAW hits the front edge of the stripe. The image shows the parallelism of the sides even in the late stages of the experiment. The SAW aperture is one half of the image width. The slower variation of the cross-sectional height along the stripe can be seen by the wider spacing of the fringes. The inset in Fig. 3.13 shows the extracted profile along a line corresponding to the centre of the SAW transducer aperture. The circles are the data points for 22 maxima and minima light intensities along the width of the stripe through the crest; the solid curve is the spherical fit to the data.

At the start of an experiment when a stripe was deposited, the stripe showed good continuous parallel sides. During the spreading, the areas with more mass accumulation spread wider. It was ensured that the optical observation were taken directly in the acoustic path of the transducers. To extract images for the analysis, significant position in the SAW spectra such as maxima and minima of the reflection were identified and images captured matching the same time axis. Therefore a time track record indicating when each of the two processes (video taping of the spreading and SAW response

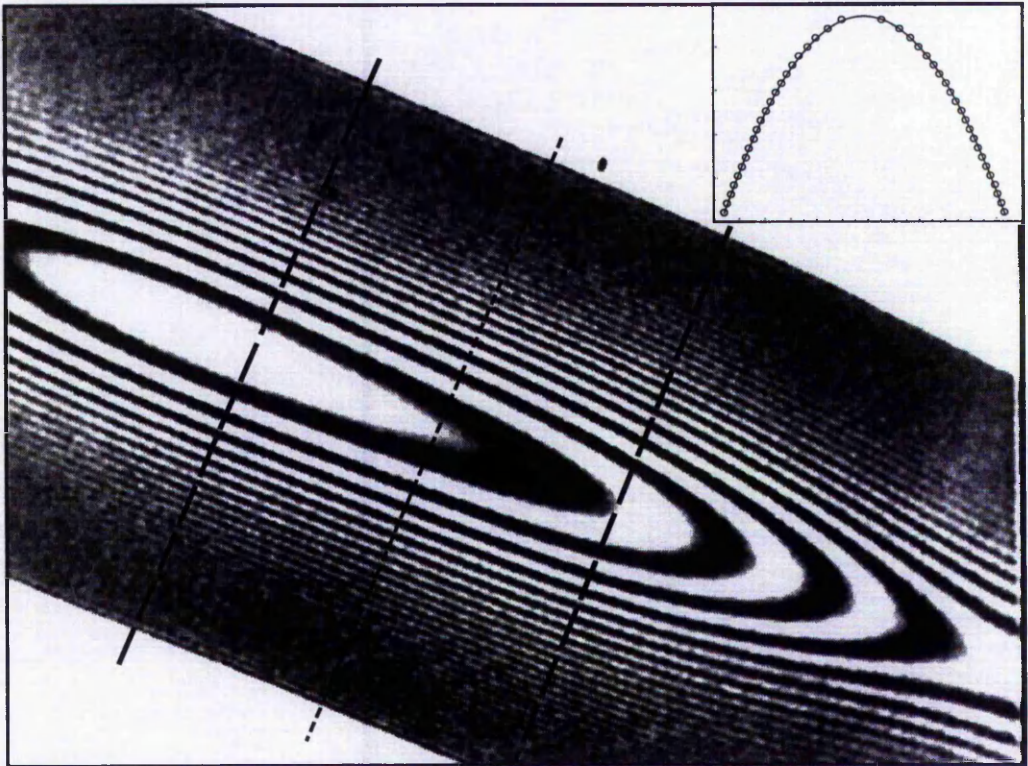


**Fig. 3.13** Across the periphery the stripe shows clearly defined bright and dark fringes. This made it possible to use image analysis to determine the contact width,  $d_0$ , and the line profile to determine contact angle,  $\theta$ , and cylindrical cap radius,  $R$ . The relative location of the aperture of the SAW transducer is indicated by the dashed lines. The inset shows the measured profile using 22 central fringes and this is well described by a circular fit (solid line).

measurements) has been triggered and an alignment of both process times was carried out. The extraction of a line profile was done by setting a measurement line perpendicular to the parallel sides of the stripe as indicated in Fig. 3.13 by the dashed line located in the middle of the transducer aperture and obtaining the grey levels varying with the changes from bright to dark fringes and vice versa. Fig. 3.14 shows a line profile which is typical for the late stages of spreading. Consecutive fringes are shown by the successive maxima and minima.

“C” programs were written to extract the peaks labelled by their position and so to create a full profile of the cross sectional shape of the stripe and fit the best possible circle through the fringes. The width of the stripe is identified directly from the images by finding the edge separating the stripe from the background light intensity. The contact width can be clearly identified even when the fringes towards the edges cannot be separately distinguished. Since the distance between two adjacent fringes is  $\lambda/4n$  ( $\lambda = 589$  nm for sodium light) of an optical wavelength, and the oil’s refractive index,  $n = 1.4035$ , a vertical resolution of 105 nm can be obtained. The height of the meniscus at the specific location of each fringe can be estimated by equation (3.13) and (3.14). The fit routine, fitting a circle through the extracted peaks, gave precise information of the contact width,  $d_0$ , contact angle,  $\theta$ , cylindrical cap radius,  $R$ , and edge position of the stripe. Fig 3.15 presents the location of each consecutive fringe in height,  $h_f$ , distance from the centre of the stripe and a best fit (solid line) indicating how well the data approaches a circular profile.

In the earliest stages a full fringe profile could not be obtained. However, the central fringes could be identified and  $R$  determined. Together with the information obtained from the contact width, the contact angle was calculated. The contact angle,  $\theta$ , using a few central fringes from the profile gave a result consistent to within  $\pm 0.04^\circ$ . A sequence of 30 images were analysed to extract the dynamic changes of the contact angle,  $\theta$ , and contact width,  $d_0$ , with respect to time. Fig. 3.16 and 3.17 show the extracted results of the analysis. The contact width,  $d_0$  is presented in Fig. 3.16 and is in good agreement with a Tanner type power law (see Chapter 2, equation (2.26) and (2.27)). With equation (2.2) and the cylindrical cap radius,  $R$ , obtained from fitting the circle

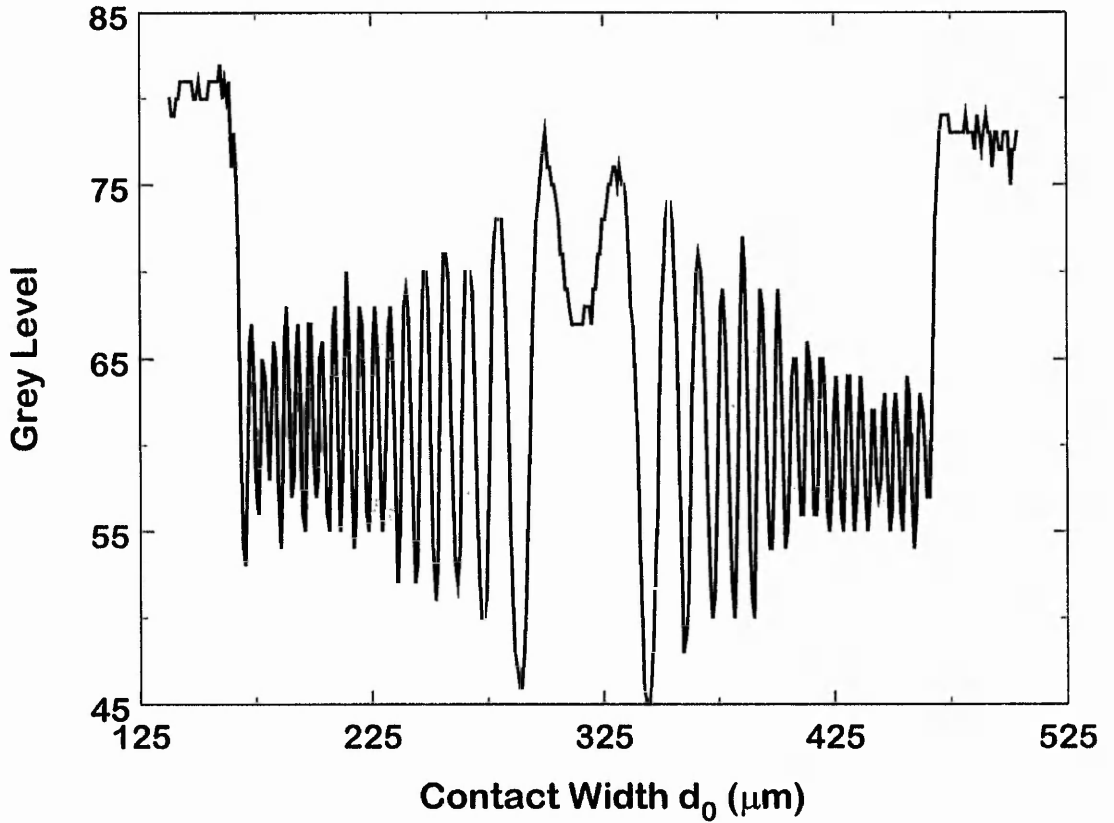


**Fig. 3.14** A full intensity line profile of one image. The peaks indicate the position of the dark and bright fringes across the stripe. The minima indicate dark fringes whereas the maxima, bright fringes.

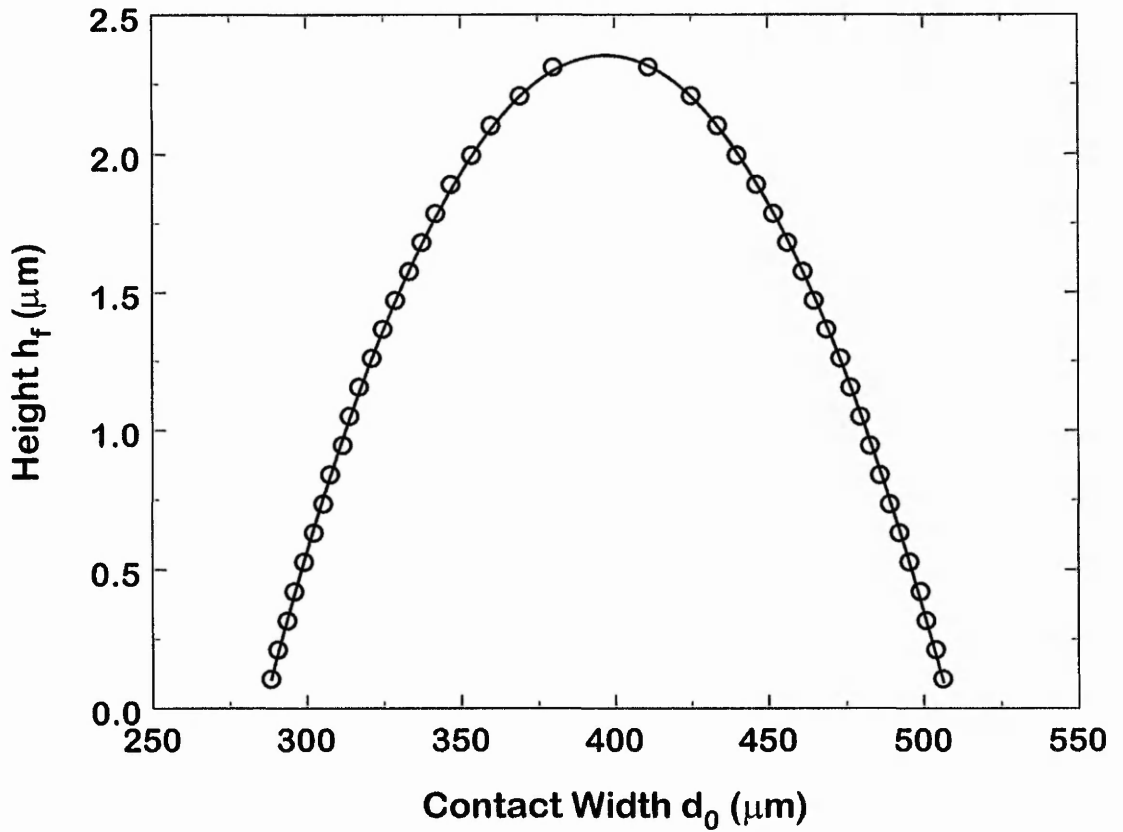


**Fig. 3.15** A full line profile of dark and bright fringes. The (oooo) indicate the extracted peaks and the solid line is the fitted circle through the peaks. The radius of the circle is estimated at  $R = 3108 \mu\text{m}$ .

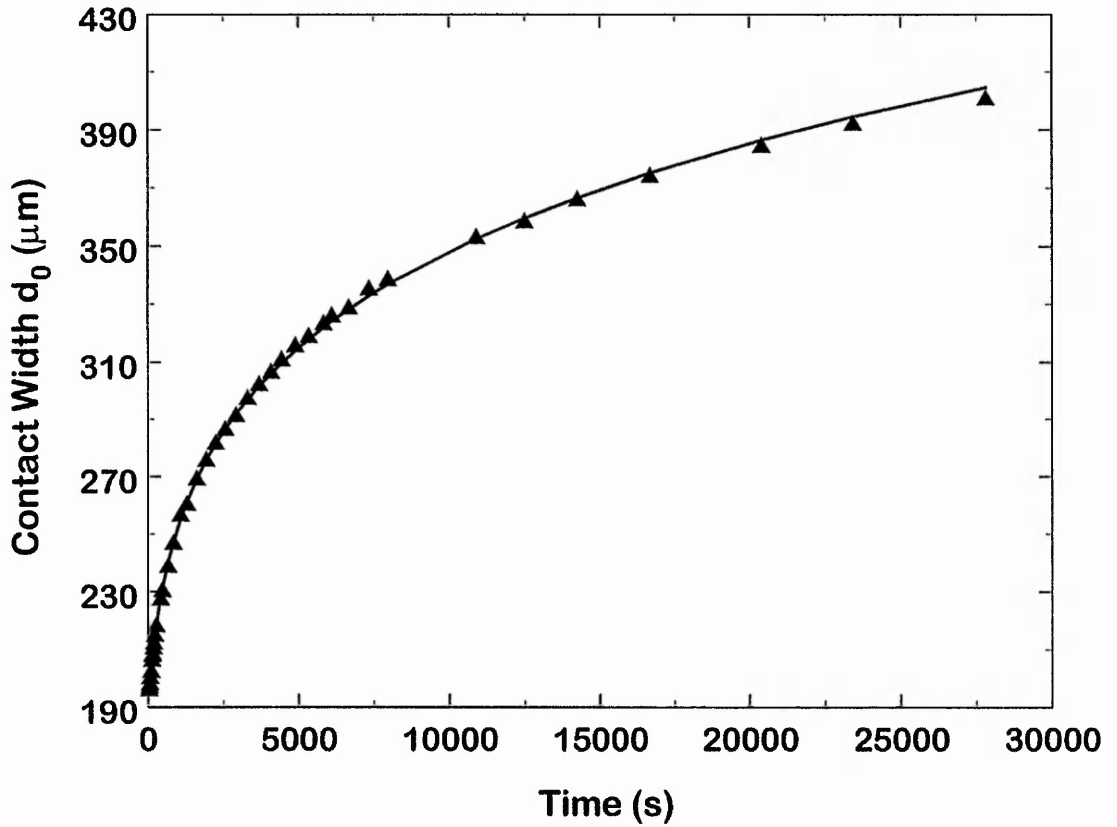


**Fig. 3.16** The extracted contact width,  $d_0$ , (triangular symbols) of 30 images is well described by the  $1/7^{\text{th}}$  power law relation (solid line).

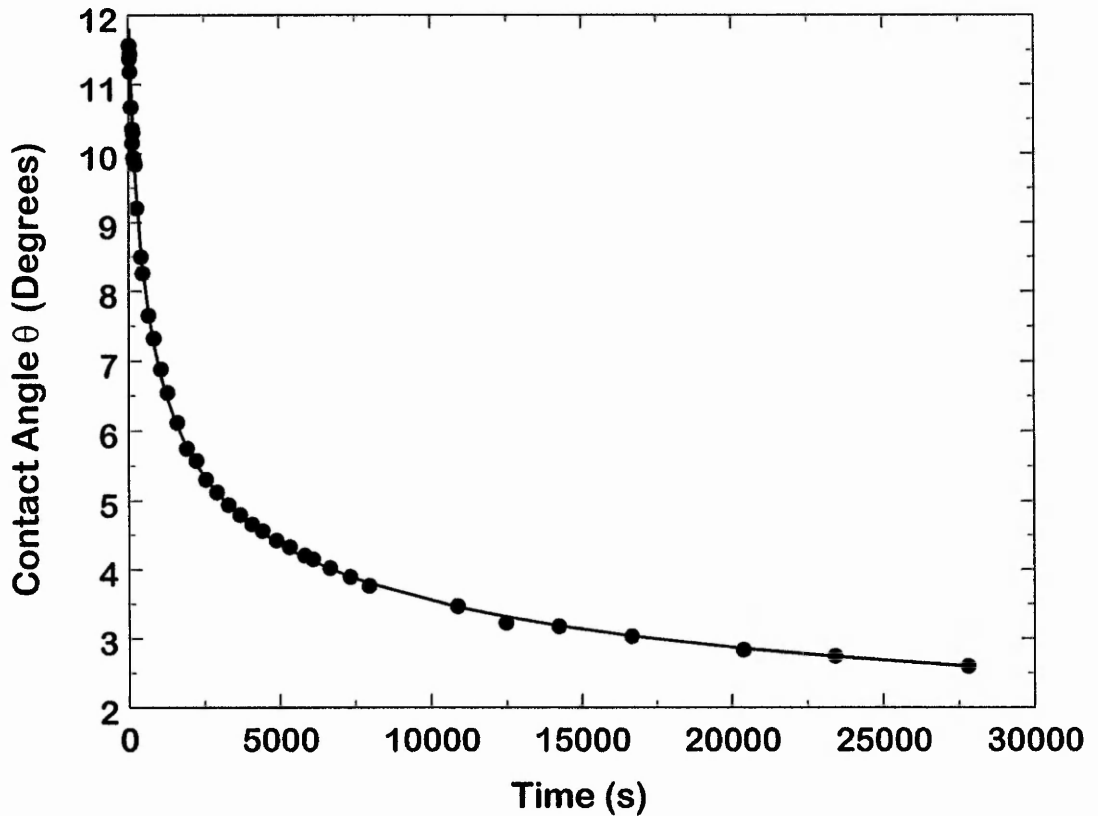


**Fig. 3.17** The contact angle decreases with time. The contact angle follows a power law (solid line) which is well fitted to the experimental data (●●●) and is proportional to  $(t+c)^n$ .

through the maxima and minima of the intensity profile, the trend of the contact angle,  $\theta$  has been evaluated. Fig. 3.17 shows the exact course of the angle with time.

### **3.7. Calibration Procedure to Estimate Acoustic Losses**

To convert the additional acoustic attenuation caused by the liquid when loaded onto the surface into decibel units a calibration method was developed. The oscilloscope measures the mean value representing the area below the peak and is a measure of the power of the SAW pulse. The calibration was carried out by cascading attenuators and placing them into the signal paths. The reduction in signal amplitude due to liquid loading could then be compared to an equivalent attenuation in dB. For the calibration a set of four different attenuators with fixed attenuation values were available; 3 dB, 6 dB, 10 dB and 20 dB of attenuation. This produced a maximum attenuation of 39 dB when cascaded together. Using all possible combinations to cascade the four attenuators gave a total of 16 calibration points. Most of the experiments carried out used power levels, where the four available attenuators, attenuated the entire acoustic signal.

Calibration were performed at the start of each spreading experiment. The calibration of the single transit signal (single transit pulse) required the attenuators to be placed directly after the SAW device as seen in Fig 3.18. The calibration for the double transit pulse required the attenuators to be placed in the reflection path, as demonstrated in Fig 3.19, after the DBM, which is responsible to gate out the cascaded amplifiers in the reflection path during the launch of the source pulse. A position in between the hybrid junction and the SAW device would have meant that the SAW amplitude would have been attenuated twice during the cause of calibration because the signal has to pass the attenuator twice before it is amplified.

The calibration table of attenuation versus mean value was processed with a statistical program and a best fit conversion function extracted from the

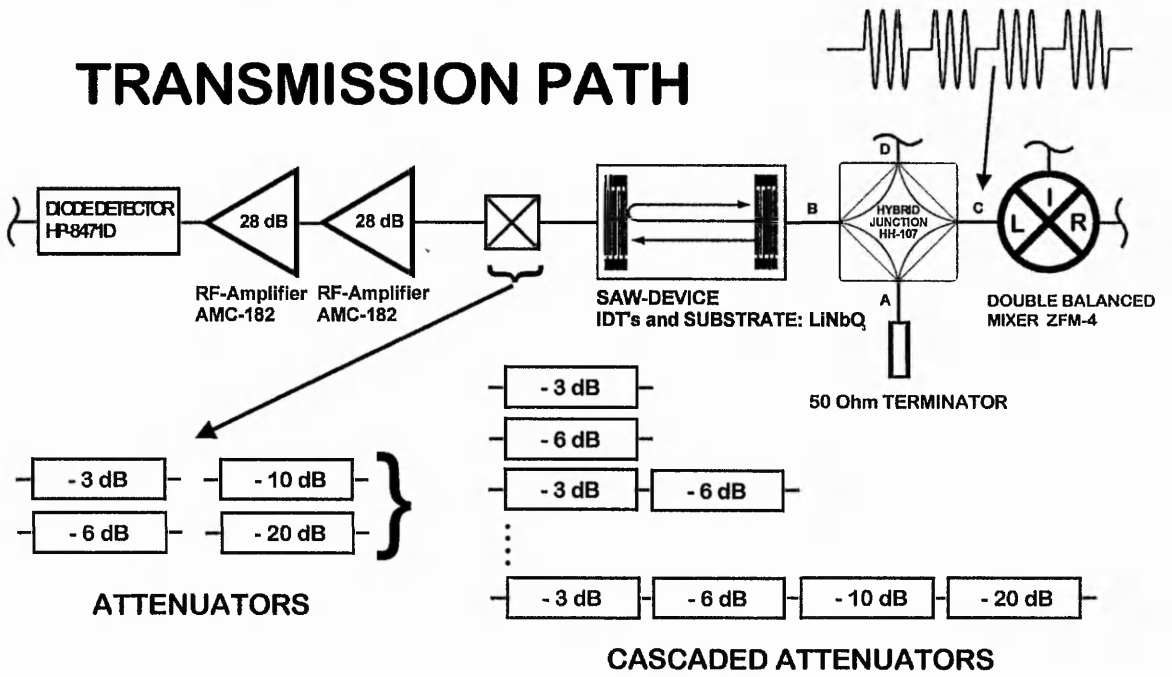


**Fig. 3.18** The calibration process for the single transit signal records the signal levels due to known attenuation.

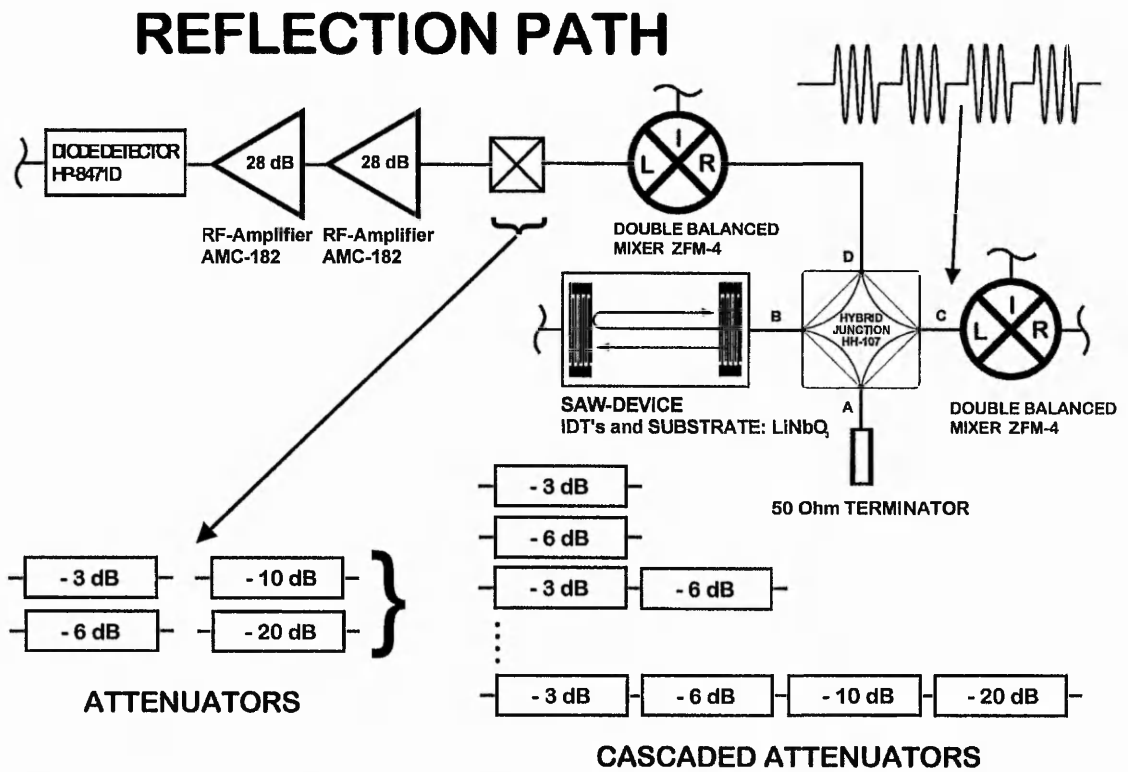


**Fig. 3.19** The calibration process for the double transit signal in the reflection path is similar to that for the single transit signal.

data. In order to get a close approximation of the calibration plot a logarithmic power series was used. With regression analysis it was possible to estimate the coefficient for each logarithmic power series and the constant. The form of the equation is:

$$\text{Atten.}(dB) = C + \sum_{k=1}^n A_n \log_{10}^n(\bar{x})$$

where  $A_n$  represents the coefficient for the power series,  $\log_{10}^n$  is the  $n^{\text{th}}$  logarithmic of the entire series and  $\bar{x}$  is the expressed mean value obtained from the measurement, and  $C$  is a constant. In general a regression fit for a power series of  $\log_{10}^6$  was good enough to get a very close approximation for the attenuation function. This allowed the mean values for the three signals to be converted from a given measurement related to volts into an acoustic attenuation calibrated in dB. Fig 3.20 illustrates the graph for the calibration. The logarithmic power series can be extrapolated from the calibration points to be used as conversion from mean value  $\bar{x}$  into acoustic attenuation.

### 3.8. The influence of the Diode Detector Threshold for the Transmission Signal Losses

The deposition of oil on the sensor surface provides an initial attenuation of the single transit signal of between 2 and 5 dB, depending on the amount of oil deposited (an example is given in Fig. 3.21). Then as the oil spreads across the surface the attenuation increases, with very large attenuation resonances occurring in Fig. 3.21 at around 180  $\mu\text{m}$  and 320  $\mu\text{m}$ , respectively. As the width increases towards such a resonance the rate of attenuation with width increases steadily. However, immediately following the attenuation resonances, the loss reduces rapidly and a local maxima in the transit signals is observed. The attenuation maximum therefore has a characteristic asymmetric shape. The changes in the double transit signal are expected to be identical in trend

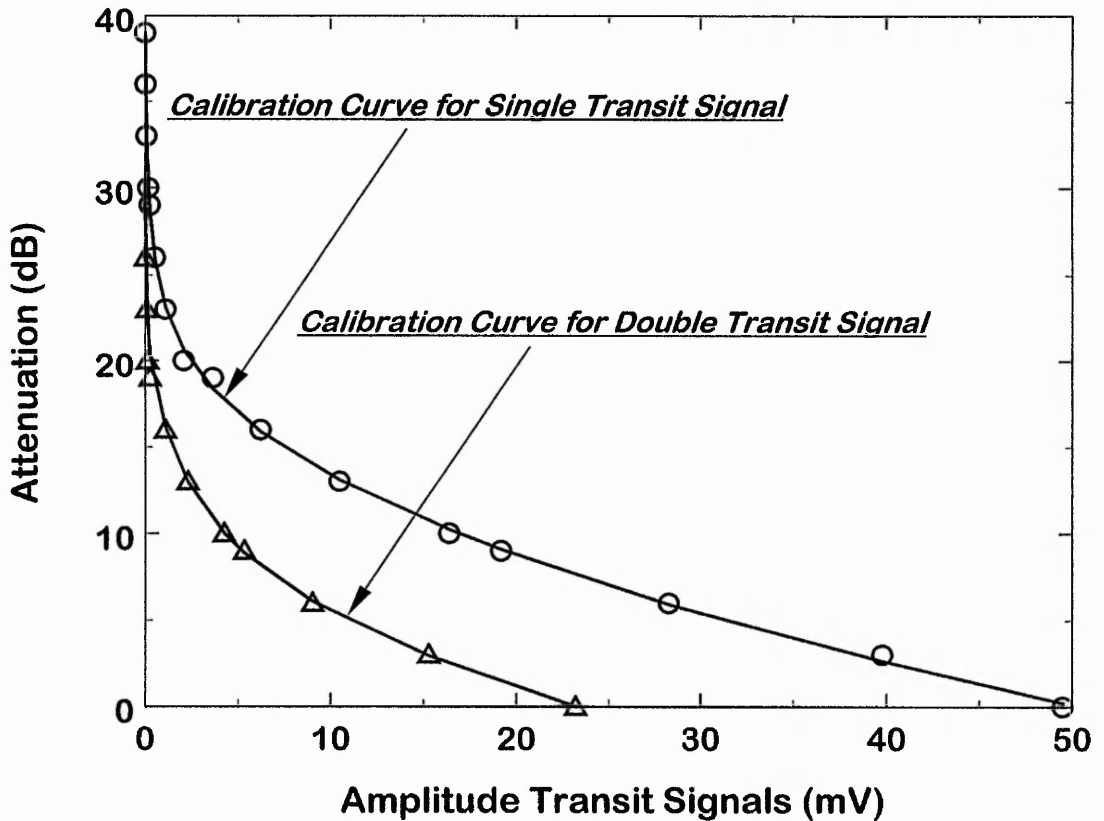


**Fig. 3.20** The calibration converts the measured mean value into acoustic attenuation caused by the spreading liquid. The graph shows the 16 calibration points for the single transit indicated by the (oooo) symbols when cascading the four available attenuators in all possible combinations and the 11 calibration points for the double transit indicated by the triangular symbols. The solid lines are the logarithmic power series fit to approximate the course of the calibration points.

and structure with the changes in the single transit signal. Fig. 3.22 represents a plot of loss of the double transit signal against the loss of the single transit signal and this should give a straight line of slope 0.5. This can be used to verify the consistency of the calibration procedure and shows how well double transit and single transit mirror each other in trend. The calibration is reasonably accurate for losses in the double transit signal of less than 9 dB, but shows increasing deviation and scatter as the losses increase towards 25 dB. In most experiments, the ratio of losses in both transmission signals follows the slope of 1/2 approximately up to 12 dB of attenuation with steady increase of deviation towards 25 dB. The course of the single and double transit is dominated by the exponential decay of the transit signal amplitudes and represents the overall trend of increasing losses. For completeness, Fig. 3.21 shows the changes in the reflection from the stripe that accompanies the changes in the transit signals.

When the fluid wets the surface the transit signals attenuate with a specific rate in dependence of the distance the stripe has moved forward across the surface. This rate of attenuation can be expressed as a straight line on a logarithmic time axis with a slope representing attenuation per unit length and a constant expressing the intercept of the straight line. It mirrors precisely the overall decay of the transit signals and the slope determines how much attenuation the fluid has caused across the surface in dependence of the surface coverage area. The rate can be expressed as simple relation:

$$\text{Attenu.}_{\text{transit}} (\text{dB}) = f(d_0) \quad \rightarrow \quad \text{Attenu.}_{\text{transit}} (\text{dB}) = m_{\text{transit}} d_0 + b_{\text{transit}}$$

where  $m_{\text{transit}}$  is the slope of the transit signal according to the double or single transit signal, and  $b_{\text{transit}}$  is the intercept respectively. Fig. 3.21 shows the expected attenuation trend indicated by the straight lines. The lines are tangents going through the local attenuation minima representing the individual attenuation rate for the two decaying transit signals. The rate of attenuation for the double transit is  $m_{\text{transit}} = 0.016$  dB/unit length and can be contrasted with an attenuation of 0.16 dB when the stripe has widened by 0.1 mm. Therefore the fluid attenuates the amplitude of the order of 1.6dB per mm. The rate of

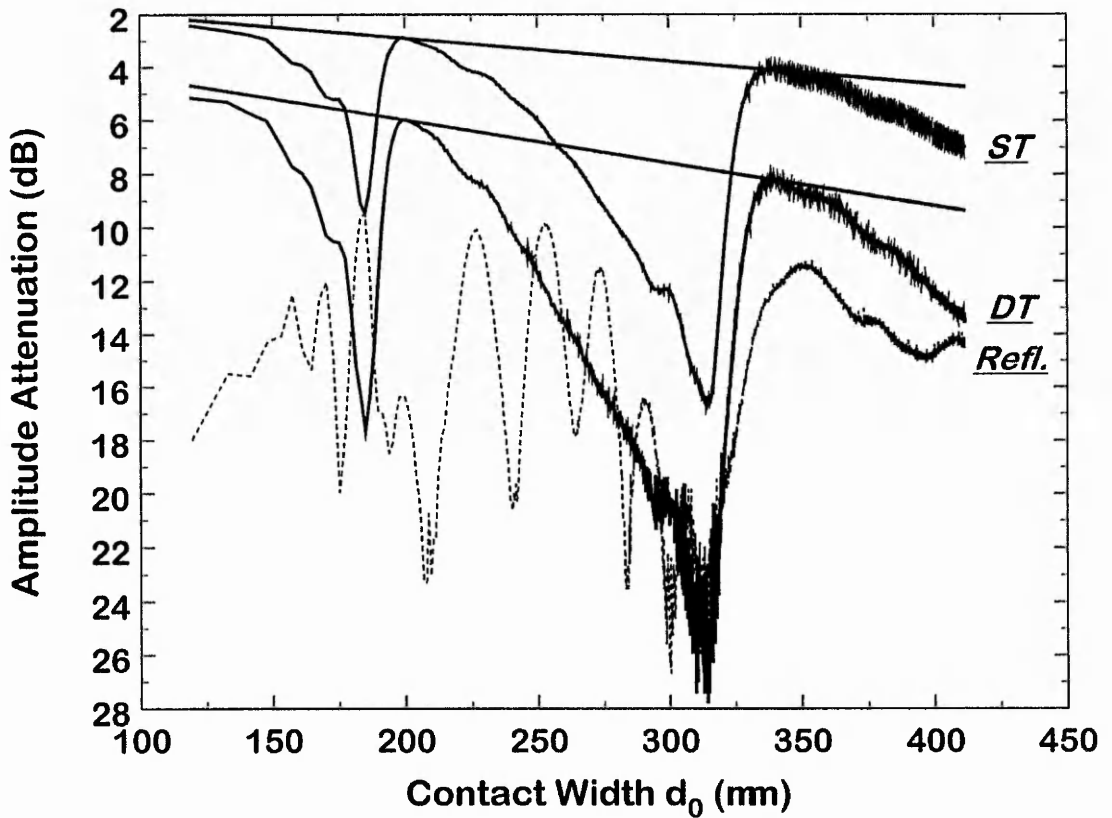


**Fig. 3.21** The straight lines for the single transit (*ST*) and double transit (*DT*) determine the fluid attenuation per unit length scale on the free surface of the SAW device. The attenuation coefficient (slope) for the single transit is 1.6 dB/mm, and for the double transit a slope of 0.87 dB/mm has been estimated.

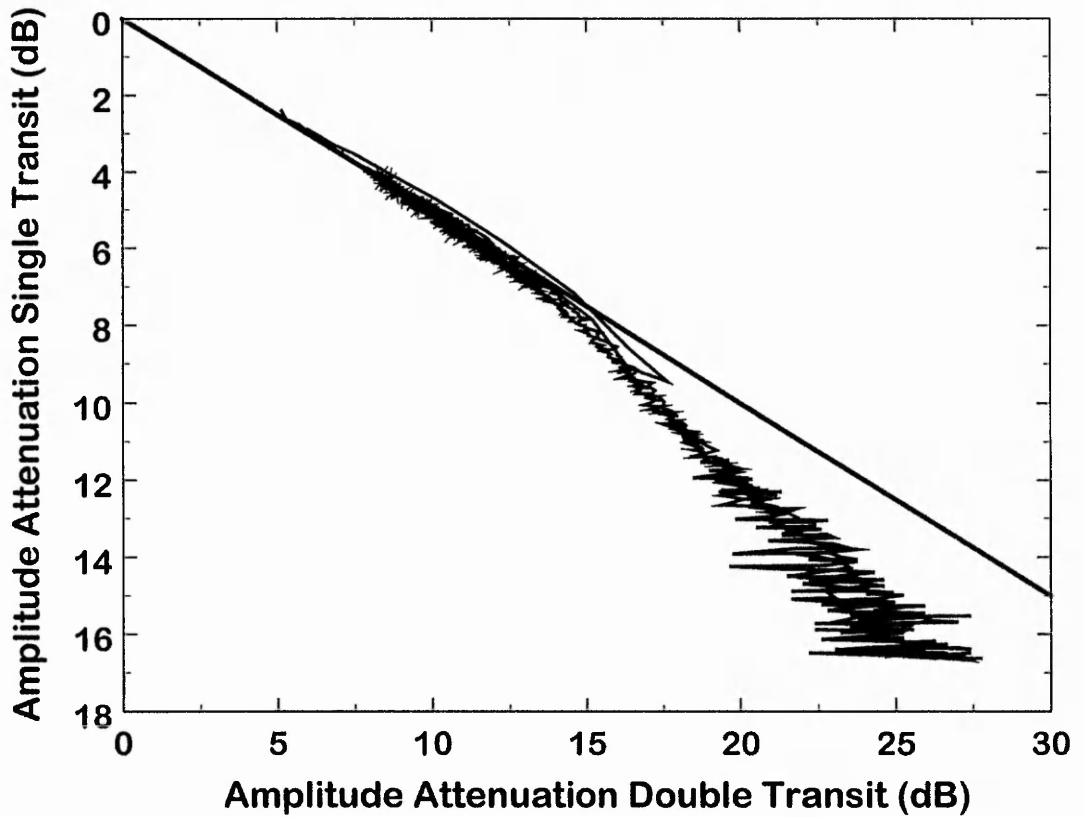


**Fig. 3.22** Plotting the single transit against the double transit shows the expected slope of 0.5 for losses approximately up to 9 dB. When the losses increase up to 25 dB an increasing deviation and scatter is evident.

attenuation for the single transit has been estimate to  $m_{transit} = 0.0087$  dB/unit length giving a 0.087 dB per 0.1mm fluid coverage and shows therefore as expected an attenuation of 0.87 dB per mm. The slope of the attenuation for the double transit is almost twice as much as for the single transit and reflects the prediction of the transit signals having a slope of 1/2 as shown in Fig. 3.22. The deviation in the transit signals towards the 25 dB mark is not affected by the attenuation characteristics of the overall decaying curves. The straight lines are hitting the local attenuation minima which occur close after the oil has swept through the attenuation resonance peaks. The intercept for the single transit has been determined to be - 1.15 dB and for the double transit an intercept of - 2.77 dB has been estimated. As we shall see later in Chapter 5 the deviation in the calibration process represents a significant limit when comparing the experimental data with the model developed in Chapter 2. The calibration is dependent on the threshold of the diodes effectively cutting off a possible estimation of the correct attenuation magnitude below the threshold. The calibration itself reflects a systematic experiment simulating the effect of a fluid loaded surface of the SAW device excluding the device insertion loss. Commencing the calibration, the amount of attenuation increases in a logarithmic power series by exchanging or/and cascading the attenuators. This represents in actual sense an increase of surface coverage and therefore a widening of the stripe of fluid, and this causes the transmission signal amplitude to drop below the diode threshold. The diode output itself is a rectified envelope of the sine wave pulse when received by the diodes of the transmission and reflection path after the pulse has interacted with the fluid. A direct comparison between source input pulse and its converted pulse response at the receiving transducer is not possible for the transmission line system presented here. The limitation is found in the maximum resolution of the digital storage oscilloscope, which cannot resolve sine wave signals far beyond 100 MHz. Amplitude distortions are already present above 80 MHz and therefore give no reliable direct comparison of source signals produced by the sine wave generator with attenuated SAW signals. The rectification of pulse modulated SAW's using a diode rectifier and a calibration procedure based on cascaded attenuators to simulate the fluid coverage of the sensor surface allows a good precision

conversion from measured mean values (volts) into dB of up to 12 dB attenuation when the rate of attenuation of the two transmission signals are compared. Since the SAW pulse for the single transit is passing the fluid only once along the solid-liquid interface, attenuation levels rarely exceed the diode thresholds. As shown later (Chapter 5), the model predicted in Chapter 2 follows exactly the same attenuation trends as measured in the experiment. More deviation is apparent in the double transit signal since the diode threshold cuts off the actual attenuation level when overlapped with the model. Significant, however is the abrupt stopping of systematic increase in attenuation at the 36 dB limit. Comparing this with the actual calibration chart measurements reveals that beyond that limit the threshold of the diodes and possible noise effects which are apparent close to the baseline of the oscilloscope trace, affects the calibration.

### 3.9. Deposition Method for Stripes of Liquid

The experiments required the application of a stripe of oil on top of the lithium niobate surface of the SAW sample. A stripe rather than a drop was chosen in order to produce an orientated signal towards the transducers. The transducer is normally a structure of a straight configuration of interlocking electrodes. It would be difficult to change this structure, therefore a straight line was the desired shape reflecting a wave front in a wanted direction. Several experiments with different materials established that using a simple razor blade with a clearly defined blade edge to deposit a stripe produced good reflection of SAW's at the stripe edge and a sufficiently small quantity of fluid, so that complete damping of the double transit pulse was avoided. The deposition procedure for the stripes was carried out for four different polydimethylsiloxane (PDMS) oils. The oils are silicone oils and are polymer melts with a high viscosity. They have been chosen for this experiment because they are non-volatile and thus conserve volume, offer a wide range of different viscosity, whilst maintaining the same density and have a characterised spreading behaviour [174]. The viscosities used were 100,000 cSt, 30,000 cSt, 10,000 cSt

and 1,000 cSt oils and were purchased from Aldrich Chemicals. To investigate the surface wave-liquid interactions in a systematic manner a total of approximately 100 experiments has been carried out. A systematic series of approx. 57 experiments has been recorded for the spreading of the 100,000 cSt PDMS oil on various SAW devices. The remaining experiments are divided in 18 experiments for the 30,000 cSt PDMS oil; 18 experiments in the category of the 10,000 cSt PDMS oil and 5 experiments for the 1,000 cSt PDMS.

To study the dynamic wetting process it is convenient to choose a system that gives complete wetting, e.g. a vanishing contact angle and a low characteristic speed of wetting,  $v^* = \gamma / \eta$ , and thus allow an adjustment of the timescale for spreading over several orders of magnitude. Here  $\gamma$  is the liquid surface tension and  $\eta$  is the viscosity of the oil. The analysis of wetting rates is simplified if the length scale of the fluid is much less than the capillary length,  $\kappa^{-1} = \sqrt{\gamma / \rho g}$ , so that gravity will not affect the cylindrical cap of the stripe and seriously increase the characteristic speed of wetting. The solution of the equation governing the dynamic changes of the profile is only possible if mass conservation is satisfied and this suggests the use of a non-volatile fluid. When these conditions are fulfilled spreading occurs with a spherical cross-sectional profile at all times and through a wide range of contact angles. The characteristic parameters are summarised in Table 3.3. The density and surface tension of these oils are  $971 \text{ kg m}^{-3}$  and  $21.5 \text{ mN m}^{-1}$ , respectively. This gives a natural length scale for the fluid of  $\kappa^{-1} = 1.5 \text{ mm}$ .

When lower viscous oils were used, capillary effects made the deposition of these fluids complicated and the deposited stripes showed much greater variation in geometry across their length. The parallelism of the edges varied often significantly due to disproportionate mass accumulation along the stripe length. In the series of oils the 1,000 cSt oil produced the biggest difficulties in deposition by the razor blade. Mostly discontinuity of the stripe occurred along its length scale making an observation of a reflection signal in the acoustic signals impossible. Also the approximation of the cross-sectional parameters such as the contact width,  $d_0$ , the cylindrical cap radius  $R$ , cylindrical cap height,  $h_0$ , and contact angle,  $\theta$  could not be correlated correctly to the SAW data. The razor blade showed good precision when higher viscous oils were deposited on

the SAW sensor. Good parallelism of the edges of the stripe could be achieved. For the lower viscosities the blade was mostly impractical, because the capillary effect caused the oil to rise up the blade and when the blade tip was approaching the substrate most of the oil had left the tip leaving a fairly discontinuous stripe spreading across the surface. A PTFE fibre of approximately 100  $\mu\text{m}$  in diameter stretched across two supports, 2.5 cm placed apart, was found to generate a desired stripe. The diameter had to be chosen carefully not to produce a too wide stripe across the acoustic path, resulting in severe attenuation of the acoustic signals. On the other hand the surface tension  $\gamma$  of the fluid caused in several cases a chain of droplets along the fibre. The camera image revealed a chain of joining droplets on the surface after deposition. Therefore pre-wetted conditions along the fibre diameter produced a barrel shape of the fluid allowing a precise deposition of a continuous stripe with good parallel edges. The fibre was dipped into a reservoir of oil and the oil then manually applied onto the substrate; this required significant practice. In some cases the fibre deposition technique required up to several hundred attempts prior to the start of an experiment.

The spreading was monitored constantly by the digital storage oscilloscope writing all acquired data to a file, allowing computer analysis using statistical packages and spreadsheets. The deposited stripes typically had an initial contact width of around 0.1 - 0.2 mm at the time of deposition and maximum heights at the cylindrical crest of between 20  $\mu\text{m}$  and 10  $\mu\text{m}$ . The contact width increased during the spreading process between 0.4 - 0.5 mm and the cap height reduced to 6 - 3  $\mu\text{m}$ . The time monitored for the spreading process was varied with the chosen viscosity. Initially the higher viscous oils spread over a time period of 6 - 8 h. Most experiments were carried out for at least eight hours allowing the oil to spread reasonably far across the free surface. For the less viscous oils time periods of 4 h were used. Since the width of the stripe is much less than the capillary length it can be expected that the fluid is reasonably close to a cylindrical cap cross-section at all times during spreading (Fig 3.13 and 3.15). However, it is possible that small deviation from the stripe geometry regarding its parallelism in length will occur towards the later stages of spreading. A given shape of oil always varies in both width and

height over its length, but these are relatively slow variations over the width of the transducer aperture.

**Table 3.3** The characteristic velocity for the spreading dynamics of PDMS oils and the capillary length,  $\kappa^{-1}$ , are listed.

<i>viscosity of PDMS oils</i>	<i>Velocity <math>v^*</math></i>
<b>1,000 cSt</b>	21.833
<b>10,000 cSt</b>	2.207
<b>30,000 cSt</b>	0.734
<b>100,000 cSt</b>	0.220
	mm s <sup>-1</sup>

# CHAPTER 4

# *RESULTS*

## 4.1. Introduction

To investigate the Rayleigh wave response to a spatial inhomogeneity present in the acoustic path of a surface acoustic wave device a stripe of liquid was deposited approximately in the centre of the path and its dynamic evolution was closely monitored. The optical information was recorded onto video tape and the signal response simultaneously stored onto the data acquisition system. The simultaneous observation enables one to correlate the time dependent dynamic evolution of the stripe width with the data obtained from the variation in amplitude of the acoustic signals. The convenience of the two independent processes to observe the wetting dynamics, enables one to plot geometrical changes directly versus amplitude variations in the acoustic signals. An individual analysis of each set of data is possible. Moreover the optical observation serves as a tool to check parallelism and orientation of the stripe in line with the transducers orientation and the shape structure of the stripe along its length scale continuously with the progress of an experiment. This allows one to identify possible variation in the acoustic signals directly linked to optical variations in the geometrical parameters of the stripe.

This chapter presents the results of partially localised stripes of fluid spreading in the acoustic path of a Rayleigh surface acoustic wave sensor. As the fluid wets the device surface a distinct pattern in the acoustic signals is observed and these changes have been correlated to dynamic changes in the stripe geometry. A selection of 11 experimental results selected from a total of approximately 100 experiments are presented. The first section will describe trends in the acoustic signals. These are directly taken from a screen shot of the oscilloscope display of the transmission/reflection system. A systematic plot of amplitude variation in all observed signals as a function of time is presented. In the next section the results from image processing to extract the geometrical parameter from the interferometry analysis are shown and a correlation process to convert the optical information into time variant geometrical changes are described. A systematic study of signal response as a function of different viscosities has been considered and a comparison is given between various

results. In the final section the focus is on reproducibility within one specific set of experiments. Herein the experimental conditions are kept constant and a comparison on grounds of geometrical parameters are demonstrated. The results indicate that the signal response of all acoustic signals show similar trends if cross-sectional parameter are approximately similar representing similar stripe volumes.

## 4.2. Trends in Acoustic Signals

In a typical experiment three acoustic pulses were observed once a stripe of oil had been deposited. An oscilloscope screen shot showing the acoustic signal response of a 168.8 MHz SAW device had three signals as displayed in Fig. 4.1; a single transit signal (top curve in the graph, the trace has been inverted for display), a reflection from the fluid edge and the double transit reflection (both the reflection and the double transit are displayed on one single trace shown in the bottom curve). The single transit and double transit occur at  $(3.45 \pm 0.05) \mu\text{s}$ , and  $(6.95 \pm 0.05) \mu\text{s}$ , respectively. The position of the single transit signal, traversing along the acoustic path once, and the double transit reflection, travelling twice the distance of the single transit time, is related to a SAW-device of a path length of 13.5 mm between the transducers. The reflection from the liquid occurs at  $(3.3 \pm 0.1) \mu\text{s}$ . The position of the reflection can be clearly identified by its trace position, and is well separated from the dominant double transit pulse.

The observed single transit signal, double transit signal and the reflection signal change significantly with time as the stripe spreads. In fact, to such an extent that the double transit peak at specific times is attenuated to an amplitude magnitude below the threshold of the diode detector. As the fluid spreads further a recovery of the transmission signals can be seen indicating the appearance of strong oscillations in these signals. This is shown qualitatively in Fig. 4.2 by the three traces for each oscilloscope channel taken at different times during the spreading process. The arrows indicate the amplitude response of each individual signal. The larger arrows demonstrate

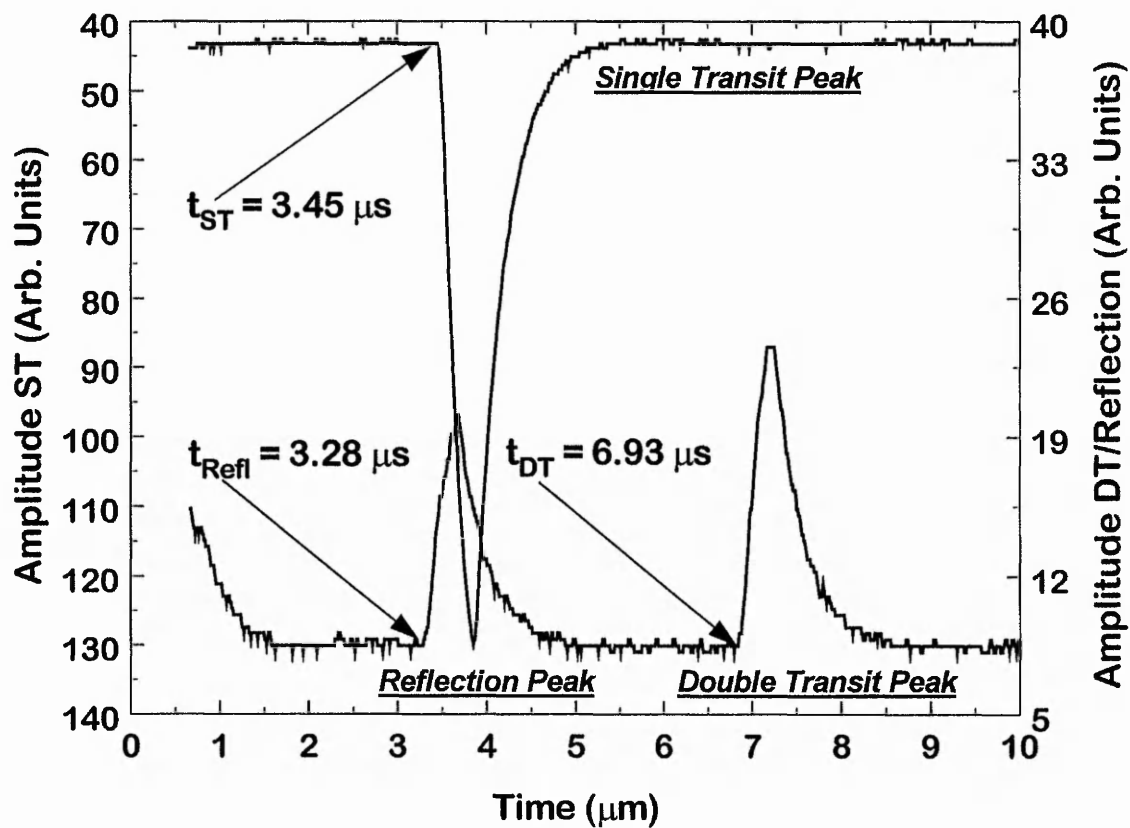


**Fig. 4.1** The presentation of a full oscilloscope screen, showing the single transit signal occurring at about 3.45  $\mu\text{s}$  and the double transit signal and the reflection at about 6.93  $\mu\text{s}$  and 3.3  $\mu\text{s}$ , respectively.

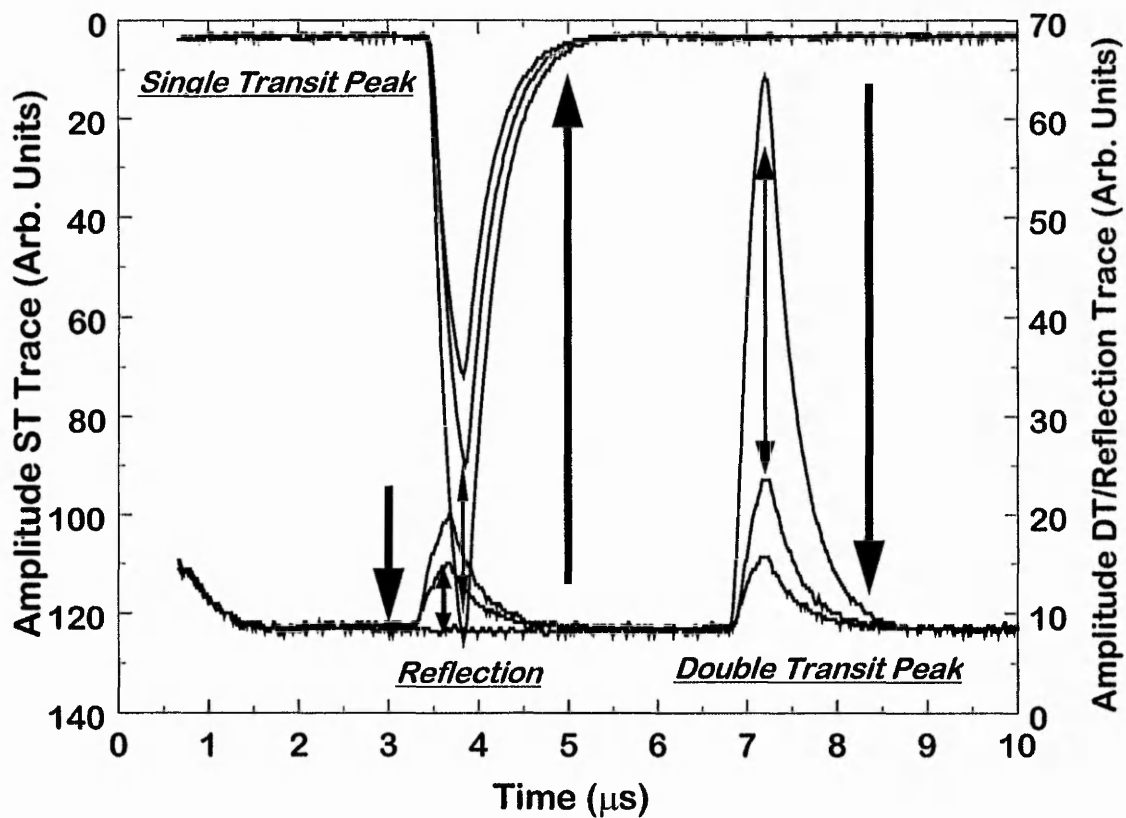


**Fig. 4.2** The signal response of the three observed signals when a deposited stripe of oil progressively wets the surface. The large arrows indicate the overall attenuation of the amplitude during a complete course of experiment. The smaller arrows display the oscillatory nature of the peaks during spreading.

the overall amplitude changes with progressing time when the fluid wets the surface. The smaller arrows indicate the oscillatory nature of the three signals appearing during the spreading. Indeed Fig. 4.3 shows the qualitative trend of the three signals with progressing time. The results in Fig. 4.1 to Fig. 4.3 obtained from a 100,000 cSt polydimethylsiloxane (PDMS) stripe of oil uses the same SAW device operating at 168.8 MHz. The input power for device operation was set to a RF-level of 500 mV peak-to-peak (RF-voltage). A plot of signal amplitude versus logarithmic time highlights the changes in signal amplitude and suggests a rich structure in these signals. A logarithmic time scale has been chosen in order to account for the very rapid changes occurring at the very beginning of the spreading process. In fact most of the observed structure in Fig. 4.3 is captured in a time period of approximately 2 hours (7000 seconds ( $\log_{10}(t)$  between 1 and 3.85)). However, the spreading period for the fluid is of the order of eight hours and the whole run is simultaneously recorded alongside optical observations. The single transit signal, indicated by ST, and the reflection have been plotted on the same vertical axis whereas for the double transit signal (DT) a secondary y-axis has been introduced to scale up the signal in magnitude. In the experiment, the transit signals do not simply show a progressive attenuation in amplitude with an exponential decay as the stripe spreads within the acoustic path at the solid-vapour interface of the sensor. The transit signals show attenuation resonances upon liquid loading and these appear to be asymmetric. A qualitative examination of the course of the single transit and double transit signals indicates a high degree of similarity. This is especially the case at the start of the experiment where single transit and double transit mirror each other in trend and structure. A good indication of the similarity can be seen especially in the back slope of the two signals where smaller oscillations are evident when the signals approach the first attenuation maxima. The superimposed oscillations on the back slope of both signals are very similar in structure and location. Later in the spreading when both signals are more attenuated, deviations of the signal trends and signal pattern are visible, when single transit and double transit approach the second attenuation maxima, appearing at around  $\log_{10}(t) = 3.85$  (approximately 7000 seconds  $\approx$  2 h) in the spreading. These deviations are significant and indicate that the

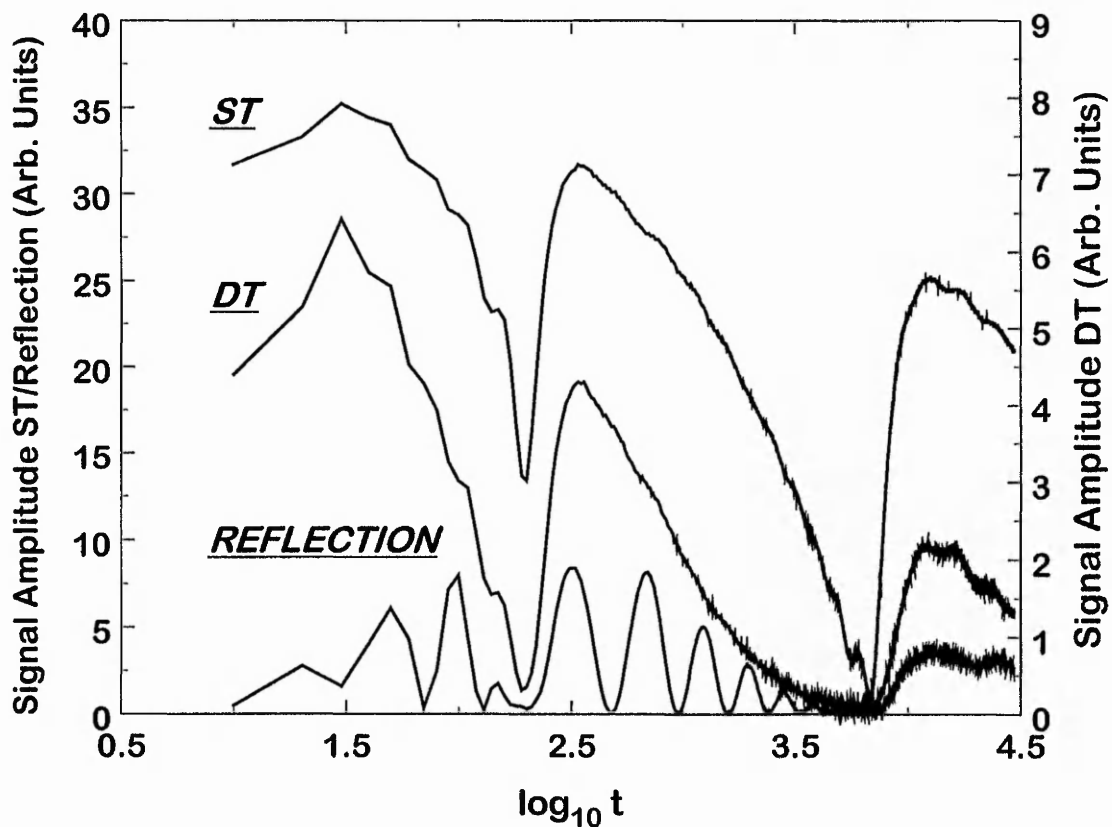


**Fig. 4.3** The response of the three signals, single transit signal (ST), double transit signal (DT) and the reflection (REFLECTION) plotted on a logarithmic time axis.

threshold of the diode detector is possibly cutting off the actual attenuation magnitude of the amplitude of the double transit pulse, although a further reduction in signal amplitude can be expected. Comparing this with the single transit attenuation where a sharp tip marks the end of the progressive attenuation at the second resonance peak, the actual trend of the double transit shows a much slower variation in attenuation with a less stringent decaying behaviour as the double transit approaches the second resonance peak. Immediately after, all signals start to recover. The attenuation maxima therefore have a characteristic asymmetric shape. It takes about 5000 seconds (on the logarithmic time axis at  $\log_{10}(t) = 3.70$ ) for all three signals to recover to signal levels which show approximately 7 dB attenuation for the single transit, 11 dB for the double transit and approx. 13 dB for the reflection. After the recovery, single transit and double transit seem to continue to mirror each other in trend and structure as this can be seen in the superimposed substructure of small oscillations in the transit signals.

The acoustic reflection caused by the advancing liquid is displayed in the bottom section of Fig. 4.3. The structure is complex and shows strong oscillations which appear rapidly after deposition of the stripe. The structure of these oscillations is inconsistent at the beginning of the spreading when the transit signals approach the first attenuation resonance but the envelope of the oscillations in the reflection seem to exactly follow the attenuation trend of the transit signals. When the first attenuation resonance is approached the oscillations in the reflection seem to die out. However, as soon as the transit signals start to recover, after the first resonance trough, the reflection seems to regrow in amplitude and with progress of the experiment, continues to show large oscillations. The overall envelope of the amplitude trends in the reflection is mirrored by the course of the transit signals. At the same time the superimposed oscillation in the reflection envelope appear in a more consistent formation as before the first resonance peak. A distinct formation of six oscillations with distinct maxima and minima are evident and they decay exponentially following the behaviour of the transit signals. At the second attenuation maxima all three signals show extremely strong attenuation and it seems that all three signals are attenuated beyond the diode thresholds.

Leaving the second attenuation maxima of the transit signals behind, the reflection regrows a second time in amplitude and then slowly decays with time. The oscillations here appear less pronounced and can be better described as a substructure superimposed on the trend of the reflection signal rather than showing a strong oscillatory behaviour with well defined maxima and minima as seen between the two neighbouring attenuation resonances in the transit signals.

When the fluid is wiped off from the substrate surface, the reflection signal vanishes and the transit signals recover to their original magnitudes in signal amplitude. During the course of an experiment the reflection did not observably change its position on the oscilloscope screen.

### 4.3. Signal Response of Different SAW Devices

Investigation of how a change in surface acoustic wave devices would influence the structure of the signal response was necessary. Also extensive and repeated experimental use of a single SAW device caused in several cases a destruction of the device and it was necessary to investigate other devices. The time variation in the SAW amplitude is of significance in all experiments and plays an integral part in the investigation of SAW-liquid interactions. In Fig. 4.4 we show the changes in the transmitted SAW signal over a period of eight hours using a simple single transit configuration and two different devices. These devices were produced using the same mask design for the interdigital transducers (IDT's) on 128° rotated y-cut lithium niobate (Yamaju Ceramics). The acoustic system set-up conditions for the pulse width settings (400 ns) and pulse repetition rate (1 kHz) which were kept constant and the experiments were performed using high viscosity 100,000 cSt polydimethylsiloxane oil. The upper curve used a device with a resonant frequency of 167 MHz and an RF input voltage of 70 mV (peak-to-peak) The lower curve shows the results of another device with a resonant frequency of 170 MHz and an RF input voltage of 86 mV. The upper curve has

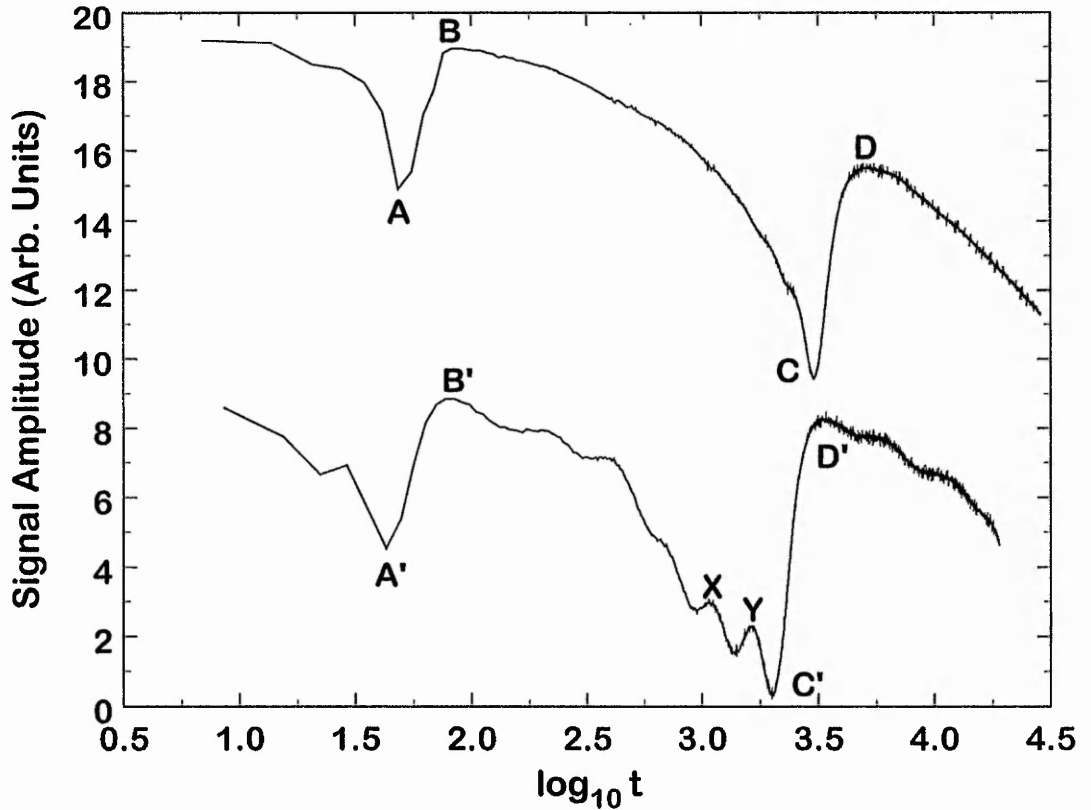


**Fig. 4.4** The single transit data show an overall attenuation, but with a rich oscillatory structure (A-D and A'-D') and some subsidiary peaks (X and Y). The upper curve (167 MHz device operated at 70 mV) has been displaced vertically upwards by 7.75 to fit on the same graph as the data from a 170 MHz device (operated at 86 mV).

been displaced vertically upwards by 7.75 units to display both graphs in the same chart. Both curves show the same trend, labelled A - D and A' - D', with two large oscillations, superimposed on an overall decay of the signal amplitude. The extent of the oscillations is significant giving a reduction of the signal levels by 90% or more. In addition to these oscillations some smaller scale structure is evident in the signals. This can be seen as edges on the negative slope from the second amplitude maxima to the second minima of the upper curve (B - C). On the lower curve, these edges appear as well pronounced peaks, labelled X and Y, on the negative slope between B' and C'. The edges observed in the back slope indicate that the structure is not unique to only one experiment. However it seems to be that the pattern evident in the upper curve of Fig. 4.4 and in Fig. 4.3 are less well developed than the labelled X and Y peaks in the bottom graph of Fig. 4.4. Investigating peak locations of X and Y in greater detail reveals that the optically measured stripe width increases between these two distinct peaks of the order of  $12\ \mu\text{m}$  and, to within the accuracy of the optics, this represents  $\lambda_R/2$ . The optical data for the upper curve show that the contact width,  $d_0$  increases from  $203\ \mu\text{m}$  at B to  $378\ \mu\text{m}$  at D. To conserve volume, a compensating decrease in height from  $13.4\ \mu\text{m}$  to  $8.0\ \mu\text{m}$  also occurs. The contact angle decreases from  $15.0^\circ$  to  $4.9^\circ$  during this time. The period between B' and D' on the lower curve corresponds to an increase of the contact width from  $140\ \mu\text{m}$  to  $229\ \mu\text{m}$  with a corresponding reduction in height from  $9\ \mu\text{m}$  to  $5\ \mu\text{m}$ . In this case, the contact angle reduces from  $14.8^\circ$  to  $4.8^\circ$ . The major amplitude maxima to maxima changes in both, single transit and double transit therefore corresponds to an increase in contact width of greater than a single acoustic wavelength and decreases in height of less than one half of an acoustic wavelength.

As the results in Fig. 4.4 have shown, devices with similar design architecture give similar structure in the transmission signals. The overall structure and subsidiary edge pattern in the back slopes of both graphs follow similar trends and significant attenuation resonances with characteristic asymmetric shape in the transit signals are well developed within both curves.

## 4.4. Optical Analysis

### 4.4.1. Theoretical Time Dependence of the Stripe Geometry

Optically it is the contact width,  $d_0$ , and the cylindrical cap radius,  $R$ , which are measured and these have a theoretical time dependence given by

$$d_0 = \left[ \frac{567 V^3 \gamma (t+c)}{L_0^3 \eta J_w} \right]^{1/7} \quad \text{and} \quad R = \left[ \frac{83349 V^2 \gamma^3 (t+c)^3}{16348 L_0^2 \eta^3 J_w^3} \right]^{1/7}, \quad (4.1)$$

where  $V L_0$  is the volume of the fluid per unit length,  $J_w$  is a cut-off parameter and  $c$  is a constant determined by the initial cross-sectional shape of the oil. These power laws for the time evolution can be obtained by balancing the changes in the surface free energy of the stripe with losses due to viscous dissipation (see Chapter 2, section 2.2.6. and 2.2.7.). The formulae are valid for systems with conserved volume of fluid, a vanishing equilibrium contact angle ( $\theta_e = 0$ ) and a dynamic contact angle less than  $60^\circ$ . The values of contact width and cylindrical cap radius shown in Fig. 4.5 correspond to the SAW data presented in Fig. 4.6 and 4.7, respectively. The y-axes in Fig. 4.6 and 4.7 have been converted from signal amplitude, measured in mV into acoustic losses (dB) due to fluid coverage on the SAW device surface. Simultaneously fitting both sets of data using  $1/7^{\text{th}}$  and  $3/7^{\text{th}}$  type power laws gives  $d_0 = 88.53 (t+166)^{1/6.74}$  and  $R = 41.91 (t+166)^{3/6.58}$  where  $d_0$  and  $R$  are in  $\mu\text{m}$  and  $t$  is in seconds. These fits have been carried out using a total of 40 selected images using optical data between 43 seconds after the deposition of a stripe and the end time of approximately 8 hours. An image was included for each maxima and minima in the SAW reflection data. The fits for  $d_0$  and  $R$  are accurate to within 1% and 2%, respectively, for all data points and are shown

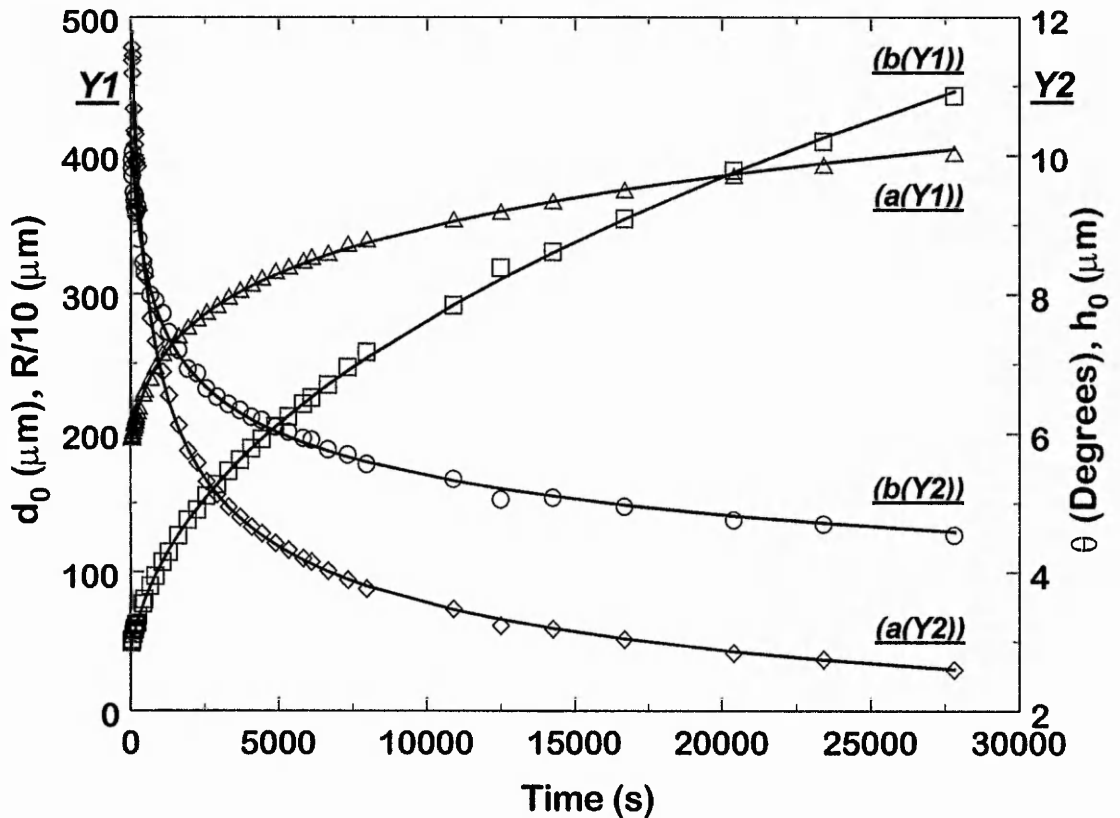


**Fig. 4.5** The geometrical cross-section parameters contact width,  $d_0$ ,  $(a(Y1))$ , cylindrical cap radius,  $R$ ,  $(b(Y1))$ , contact angle,  $\theta$ ,  $(a(Y2))$ , and height,  $h_0$ ,  $(b(Y2))$ . The graph uses two separate axis ( $Y1$  and  $Y2$ ) to accommodate all four different parameters. The course of the contact width,  $d_0$  and cylindrical cap radius,  $R$  are hardly distinguishable from the  $n = 7$  fits. Contact angle,  $\theta$ , and height,  $h_0$  have been deduced from the two other parameters.

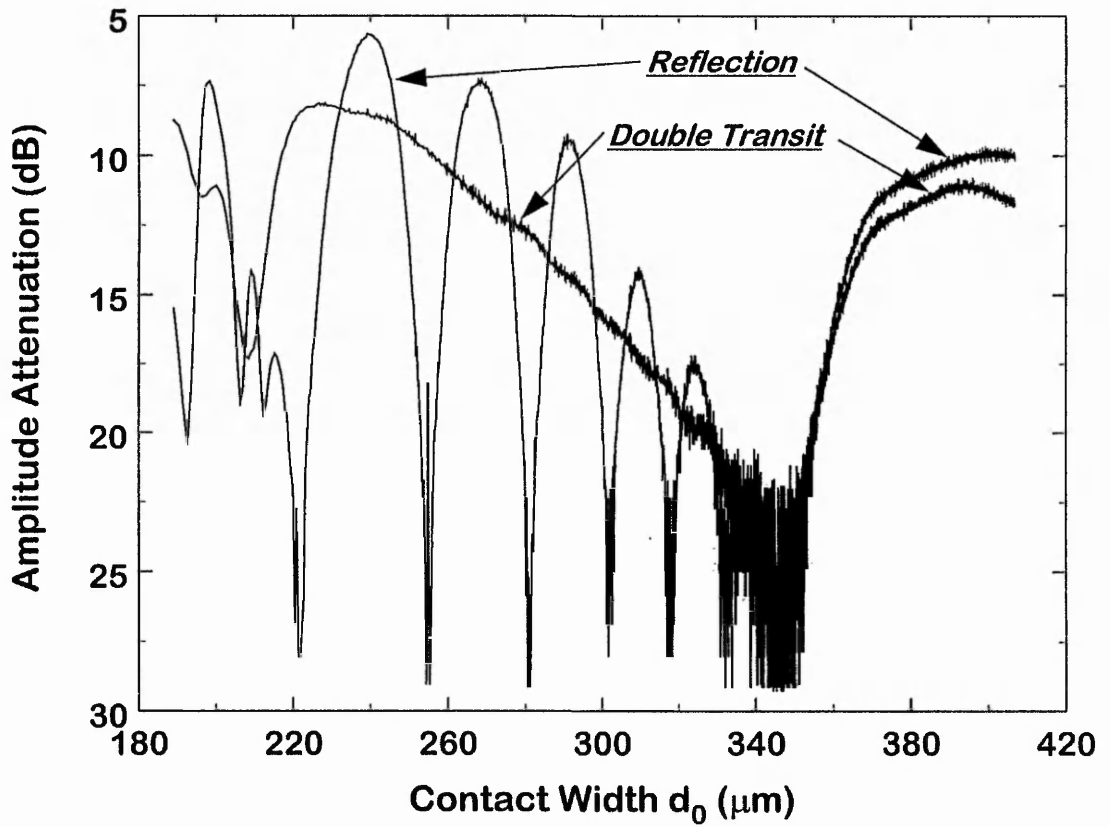


**Fig. 4.6** The conversion from time into contact width,  $d_0$  is plotted against amplitude attenuation. Replacing the time axis with the contact with,  $d_0$  reveals rapid changes (see also Fig. 4.5) in the beginning of the spreading, but slows down logarithmically at later stages in time.

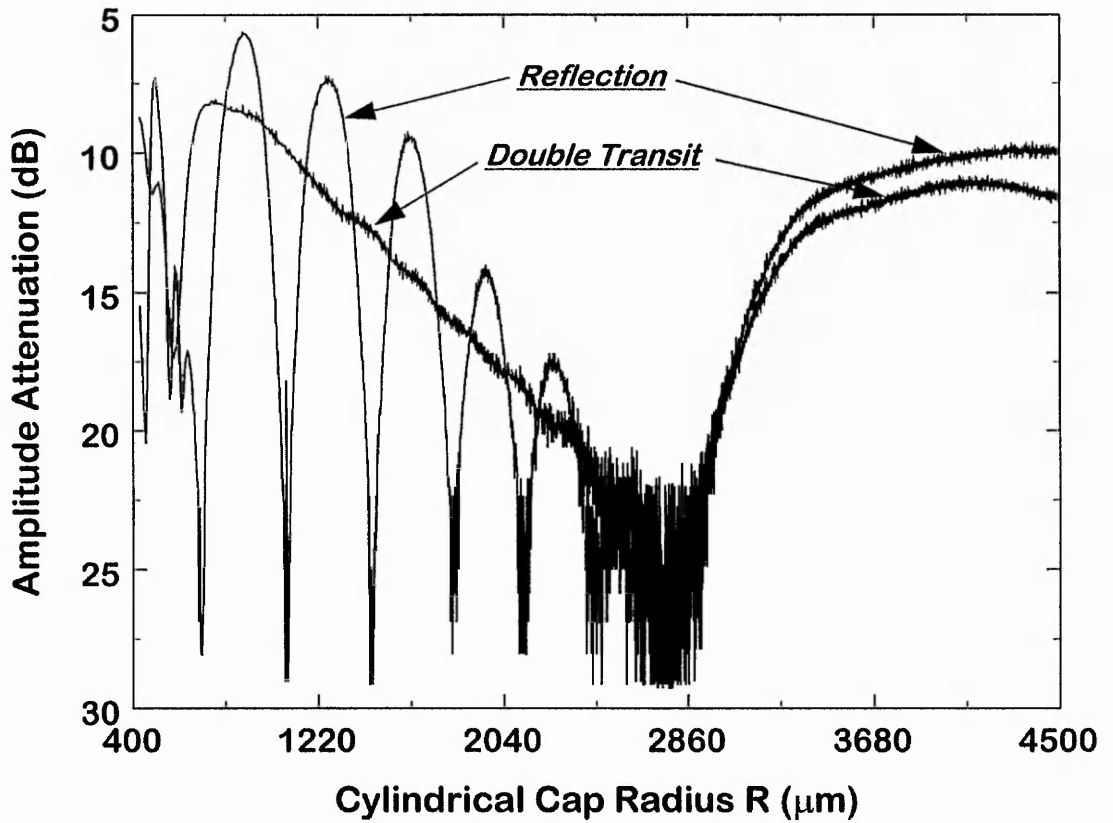


**Fig. 4.7** The cylindrical cap radius,  $R$  shows more even changes in slope according to the  $3/7^{\text{th}}$  power law. It appears that changes in the trend of the reflection and the double transit are clearer at the later stages of the spreading process.

by the solid lines in Fig. 4.5. To show the data for  $R$  on the same graph they have been divided by a factor of ten. For a cylindrical cap cross-section, knowledge of  $d_0$  and  $R$ , gives the dynamic contact angle,  $\theta$ , and height,  $h_0$  using,

$$d_0 = 2R \sin \theta \quad \text{and} \quad d_0 = 2h_0 / \tan(\theta/2) \quad (4.2)$$

and for angles less than  $60^\circ$  give time dependencies of,

$$h_0 = \left[ \frac{27V^4 \eta J_w}{896 L_0^4 \gamma (t+c)} \right]^{1/7} \quad \text{and} \quad \theta = \left[ \frac{128V \eta^2 J_w^2}{147 L_0 \gamma^2 (t+c)^2} \right]^{1/7} \quad (4.3)$$

To account for the other two geometrical parameters Fig. 4.5 shows in addition the time dependent contact angle,  $\theta$  and height,  $h_0$  calculated from equation (4.2). A systematic conversion from time into the relevant geometrical parameter  $\theta$  and  $h_0$  for the SAW data is presented in Fig. 4.8 and 4.9, respectively and a conversion from the mean value (mV) into acoustic losses (dB) caused by fluid loading has been carried out. In order to accommodate the other two parameters for the geometrical cross-section of the stripe, the contact angle,  $\theta$  and the cylindrical cap height,  $h_0$  have been plotted on a secondary y-axis indicated by Y2 allowing all four possible graphs to be displayed in the same diagram. These fits are using a three parameter fit routine to extract from

$$d_0 = k_1 (t+c)^{1/n} \quad \text{and} \quad R = k_2 (t+c)^{3/n} \quad (4.4)$$

the parameters  $k_1$ ,  $k_2$ ,  $c$  and  $1/n$  and  $3/n$ , respectively. Where  $k_1$ ,  $k_2$  and  $c$  are constants and represent the initial volume and shape whilst  $n$  indicates the parameter for the power laws. Rearranging equation (4.4) using equation (4.2) shows the dependency of contact angle,  $\theta$  and cylindrical cap height,  $h_0$  from  $d_0$  and  $R$  by:

$$\theta = \frac{k_1}{2k_2 (t+c)^{2/7}} \quad \text{and} \quad h = \frac{k_1^2}{8k_2 (t+c)^{1/7}} \quad (4.5)$$

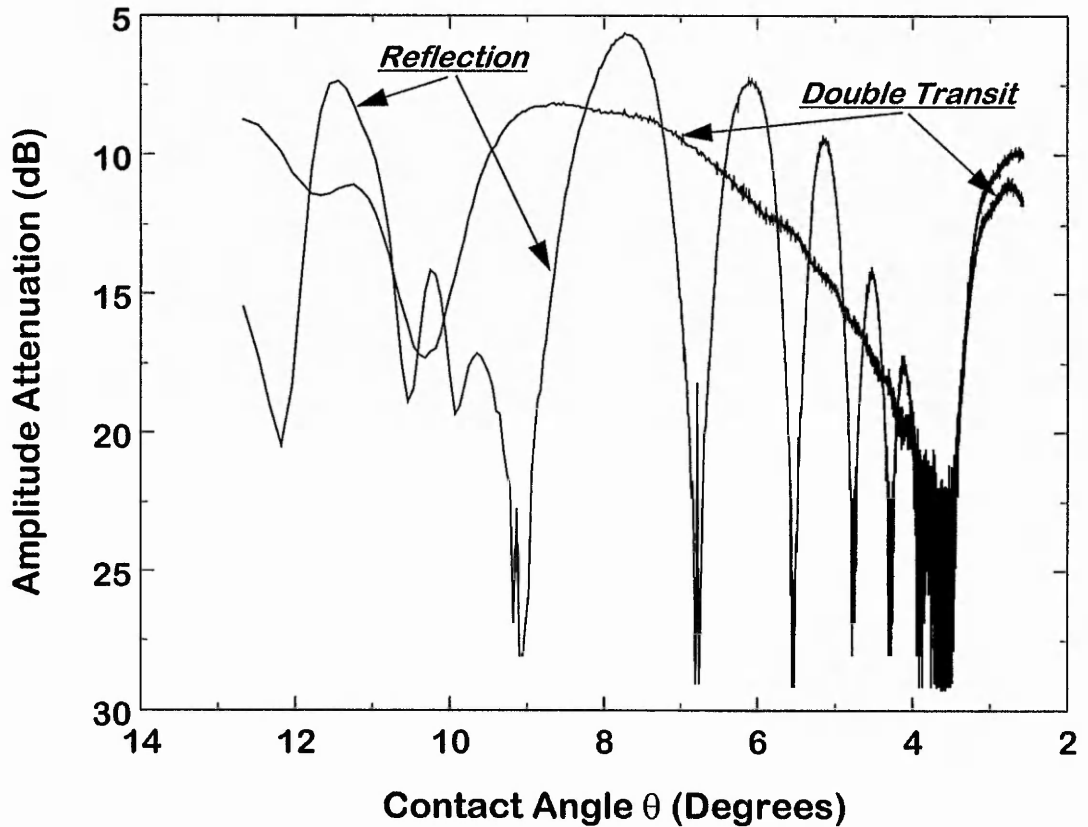


**Fig. 4.8** The contact angle,  $\theta$  has been calculated using equation (4.2). The angle reduces rapidly at the start of the experiment and shows an exponential decay when the stripe spreads. This is well demonstrated in the trend of the graph. Both, double transit and reflection show a detailed trend at the very start of the experiment. At later stages the curves appear more squeezed together, due to small changes in the slope of the fit.

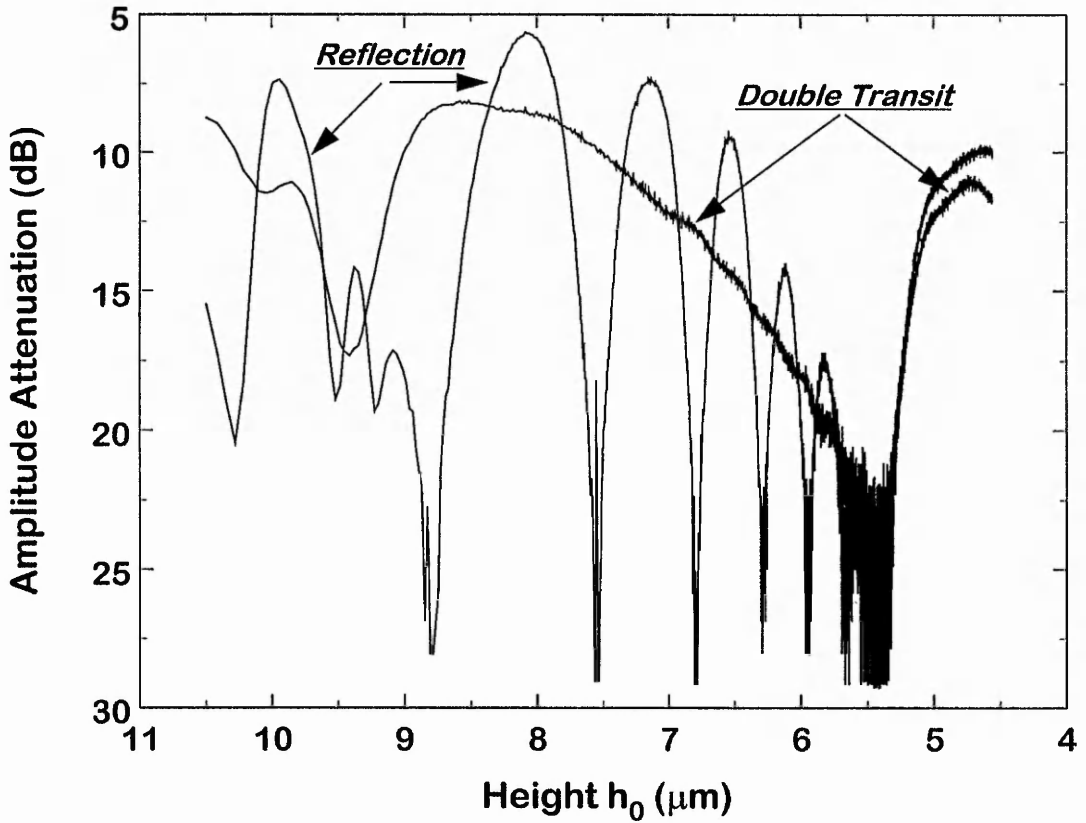


**Fig. 4.9** One of four possible geometrical parameter extracted from images from the cylindrical cap cross section is the height,  $h_0$  of the stripe. The trend of the fit presented in Fig. 4.5 is very similar to the fit of the contact angle since both parameters are closely related. The trend of the double transit and reflection demonstrates this well.

where  $\theta$  is in radians. Fitting the data to the equations in (4.4), using a logarithmic transform of these equations, yields to

$$\log_{10} d_0 = \log_{10} k_1 + n^{-1} \log_{10} (t + c) \quad \text{and} \quad \log_{10} R = \log_{10} k_2 + (3/n) \log_{10} (t + c)$$

in which a value for  $c$  was chosen and then a straight line regression performed to find  $k_1$ ,  $k_2$  and  $n$ . The coefficient of interest in the fit was then used to determine an improved value for  $c$  until an optimum value was found which normally should match very closely the measured data obtained from the optical observations. The fits obtained in this way were hardly deviating from the  $n = 7$  exponent.

The data presented in Fig. 4.5 to Fig. 4.9 have been extracted from one experiment in order to demonstrate the time dependence between the four parameters describing the geometry of the stripe. The experiment uses a similar device to that explained in section 4.3 and settings have been chosen according to the conditions demonstrated for the results in Fig. 4.3. The viscosity of the PDMS oil was 100,000 cSt. Fig. 4.6 to Fig. 4.9 have been converted from time into the relevant geometrical parameter to demonstrate the nature of each fit. Each of these geometrical fits is mainly characterised by changes in slope and a conversion from time into one of these parameters emphasises one part in the SAW data. If we compare for example Fig. 4.6 with Fig. 4.7 the changes in slope of each individual geometrical parameter shows for the contact width,  $d_0$  in Fig. 4.6 a more even trend of the double transit and the reflection whereas the graphs in Fig. 4.7 seem to appear squashed at the start of the graph. The details in the graphs are clearer at later stages when the cylindrical cap radius has considerably increased. Considering Fig. 4.5 we can deduce from the slope information of both fits that changes in slope in the contact width are more significant at the start of the experiment and approaches a possible constant value when the spreading reaches the eight hour mark. Whereas the cylindrical cap radius shows more even changes in trend with a less significant change in slope right at the beginning of the stripe evolution. This is well reflected in the power laws (equation (4.1)). The slope is

determined by the exponent and for an exponent  $1/7$  this gives a slope of 0.14 units whereas for an exponent  $3/7$ , the slope increases to 0.43 units.

#### 4.4.2. Trends in Acoustic Signals as a Function of Dynamic Changes in Stripe Geometry

A more quantitative investigation of the signal trends is shown in Fig. 4.10. Correlations between the dynamically evolving stripe of oil monitored optically and the structure in the acoustic signals varying significantly with time shows that the signal pattern is repeatedly obtained throughout a variety of different experiments. The form of the double transit signal is identical to that of the single transit (compare Figs. 4.3, 4.4) with the same overall decrease in amplitude and structure of maxima and minima. The data from a reflection experiment monitoring the spreading of a 100,000 cSt PDMS oil is shown in Fig. 4.10. The upper curve, which has been shifted upwards by 10.5 arbitrary units, is the double transit signal. This gives more clarity for the trend of the different signals in the graphs. The device employed for the experiment was set to a resonant frequency of 169.4 MHz and an RF-voltage input of 220 mV peak-to-peak. The use of time rather than a logarithmic time axis in Fig. 4.10 shows more clearly the overall decay in amplitude of the transit signal. In particular, the exponential decay in amplitude of the signal can be well observed. The bottom curve in the chart demonstrates the reflection from the stripe of oil. A structure can be seen during the same period ( $t < 2500$  s) as the subsidiary peak structure in the double transit signal occurs. In the first 40 min of the experiment, the contact width,  $d_0$  increases from  $<214$   $\mu\text{m}$  to 299  $\mu\text{m}$  with a corresponding decrease in height from  $>11$   $\mu\text{m}$  to 8  $\mu\text{m}$ . during this time the contact angle decreases from  $>12^\circ$  to ca.  $6^\circ$ . Subsequently, the contact width increases to 415  $\mu\text{m}$  whilst the cylindrical cap height and the contact angle reduce to 5.5  $\mu\text{m}$  and  $3^\circ$ , respectively. The increase in the width of the stripe over the last five peaks in the SAW reflection signal is 91  $\mu\text{m}$  giving an average peak to peak change in width of approximately 23  $\mu\text{m}$ . This value is close to the

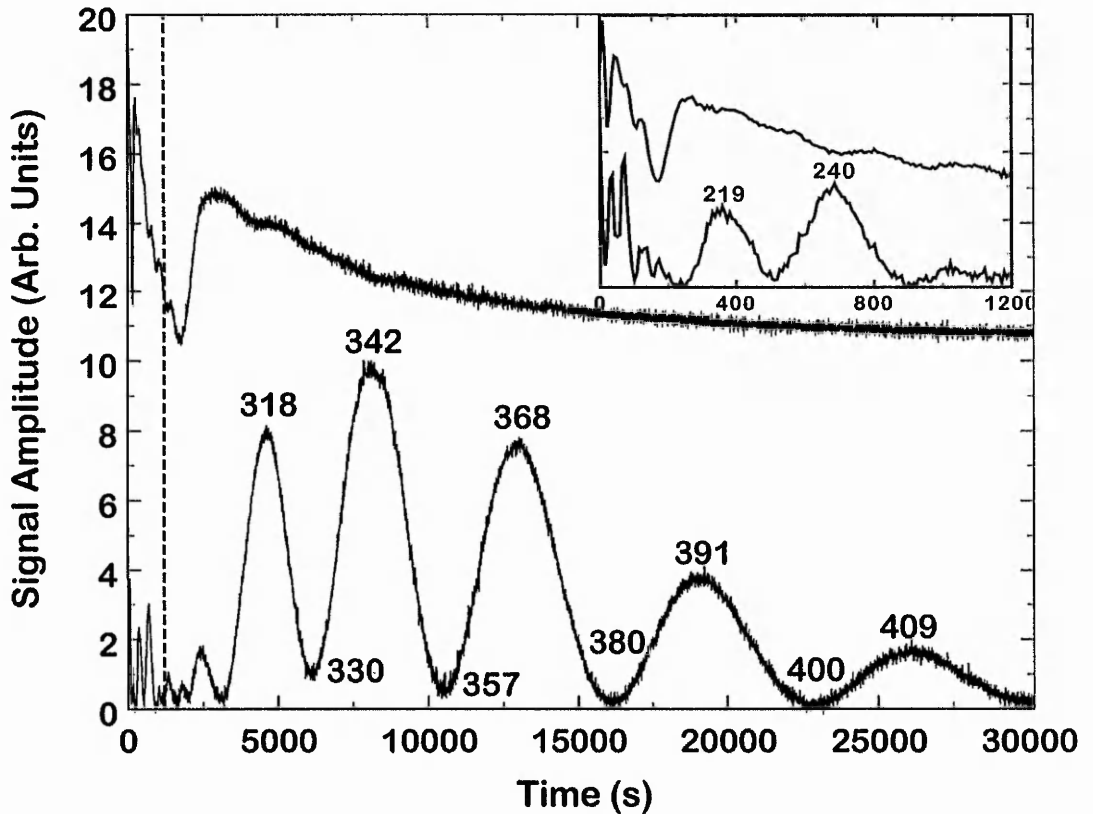


**Fig. 4.10** The reflection from the stripe (lower curve) showing significant oscillations as the oil spreads in comparison with Fig. 4.6; the numbers labelling the oscillations are the measured contact width,  $d_0$  in  $\mu\text{m}$ , of the stripe where the amplitude of the double transit either goes through a maxima or a minima. The upper curve is the double transit signal. The inset shows the changes in both signals at the early stages of the spreading process indicated by the vertical dashed line in the main graph.

SAW wavelength of 22  $\mu\text{m}$  (170 MHz SAW device), although the precise peak to peak change in width varies considerably. The differences in widths are accurate to approximately  $\pm 3 \mu\text{m}$ . The inset in Fig. 4.10 shows the structure in the initial stage of spreading, indicated by the vertical dashed line on the main graph. The double transit signal in the inset is remarkably similar in form and trend to the course of the double transit signal on the main graph. The subsidiary peaks on the double transit signal cannot be clearly identified with either peaks or troughs of the reflection signal. It is interesting that the two larger peaks shown in the inset correspond to a change in width of 21  $\mu\text{m}$ , which is close to the acoustic wavelength of 22  $\mu\text{m}$ . The conversion from time into the two most significant geometrical parameters of the stripe, contact width,  $d_0$  and cylindrical cap radius,  $R$  have been performed from fits using 33 images, chosen from data between 5 minutes after start of the experiment and the end of 8 h. The values of contact width and cylindrical cap radius corresponding to the SAW data in Fig. 4.10 are shown in Fig. 4.11. Simultaneously fitting to both sets of data using the relevant power laws (equation (4.1)) gives for the contact width,  $d_0 = 95.2 (t-41)^{1/7}$  and the cylindrical cap radius,  $R = 45.91 (t-41)^{3/7}$  with an exact exponent of 1/7 and 3/7 reflecting a high accuracy and showing a good agreement with the power laws.

The most striking feature in these graphs is the appearance of very significant and large oscillations in the reflection signal. In contrast to this, it is interesting that the distinct but not very clearly defined structure of oscillations in the reflection curve appears right from the start after the deposition of the stripe. Their appearance is not very consistent in structure in comparison to the well defined set of reflection resonances appearing later in the spreading at approximately 2100 seconds (35 minutes). These oscillations may indicate a possible similarity to the peaks present after the first attenuation maxima of the double transit. At approximately 2100 seconds the double transit signal reaches its maximum signal attenuation. Immediately after the transit signal starts to recover. It takes approximately 20 minutes for the signal amplitude to regrow to a signal level of 15 arbitrary units which is 4.5 arbitrary units above the maximum attenuation point of the double transit signal. It is notable that once this turning point has been reached the set of well defined and nicely structured

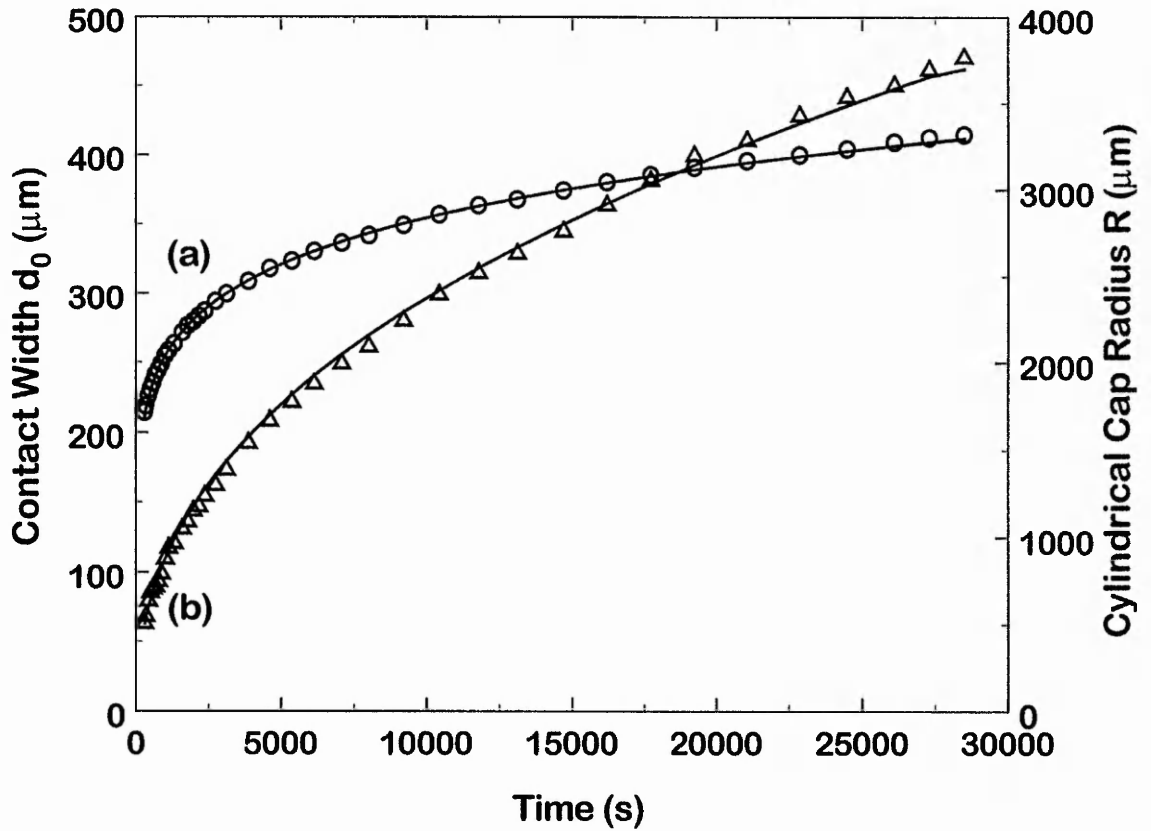


**Fig. 4.11** Contact width,  $d_0$ , graph (a) and cylindrical cap radius,  $R$ , graph (b) for the experiment in Fig. 4.10 using 33 stripe images are well fitted by the predicted power laws (solid curves).

peaks in the reflection appear and continue to oscillate well to the end of the experiment. The actual measurement time of the spreading is determined by the recording time of the video tape and this is limited to eight hours for an uninterrupted observation. A significant difference between this result and results demonstrated in e.g. Fig. 4.6 is that the double transit (Fig. 4.10) shows exactly one significant attenuation resonance peak of asymmetric shape. After the recovery of the double transit the signal gradually attenuates exponentially right to the end of the experiment. Contrasting this with Fig. 4.6 the appearance of a second attenuation resonance in the double transit means that the reflection also vanishes at this point in time. When the double transit regrows in signal amplitude the reflection signal does mimic this trend, but strong reflection resonances seem not to reappear. The attenuation behaviour of the transit signal appears to affect the oscillatory behaviour of the reflection. The absence of this attenuation maxima in Fig. 4.10 allows the oscillations to persist up to the end of the observation time. In both reflection curves of Figs. 4.6 and 4.10 the existence of an envelope can be seen. When the transit signal starts to recover in amplitude the reflection follows this trend mirroring the course of the transit signal. The envelope follows precisely the same tendency of exponential decay as the trend of the transit signal. However the maximum peak amplitude of the reflection in both charts does not coincide with the attenuation minima in the double transit. In Fig. 4.10 the appearance of the largest peak in the reflection is appearing 1 hour 26 minutes later than the attenuation minima in the double transit which appears at approximately 50 minutes into the spreading. Whereas the time difference between the largest reflection peak and the local attenuation minima in the double transit in Fig. 4.6 is about 3 minutes 40 seconds. The graph in Fig. 4.10 is showing exactly six distinct oscillations superimposed on the exponentially decaying envelope of the reflection. The contact width for each of the main minima and maxima (peaks) in the reflection are indicated in micrometers.

## 4.5. Fluid Viscosity Dependence on SAW-Liquid Interaction

A comparison between four different experiments plotted against contact width,  $d_0$  are given in Figures 4.12 to 4.15. Each graph represents a different viscosity to investigate the viscosity dependence and the variation in characteristic speed of wetting. The speed alters significantly with viscosity. Fig. 4.12 shows an experiment where a 100,000 cSt viscosity oil wets the surface. The conversion of signal amplitude into attenuation due to liquid loading allows a better comparison of liquid attenuation with respect to SAW input power attenuation. Conversion charts for all four experiments are shown in the Appendix. The experimental conditions for the experiments, such as signal parameters for the electronics (pulse width, input power (RF-voltage), resonant frequency) were kept constant to allow a direct comparison of the different viscosities. In all experiments the pulse width was set to a pulse length of 400 ns with a repetition rate of 1 kHz. The resonant frequency was set in all four experiments to 168.8 MHz. In 90% of all conducted experiments for this particular device the centre frequency maintained a resonant frequency of 168.8 MHz. However, small variations in the resonant frequency of the sensor were possible, but varied only in a range between 168.6 MHz to 169.0 MHz. The experiments used an RF-voltage input of 500 mV peak-to-peak. This was necessary since high attenuation, caused by fluid damping was anticipated. The attenuation in the transit signals can be expected to depend on the mass loading per unit area of the surface. All experiments used the fitted time dependence of the contact width,  $d_0$  and the cylindrical cap radius,  $R$  and estimates from these parameters following the power laws allowed the two remaining parameters  $\theta$  and  $h_0$  to be calculated. A conversion from the mean value produced by the peak amplitude of the diodes (mV) into attenuation (dB) was performed.

In Fig. 4.12 after the deposition, the fluid advances to either side towards the transducers. Immediately the appearance of a strong reflection having a larger signal amplitude than the decaying double transit signal is visible. The decay time from the start of the stripe deposition to the first strong attenuation

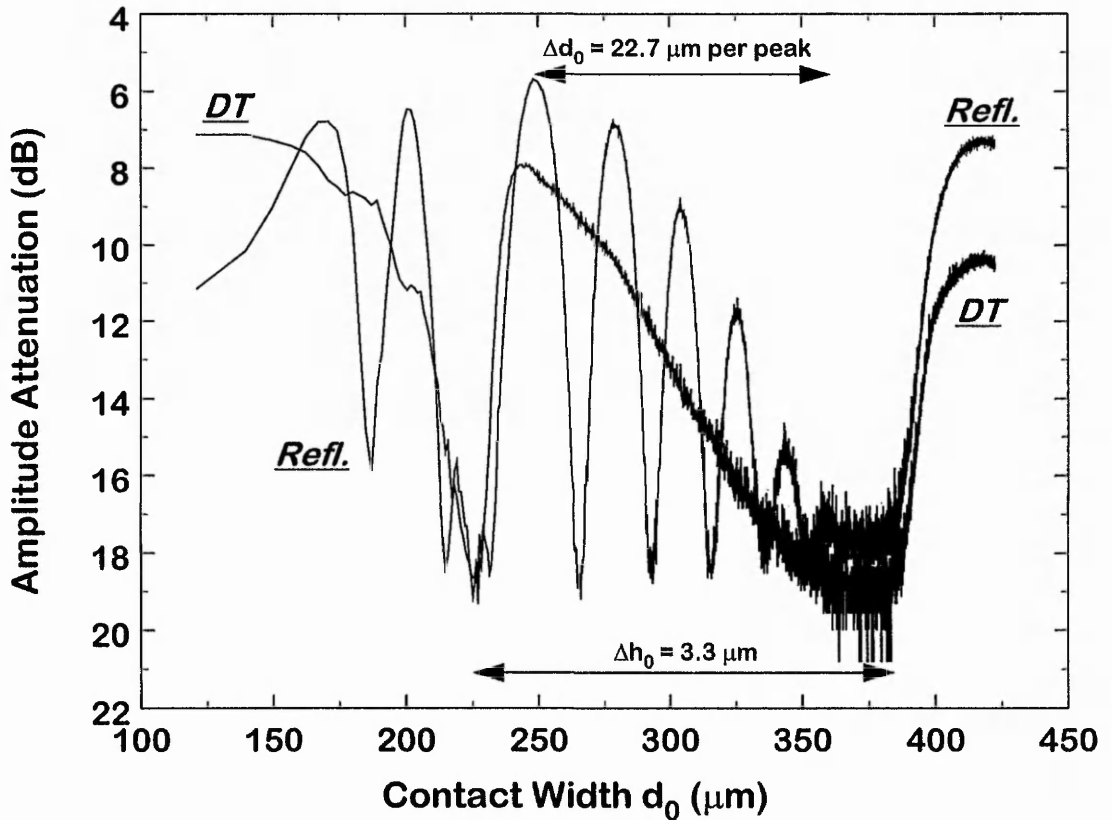


**Fig. 4.12** The acoustic trends during the spreading of a 100,000 cSt PDMS oil. The two signals are decreasing steadily with time showing an maximum of attenuation of the order of 19 dB. The double transit signal has two distinct attenuation maxima when the stripe progressively advances from 225  $\mu\text{m}$  to 378  $\mu\text{m}$ . The reflection shows six well defined oscillations corresponding to a change in  $d_0$  of 113.5  $\mu\text{m}$  from the first peak to the last peak.

of both signals is about 7 minutes and corresponds to an initial width of 225  $\mu\text{m}$ . In the same period two strong resonance peaks in the reflection signal are observable followed by two, considerably smaller peaks. It takes around 4.5 minutes until the double transit recovers to a level of 7 dB in attenuation with respect to the unloaded surface. The double transit then gradually decays to a second large attenuation maxima within a time of 4 hours and 20 minutes giving a maximum of 19 dB attenuation. The stripe advances in that time to a width of 378  $\mu\text{m}$ . After the recovery of the double transit signal at the first attenuation maxima, six well defined and distinct peaks appear in the reflection signal. Their shape and formation as well as their trend is much clearer defined compared to the structure seen in the first seven minutes of the spreading. At the beginning of the first peak the contact width,  $d_0$  is about 232  $\mu\text{m}$ , increasing to 365  $\mu\text{m}$  at the end of the last peak in the series. At the same time period  $R$  increases from around 763  $\mu\text{m}$  to 2873  $\mu\text{m}$  at the sixth peak.  $\theta$  decreases from 8.7° to 3.6° and the height,  $h_0$  decreases from 8.8  $\mu\text{m}$  to 5.7  $\mu\text{m}$ . The time period for the progressing reflection resonances in the reflection signal is 2 hours and 43 minutes which is considerably shorter than the actual time period for the two attenuation maxima in the double transit. The second attenuation maxima occurs 1 hour 32 minutes after the last observed reflection peak which appears approximately 2 hours 47 minutes in the wetting. The horizontal axis in Fig. 4.12 has been converted using the fitted time dependence of the contact width,  $d_0$  as deduced from the optical information obtained during the course of spreading. The fit was performed using 42 images and gave power law relations of  $d_0 = 99.95 (t-80)^{1/7.13}$  and  $R = 65.69 (t-80)^{1/7.33}$ . These give a total contact width change for the six observed peaks of 113.5  $\mu\text{m}$  giving an average peak to peak change in width of approx. 22.7  $\mu\text{m}$ . Separations of adjacent peaks start with a value of 30.6  $\mu\text{m}$  between the first and the second peak in the spectra and then decrease systematically to 17.7  $\mu\text{m}$  between the fifth and the sixth and last observed peak. In this time period the height is decreasing from 8.3  $\mu\text{m}$  to 5.8  $\mu\text{m}$  and the contact angle decreases from 7.6° to 3.7° respectively. The changes in height starting at a stripe width of 225  $\mu\text{m}$  (at the peak tip of the first attenuation maxima for the double transit), and measured up to the second attenuation maxima is about 3.3  $\mu\text{m}$  as indicated in Fig. 4.12

by the arrow at the bottom of the graph. The contact width has increased by  $153\ \mu\text{m}$  which is notably larger than one acoustic wavelength. Initially when the stripe was deposited its width started with a length of  $120\ \mu\text{m}$  and increased up to  $422\ \mu\text{m}$ . In the same time the contact angle decreased from around  $20.0^\circ$  to a value of  $2.8^\circ$  and the height decreased from  $13.4\ \mu\text{m}$  to  $5.0\ \mu\text{m}$ .

Fig. 4.13 shows the spreading of a 30,000 cSt PDMS oil and plots fluid attenuation of the three signals, single transit, double transit and reflection, versus changes in contact width,  $d_0$ . Here the later stages of the spreading process takes up a major part of the wetting. However most of the important pattern signifying oscillations in the reflection and the maxima in attenuation of the transit signals is within a time of approx. 4.5 hours. The exact duration is dependent of the characteristic speed of the fluid and the stripe width of the fluid at the start of deposition. The graph shows the same signature, as all previously discussed graphs. An ill defined first section for the reflection signal exists due to the slow sampling rate reducing significantly the amount of possible data points to be taken and a high initial spreading rate. The second part, in between the attenuation resonance peaks of the transit signals, shows a clear signal pattern in trend in the reflection signal. The third part, following subsequently after the second resonance peak of the transit signals, shows possible oscillations superimposed on the course of the reflection signal. These oscillations are not as clear and structured as this can be seen in the peak structure (seven peaks) appearing in the middle section of the reflection signal. The transit signals are consistent in trend and mirror each other in signature and attenuation. The existence of superimposed oscillations is much clearer in the single transit with one distinct trough labelled as T and one peak close to the attenuation maximum labelled as P. The separation of the two adjacent peaks reveals a change in contact width,  $d_0$  of around  $12.3\ \mu\text{m}$  which is close to half of an acoustic wavelength of the SAW resonance frequency. The peak to peak distance between minimum T and maximum P in the single transit can only be approximated since the formation of the trough (T) is weaker than for the peak (P) close to the attenuation maxima. The envelope of the reflection follows exactly the decay pattern of the transit signals. The first attenuation resonance peak occurs at 3 minutes 40 seconds and introduces a set of

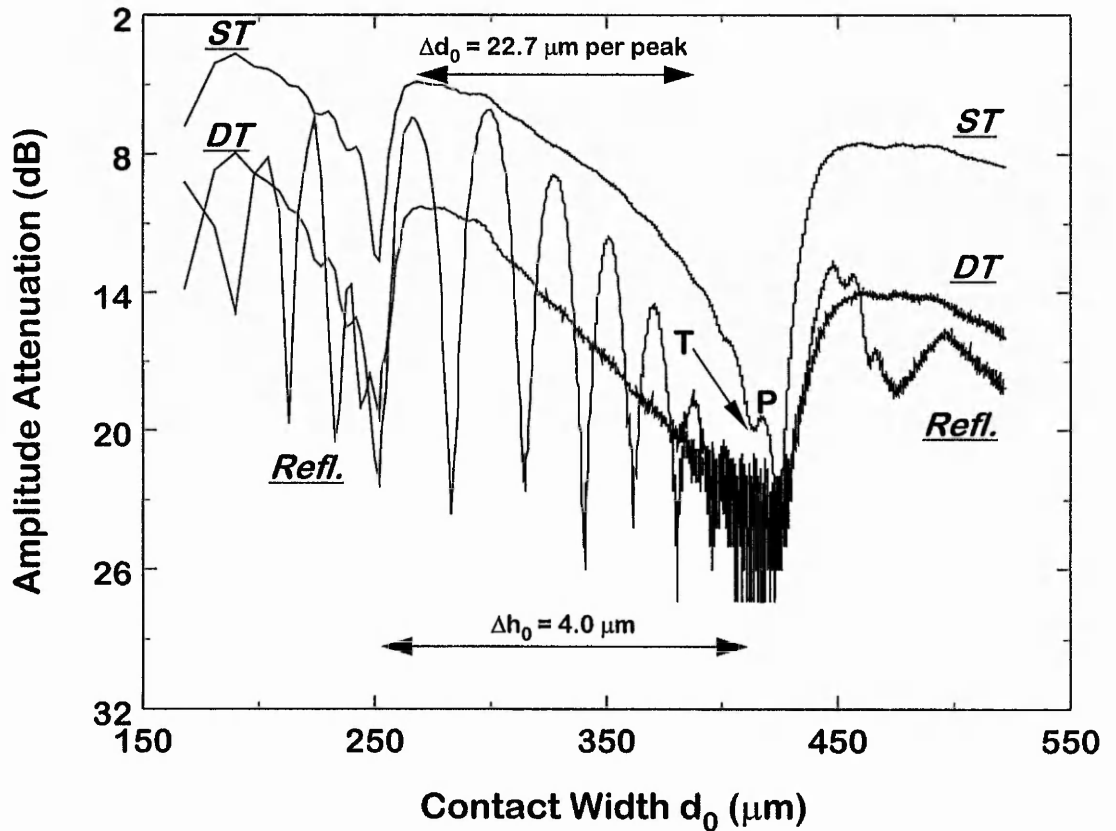


**Fig. 4.13** The acoustic signal trends during the spreading of a 30,000 cSt PDMS oil. The appearance of the two attenuation maxima in the transit signals (ST single transit and DT double transit) within a time period of 2 hours is considerable less as the time period in Fig. 4.12 (4 hours). Significant is the existence of the two peaks labelled with T for the minima and P for the maxima. The separation of the two peak tips is around 12.3  $\mu\text{m}$ , which is close to half an acoustic wavelength.

7 oscillations in the reflection signal straight after the transit signals start to regrow in magnitude. The initial contact width at the bottom tip of the first peak in the reflection signal in the middle section is 252  $\mu\text{m}$  and increases to 406  $\mu\text{m}$  within 1 hour and 28 minutes. The second attenuation peak in both transit signals appears at approximately 2 hours and this is considerably shorter in time as described for Fig. 4.12. The increase in contact width of the stripe over the seven oscillations in the SAW reflection signal is 136.1  $\mu\text{m}$  giving an average peak to peak separation of approximately 22.7  $\mu\text{m}$ . The cylindrical cap radius increases from 871  $\mu\text{m}$  to 3807  $\mu\text{m}$  over the seven peaks (middle section) and the height,  $h_0$  and contact angle,  $\theta$  decrease during the same period (1 hour and 28 minutes) from 9.1  $\mu\text{m}$  ( $8.3^\circ$ ) to 5.4  $\mu\text{m}$  ( $3.1^\circ$ ) respectively. It is interesting that the average peak to peak distance and the increase in width of the middle section peaks in comparison to Fig. 4.12 is very close although the time variation between these two graphs is considerably different. The fits for the contact width and the cylindrical cap radius are  $d_0 = 112.08 (t+5)^{1/6.70}$  and  $R = 59.98 (t+40)^{3/6.23}$ . The conversion chart for the contact width,  $d_0$  as a function of time can be found in the Appendix. The first and the second attenuation maxima for the transit signals occur at a contact width of about 252  $\mu\text{m}$  and 425  $\mu\text{m}$ , respectively, representing a relative decrease in height of 4.0  $\mu\text{m}$ . The contact angle reduces from  $8.3^\circ$  to  $2.8^\circ$  respectively. At this time the cylindrical cap radius evolves from 871  $\mu\text{m}$  to 4412  $\mu\text{m}$ . The third and last section of the double transit, which is a total of approximately 6 hours long, starting at the second attenuation maximum. The radius grows in the 6 hours of the order of 3985  $\mu\text{m}$  in size in comparison to an increase in size of  $R$  of 3541  $\mu\text{m}$  in the middle section interval between the two attenuation resonances of the transit signals.

With the introduction of a 30,000 cSt oil the characteristic speed of the fluid increased by a factor of three. However as the results have shown, this had no significant impact in the structure and characteristic appearance of any of the three acoustic signals. A reduction in viscosity of factor ten would mean that the velocity of the spreading would be ten times higher. Table 3.4 in Chapter 3 presents exactly an increase in  $v^*$  from 0.220  $\text{mm s}^{-1}$  to 2.207  $\text{mm s}^{-1}$  from a 100,000 cSt viscous oil to a 10,000 cSt oil which matches the changes

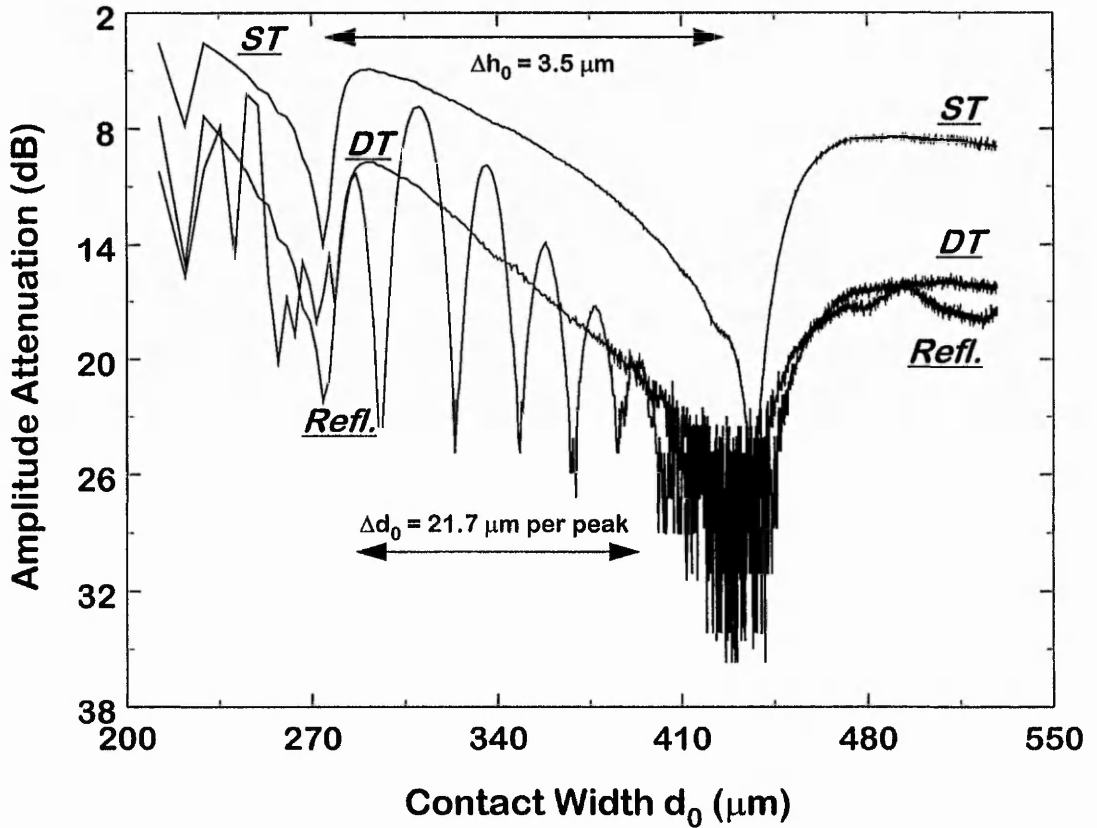


**Fig. 4.14** The acoustic signal trends during the spreading of a 10,000 cSt PDMS oil. The total separation of the six peaks in the reflection signal (108.4  $\mu\text{m}$ ) is close to that in Fig. 4.12. Interesting is that the reduction in viscosity alters the duration of the middle section between the two attenuation maxima. The changes are significant and change from 4 h (Fig. 4.12) to 1 h (Fig. 4.14).

in viscosity of a factor of ten and was anticipated since  $v^* = \gamma / \eta$  is mainly dependent on  $\eta$  for these oils. This is also reflected in the appearance of the attenuation maxima which are separated in Fig. 4.14 by about 1 hour and 5 minutes. This is again shorter than the time difference in Fig. 4.13 and reflects the characteristic speed of the fluid. The stripe increases from 274  $\mu\text{m}$  to around 437  $\mu\text{m}$  respectively and is close to the contact width evolution in Fig. 4.13. The time dependent fits for the contact width,  $d_0$  and the cylindrical cap radius,  $R$  for this graph are calculated from 24 images giving for the 1/7<sup>th</sup> power law a contact width relation of  $d_0 = 128.9 (t+30)^{1/6.81}$  and for the 3/7<sup>th</sup> power law a cylindrical cap radius relation of  $R = 106.5 (t+30)^{1/6.62}$ . The graph in Fig. 4.14 shows six well defined reflection resonance peaks representing a total separation from the first to the last peak of 108.4  $\mu\text{m}$  giving an average peak to peak separation of 21.7  $\mu\text{m}$  and is close to the value deduced from the data of Fig. 4.12. The time interval for the six peaks is about 36 minutes 55 seconds (first part of the middle section) which compares to 28 minutes and 5 seconds for the rest of the spreading, in the second part of the middle section, up to the second attenuation maximum. This suggests that the oscillation (six peaks) stop to appear at about half of the time in the middle section between the two attenuation maxima. The cylindrical cap radius,  $R$  increases to 3633  $\mu\text{m}$ . At the start of the reflection resonances,  $R$  is 1151  $\mu\text{m}$  indicating that with falling viscosity,  $R$  seems to start at larger values. At this instant in time the contact width has increased by 126  $\mu\text{m}$  to a value of 405  $\mu\text{m}$ . Contact angle,  $\theta$  and height,  $h_0$  decrease from 7.0° (8.5  $\mu\text{m}$ ) to 3.2° (5.6  $\mu\text{m}$ ), respectively. The height reduces between the two attenuation resonance peaks from 8.6  $\mu\text{m}$  to 5.2  $\mu\text{m}$  representing a reduction in height of 3.5  $\mu\text{m}$ . It is noticeable that the height only decreases by 0.4  $\mu\text{m}$  between the last observed reflection peak and the second attenuation maxima despite the same time interval for the first part of the middle section. The contact angle starts after deposition of the stripe at about 12.0° and reduces during the course of the experiment to 1.8°. During that time the contact width has increased from <222  $\mu\text{m}$  to 529  $\mu\text{m}$  and the height reduces from >11  $\mu\text{m}$  to 4.2  $\mu\text{m}$ . The cylindrical cap radius,  $R$  increases, during the 1 hour and 5 minutes interval of the middle section from 1094  $\mu\text{m}$  to

4628  $\mu\text{m}$  and in the third section after the second attenuation resonance peak,  $R$  increases by a further 3668  $\mu\text{m}$  which represents the remaining two hours. After a recording time of approximately four hours the cylindrical cap radius,  $R$  is finally grown to a value of 8296  $\mu\text{m}$ . Comparing the difference in cylindrical cap radius in the middle section with the cylindrical cap radius in the third section reveals a very similar increase in radius in the two sections, middle section and third section, and differs only by about 135  $\mu\text{m}$ .

A reduction in viscosity of factor 100 in comparison to the 100,000 cSt oil shows no significant changes in the overall structure of the SAW signals. The graph in Fig. 4.15 presents the data obtained from the dynamic evolution of a 1,000 cSt PDMS oil. This oil spreads about 100 times faster than the 100,000 cSt oil and is therefore much more delicate to apply to the surface. Energetically, the liquid prefers to chain up as droplets on a fibre used for deposition. This significantly influences the shape of an applied stripe. Generally most of these stripes are disrupted in continuity along the stripe length. It required significant practice to apply this oil to the SAW substrate. However, as presented in Fig. 4.15 a successfully deposited stripe produces a similar pattern of SAW-liquid response in comparison to the other experiments. It is to note that despite a 100 times higher characteristic speed,  $v^*$  the pattern are precisely repeated in trend. The patterns include asymmetric attenuation resonances in the double transit signal and reflection resonances of a particular number of consistent peaks as observed in all the other results. The existence of six well defined oscillations in between the two attenuation maxima (double transit) starting at 306  $\mu\text{m}$  (contact width increases to 449  $\mu\text{m}$  at the end of the last oscillation) is astonishing and suggests, that such viscosity changes do not influence the structure of the reflection. The separation of the two attenuation maxima in the double transit is about 14.5 minutes and is about 18 times shorter than the separation in Fig. 4.12. The six oscillations cease at around half the time (7 minutes and 39 seconds) in between the two attenuation maxima (attenuation resonances). The cylindrical cap radius at the beginning of the oscillations is 1468  $\mu\text{m}$ , which confirms the relation between falling viscosity and increasing values of  $R$ . The reduction in height is of the order of 2.5  $\mu\text{m}$  to a height of  $h_0 = 5.5 \mu\text{m}$  at the last oscillation minima. Comparing this with the

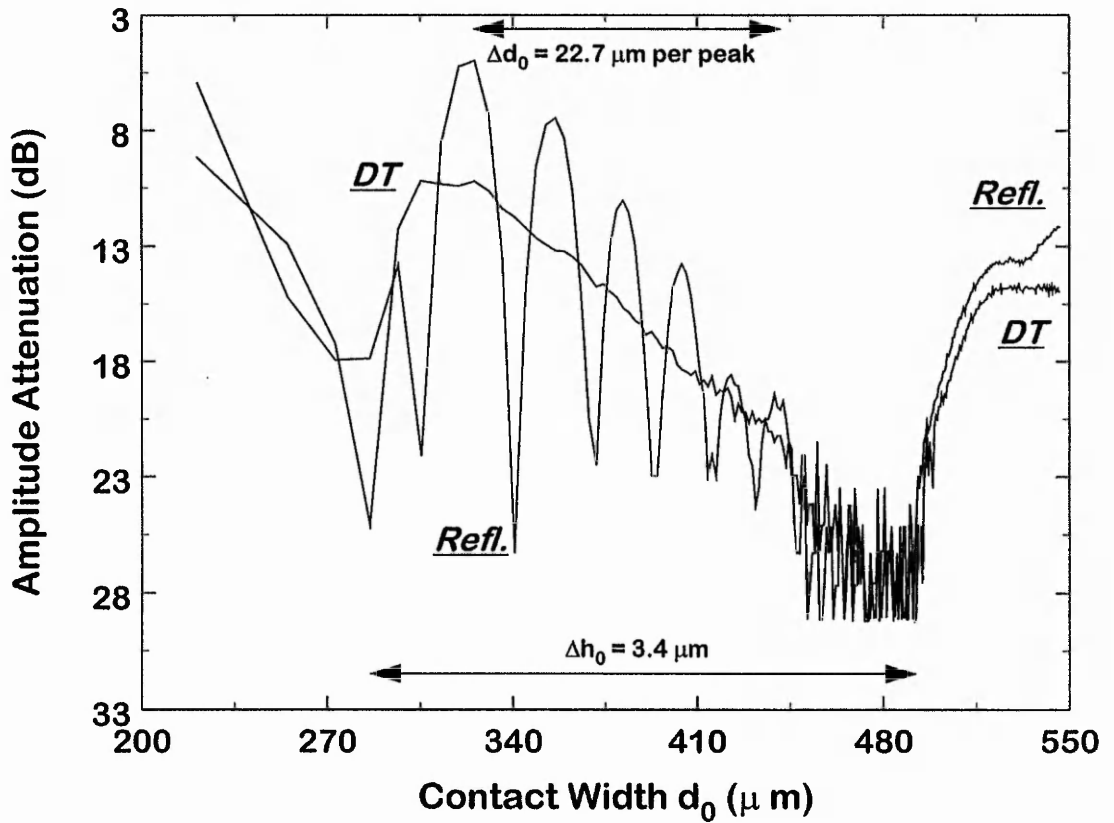


**Fig. 4.15** The acoustic signal trends during the spreading of a 1,000 cSt PDMS oil. The pattern of strong oscillations superimposed to the overall trend of an exponential decay in the reflection is apparent. The period between the attenuation maxima in the double transit (14.5 min) is 18 times shorter in comparison to the separation of attenuation maxima in Fig. 4.12.

other three results shows similarities in height at the last oscillation minima varying from 5.4  $\mu\text{m}$  (Fig. 4.13) to 5.7  $\mu\text{m}$  (Fig. 4.12) (see also Table 4.1 (a) - (c)). It is noticeable, that in between the two attenuation maxima the contact width increases from 286  $\mu\text{m}$  to 492  $\mu\text{m}$  which is close to the increase of the contact width in Fig. 4.9 and Fig. 4.10. The average peak to peak separation of the six reflection peaks is 22.7  $\mu\text{m}$  giving a total length (first peak to the last peak) of 113.4  $\mu\text{m}$ . The separation of these peaks decreases systematically from 30.5  $\mu\text{m}$  to 16.3  $\mu\text{m}$ . This indicates that the average separation is close to the SAW wavelength as observed in all previously presented results. The complete run was finished in about 29 minutes and 14 seconds and this is notably shorter than the other experiments. Other experiments using the 1,000 cSt oil have shown similar trends in the acoustic signals and confirm that the majority of acoustic events were happening within a time span of approximately 30 minutes to 1 hour. The stripe initially begins with a width of 255  $\mu\text{m}$  and increases to 546  $\mu\text{m}$ . The height and the contact angle reduces from 8.8  $\mu\text{m}$  ( $7.9^\circ$ ) to 4.4  $\mu\text{m}$  ( $1.8^\circ$ ) which starts with lower values than this is the case for the other experiments. The cross-sectional parameters have been determined to be  $d_0 = 172.4 (t+5)^{1/6.48}$  and  $R = 233.7 (t+10)^{3/6.24}$ .

## 4.6. High Degree of Similarity in Acoustic Signals

### 4.6.1. Comparison of Signal Trends of Two Different Double Transits and Two Reflection Signals

To show the close similarity in structure and peak position, changes in the double transit signal and the reflection signal of two individual runs over an 8 h period have been plotted versus contact width,  $d_0$  to compare directly the trend of the graphs. In Fig. 4.16 the trend of the two double transit signals are compared. Both graphs represent the spreading of a 100,000 cSt oil maintaining the same experimental conditions as for Fig. 4.12 to Fig. 4.15. Graph (a) has been shifted by - 5.5 dB and graph (b) by + 17.0 dB to

accommodate both graphs and increase clarity for comparison. The fit to the power laws for curve (b) is extremely good and gives  $d_0 = 94.1 (t+14.9)^{1/7}$  and  $R = 58.8 (t-247.1)^{1/7}$ , whereas for curve (a) the fits show a marginal deviation from the  $1/7^{\text{th}}$  and  $3/7^{\text{th}}$  exponent, with  $d_0 = 92.8 (t+5)^{1/6.90}$  and  $R = 46.9 (t+5)^{1/6.72}$ . Comparing the contact width of graph (a) with graph (b) one can see that the evolution of the contact width,  $d_0$  is very similar in both experiments. The first attenuation resonance maxima (Fig. 4.16) of curve (a) appears at  $t = 275$  seconds and the contact width,  $d_0$  of the stripe is at this point in time  $211 \mu\text{m}$ . After a time interval of 2 hours and 52 minutes the second attenuation maxima appears and the contact width has grown in this time period to approximately  $358 \mu\text{m}$ . Comparing this with curve (b), here the first attenuation maxima appears at about  $225 \mu\text{m}$  and the contact width,  $d_0$  increases to a value of  $352 \mu\text{m}$  at the peak tip of the second attenuation maxima. It is interesting that the spreading process in this time interval is only seven minutes (2 hours and 45 minutes) shorter than for curve (a) (2 hours and 52 minutes). In the same time period the cylindrical cap radius,  $R$  of curve (a) increases from  $592 \mu\text{m}$  to approximately  $3015 \mu\text{m}$  whereas at the same time height,  $h_0$  and contact angle,  $\theta$  decreases from  $9.5 \mu\text{m}$  ( $10.3^\circ$ ) to  $5.4 \mu\text{m}$  ( $3.4^\circ$ ), respectively to compensate the changes in contact width since the stripe volume is constant during the spreading process. If we follow the changes in all geometrical parameters of curve (b) (Fig. 4.16), small deviations are evident compared with curve (a). The cylindrical cap radius at  $t = 441$  seconds (first attenuation resonance peak) is  $R = 562 \mu\text{m}$  and increases in 2 hours and 45 minutes (second attenuation maxima) to a value of  $3056 \mu\text{m}$ , which is close to the value obtained for curve (a). More significant deviations are apparent in height and contact angle. Here  $h_0$  starts with  $12.7 \mu\text{m}$  in comparison to  $9.5 \mu\text{m}$  for curve (a). However, both graphs approach a fairly similar value at the second attenuation maxima, which is for curve (a)  $5.4 \mu\text{m}$  and for curve (b)  $5.1 \mu\text{m}$ . Also the deviation in contact angle at the tip of the first attenuation resonance peak of the two graphs is more significant. For curve (b)  $\theta$  starts with  $12.8^\circ$  and systematically decreases to  $3.3^\circ$  at the second attenuation maxima whereas  $\theta$  for curve (a) is considerably smaller and has a value of  $10.3^\circ$ , but approaches an almost similar value of  $3.4^\circ$  at the second asymmetric resonance peak. However, if we

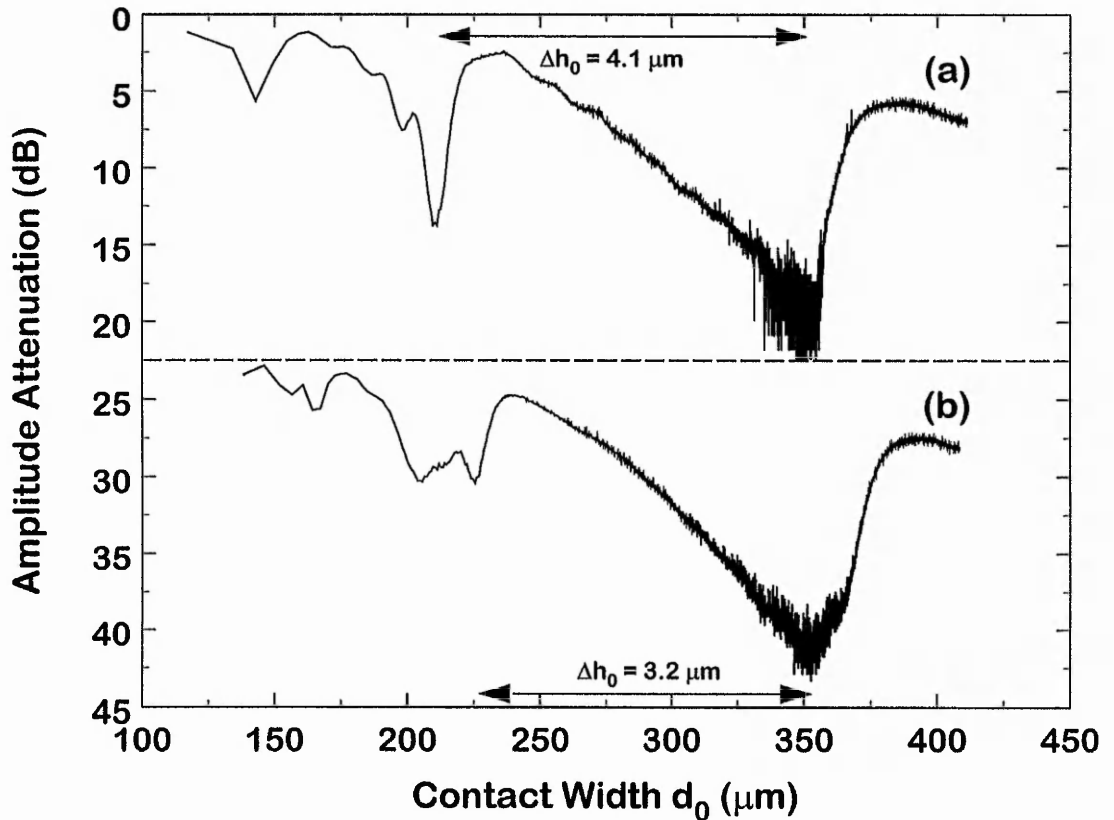


**Fig. 4.16** To compare the trend of the double transit signals of a spreading stripe of oil of 100,000 cSt, two individual experiments have been plotted in the same graph sheet. To make the comparison easier curve (a) is shifted upwards by 5.5 dB and curve (b) has been shifted downwards by 17.0 dB. The time interval between the two attenuation resonances of asymmetric shape differs only by 7 minutes and a similar cross-sectional area of  $1.3 \times 10^{-9} \text{ m}^2$  may explain the similar overall signal trend of both curves.

determine the average cross-sectional area of both experiments for the whole course of spreading, we get a similar value of approximately  $1.3 \times 10^{-9} \text{ m}^2$  for the two graphs. This is well confirmed by the trends seen in Fig. 4.16. The appearance of the attenuation resonance peaks at almost similar time intervals and the good similarity in contact width and cylindrical cap radius suggests that a close similarity in stripe volume between two different experiments produces similar signal response and therefore a similar structure in signal trend.

The formation of a series of reflection resonances from both experiments is presented and compared in Fig 4.17. The results compare the reflection resonances, obtained from the same set of experimental results as discussed for Fig. 4.16. The oscillatory changes in acoustic amplitude of the reflection signal in both graphs in Fig. 4.17 seem to start almost at the same value in contact width. To enable an easier comparison in trend and structure of the two runs, curve (a) has been shifted upwards by 3 dB and curve (b) is shifted downwards by 15 dB. The contact width of the stripe is for graph (a) at the first peak of a set of five consecutive peaks is about  $239 \mu\text{m}$  and for graph (b) about  $243 \mu\text{m}$  which represents a difference of  $4 \mu\text{m}$ . Both stripes spread to about  $409 \mu\text{m} \pm 0.2 \mu\text{m}$  at the end of the experiment. Detailed examination of the separation of adjacent peaks shows a large variability in contact width changes. The separation of these peaks decreases systematically from  $27.9 \mu\text{m}$  to  $14.3 \mu\text{m}$  for curve (a) and  $29.9 \mu\text{m}$  to  $15.6 \mu\text{m}$  for curve (b). However, the average separation of the five successive peaks is  $21.6 \mu\text{m}$  for (a) and  $22.7 \mu\text{m}$  for (b) and this is again close to the Rayleigh wavelength of  $22 \mu\text{m}$ . The reflection shows a systematic series of oscillations whose overall amplitude is being modulated on a longer time scale. This modulation period corresponds to a reduction in height of around  $4.1 \mu\text{m}$  in (a) and  $3.2 \mu\text{m}$  in (b), respectively.

#### 4.6.2. The Influence of the Stripe Geometry on the Signal Structure

In contrast to Fig. 4.16 and Fig. 4.17, the two separate results shown in Fig. 4.18 and Fig. 4.19 commenced under the same conditions as previous

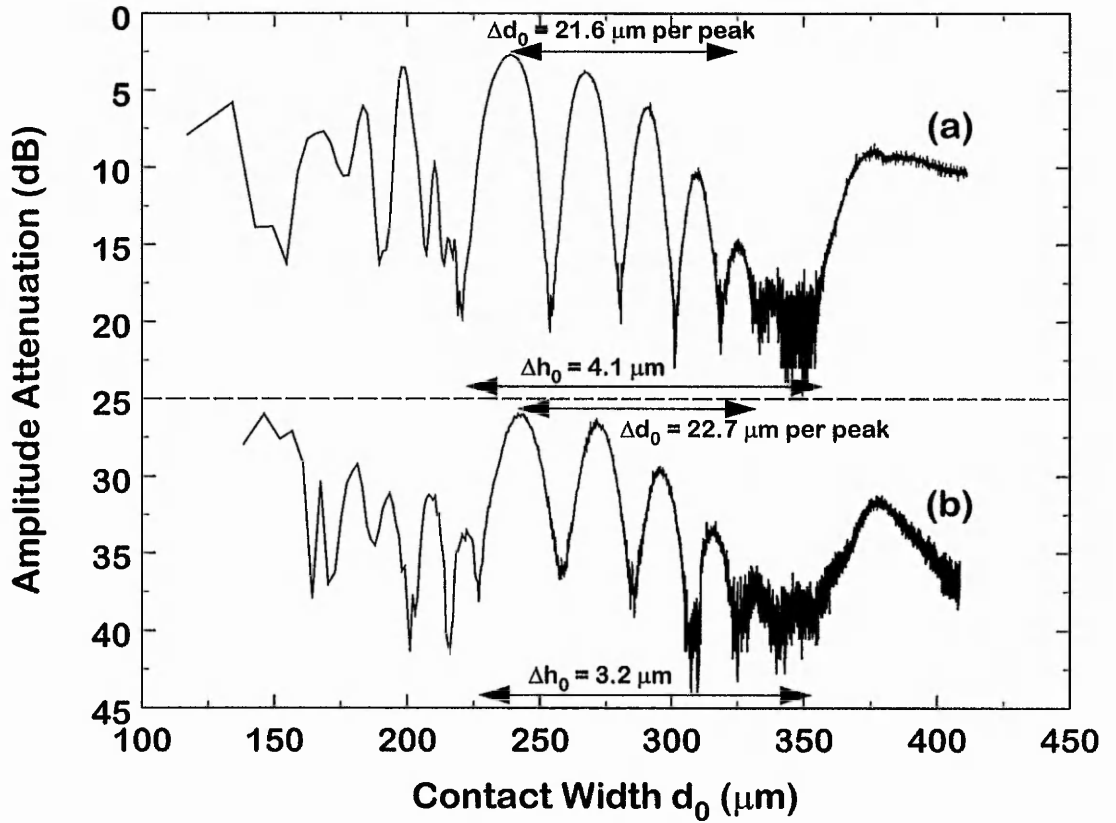


**Fig. 4.17** In the reflection data, obtained from the same experiments, as discussed for Fig. 4.16, a comparison of the time dependent power laws for the contact width,  $d_0$  shows a close similarity for both graphs. To accommodate both curves in the same graph sheet curve (a) is shifted by -3 dB and curve (b) by +15 dB.

experiments gave not only a similar pattern of reflection and attenuation, but also show extremely similar absolute values in magnitude changes in amplitude between the two runs. Fig. 4.18 and Fig. 4.19 presents, the overlay of two double transits (Fig. 4.18) and the overlay of two reflection signals (Fig. 4.19) for two separate experiments. In order to present the extremely good similarity, one of the graphs has been plotted using a dashed line. It is interesting that both curves (Fig. 4.18) are following almost exactly the same trend. However deviations are present in the subsidiary peak structure superimposed on the back slope after the first attenuation maximum. It seems that both curves follow exactly the same trend up to the first attenuation maximum with minimal differences in magnitude of the amplitude. After recovering to a local attenuation minimum, curve (b) (solid line) shows asymmetric behaviour in back slope oscillations compared to curve (a). However, since the definition in shape of these back slope oscillations are not very precise the asymmetric behaviour observed at the later stage starts to overlap and a definite separation at the approach of the second attenuation maximum is difficult. In particular the exact overlap of the second attenuation maxima at the same point in time is remarkable and  $d_0$  at the first maximum is  $208 \mu\text{m}$  for curve (a) and  $209 \mu\text{m}$  for curve (b). However the appearance of the first maximum on the time axis varies. The time match for the contact width for curve (a) corresponds to 147 seconds whereas for curve (b)  $t = 275$  seconds. The variation in time is significant but contrasting this with the actual surface area coverage, curve (a) initially starts with a wider stripe and therefore sweeps through the first attenuation maxima at an earlier stage. It is interesting that all geometrical parameters reflect this identically and suggest that the stripe cross sectional shape is identical at this particular point in time.  $R$  has been estimated to  $576 \mu\text{m}$  for curve (a) and  $550 \mu\text{m}$  for curve (b) within the accuracy of the optical observation. The evolution of the stripe to the second attenuation maximum is remarkably similar and the estimation of the geometrical parameters at the second attenuation maximum reveals that deviations are marginal. The contact width,  $d_0$  has evolved in 3 hours to  $352 \mu\text{m}$  for curve (a) and for curve (b) to  $356 \mu\text{m}$  (2 hours and 52 minutes) (see Table 4.1 (a) for comparison).

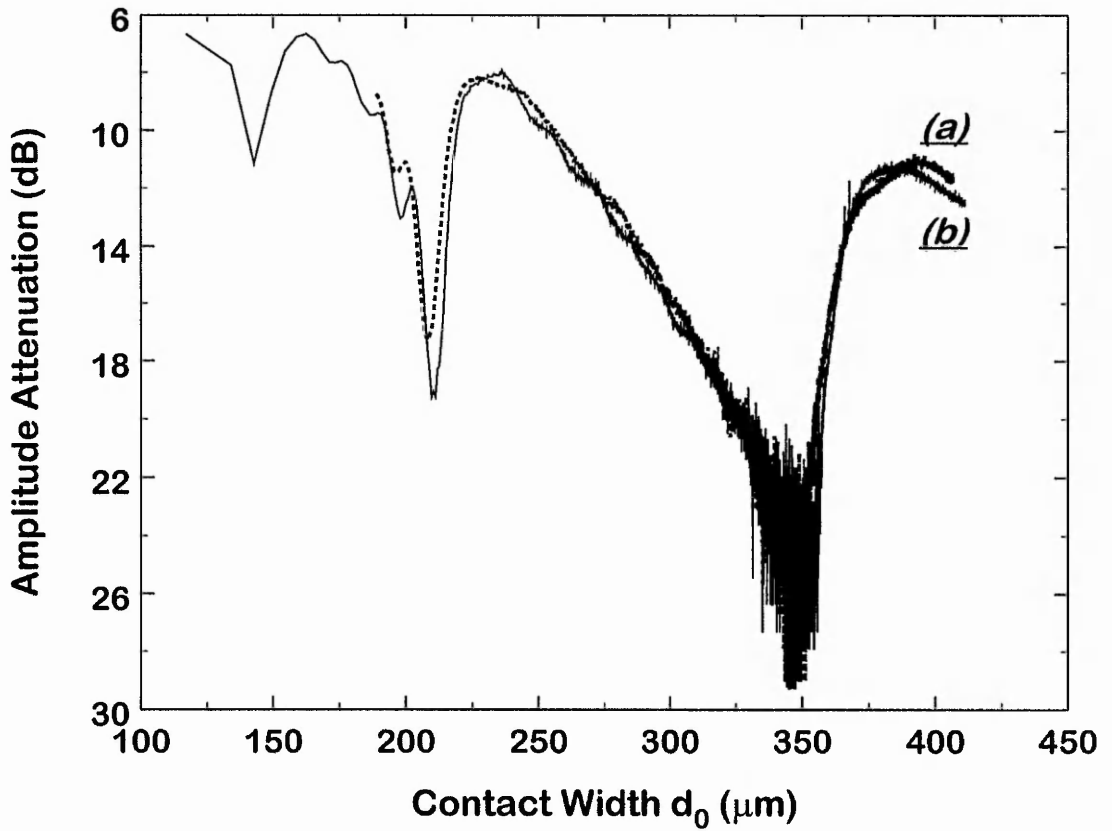


**Fig. 4.18** The course of the double transit curves for two 100,000 cSt experiments, curve (a) is shown as dotted line and curve (b) is shown as solid line and these curves are extremely similar. Both graphs follow exactly the same trend. Even the level of attenuation is almost identical.

An overlay of the two reflection graphs (Fig. 4.19) reveals an extremely good quantitative agreement. The consistency with which the two curves match each other is extremely high, apart from the deviation at the end of the spreading in the third section. In fact, if the deviation after the second attenuation maximum did not occur it would be hard to distinguish the two plots. Even the trend of both curves before the start of the five distinct peaks is entirely similar. The appearance of the five peaks in relation to the evolving stripe width is identical and the separation for the peaks is reasonable close, in contrast to the accuracy of the optical measurements and herein resulting fits. The separation of reflection resonances for curve (a) in Fig. 4.19 starts with 28.8  $\mu\text{m}$  peak to peak and reduces to 14.6  $\mu\text{m}$  for the last two peaks. The comparison with curve (b), where the two first peaks are separated by 27.9  $\mu\text{m}$  and reduces to 14.3  $\mu\text{m}$ , is close. The peak to peak average calculates for curve (a) to 21.0  $\mu\text{m}$  and for curve (b) to 21.6  $\mu\text{m}$ . The accuracy for the measurements is high and reflects the consistency of results throughout the whole series of experiments. Although, the percentage accuracy in width measurements is extremely high, the differences in width are only accurate to approximately  $\pm 3 \mu\text{m}$ . A full set of optical parameters and their time dependent relation can be obtained in Table 4.1 (a) - (c).

Qualitatively identical trends in the results are likely, since a good agreement of all geometrical parameters exist in the two experiments. In particular the calculation of the average cross-sectional areas, which has been determined for curve (a) to  $1.30 \times 10^{-9} \text{ m}^2$  and for curve (b) to  $1.29 \times 10^{-9} \text{ m}^2$  (see also Table 4.1 (a)), gives a good indication for the high similarity of the two different experiments and suggests that similar quantities of stripe volume spreading within the acoustic path of the sensor can produce identical results.

Table 4.1 (a) presents a summary of changes in the reflection signal between the attenuation maxima of the transit signals in dependence of different viscosities. Table 4.1 (b) gives a comparison between the different time dependent parameter for the reflection resonances in the middle section of Fig. 4.12 to Fig. 4.16 and Fig. 4.18 at the start of the resonances peaks at the foot of the peaks up to the last minima where the oscillations cease. Table 4.1 (c) deals with the comparison of the geometrical parameters

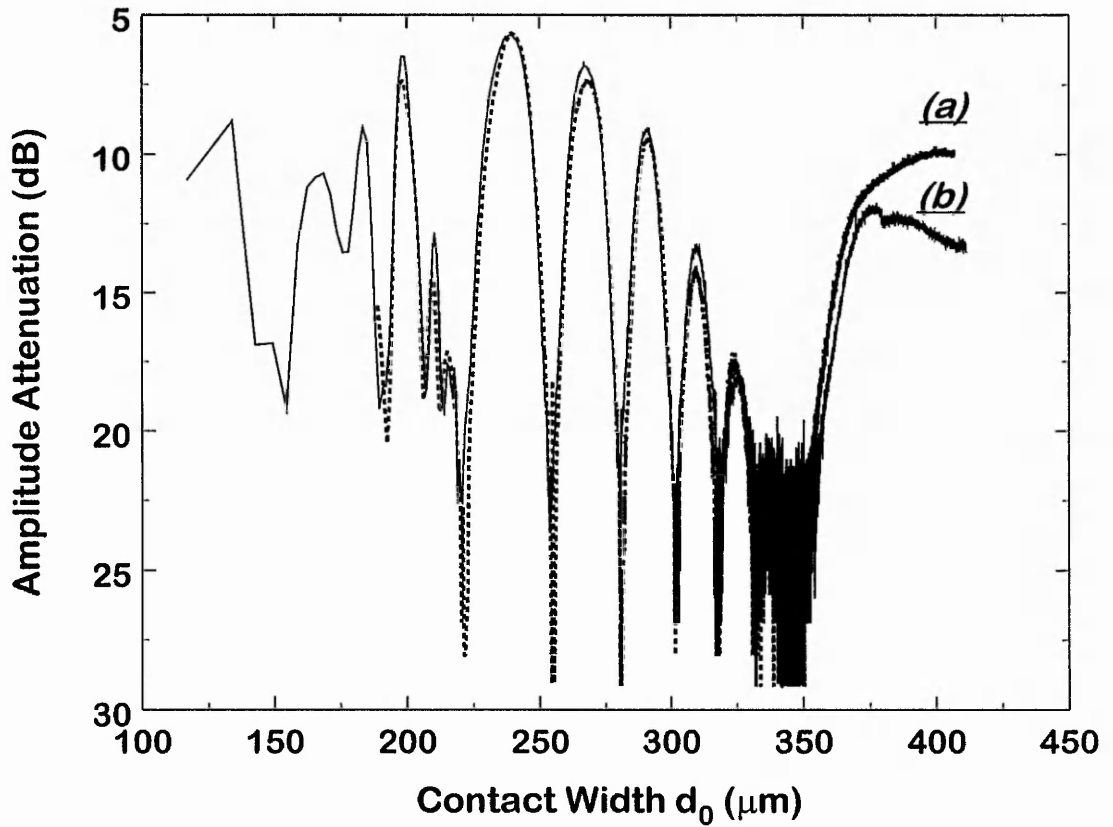


**Fig. 4.19** The overlap of the five consecutive peaks is remarkably similar. The average separation of the peaks (21.0  $\mu\text{m}$  for curve (a) and 21.6  $\mu\text{m}$  for curve (b)) differs only by 2.8% considering the accuracy of the optical measurement.

contact width,  $d_0$  and the cylindrical cap radius,  $R$  obtained from the optical observation of the different experiments.

**Table 4.1 (a)** Geometrical relation for reflection resonances in dependence of viscosity and changes of height and contact width of the stripe between attenuation resonances (double transit).

Fig.	$\eta$	No. Peak	$\Delta d_0$ of Peak	Av. Peak	$\Sigma \Delta d$ Peak	$\Delta d_0$ Max.	$\Delta h_0$ Max.	$\Delta t$ Att. Max.	Area CS*
4.12	100,000	6	30.6-17.7	22.7	113.5	153	3.3	4h 20m	1.40
4.13	30,000	7	33.8-13.7	22.7	136.1	173	4.0	1h 56m	1.50
4.14	10,000	6	24.1-18.3	21.7	108.4	163	3.5	1h 05m	1.56
4.15	1,000	6	30.5-16.3	22.7	113.4	206	3.4	14.5m	1.64
4.16/17 (a) <sup>1)</sup>	100,000	5	27.9-14.3	21.6	86.2	147	4.1	2h 52m	1.30
4.16/17 (b)	100,000	5	29.9-15.6	22.7	90.6	127	3.2	2h 45m	1.28
4.18/19 (a)	100,000	5	28.8-14.6	21.0	83.9	144	3.8	2h 58m	1.29
4.18/19 (b) <sup>1)</sup>	100,000	5	27.9-14.3	21.6	86.2	147	4.1	2h 52m	1.30
									x10 <sup>-9</sup>
	cSt		$\mu\text{m}$	$\mu\text{m}$	$\mu\text{m}$	$\mu\text{m}$			m <sup>2</sup>

CS\* = average cross-sectional area

<sup>1)</sup> using the same experimental data set.

**Table 4.1 (b)** Geometrical relations for reflection resonances (set of peaks - oscillations).

Fig.	$\eta$	$d_0$ Oscil.	$\Delta d_0$ Oscil.	$\Delta t$ Oscil.	$R$ Oscil.	$\theta$ Oscil.	$h_0$ Oscil.	$\Delta h_0$ Oscil.
4.12	100,000	232 - 365	133	2h 43m	763 - 2873	8.7 - 3.6	8.8 - 5.7	3.0
4.13	30,000	252 - 406	154	1h 28m	871 - 3808	8.3 - 3.1	9.1 - 5.4	3.7
4.14	10,000	279 - 405	126	36m 55s	1150 - 3633	7.0 - 3.2	8.5 - 5.6	2.9
4.15	1,000	305 - 449	144	7m 29s	1468 - 4616	6.0 - 2.8	8.0 - 5.5	2.5
4.17 (a) <sup>1)</sup>	100,000	221 - 334	113	1h 47m	679 - 2420	9.4 - 4.0	9.0 - 5.8	3.2
4.17 (b)	100,000	227 - 340	113	2h 05m	587 - 2732	12.1 - 3.6	9.4 - 5.3	4.1
4.19 (a)	100,000	222 - 333	111	1h 56m	705 - 2450	9.1 - 3.9	8.8 - 5.7	3.1
4.19 (b) <sup>1)</sup>	100,000	221 - 334	113	1h 47m	679 - 2420	9.4 - 4.0	9.0 - 5.8	3.2
	cSt	$\mu\text{m}$	$\mu\text{m}$		$\mu\text{m}$	$^\circ$	$\mu\text{m}$	$\mu\text{m}$

**Table 4.1 (c)** Geometrical fits for the contact width,  $d_0$  and cylindrical cap radius,  $R$ , obtained from the optical measurements for PDMS oils spreading on lithium niobate.

Fig.	$\eta$	$d_0$ $k_1$	$d_0$ $C$	$d_0$ $n$	$R$ $k_2$	$R$	$R$ $n$
4.12	100,000	99.95	- 80	7.13	65.69	- 80	7.33
4.13	30,000	112.08	5	6.70	59.98	40	6.23
4.14	10,000	128.93	30	6.81	106.48	30	6.62
4.15	1,000	172.4	5	6.48	233.7	10	6.24
4.16/17 (a) <sup>1)</sup>	100,000	92.8	5	6.90	46.9	5	6.72
4.16/17 (b)	100,000	94.1	14.9	7	58.8	- 247.1	7
4.18/19 (a)	100,000	88.5	166	6.74	41.9	166	6.58
4.18/19 (b) <sup>1)</sup>	100,000	92.8	5	6.90	46.9	5	6.72
	cSt						

<sup>1)</sup> using the same experimental data set.

## 4.7. Summary

As the results have shown, a rich structure in all three acoustic signals: single transit, double transit and the reflection were observed. As the stripe progressively wets the surface the transit signals show a distinct pattern of two sometimes three strong attenuation maxima with an asymmetric shape superimposed on the exponential decay of the signal amplitude. These attenuation resonances influence the overall magnitude of all three acoustic signals and cause at the resonance tips severe damping of the acoustic signals. Moreover, a subsidiary peak structure along the back slope of the transit signals is visible. Both transit signals, single transit and double transit, mirror each other in trend and structure. Also the subsidiary peak structure is a good indication for these similar signal trends in the transit signals. However, it is not possible to identify a precise correlation between the subsidiary peaks in the transit signals and the peaks and troughs observed in the reflection. Nonetheless the experiments do suggest that the overall amplitude of the transit signals provide an envelope modulating the magnitude of the reflection peaks. Although an inconsistent structure of significant peaks is visible immediately after the deposition of a stripe of fluid, they appear in a very consistent manner in the middle section of the reflection enclosed by two attenuation resonances of the transit signals. Table 4.1 (a) reveals that these reflection resonance peaks appear consistently throughout the experiments in a series of five to seven peaks and to within the accuracy of the optical system the average peak separation seems to correlate with changes in the contact width of one acoustic SAW wavelength. In detail, a variation in peak to peak separation in the reflection is present throughout all experiments. These are systematic changes occurring with  $\Delta d$  initially greater than a SAW wavelength and then decreasing to less than a SAW wavelength. There is also some evidence that the subsidiary peak structure seen on the transit signals corresponds to changes in width of one half SAW wavelength, although this conclusion is based on very few peaks. The strong attenuation maxima in the transit signals represent much greater changes in the contact width of the oil than a SAW wavelength. The height of the fluid is changing by 3 - 4  $\mu\text{m}$

between consecutive maxima in the double transit to account for the mass and volume conservation during the spreading process. The cross-sectional area of the stripe within the acoustic path does show a systematic increase as the viscosity decreases, which coincides with the observed increase in cylindrical cap radius.

Keeping the experimental conditions similar, Fig. 4.16 to Fig. 4.18 show a possibility of reproducibility within different experiments. In particular, the similarity in geometrical parameters which are well reflected in the cross-sectional area of the stripe does suggest that loading by an identical volume of fluid upon the substrate surface may produce quantitatively identical results. Moreover, it reflects the high accuracy of the optical evaluation of the stripes. The optical analysis for the measurements is well established and reflects the consistency of experimental results throughout the whole series of experiments.

**CHAPTER 5**

***ANALYSIS AND  
DISCUSSION***

## 5.1. Introduction

The particle displacement of Rayleigh surface acoustic waves consists of two displacement directions; a longitudinal component moving the particles backwards and forwards parallel to the plane of wave propagation and a vertical shear component moving the particles up and down normal to the surface of wave propagation. The superposition of these two components results effectively in a retrograde elliptical motion. The dominant vertical particles displacement leads to a significant interaction with any medium adjacent to the surface which results in a compressional wave generation into the liquid. Ricco and Martin [152] mentioned a second dissipative factor of the Rayleigh wave, the in-plane motion or longitudinal component of wave-propagation which couples viscously a shear wave into an adjacent liquid when contacting the device surface. However, the vertical displacement results in frequency-dependent attenuation of 4 dB/cm MHz. They concluded, that device operation above 10 MHz would make Rayleigh wave operating SAW devices impractical for liquid sensing. On the other hand, if the device's acoustic path is covered with a partially localised liquid which dynamically spreads within the acoustic path the transit signals, propagating along the solid-liquid interface experiences an exponential decay in signal amplitude when the fluid diameter increases. This suggests that the increasing coverage is the dominant factor for the decay in signal amplitude. However, the existence of significant asymmetric attenuation resonance peaks superimposed onto the exponentially declining amplitude of the transit signals can be related to changes in fluid geometry and has never been observed before using dynamically evolving liquids on Rayleigh type surface acoustic wave sensors. As the fluid spreads the increasing surface coverage requires a reduction in height of the fluid to obey volume conservation producing large attenuation resonance in the transmission signals at specific fluid cross-sectional geometries. The increasing fluid coverage and the viscous coupling of horizontally polarised shear waves into the liquid may play an integral part in the studies conducted here. The existence of systematic reflection resonances occurring in the reflection of SAW's from a stripe of fluid allows a methodical study of reflection coefficients in a wide range. The

existence of transmission and reflection resonances and the effect of a dynamically changing stripe of oil modulating the amplitude of transmission and reflection signals allows one to investigate the interaction of SAW's with spatial inhomogeneities in a more detailed way. The spreading of a single stripe of oil produces an enormous range of specific geometrical stripe parameters. The concentration of partially localised liquids with restricted surface area coverage has opened a new pathway to study surface wave–liquid interaction using SAW devices.

This chapter will discuss possible effects of surface acoustic wave resonances in the transmission and reflection signals caused by a spreading stripe of oil. The extent to which the shear motion induced in the liquid can account for observed transmission resonances will be discussed by applying the model reviewed in Chapter 2. A set of four different results will be used to illustrate in detail the feasibility of the developed theory and to discuss the dependence of geometrical parameters such as the stripe geometry in relation to the signal responses observed during the SAW-liquid interaction; the conclusion based on this set of results are typical of the many other sets of results obtained. In the first section we will discuss the influence of the shape and the resonance structure observed in both transit signals as seen in the results presented in Chapter 4 and the effects that the  $\omega\tau$  limits exhibit on the here presented approximation model. The next section will show how the cylindrical cap cross-sectional profile and volume conservation of the stripe have been incorporated into the model. Subsequently the importance of the relaxation time to evaluate and compare the fluid behaviour with the model will be discussed. Finally possible mechanisms for the existence of strong oscillations in the reflection due to a steadily changing front edge and back edge of the stripe of fluid are discussed. A qualitative model using a triangular shape approximation will be presented.

## 5.2. Influence of the $\omega\tau$ Limits on the Resonance Structure

In the model reviewed in Chapter 2 and ref. [148], the fluid acts as a resonant cavity for the generated horizontally polarised shear waves having a node at the liquid-vapour interface and an antinode at the solid-liquid interface considering that the small stripe of oil deposited onto the surface adopts an approximately spherical cap form seen from its cross section. When the oil spreads across the surface, but with the maximum height reducing to conserve mass, the attenuation at any location is simply assumed to be equal to a uniform fluid coverage of thickness equal to the local thickness. The consequence is that in the limit of  $\omega\tau \rightarrow \infty$  the acoustic losses as given in equation (2.73) (Chapter 2):

$$L \approx -20 \log_{10} e \frac{d}{\rho_s \xi \lambda_R \nu_R} \operatorname{Re} \left[ \frac{\beta}{1 + i\omega\tau} \right], \quad (5.1)$$

show a regular sequence of sharp peaks (resonance peaks) with a significant amplitude reduction and a slower overall modulation of the envelope of these peaks. Fig. 5.1 shows the real part of the dimensionless quantity  $\beta\delta/[\eta(1+i\omega\tau)]$  proportional to the attenuation as a function of fluid thickness divided by penetration depth,  $t_f/\delta$ . The frequency shift in angular frequency (equation (2.74), Chapter 2),

$$\Delta\omega \approx -\frac{1}{\rho_s \xi \lambda_R} \operatorname{Im} \left[ \frac{\beta}{1 + i\omega\tau} \right], \quad (5.2)$$

also demonstrates a quite dramatic change with a repeated pattern of large deviations as demonstrated in Fig. 5.2, both positive and negative about the unperturbed frequency [148]. Here the dimensionless quantity  $\beta\delta/[\eta(1+i\omega\tau)]$  is purely imaginary (Fig. 5.2) and proportional to the frequency shift. In the case of  $\omega\tau = 1$  the pattern in both the attenuation and the frequency shift is

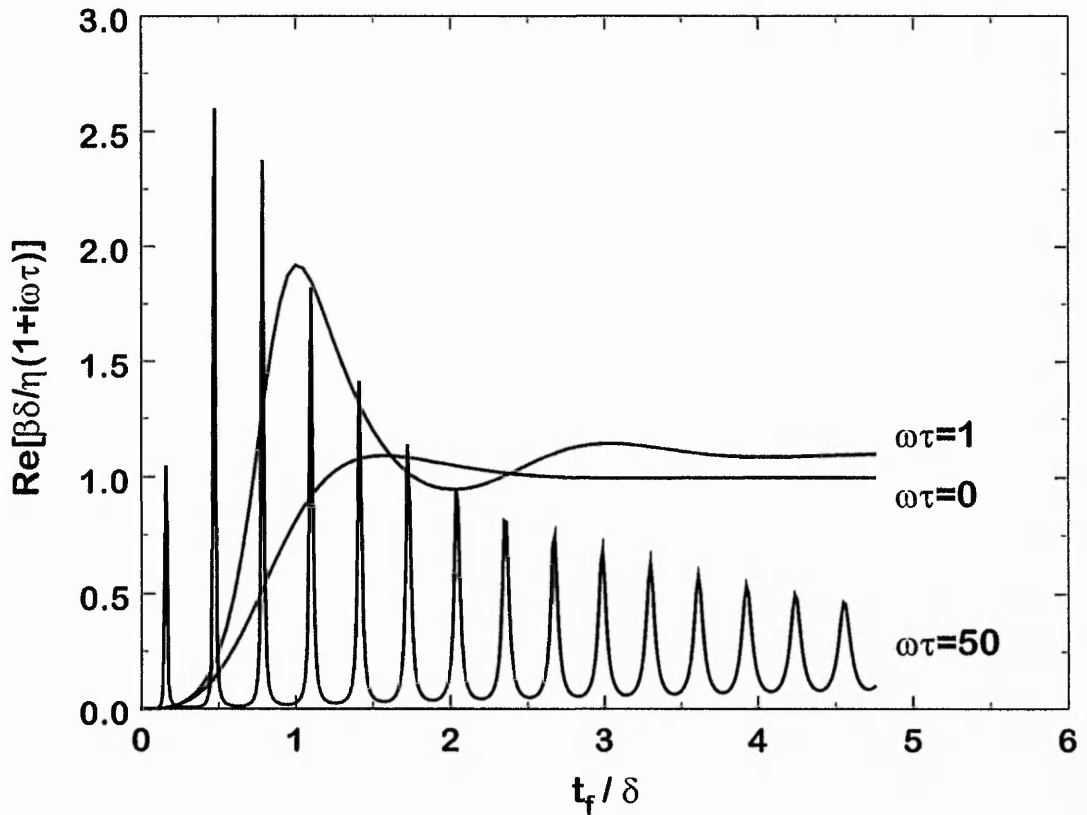


**Fig. 5.1** For a uniform fluid layer the attenuation given as a dimensionless quantity undergoes a transition with increasing  $\omega\tau$ . With increasing thickness of the fluid layer, in the  $\omega\tau = 0$  limit the attenuation increases to a maximum slightly greater than the penetration depth and then relaxes to a saturation value. If  $\omega\tau$  reaches unity the overshoot becomes larger and the model adopts itself to the behaviour of a damped oscillator. In the  $\omega\tau = 50$  limit the character of the loss changes completely with a clear and sharp oscillatory behaviour even for thicker films.

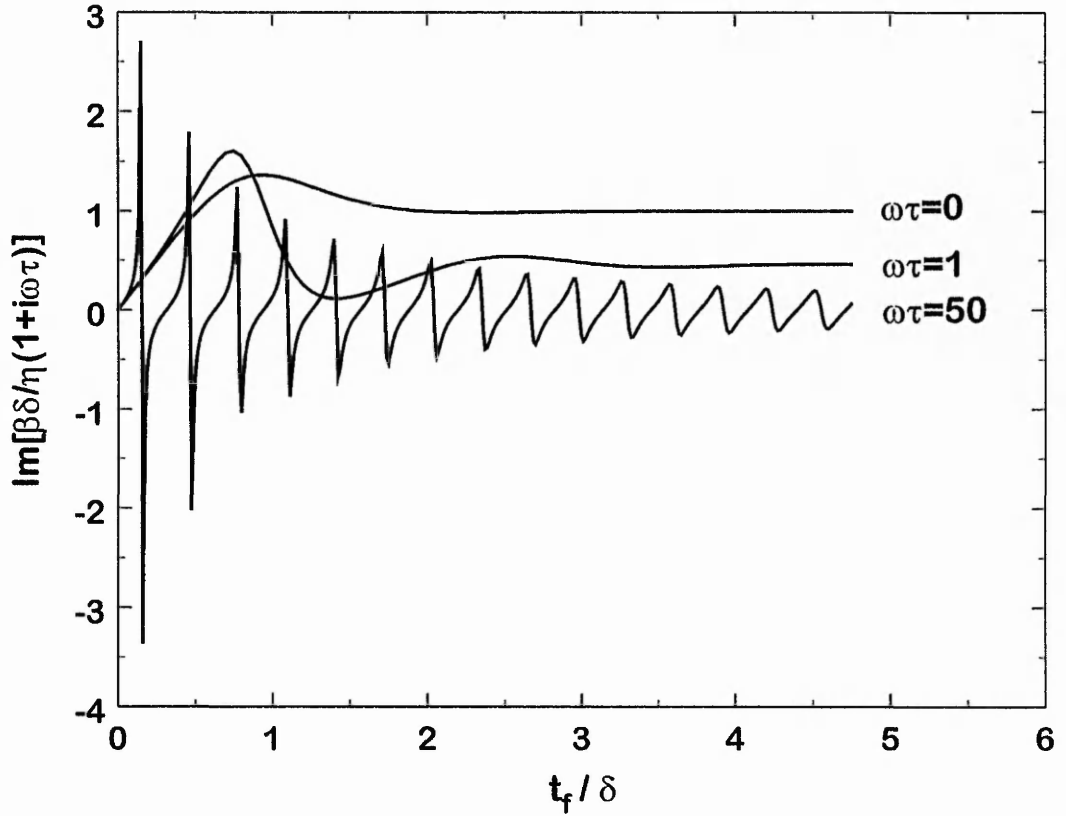


**Fig. 5.2** The frequency changes correspond in behaviour to the losses in Fig. 5.1 with distinct changes in character as the fluid loading changes from a Newtonian liquid ( $\omega\tau \ll 1$ ) to an amorphous solid ( $\omega\tau \gg 1$ ).

characterised by a single oscillation showing a strong overshoot and a rapid decay exponentially forcing the oscillation to adapt to a constant value when the fluid coverage becomes thicker, this can be associated with the behaviour of a damped oscillator. Considering that the fluid theoretically would reach the  $\omega\tau \rightarrow 0$  limit representing the Newtonian behaviour, both the acoustic losses and the frequency shift would saturate when the fluid starts as a relatively thick fluid characterised in a large cross section height of the liquid stripe, so that the fluid depth could exceed a few penetration depths. This would mean the surface acoustic wave device behaves as a sensor of the extent of wetted area. This change with relaxation time represents a significant transition in fluid characteristics and, when  $\omega\tau$  is large, it is possible for shear wave resonances to occur when the fluid thickness matches the conditions,

$$t_f = n\lambda_s / 4 \quad (5.3)$$

where  $n = 1, 2, 3, \dots$

### 5.3. Area Approximation of the Cross-Section of the Cylindrical Cap

The model (Chapter 2) describes shear motion induced attenuation resonances with asymmetric shape. However, this model is for static and uniform thickness fluid coverages. In the experiments transmission signals are dependent on the dynamically changing geometry that the stripe undergoes during the wetting process. Moreover, when the stripe is placed onto the substrate, its cross-section approximates a spherical cap shape so that the fluid is not of uniform thickness. In the course of the spreading the stripe shape undergoes a continuous change of the cross-section parameters, but subject to conservation of mass and volume. Hence, the widening of the stripe is followed by a reduction in the cylindrical cap height of the cross-section. To allow for these conditions equation (2.71) of Chapter 2,

$$\beta = \left( \frac{\eta\sqrt{2i}}{\alpha} \right) \left( \frac{1 - ik^2\alpha^2}{2} \right) \tanh \left( \frac{\sqrt{2i}t_f}{\alpha} \right) \quad (5.4)$$

is used, but with the redefinition of  $\beta$  as,

$$\beta \rightarrow \frac{2}{d} \int_0^{d/2} \beta(t_f(x)) dx, \quad (5.5)$$

where the fluid thickness,  $t_f$ , is now allowed to vary across the stripe width. In the complete wetting situation the contact angle is always less than  $90^\circ$  so that the thickness of the cross-section of the stripe is given by,

$$t_f = h_0 - R + \sqrt{R^2 - x^2}. \quad (5.6)$$

Thus, for any given stripe cross-section, the attenuation can be calculated by numerically evaluating equation (5.5). However, in the experiments a spreading stripe maintains mass so that the cross-sectional shape of the stripe evolves with a constant area,  $A_{CS}$ . It is therefore necessary to reduce the height,  $h_0$ , as the contact width,  $d_0$ , increases. From equation (5.6) the cross-sectional area can be found,

$$A_{CS} = (h_0 - R)d_0 + R^2 \left[ \theta + \frac{1}{2} \sin(2\theta) \right]. \quad (5.7)$$

Although this expression contains all four geometrical parameters it actually depends on the two measured parameters  $d_0$  and  $R$ , since the contact angle,  $\theta$ , is given by

$$d_0 = 2R \sin \theta, \quad (5.8)$$

and the height by

$$h_0 = \frac{d_0}{2} \tan\left(\frac{\theta}{2}\right). \quad (5.9)$$

Knowing the cross-sectional area and the initial contact width, a sequence of geometrical parameters for a constant volume stripe can be constructed. This is done using a computational iteration algorithm [148] to numerically estimate the cross-sectional area since equation (5.7) is non-linear. The small angle approximation (section 2.2.7., Chapter 2) allows equation (5.7) to be simplified using equations (5.8) and (5.9) giving an cross sectional area of

$$A_{CS} \approx \left(\frac{d_0^2}{8R} - R\right) d_0 + R^2 \left[\frac{d_0}{R}\right], \quad A_{CS} \approx \frac{d_0^3}{12R}. \quad (5.10)$$

This approximation enables the computational results to be examined analytically.

For any experiment  $d_0$  and  $R$  are measured during the course of spreading and this gives a set of estimates of the cylindrical cap radius of the stripe. The area given by equation (5.7) is therefore an experimentally determined parameter. Other parameters used to complete the numerical iteration for the model are the relaxation time  $\tau$  and the parameter  $\xi$  arising from the assumption that the thickness of the elliptical motion of the Rayleigh wave in the substrate is approximately equal to one SAW wavelength. The depth dependence for the substrate oscillating is expressed by  $t_s = \lambda\xi$  with  $\xi$  adjusting the attenuation, as given in equation (5.1), and similarly the shift in angular frequency (equation (5.2)).

The model considers the condition of the surface wave speed,  $v_R$  and that of the shear wave speed in a Maxwellian fluid,  $v_s = \sqrt{(\mu/\rho)}$ . The relaxation time,  $\tau$  (equation (2.55), Chapter 2) represents the ratio of viscosity to shear modulus,  $\tau = \eta/\mu$ .

## 5.4. Transmission Resonances in the SAW Transit Signals

### 5.4.1. Starting Conditions and the Influence of Relaxation Rate $\tau^{-1}$ and the Parameter $\xi$

The model requires for processing the attenuation trends in the transit signals the determination of the area from the measured  $R$  and  $d_0$ . It is also necessary to identify the starting point when the stripe of oil was applied to the surface to synchronise the model with the actual starting point of the experimental data. With  $d_0$  and  $R$  from the image processing analysis the cross-sectional area from the image sequence could be estimated. The results were listed in a spread sheet. An averaging procedure was used to estimate the average value for the cross-sectional area. The average cross-sectional area value was compared with the calculated area values from each single measurement. Most values were within 3% of the average, but several deviated by more than this and these were then eliminated from the average. Such deviations tended to occur when  $R$  had been estimated using relatively few interference fringes. To obtain the exact starting conditions for  $d_0$  and  $R$ ,  $d_0$  was estimated from the experimental data and kept constant and then a value for  $R$  was found numerically to match the cross-sectional area with the average area value.

The fit then needed only an adjustment of the relaxation rate  $\tau^{-1}$  and the parameter  $\xi$ . The influence of  $\xi$  can be clearly seen in equation (5.8) since  $\lambda_R$  is a constant.  $\xi$  adjusts the attenuation and so scales the overall losses by a factor of  $1/\xi$ . The fit uses  $\xi$  to adjust overall attenuation, but this parameter does not alter the pattern of the attenuation. In contrast to  $\xi$ , the location of attenuation resonances as shown in Chapter 4 in the transmission signals depends on the correct estimation of  $\tau^{-1}$ , the measured frequency and the fluid volume. To fit the model to the experimental data an arbitrary value for  $\tau^{-1}$  has

been chosen and  $\xi$  was set to one at the beginning of the computational fitting procedure. Both parameters were then manually adjusted to obtain a better fit to the data.

### 5.4.2. Transmission Resonances with Asymmetric Shape

Here we will show the results of four separate experiments applying the fits of the model to the attenuation behaviour of the double transit signal. The fits have been applied to a series of experiments using a SAW device with a resonant frequency of 168.8 MHz. The sine wave input pulse had a peak to peak amplitude of 500 mV with a pulse duration of 400ns and a repetition rate of 1 kHz. The parameters converting time into the relevant geometrical parameter are displayed in Table 5.1. A fit to a set of experimental data for the double transit signal is given in Fig. 5.3 to Fig. 5.6. The relaxation rate used, varied between 12.8 and 13.2 MHz (Table 5.2). The relaxation rate is closely related to either the shear modulus,  $\mu$  or the shear speed,  $v_s$  using

$$\tau^{-1} = \frac{\mu}{\eta} = \frac{\rho_f v_s^2}{\eta}. \quad (5.12)$$

Since the density of the oil is  $971 \text{ kg m}^{-3}$  the fitted relaxation rate then gives the shear speeds (Table 5.2). The values are in a margin of  $v_s = (1140 \pm 9) \text{ ms}^{-1}$ . Further information about the cross-sectional area of the stripe, which is the average value of all geometrical parameters obtained from one entire image sequence, such as contact width,  $d_0$ , cylindrical cap radius,  $R$ , contact angle,  $\theta$  and the height,  $h_0$  representing the starting condition for equation (5.4) processed in equation (5.2) with the aid of equation (5.3) is given in Table 5.2.

**Table 5.1** Geometrical fits for the contact width,  $d_0$  and cylindrical cap radius,  $R$ , obtained from the optical measurements for PDMS oils spreading on lithium niobate.

Fig.	$\eta$	$d_0$	$d_0$	$d_0$	$R$	$R$	$R$
		A	c	n	A	c	n
5.3	100,000	99.08	0	7.58	55.07	0	7.14
5.4	100,000	88.53	166	6.74	41.88	166	6.58
5.5	100,000	99.95	-80	7.13	65.69	-80	7.33
5.6	100,000	92.84	5	6.90	46.94	5	6.72
	cSt						

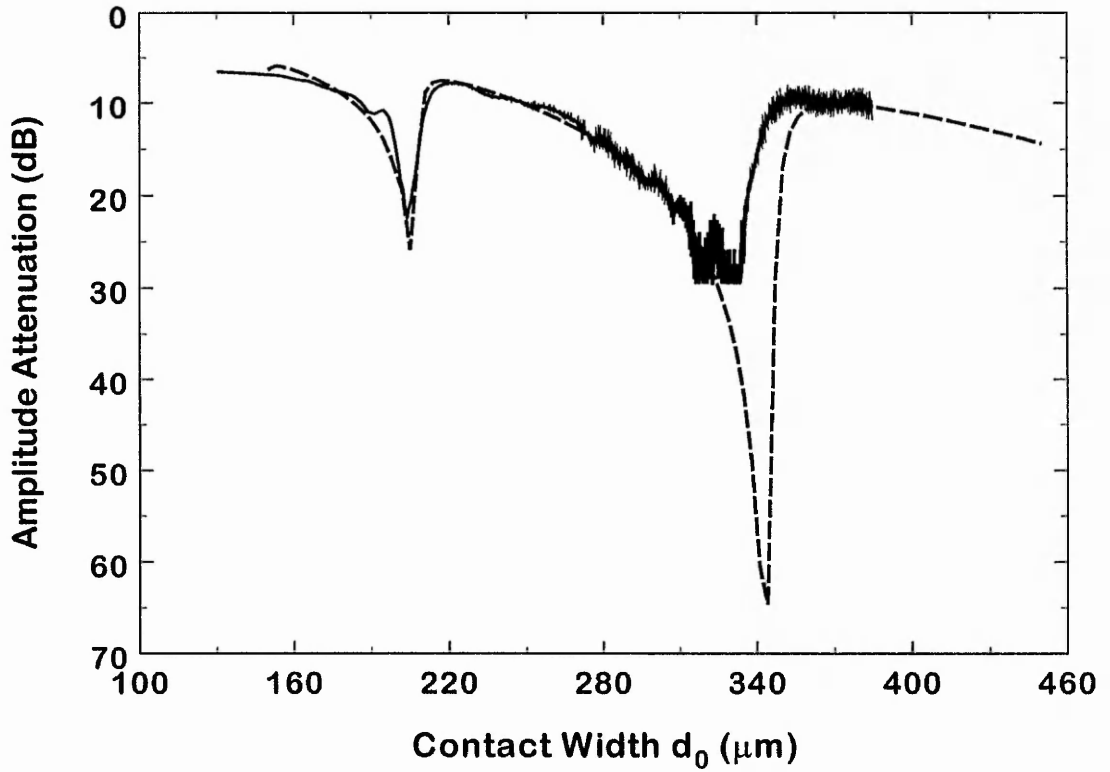
**Table 5.2** Starting conditions for the computational model to match correctly the fluid width after deposition and the other geometrical parameter for a 100,000 cSt PDMS oil on a 168.8 MHz SAW device.

Fig.	Start $d_0$	Start $R$	Start $\theta$	Start $h_0$	Area $CS^*$	$t_s$	$\delta$			$\mu$	$v_s$
5.3	150	235.71	10.54	9.22	1.231	19.06	13.89	12.8	0.79	1.251	1131
5.4	190	451.24	12.15	10.11	1.283	18.41	13.83	13.05	0.77	1.275	1142
5.5	185	384.39	13.92	11.30	1.397	20.74	13.89	13.1	0.86	1.279	1144
5.6	130	148.51	25.96	14.98	1.312	18.48	13.90	13.2	0.765	1.290	1149
					$\times 10^{-9}$					$\times 10^9$	
	$\mu\text{m}$	$\mu\text{m}$		$\mu\text{m}$	$\text{m}^2$	$\mu\text{m}$	$\mu\text{m}$	MHz	-	$\text{Nm}^{-2}$	$\text{ms}^{-1}$

$CS^*$  = average cross-sectional area

The theoretical model demonstrates all the main features present within the experimental data. The fits to the experimental data (Fig. 5.5 to Fig. 5.8) is shown as the dashed line. The overall decrease in attenuation is accompanied by resonances of asymmetric shape. The magnitude of the resonance peaks calculated from the model represents the amount of energy dissipated into the liquid predicted only from the shear wave contribution penetrating into the liquid. However the limitation of the calibration shows clearly the cut off effect by the diode thresholds seen in Fig. 5.5 to Fig. 5.8 in the further evolution of the transit signal model beyond the 36 dB mark. The exact location of the attenuation resonances in time within the series of experiments is dependent on the starting conditions such as the contact width and the amount of applied volume of oil to the surface. Variation in these conditions let an asymmetric resonance appear earlier in time or later, since the contact width is a time dependent parameter. The surface coverage by the fluid drives the overall characteristics of the attenuation. Wider stripes tend to cover a substantial amount of the device surface and cause an extended wave-fluid interaction which can be accounted as the dominant factor for a progressive attenuation. When comparing the four different graphs, it is interesting that the deviation of the relaxation rate between these four experiments is just of the order of  $\pm 0.2$  MHz ( $\pm 1.6\%$ ) from the average relaxation rate (13 MHz). The deviation in shear speed (equation (5.12)) is even less significant and represents a deviation of around  $\pm 0.1\%$  from  $v_s = (1140 \pm 9) \text{ ms}^{-1}$  (see Table 5.2). However, the absolute magnitude of attenuation do differ in detail. To match the absolute attenuation the fits in Fig. 5.5 to Fig. 5.8 used reduced values for  $\xi$  (Table 5.2) when compared with the initial starting parameter setting  $\xi = 1$ . Here, alteration in this parameter act to scale the overall loss by  $1/\xi$ .

Physically, a reduced  $\xi$  ( $\xi < 1$ ) could be due to several effects. The scaling parameter is used in the resonance model to adjust the thickness of substrate oscillating and is ideally one to account for approximately one SAW wavelength penetrating into the substrate. However, an adjustment of this parameter to less than one is present in the experiments. An explanation can be found in the physical cause of this reduction. The variation in  $\xi$  may be due to a small misalignment of the transducer orientation on the SAW substrate. This may



**Fig. 5.3** The numerical model (dashed line) shows all the main features present within the experimental data. The asymmetry in the resonances and their location are described by the model. The relaxation rate was estimated to  $\tau^{-1} = 12.8$  MHz.

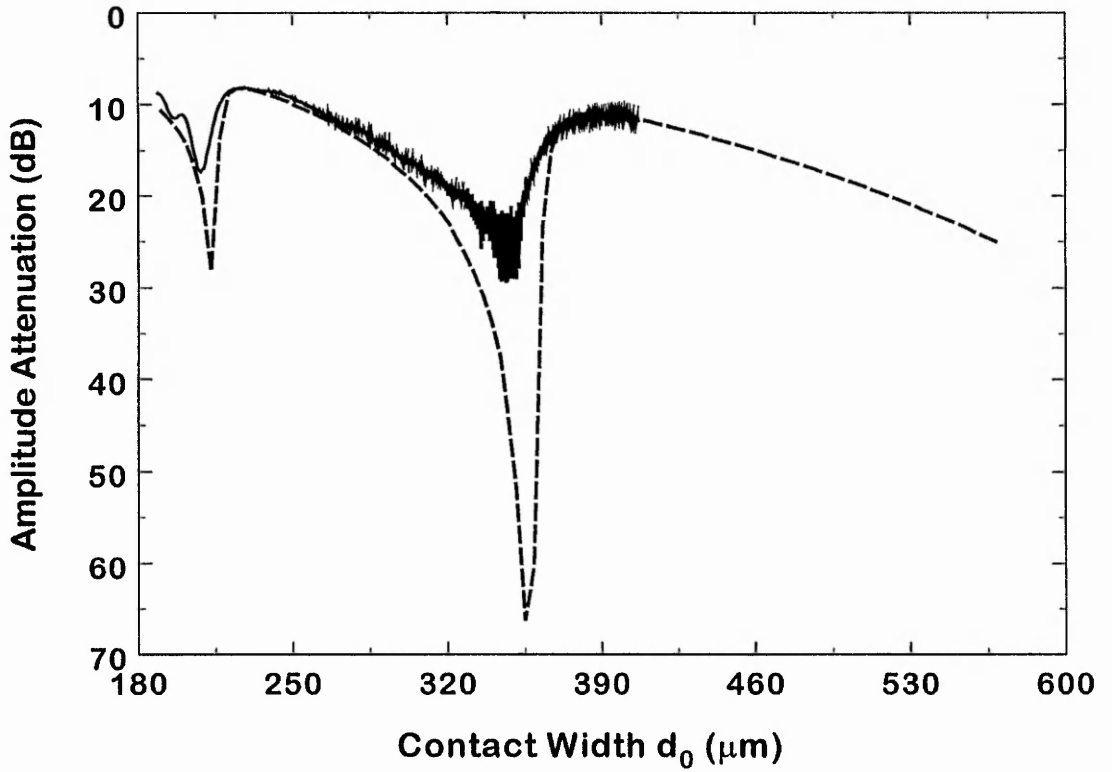


**Fig. 5.4** The losses in the stripe is modelled using a cylindrical cap cross-section of constant area and a relaxation rate of  $\tau^{-1} = 13.05$  MHz.

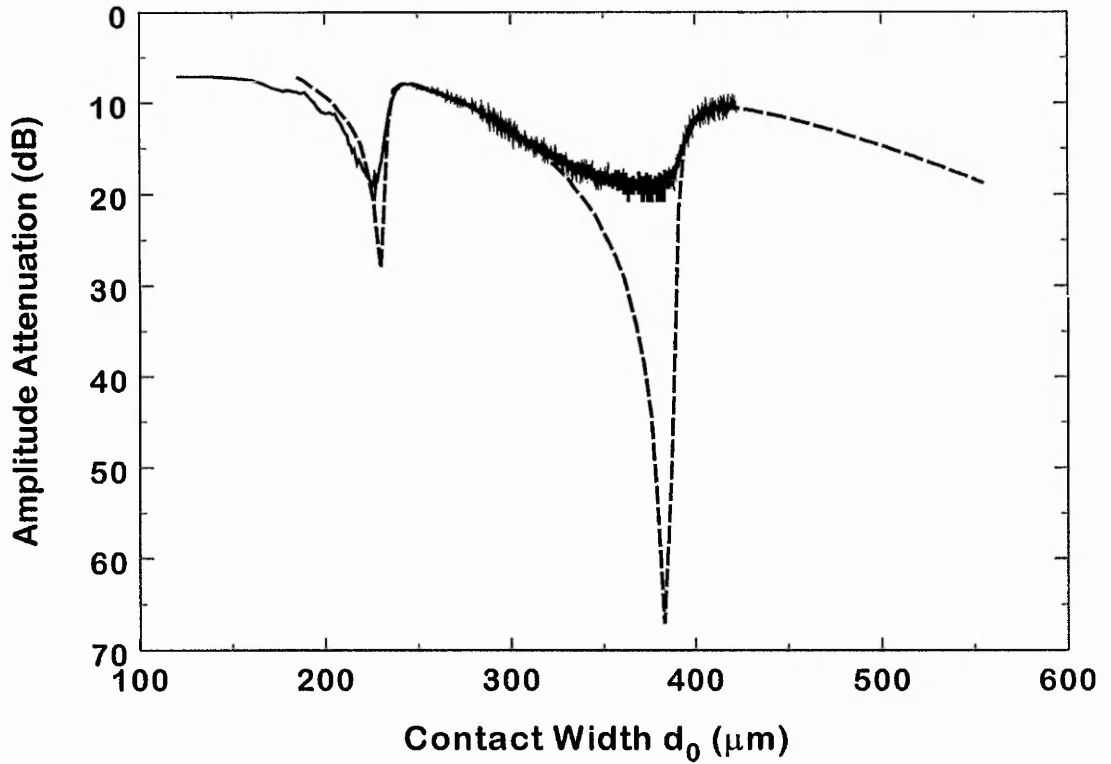


**Fig. 5.5** Variation in the relaxation rate adjusts the location of the resonances of the model to that of the experimental data (Table 5.2). Alteration in  $\xi$  allows to scale the overall loss by  $1/\xi$ .

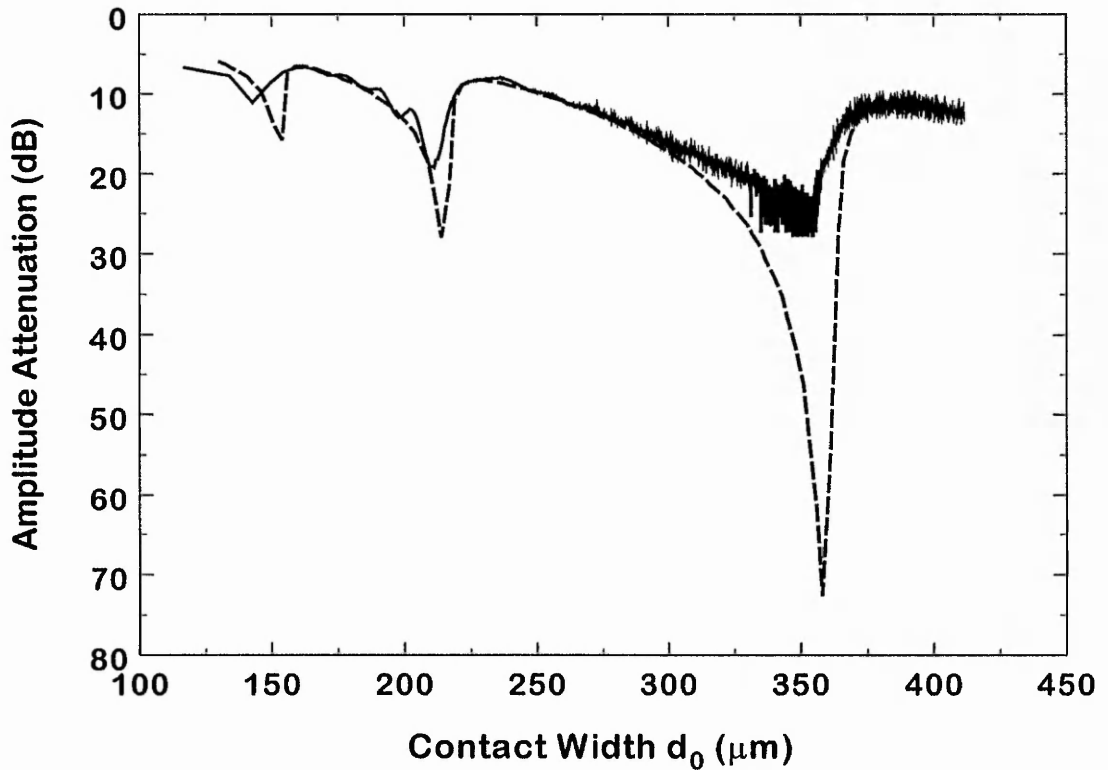


**Fig. 5.6** In all four experiments (Figs. 5.3 to 5.6) variation in the relaxation rate was found to vary  $\pm 0.2$  MHz from the average relaxation rate of 13 MHz. This is close and shows a deviation between experiments of 1.6% reflecting the good accuracy of the model in predicting the relaxation time.

result in a slight reduction of the wave speed,  $v_R$  of the SAW when compared with the theoretically determined value for the surface wave speed,  $v_R$ . As a result, the predicted  $v_R$  is too large compared to the real speed of the surface wave. A compensation for this effect is than achieved by re-scaling  $\xi$ . Within any one experiment a misalignment of the stripe of oil, or the effect of reflections and mode conversion would also alter the precise value of the losses and the fraction of losses properly attributed to the shearing mechanism in the fluid.

### 5.4.3. Viscosity Dependence of the Relaxation Rate $\tau^{-1}$

Equation (5.12) shows a clear dependence of the relaxation rate  $\tau^{-1}$  on the viscosity. This suggests that a reduction of viscosity by a factor of 10 should increase the relaxation rate by the same magnitude. In section 5.4.2. we have seen that the relaxation rate was within a range of  $(13 \pm 0.2)$  MHz for oils with  $\eta = 100,000$  cSt. If we use an oil with a viscosity of 30,000 cSt we should obtain a fitted relaxation rate 10/3 times larger than for the 100,000 cSt oil. Indeed Table 5.4 shows the fitting values for two different viscosities, 30,000 cSt PDMS oil and 10,000 cSt PDMS oil, and this confirms the expected trend. The model does reflect correctly the predictions for the lower viscosities when compared with the model parameter in Table 5.2. Fig. 5.7 represents the modelling of an experiment using a 30,000 cSt oil. The graphs show the transmission signals of the single transit (curve (a)) and the double transit (curve (b)). Here the fitted data obtained from the model show a close similarity between single transit and double transit in trend. If we compare the model parameter (Table 5.4) between single transit fit and double transit fit it presents an extremely good similarity and confirms in terms of the relaxation rate that both curves are mirroring the trend in location of attenuation resonances. A re-scaling for  $\xi$  (Table 5.4) must be allowed to adjust the model to the experimental data. The double transit has been shifted by 2 dB downwards to enable a better comparison between the two graphs and to see clearer the trend of the single transit fit. It is interesting that the fit is exactly following the same magnitude of attenuation in the second

attenuation peak of the single transit when overlapped with the experimental results, suggesting a good accuracy of the model. Bringing this in contrast with the trends in the double transit signal it is clear that a deviation in the second attenuation resonance peak between fit and experiment is not due to an accuracy problem of the model itself (see also section 3.8., Chapter 3). Another indication for the good accuracy of the model can be found in the magnitude of the resonance peak in the fitted data, which agrees well with the magnitude of the attenuation peak in the double transit signal (curve (b)). The prediction of the relaxation rate of 43.3 MHz using equation (5.9) and the fitted value at 100,000 cSt compares well with the estimated relaxation rate of 44.9 MHz (Table 5.4, Fig 5.7a) and 44.6 MHz (Table 5.4, Fig 5.7b).

A reduction in viscosity of factor 10 should increase the relaxation rate to 130 MHz. For the 10,000 cSt oil the fit gives 128 MHz which is well within the limit when taking the error into account (see Table 5.4 in comparison to Table 5.2). Fig. 5.8 shows the spreading of a 10,000 cSt PDMS oil. An offset for the double transit (curve (b)) has been introduced to shift the graph by 3 dB downwards. The fitted relaxation rate is consistent between viscosities. However, the attenuation resonances in the single transit (curve (a) of Fig. 5.8) shows a smaller magnitude of attenuation than in the actual experimental data. If we investigate equation (2.69); Chapter 2, the term  $\delta^2 k^2/2$  can be effectively neglected if the condition  $\omega\tau \gg \delta^2 k^2/2$  is fulfilled [148]. This leads to the condition of equation (5.10) and is in particular valid in the region of high viscosity fluids. If  $\omega\tau$  gets closer to the Newtonian region of liquids ( $\omega\tau \rightarrow 0$ ) the  $\delta^2 k^2/2$  term is larger and influences the behaviour of attenuation resonances in magnitude (equation (5.8)) and frequency shift (equation (5.9)). This influence results in a reduction of the attenuation magnitude, as observed for the trends in the model in both, double transit and single transit (Fig. 5.8). However, the reduction in magnitude in attenuation described by the model does not affect the location of the attenuation resonances. The direct comparison between model and the experimental data shows a good prediction of the trend of both transmission signals. This is well confirmed by all model parameters (Table 5.4) and the magnitude of the relaxation time (127.8 MHz) when compared with the 100,000 cSt oil ( $13 \pm 0.2$  MHz) and this does validate the theoretical prediction.

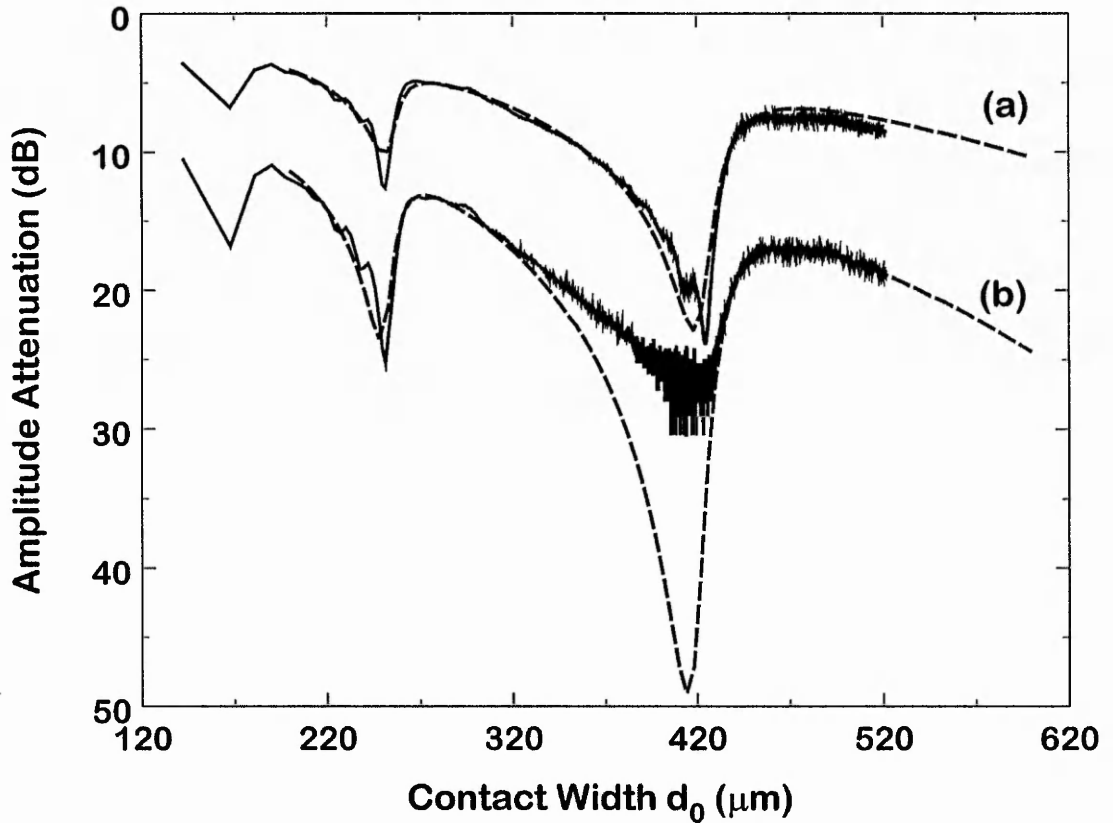


**Fig. 5.7** Comparing the trend in the transit signals of a 30,000 cSt oil with the trend of the fitted data (dashed lines) shows a close similarity of location of the attenuation resonances. Remarkable is the good agreement in magnitude between the fitted values and the actual signal data for the single transit (curve (a)) at the second attenuation maxima and for the double transit (curve (b)) at the first attenuation maxima. The double transit (curve (b)) has been shifted downwards by 2 dB.

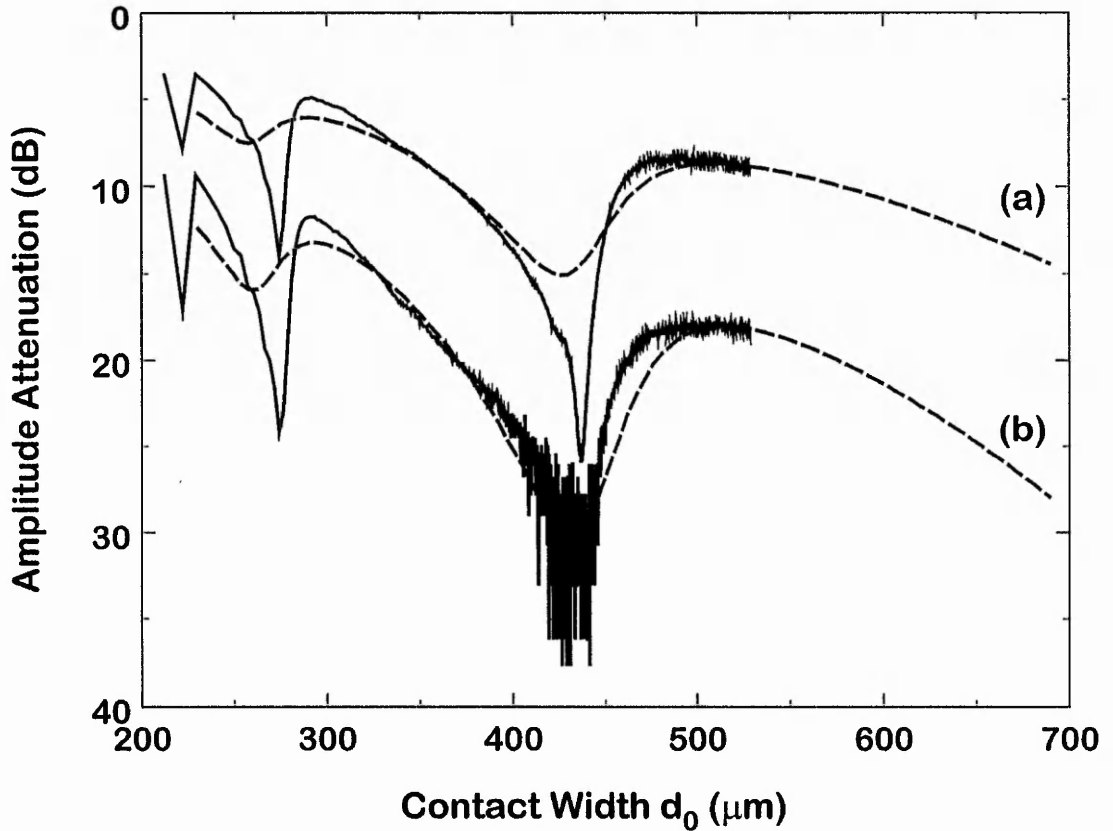


**Fig. 5.8** The magnitude in attenuation for both traces (single transit, curve (a), and double transit, curve (b)) is smaller than in the actual experimental data (10,000 cSt PDMS oil). However, the model predicts correctly the location of the attenuation maxima. The relaxation rate, considering the magnitude changes of factor 10, is remarkably similar and shows the consistency of the model. Here the double transit (curve (b)) has been vertically shifted downwards by 3 dB.

**Table 5.3** Geometrical fits for the contact width,  $d_0$  and cylindrical cap radius,  $R$ , obtained from the optical measurements for PDMS oils spreading on lithium niobate.

Fig.	$\eta$	$d_0$ A	$d_0$ c	$d_0$ n	$R$ A	$R$ c	$R$ N
5.7	30,000	112.08	5	6.70	59.98	40	6.23
5.8	10,000	128.93	30	6.81	106.48	30	6.62
	cSt						

**Table 5.4** Starting conditions for the computational model to match correctly the fluid width after deposition and the other geometrical parameter for 30,000 cSt PDMS and 10,000 cSt PDMS on an 168.8 MHz SAW-device. The letter a indicates the parameter for the single transit, while b displays the parameter for the double transit.

Fig.	Start $d_0$	Start $R$	Start $\theta$	Start $h_0$	Area CS*	$t_s$	$\delta$	$\tau^{-1}$	$\ell$	$\mu$	$\nu_s$
5.7a	200	450.53	12.82	11.24	1.502	20.73	7.48	44.9	0.89	1.315	1161
5.7b	200	450.53	12.82	11.24	1.502	20.28	7.52	44.6	0.86	1.306	1158
5.8a	230	656.46	10.09	10.15	1.559	20.50	4.39	127.8	0.85	1.245	1131
5.8b	230	656.46	10.09	10.15	1.559	22.40	4.37	127.8	0.94	1.245	1131
					x10 <sup>-9</sup>					x10 <sup>9</sup>	
	$\mu\text{m}$	$\mu\text{m}$		$\mu\text{m}$	$\text{m}^2$	$\mu\text{m}$	$\mu\text{m}$	MHz	-	$\text{Nm}^{-2}$	$\text{ms}^{-1}$

CS\* = average cross-sectional area

The relaxation rate needed to fit the experimental data is consistent from one experiment to the next, although the scaling parameter  $\xi$  does vary.

## 5.5. Resonances in the Reflection Coefficient of SAW's

The model reviewed and discussed here describes many of the features seen in the transit signals. The inclusion of a single relaxation time to account for the variation in fluid viscosity and for the transition effects in the fluid properties can be seen as a valuable tool for characterising the surface acoustic wave liquid interaction. However, this model focuses on transmission attenuation resonances and describes the exponential decay in the transmission signals, but has not been designed to account for the strong oscillatory structure seen in the reflection signal (Fig. 5.9). In this section a possible mechanism to explain the complex nature of the reflection resonances and their non equidistant separation is outlined.

### 5.5.1. The Step Model

In order to account for possible reflection observed in the reflection signal of the fluid loaded SAW device, the idea is to approximate the shape of a dynamically evolving stripe into two consecutive steps of fixed height,  $h_0$  separated by a distance of  $2a$  as shown in Fig. 5.10. This model can be described by a wave propagating along a string of variable density. In such a case the density regions are given by one region for  $x > |a|$  accounting for a density,  $\rho_0$  and a second region of higher density  $\rho_1$  in the interval  $x < |a|$ . The model is equivalent to a damped harmonic oscillator in the denser region ( $\rho_1$ ), similar to the one described in equation (2.45), Chapter 2. The wave outside of  $x > |a|$  is freely propagating in the density region  $\rho_0$ . In the interval  $x < |a|$  the damped harmonic oscillator is described as

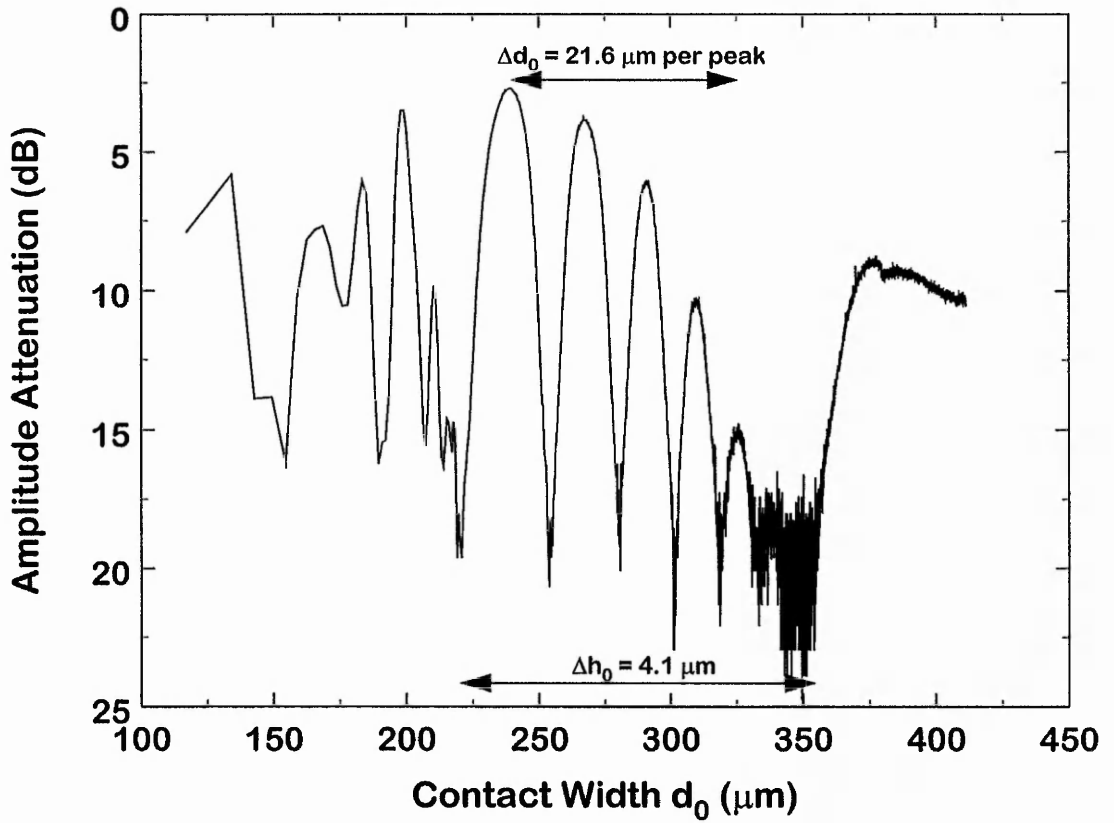


**Fig. 5.9** The resonant reflections occur with a separation in  $\Delta d_0$  of approximately  $21.6 \mu\text{m}$  which is of the order of one SAW wavelength of the unloaded SAW device.

$$\frac{d^2\psi}{dx^2} + 2\kappa \frac{d\psi}{dx} + k_1^2\psi = 0. \quad (5.13)$$

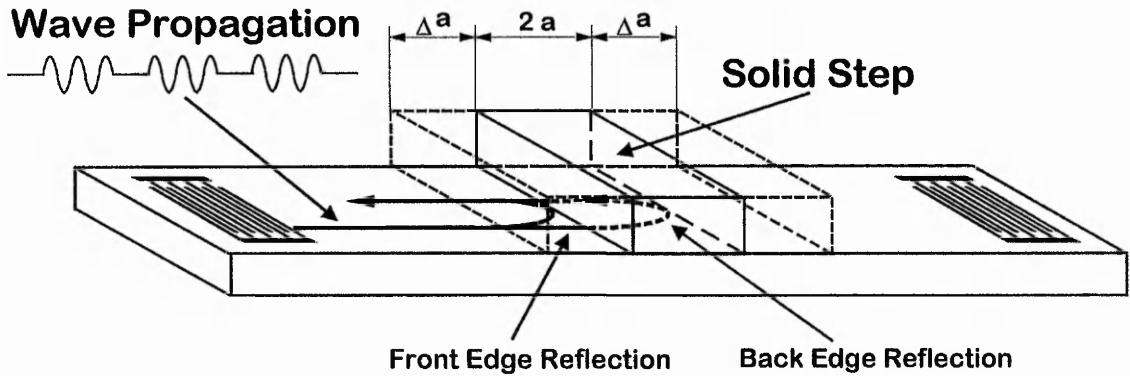
The overall solution of this problem requires three parts

$$\psi(x) = \begin{cases} Ae^{ikx} + Be^{-ikx} & (x < -a) \\ [Ce^{ikx} + De^{-ikx}]e^{-\kappa x} & (-a \leq x \leq a) \\ Fe^{ikx} & (x > a) \end{cases} \quad (5.14)$$

where  $\kappa$  is the damping coefficient and  $F$  is the amplitude coefficient for a transmitted wave propagating in the  $x > a$  region. The solutions in the three regions must be matched at  $x = \pm a$  to obtain relations between the constants  $A$ ,  $B$ ,  $C$  and  $D$ . If the wave is propagating freely in the lower density region it hits the face of the step at  $x = -a$  and one part of the wave energy is reflected back from the face of the step (front edge reflection). The remaining part of the wave energy enters the step and propagates along the path of  $2a$  until it reaches the face of the second step causing a second reflection at  $x = a$  (back edge reflection). The wave undergoes in the denser region an exponential damping in wave amplitude. The reflection from the denser region interferes with the wave reflected at the front edge of the step model. Solving (5.14) leads to the determination of transmission and reflection coefficients [175]

$$TC = \frac{|F|^2}{|A|^2}, \quad \text{and} \quad RC = \frac{|B|^2}{|A|^2} \quad (5.15)$$

representing the fraction of incident energy which is transmitted ( $TC$ ) or reflected ( $RC$ ). We can then write for the reflection coefficient after algebraic manipulations:



## Two Consecutive Steps Approximation

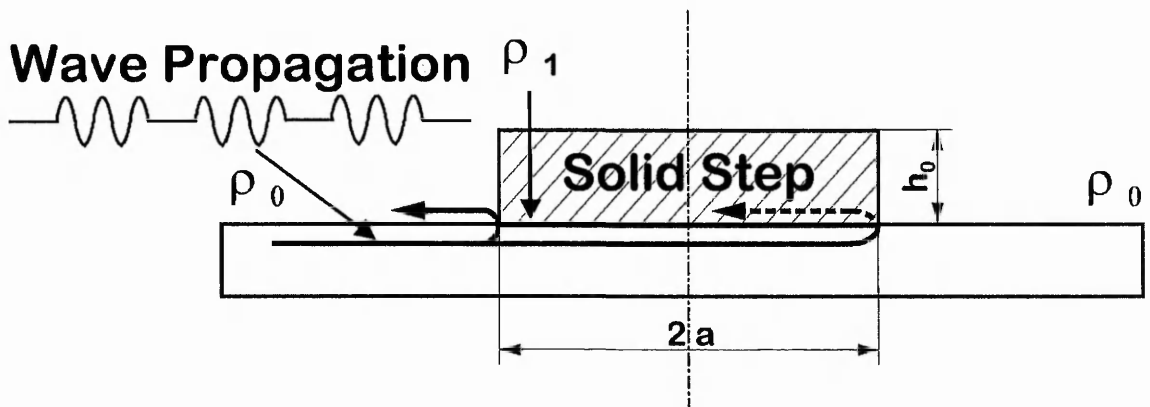


**Fig. 5.10** The model of two consecutive steps with a separation of  $2a$  and a fixed height,  $h_0$  can be regarded as a string with variable density,  $\rho_0$  and  $\rho_1$ . A wave propagating freely at region  $\rho_0$  is partially reflected from the face of the first step. The remaining part of the wave propagates inside the denser region  $\rho_1$  decaying exponentially in amplitude and is reflected on the face of the second step. The back edge reflection interferes with the front edge reflection and produces periodic reflection resonances of  $\lambda_1/2$ .

$$RC = \frac{\kappa^2 \sin^2 2k_1 a}{4 + \kappa^2 \sin^2 2k_1 a} \quad (5.16)$$

where  $k_1$  represents the wave vector in the denser region  $\rho_1$  and is given as  $k_1 = 2\pi/\lambda_1$  where  $\lambda_1$  is the wavelength of the wave propagating inside the step. Here the  $\sin^2 2k_1 a$  term describes possible oscillations in the reflection coefficient when the width of the step function is increasing with an expansion in  $2a$  of the order of  $2\Delta a$  considering the symmetry of the model so that  $2a \rightarrow 2a + 2\Delta a$ . The oscillations have a repetitive nature and are repeated at periods of  $\pi$  so that  $2k_1 a \rightarrow 2k_1 a + \pi$ . We then obtain a relation,

$$2\Delta a = \frac{\pi}{k_1} = \frac{\lambda_1}{2}. \quad (5.17)$$

These give reflection resonances of equidistant periods of  $\lambda_1/2$ . The result obtained from the step model (equation (5.17)) states as the stripe width increases by  $2\Delta a$ , reflection resonances will occur at separations of  $2\Delta a = \lambda_1/2$ . If we compare this with the actual changes in the contact width,  $d_0$  of  $\Delta d$  we should obtain for small surface loadings a relation  $\Delta d = \lambda_1/2 \approx \lambda_0/2$ , where  $\lambda_0$  is the wavelength of the acoustic wave. The observations in the experimental data, however, show that the average changes in the contact width,  $\Delta d$  is approximately  $\lambda_0$ . Another problem in the step model approximation is that reflection resonances should appear at equidistant spacing of  $2\Delta a$ . The evaluation of the experimental data for the reflection on the other hand do indicate changes in peak separation from a wavelength larger than the SAW wavelength,  $\lambda_R$  of the unloaded SAW device to less than a SAW wavelength,  $\lambda_R$ . This is clearly not covered by the step model approximation discussed here.

## 5.5.2. Dispersion

The approximation discussed in section 5.5.1. models the stripe as two consecutive steps and so does not include a change in height,  $h_0$ . A change in height,  $h_0$  introduces dispersion of the surface wave which causes a variation in acoustic wavelength of a SAW under the fluid loaded part of the SAW substrate. In a thin film limit the dispersion increases with larger values of thickness and in the case of volume conservation this indicates smaller values for the stripe width,  $d_0$ . The increase in mass loading per unit area should result in a systematic decrease in wave velocity. However, the stripe does not represent a thin film limit. The changes in phase speed of the acoustic wave, arising from the resonator model discussed in section 5.2. equation (5.8) and the condition ( $\Delta\omega/\omega = \Delta v/v$ ) gives

$$\Delta v = -\frac{1}{2\pi\rho_s\xi} \operatorname{Im} \left[ \frac{\beta}{1+i\omega\tau} \right]. \quad (5.18)$$

and this can be used to examine possible dispersion. The factor  $k_1d$  of section 5.4.1., needs to be modified, to take account of surface wave dispersion. Hence,  $k_1$  can be expressed as  $k_1(h)$ . Within the context of the resonator model, reviewed in Chapter 2, section 2.3. the analysis of equation (5.1) reveals, when the  $\omega\tau$  term dominates that the argument of the tanh term in equation (5.4) becomes purely imaginary and may then contribute to a strong oscillatory behaviour with a period dependent on  $t_f$ . This is shown in Fig. 5.1 and Fig. 5.2 for  $\omega\tau = 50$ , and so indicates a periodic variation. Closer examination of the periodic structure of the tanh term shows that within changes of the slope characteristic at the point where the slope is approaching zero ( $\Delta\omega/\omega = 0$ ) the acoustic wavelength (we will call the acoustic wavelength under the fluid loaded substrate,  $\lambda_{dis}$ ) is approximately the wavelength of the unloaded substrate,  $\lambda_R$  and this is periodically repeated. The extreme limits of  $\Delta\omega/\omega$  define one periodic variation and span over several wavelengths. The dispersion wavelength decreases from a value larger than the SAW wavelength,  $\lambda_R$  of the unloaded

substrate to a value less than the SAW wavelength of the unloaded substrate. Fig. 5.11 shows quantitatively the variation of the acoustic wavelength under fluid loading condition. The periodic repetition of the structure appears at the positions where significant attenuation resonances are present (positions A and B). The symmetry line emphasizes the zero slope point in the tanh term where  $\Delta\omega/\omega = 0$ .

A comparison with experimental data may indicate a dispersion wavelength close to the SAW wavelength at this point. However, this argument is based only on a single periodic variation in the tanh term as this can be seen in Fig. 5.11, but does seem to be consistent within all experiments. The present experimental results indicate that a periodic repetition of reflection resonances in the reflection signal may exist more than once, but are only clearly structured between two consecutive attenuation resonances such as A and B in Fig. 5.11. A closer look at the results presented in Chapter 4 reveal an inconsistent structure of resonance peaks to appear before the first resonance peak reaches its maximum. Moreover the structure follows the same overall attenuation characteristics as this is seen in the reflection resonances between A and B in Fig. 5.11. Especially the strong oscillatory structure before resonance peak A (Fig. 5.11) shows a possible similarity to the reflection resonance structure seen between A and B but is very inconsistent in period and course of signal amplitude response. A possible explanation for this problem can be seen in the relatively low speed of the data acquisition of the measurement system and only a dramatic decrease in the acquisition time may resolve the problem.

The suggested dispersion may explain the variation in the acoustic wavelength. However, dispersion is only capable of describing the changes in acoustic wavelength and is not able to explain the existence of reflection resonances. The step model including dispersion would explain the structure in the reflection resonances observed in all experimental data, but the condition  $\Delta\omega/\omega = 0$  would suggest that  $\lambda_{dis} \approx \lambda_R/2$ , which contradicts with the observed  $\lambda_{dis} \approx \lambda_R$  in the centre (centre line, Fig. 5.11) between the two attenuation resonances A and B.

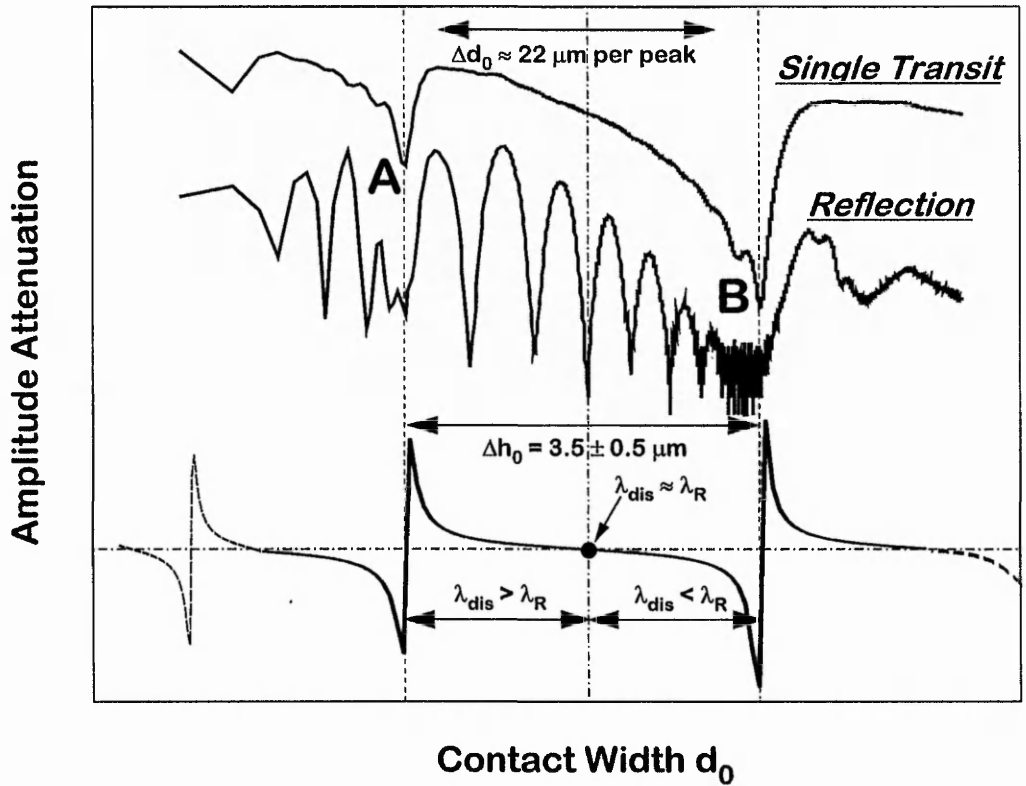


**Fig. 5.11** The periodic variation as shown in Fig. 5.2 with a repeated pattern of large deviations, both positive and negative about the unperturbed frequency with possible location at consecutive attenuation resonances at A and B in the single transit signal. The periodic variation are showing dispersion of the acoustic wavelength,  $\lambda_{dis}$  from larger than the unloaded wavelength,  $\lambda_R$  to less than the unloaded wavelength,  $\lambda_R$ .

### 5.5.3. Triangle Model Approximation

To model the reflection resonances it is necessary to amend the step model approximation which uses the two consecutive steps. A possible approximation is a triangle geometry as presented in Fig. 5.12, since it will have no perpendicular faces to the surface. Such a model would introduce a geometry with slopes which approximates closer the nature of the stripe. However, solving such a model is more involved and has not been attempted. Physically, a front edge and back edge reflection is likely to occur thus leading to interference effects and resonances. In the step model with its perpendicular faces (Fig. 5.10) localised reflections occur directly at the faces of the steps. In the triangle model the reflections are distributed across each of the slopes as this is outlined in Fig 5.13, so that the effective centres of reflections are no longer at the edges of the stripe. If we consider the effective reflection centre to be in the centre of the slope then  $d$  needs to be changed by  $\lambda_1$  to move the reflection centres apart by  $\lambda_1/2$  and so move from one reflection resonance to the next. The changes in contact width by  $2\Delta d$  would then account for separation of existing consecutive resonance peaks in the reflection signal of the order of one acoustic wavelength. To account for variation in acoustic wavelength the model needs to consider, additional to the separation of reflection resonance peaks of equidistant separation of one wavelength, the effect of dispersion which provides a possible explanation for the variation in the reflection resonances. Here the triangle model is capable to model the existing variation in fluid height of the spreading stripe. Other than in the previously discussed two consecutive step model, a variation in height in the triangle approximation (Fig. 5.12) effectively includes the effect of wavelength dispersion. However, further work is required to develop such a model for computational analysis.

Investigating dynamic wetting using surface acoustic waves has proven to show more than the simple exponential decline of the transmission signals. It has revealed a rich structure of possible attenuation resonances with asymmetric shape. The existence of a reflection signal reflected at the edge of a dynamically evolving stripe showed a periodic structure of resonance peaks

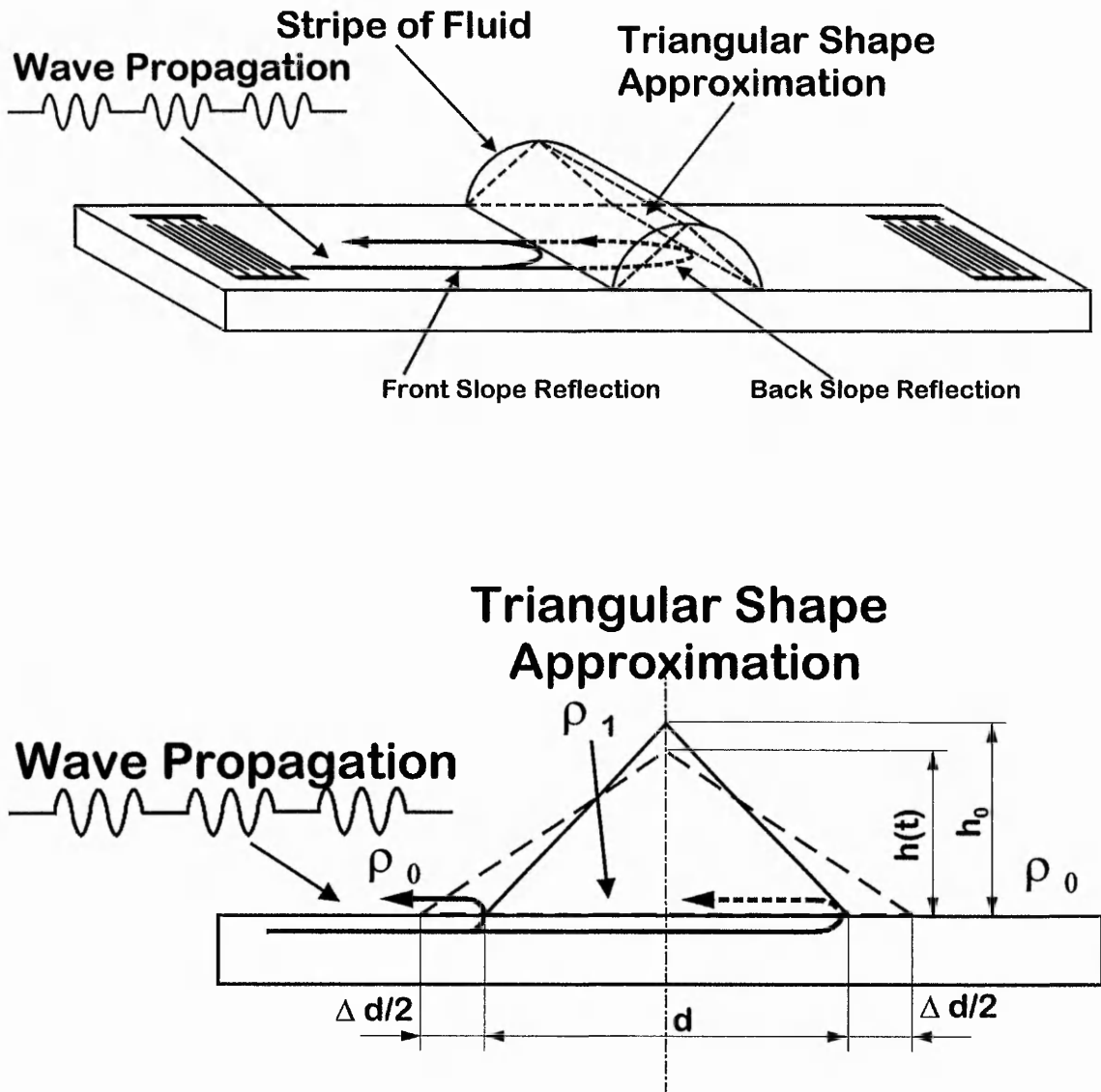


**Fig. 5.12** The amended model uses a triangular shape approximation. The model follows the same principle discussed for the reflection resonances in the step model. Variation in  $d$  by  $\Delta d$  shows periodic equidistant separation by a full wavelength of reflection resonances. However, the triangle model, other than the two consecutive step model accounts for changes in height by  $h(t)$ , which allows dispersion to occur.

## Triangular Shape Approximation

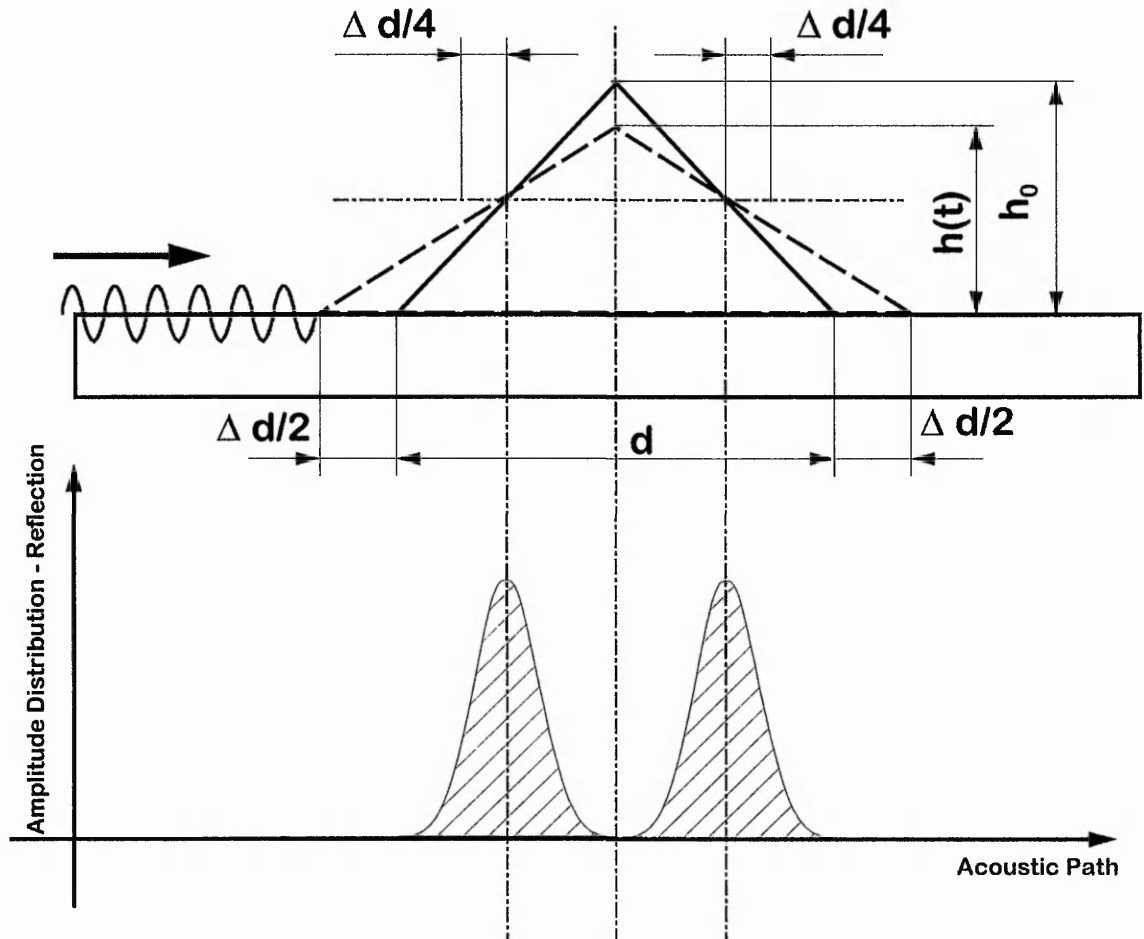


**Fig. 5.13** The energy distribution of the reflection along the slopes of the triangular shape can be seen. The step model on the other hand has localised reflection directly at the faces of the two consecutive steps.

with a variation in separation of these peaks about larger than a SAW wavelength to less than a SAW wavelength of the unloaded substrate. The results discussed here do indicate that the surface acoustic wave technique, which monitors changes in the geometrical parameters of the liquid, means that the deconvolution of this information is by no means straight forward. These problems may be at their most extremes with experiments that use both highly viscous liquids and macroscopic shapes of fluids.

In the resonance model discussed here, longitudinal waves in the liquid, which are also excited by surface acoustic waves, are neglected. However, it is clear that the main structure of the attenuation in the transmission coefficient are described by the model. In contrast to the scaling parameter,  $\xi$  the location of the resonances depends on the relaxation rate,  $\tau^{-1}$ , and the measured frequency and fluid volume. These parameters are more precisely defined and a greater consistency in the relaxation rate can be expected.

In the extreme limits of a single relaxation time especially at the Newtonian region and with thin films the acoustic technique will be highly mass sensitive and this could mean that changes in the film thickness or wetted area may simplify the matter. However, the prediction based on the model propose, due to the large relaxation time limit, that the fluid behaves acoustically as a creeping amorphous solid. The resonances in the transmission coefficients are then due to the stripe height acting as a vertical cavity that matches wave resonances in the fluid.

# CHAPTER 6

# *CONCLUSION*

## 6.1. Conclusion

The dynamic evolution of liquids partially localised on a solid substrate has traditionally been studied or investigated using optical observations such as contact angle meters or interferometry. These conventional techniques work either by using plan views, as in interferometric measurements, or using side view measurements as in the contact angle meter approach to investigate the contact angle formation. Studies of the dynamic changes of the side profile of a droplet of liquid allow simple cross-section parameters to be obtained such as the diameter of the droplet, and the spherical cap with respect of time. With the aid of video image analysis, the changes in droplet geometry can be conveniently extracted. This enables one to investigate the dynamics of a spreading liquid on various interfaces and gather information of the spreading process.

Alternatively, the use of the acoustic technique to sense dynamic changes in fluid shape has been rarely considered in the literature. The perceived potential of the acoustic technique lies not in the ability to measure liquid properties better, but to provide information about solid-liquid interactions both in-situ and with high mass sensitivity. The use of surface acoustic waves introduces the potential to sense the dynamics of a liquid spreading on the solid-liquid interface directly in the spreading plane and to investigate the changes of the wetting behaviour of the liquid in real time. SAW's are more sensitive to mass loading than for example the widely used QCM's and therefore allow changes in sub-monolayer surface coverage to be detected. Moreover, acoustic devices can sense changes in elasticity, in contrast to interfacial mass and this gives them clear potential to be used in studying the properties of films, etc.

This thesis has investigated the dynamic evolution of localised highly viscous stripes of non-volatile oils by monitoring changes in acoustic signals generated by Rayleigh surface acoustic waves. Three signals have been identified, a reflection due to the front edge of the fluid reflecting the signal back to the transducers and two transit signals; a single transit signal passing once through the liquid phase along the solid-liquid interface and a double transit

signal passing twice through the liquid when propagating in the acoustic path. Changes in geometrical proportions of stripes spreading along the solid-vapour interface show that geometrical parameters defining the stripe's contact width, contact angle, height and cylindrical cap radius follow well-defined power laws. As the oil spreads it interacts with the pulsed surface wave and produces a rich structure in the transit signals and the reflection. The signal response of the transit signals does not simply show an exponential decay in signal amplitude when the fluid coverage increases but show oscillatory changes in signal amplitude with strong local attenuation resonances of asymmetric shape. These asymmetric resonances occur slowly as the fluid width increases by several acoustic wavelength. Both transit signals are mirroring each other in trend and are progressively attenuated as the oil wets the surface. An approximate single relaxation time viscoelastic fluid model has been developed to explain the overall resonance behaviour of the transit signals. The viscoelastic behaviour of the fluid follows the Maxwellian model which approximates the viscoelasticity of an arbitrary liquid by a spring-dashpot element. Variation in fluid viscosity have been conducted to investigate the influences of characteristic speeds of the different fluids, modulating signal response and signal characteristics, to study and compare location and appearance of the transmission resonances within experiments. Signal characteristics, when applying the model to the signal trends, suggests that all examined fluids are within a large relaxation time limit and that the stripe of fluid acts acoustically as a creeping amorphous solid rather than a liquid. The resonances in the transmission coefficient may then be due to the stripe height acting as a vertical cavity that matches shear wave resonances in the fluid.

The appearance of strong reflection resonances in the reflection show a systematic formation of peaks which varies from five to seven peaks between experiments. The magnitude in amplitude of the reflection changes as the liquid spreads along the surface and the overall envelope of the reflection resonances indicates that the amplitude of the reflection signal is being modulated by the progressive attenuation of the transmission signals. These reflections show maxima and minima that are correlated with optically observed changes in contact width. Possible approaches to model the characteristics of reflection maxima and minima based on front edge and back edge reflections from an

effectively solid stripe have been discussed. A simple consecutive step model has been described. Such an approach provides periodic changes in the reflection signal as the stripe width increases. A triangular cross-sectional shape has then been discussed as an alternative approximation to the stripe. Other than the step model the triangular model introduces distributed reflections from the front edge and the back edge slopes and provides a possible mechanism for shortening the stripe width change, needed for the periodic variation in reflection signals. The consequences for the reflection signal of the shear wave model used for the transit signals have also been discussed. The model should introduce a variation in the phase velocity of the SAW's when propagating along the solid-liquid interface. The phase velocity is modulated by the changes in stripe width and fluid height and so systematically changes the separation between reflection maxima as the stripe spreads. A prediction of the model is that the pattern of reflection maxima will repeat between each pair of consecutive minima in the transit signals.

The high level of detail in geometrical variations of contact width and height that highly viscous stripes of oil produce on the solid substrate of a SAW device suggests that the use of the acoustic technique for investigating dynamic changes of liquids spreading across the surface of the SAW sensor can clarify the mechanisms of acoustic wave-liquid interactions. Such interactions could then be used for acoustic testing of small amounts of liquid. Investigation into the viscoelastic behaviour of the liquid reveals that the large relaxation time limit corresponds to a creeping solid. This has direct implications for the application of other acoustic sensors probing liquid properties such as viscosity or the elasticity of a fluid. Attenuation resonances observed in the spreading process, which are also likely to occur in QCM techniques, suggests care is needed as the fluid examined may be acoustically solid rather than liquid. The interpretation of the oil as an acoustic solid, the high level of symmetry of the stripe and its dynamic evolution may also provide a simple test problem for the interaction of SAW's with spatial surface inhomogeneities.

## 6.2. Further Development

A novel approach of characterising the dynamic evolution of small amounts of viscous liquids using a Rayleigh surface acoustic wave sensor has been presented and possible mechanisms explaining the main features observed in the reflection and transmission coefficient of SAW's have been discussed. The experimental data show a high degree of consistency within experiments. The presence of asymmetric transmission resonances and the existence of oscillations described as reflection resonances with a dispersive nature in separation of strong maxima in the reflection should enhance knowledge in the understanding of surface acoustic wave-liquid interactions. The combination of the acoustic technique with the spreading of partially localised fluids has rarely been considered in the literature and much work needs to be done to understand the complex nature of these interactions.

The presence of transmission resonances in both the double transit and single transit signal, may be attributable to shear wave resonances in the liquid. These resonances occur cyclically and correspond to the stripe height matching  $n\lambda_s/4$ , where  $n$  is odd and  $\lambda_s$  is the shear wavelength. However, experimental data so far obtained only show two to three distinct resonances in the transmission coefficient. The  $\omega\tau$  limit characterises the period of these resonances. In our situation this is dependent on the viscosity and the shear modulus of the fluid and on the frequency of operation of the SAW device. The appearance of reflection resonances in the reflection signal between two consecutive attenuation resonances in the transmission signals has indicated that the systematic series of maxima evident in the experimental data may be cyclic and depend on the systematic appearance of the transmission resonances. With the limited number of these transmission resonances observed in the experiments, only one systematic series of peaks in the reflection could be resolved. The appearance of inconsistent peaks shortly after deposition of the stripe, however, suggest the possibility of periodic sets of maxima in the reflection coefficient. To investigate that matter in greater detail, it would be necessary to increase the frequency of operation of the surface acoustic wave device to decrease the wavelength and so observe more

resonances for a given stripe. This would allow more sets of transmission and reflection resonances to appear. Alternatively, a faster data capture system could be constructed. It is predicted that one sequence of reflection resonances with a systematic set of maxima is similar to the neighbouring set; and that each of these sets of reflections are consistent with the optically observed changes in width of the oil of one surface acoustic wavelength of the unloaded substrate.

Limitation in the deposition technique of liquid stripes by applying the fluid with a razor blade onto the substrate surface requires an alternative method of stripe deposition to control the amount of deposit volume and so achieve a better rate of similar volumes of fluid deposited on the substrate. The razor blade deposition technique is more likely to show scatter of the stripe shape along the stripe length and inhomogeneous distribution of fluid volume across the stripe length is possible. Also the technique is considered as less practicable if oils of lower viscosity are deposited. Discontinuous stripe formations along the stripe length are more likely to occur affecting significantly the analysis and the signal responses. The hydrostatic pressure will cause the fluid to rise up the blade tip. Tests with stretched fibres have shown more reliable results and a higher consistency in stripe geometry and volume distribution of the fluid along the stripe length. However the width of a deposit stripe is largely dependent on the diameter characterising the fibre. The fibre diameter will mainly define the volume of oil applied onto the substrate. A reduction in fibre diameter also could mean that lower viscous oils will not completely wet the fibre due to a reduced surface area. The hydrostatic pressure will largely affect the formation of oil along the fibre and eventually cause a chaining up of small droplets which will distort the stripe geometry along the contact lines considerably resulting in a misshaped stripe. This will put constraints on the deposition techniques. However, the fibre deposition technique will ensure that the deposition of liquid stripes of the same viscosity will produce more similar stripes of similar volume per unit length along the substrate. The diameter of such a fibre controls better the deposited amount of oil on the surface. The hydrostatic pressure will force the oil to build a barrel shape around the fibre diameter and therefore ensure that the accumulation of the oil will be less localised and more evenly distributed along the fibre. With

the razor blade method this is difficult to achieve when especially low viscosity oils are used.

An application of the acoustic technique may be to examine the existence of a mesoscopic precursor film which spreads ahead of the body of the fluid. At a very detailed level, polydimethylsiloxanes, as used in all the experiments may represent some quite specific features. Although a spherical cross-section of the stripe is observed at the macroscopic level, this may not hold at the microscopic level. As the fluid profile approaches the solid surface van der Waal's forces acting at the contact line of the fluid and may cause deviations from the cylindrical cap shape. The possibility of a precursor film of molecular thickness spreading ahead of the fluid may exist in the long time limit. To probe such a precursor, a drop of oil rather than a stripe could be located outside of the acoustic path close to the SAW transmission path. Changes in transit signals might then be observed as the drop's precursor spreads into the acoustic path long before the macroscopic cap would reach the path. Such changes may then indicate the presence of a precursor film spreading ahead of the bulk of the drop. It is also possible to use the SAW device to observe the spreading of a drop rather than a stripe within the acoustic path. This would enable one to investigate the drop geometry using the acoustic technique and compare transmission resonances within the two geometries. This problem could be simply inverted by the idea of observing the evaporation rate of a drop of volatile liquid in the acoustic path instead of the spreading process. This would represent a small  $\omega\tau$  limit and the liquid can be considered as a Newtonian fluid ( $\omega\tau \rightarrow 0$ ). The liquid entrained in a shearing motion by the substrate is then in the limit of the film thickness of the order of a penetration depth (Chapter 5). This would imply that attenuation resonances due to shear waves would vanish. However, the existence of compressional waves caused by the out-of-plane motion of the Rayleigh surface acoustic wave may then influence the amplitude response which will result in strong signal attenuation when the SAW interacts with the fluid. Provided that the fluid thickness is greater as the penetration depth the acoustic film will act as an interfacial mass sensor.

Another aspect of surface waves propagating on piezoelectric substrates is the existence of an electric field displacement in addition to the acoustic disturbance. This electroacoustic interaction could be used to probe and monitor the interfacial changes of conducting liquids due to ionic changes in solution. This will provide the possibility to study transition effects in liquids. If the surface is chemically modified in order to control the polarisation of the surface, for example by silanisation, the wetting dynamics of a spreading liquid could be controlled since different equilibrium condition on the surface can be achieved. The surface free energy controls the wetting dynamics and this could be probed in-situ and in real time by SAW's.

In the model for the transmission resonances the vertical displacement component of the Rayleigh surface acoustic wave, the out-of-plane component is neglected. The fitted relaxation rate for the PDMS oils corresponds to the amorphous solid limit. It is not expected, that in this limit neglecting the overlayer compressibility will be critical for the Rayleigh wave mode, although it may influence the precise value of the fitting parameter. However, the characterisation of the wetting dynamics and the existence of the resonances in the transmission is not greatly affected by excluding the vertical displacement of the acoustic wave in the model. It is clear that the main structure of the resonances is well described by the proposed model. In order to confirm the contribution of the in-plane motion of the surface acoustic wave it would be of interest to use horizontally polarised surface acoustic waves (SH-SAW's). This would enable one to determine whether transmission resonances are entirely due to shear waves in the fluid or if contributions by compressional waves also excited by the Rayleigh SAW's contribute to the losses in acoustic wave energy.

This thesis has provided the framework for investigating interaction mechanisms of Rayleigh surface acoustic waves with partially localised highly viscous liquids. The wetting dynamics of different viscosities of PDMS liquids have been investigated and correlated with dynamic changes in fluid geometry. The observation of resonances in the transmission and reflection coefficient complements other work investigating Rayleigh SAW's interacting with spatial surface inhomogeneities. The use of a surface acoustic wave technique which is intrinsically located in the plane of the solid-liquid interface could be a useful

tool to study such phenomena in more detail and enhances the theoretical understanding of such interaction effects.

# ***APPENDIX***

## Appendix

### Conversion Charts for Amplitude Attenuation Levels and Contact Diameter, $d_0$ Predicted from the Power Law relation

For each experimental result displayed in Chapter 4 a set of two graphs are presented. The first graph for each experimental result shows the power law relation of the contact width,  $d_0$  in dependence of the time in which a stripe of liquid evolves. The second graph is the conversion chart of the amplitude magnitude obtained by the mean function measurements (Chapter 3, section 3.5) using a logarithmic power series and converting the equivalent losses in SAW amplitude caused by the spreading liquid into attenuation (dB).

Table A1, represents the coefficient extracted from the power law fits for the contact width parameter,  $d_0$ . The second table, Table A2, contains the necessary coefficient for the logarithmic power series for the conversion charts (see also Chapter 3, section 3.7)

**Table A1** Geometrical fits for the contact width,  $d_0$  from the optical measurements for PDMS oils spreading on lithium niobate.

Fig.	$\eta$	$d_0$ $k_1$	$d_0$ $c$	$d_0$ $n$
4.12	100,000	99.95	- 80	7.13
4.13	30,000	112.08	5	6.70
4.14	10,000	128.93	30	6.81
4.15	1,000	172.4	5	6.48
4.16/17 (a) <sup>1)</sup>	100,000	92.8	5	6.90
4.16/17 (b)	100,000	94.1	14.9	7
4.18/19 (a)	100,000	88.5	166	6.74
4.18/19 (b) <sup>1)</sup>	100,000	92.8	5	6.90
	cSt			

**Table A2**

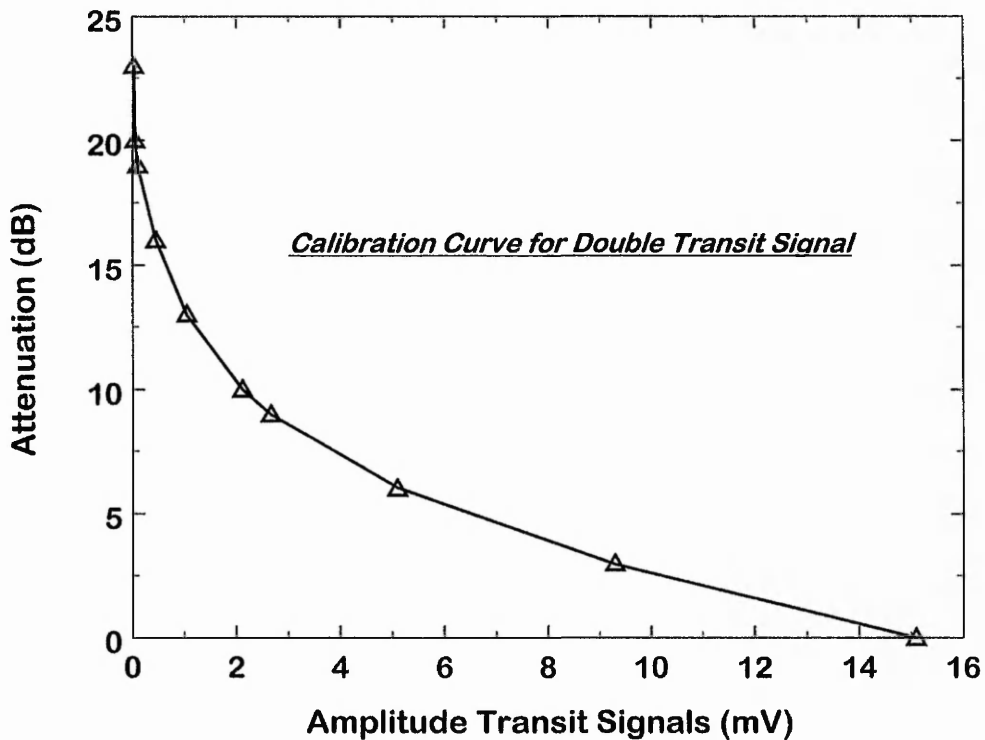
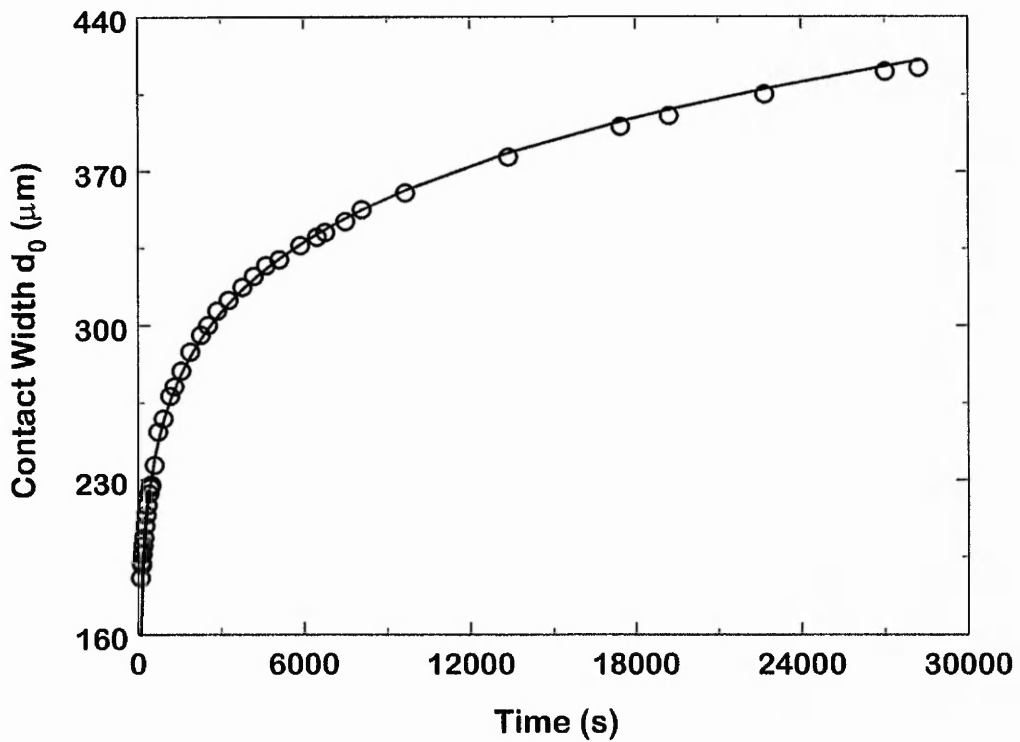
The coefficient,  $A_1 - A_8$  and the constant,  $C$  for the logarithmic power series to determine the conversion function for the amplitude magnitude of the single and double transit to convert the mean value into attenuation in dB.

Fig.	$C$	$A_1$	$A_2$	$A_3$	$A_4$	$A_5$
DT - 4.12	-13.1661	9.18638	2.0312	-1.7948	0.5065	0.81467
ST - 4.13	-23.4899	8.8377	-0.381	1.177	0.7758	-0.328
DT - 4.13	-16.4595	8.4059	3.761	-0.427	-2.744	1.732
ST - 4.14	-22.9385	8.5678	-0.401	1.189	0.8019	-0.327
DT - 4.14	-16.4001	8.3999	3.689	-0.432	-2.801	1.820
DT - 4.15	-15.9769	9.1036	3.661	-2.144	-2.483	3.227
DT - 4.16 (a) <sup>1)</sup>	14.0954	-4.59716	-0.49697	0.13717	0.11527	-0.023991
DT - 4.16 (b)	-16.2412	8.3718	5.571	1.175	-5.520	0.0108
DT - 4.18 (a)	-16.0942	8.8923	4.797	0.9606	-4.373	0.1656
DT - 4.18 (b) <sup>1)</sup>	-16.2412	8.3718	5.571	1.175	-5.520	0.0108

Fig.	$A_6$	$A_7$	$A_8$
DT - 4.12	-0.14468	-	-
ST - 4.13	-0.028	0.0626	-
DT - 4.13	0.573	-0.3787	-
ST - 4.14	-0.030	0.0630	-
DT - 4.14	0.582	-0.3888	-
DT - 4.15	0.567	-0.869	0.015
DT - 4.16 (a) <sup>1)</sup>	-0.010417	-	-
DT - 4.16 (b)	1.8131	-	-
DT - 4.18 (a)	1.3911	-	-
DT - 4.18 (b) <sup>1)</sup>	1.8131	-	-

<sup>1)</sup> using the same experimental data set.

DT = double transit pulse; ST = single transit pulse



**Fig. A1** The contact width,  $d_0$ , (top chart) for experiment Fig. 4.12 using 39 stripe images (Table A1). Conversion of acoustic losses of the double transit measured in mV (mean value) into attenuation (dB), Table A2.

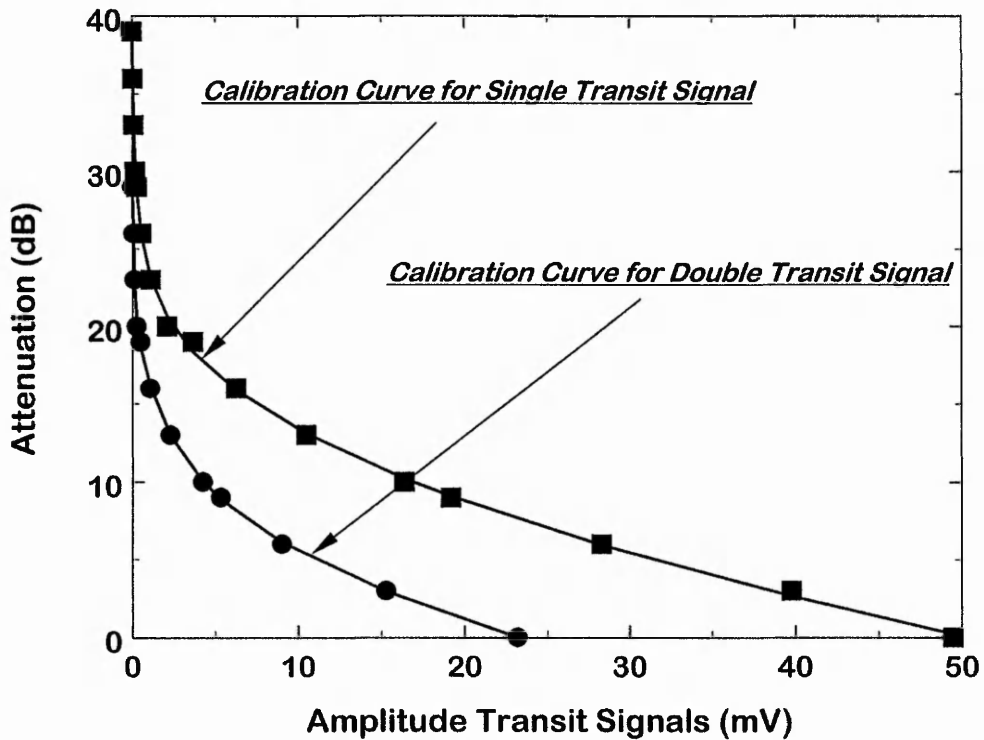
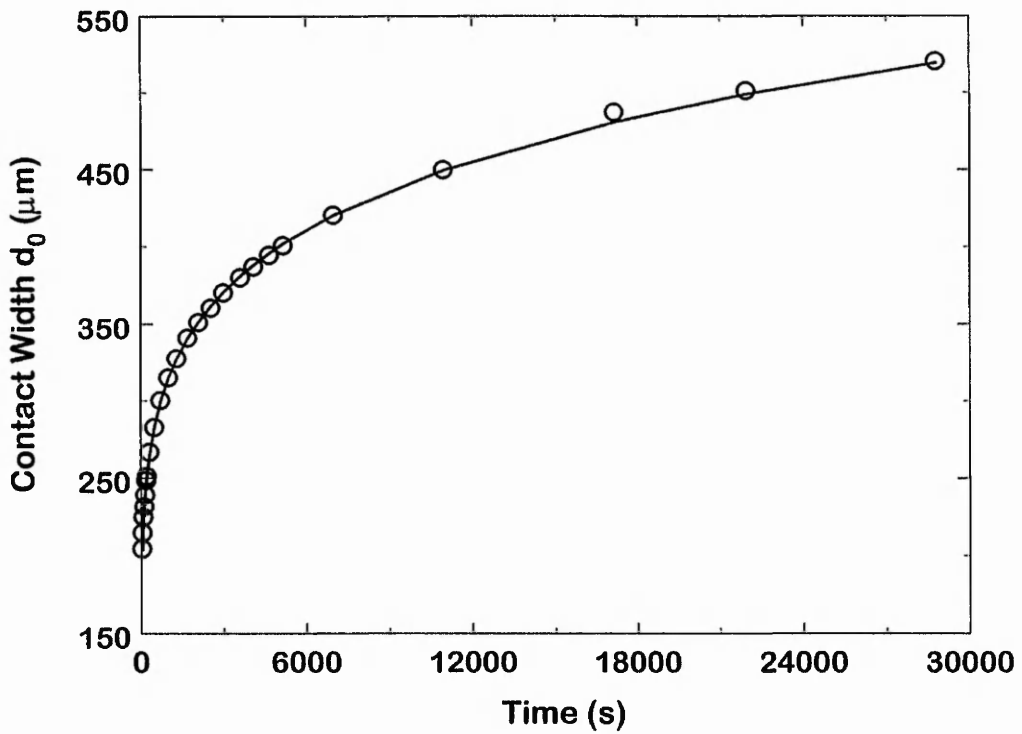


**Fig. A2** Contact width,  $d_0$ , (top chart) for experiment Fig. 4.13 using 25 stripe images (Table A1). Conversion of acoustic losses of the double transit and single transit measured in mV (mean value) into attenuation (dB), Table A2.

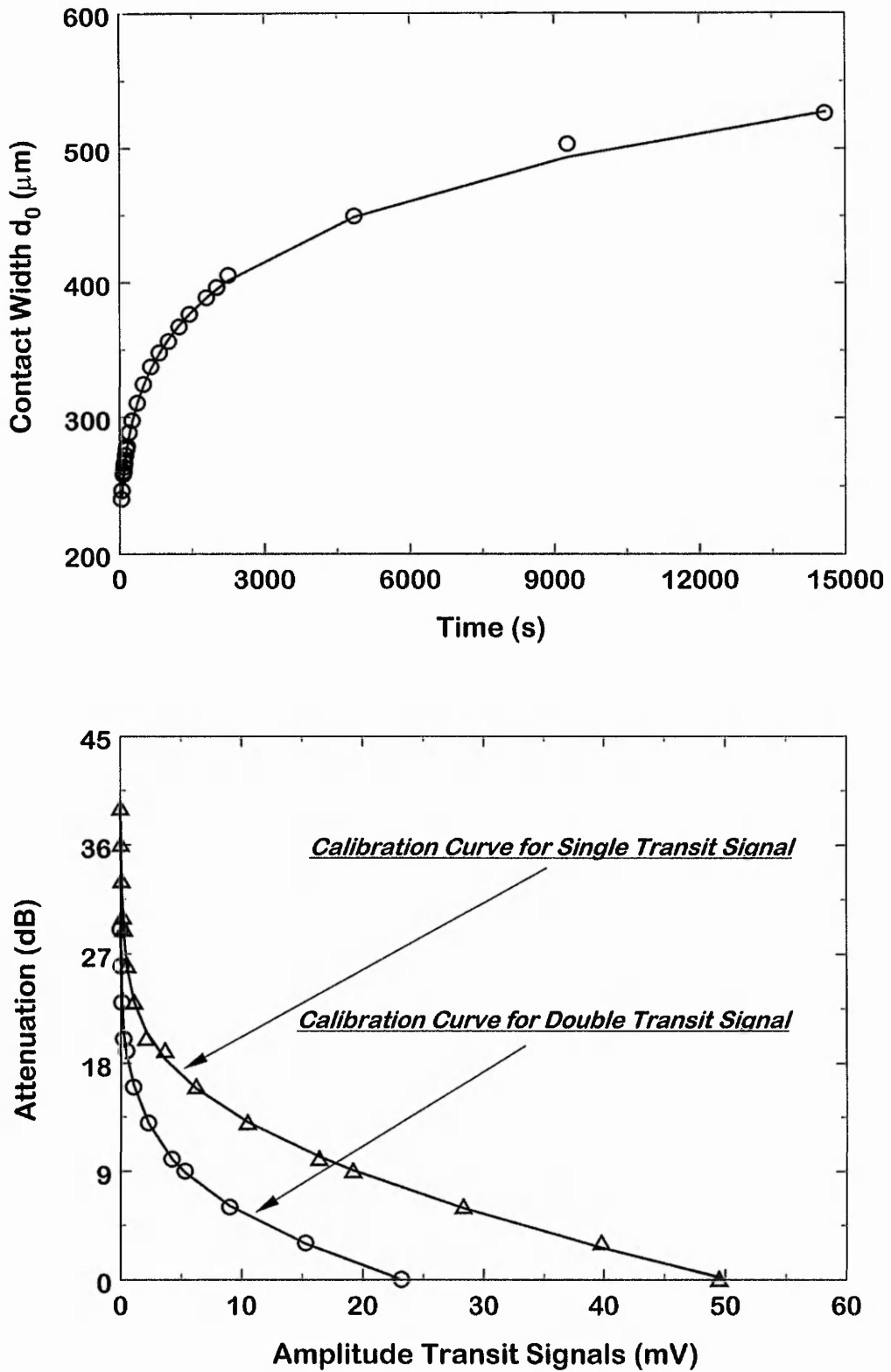


**Fig. A3** Contact width,  $d_0$ , (top chart) for experiment Fig. 4.14 using 24 stripe images (Table A1). Conversion of acoustic losses of the double transit and single transit measured in mV (mean value) into attenuation (dB), Table A2.

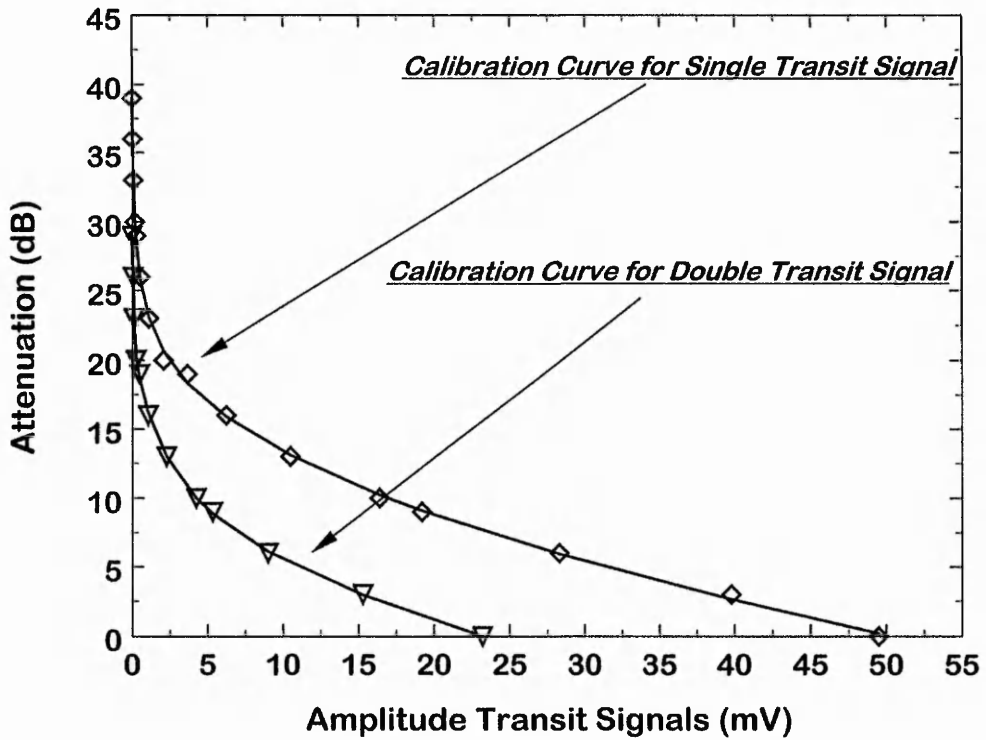
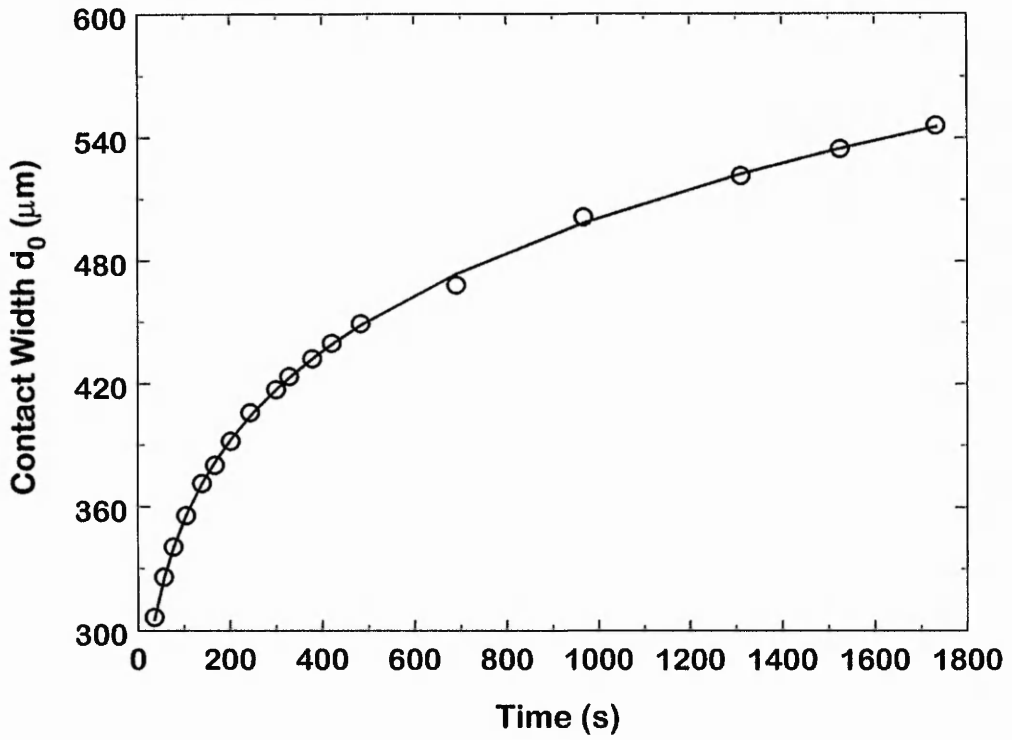


**Fig. A4** Contact width,  $d_0$ , (top chart) for experiment Fig. 4.15 using 18 stripe images (Table A1). Conversion of acoustic losses of the double transit and single transit measured in mV (mean value) into attenuation (dB), Table A2.

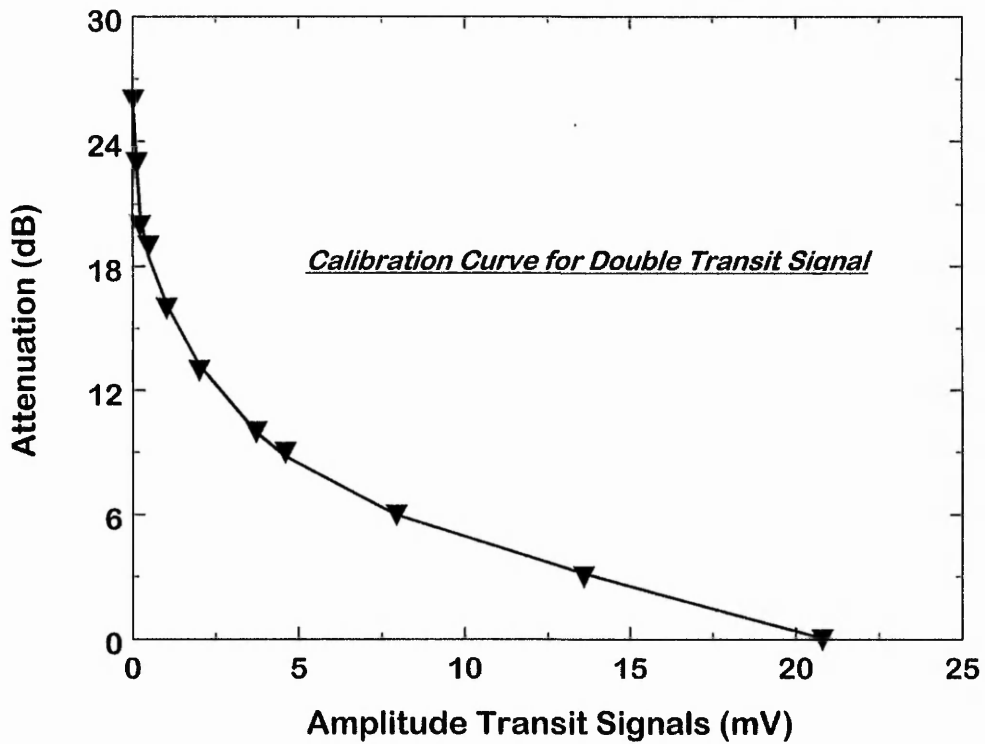
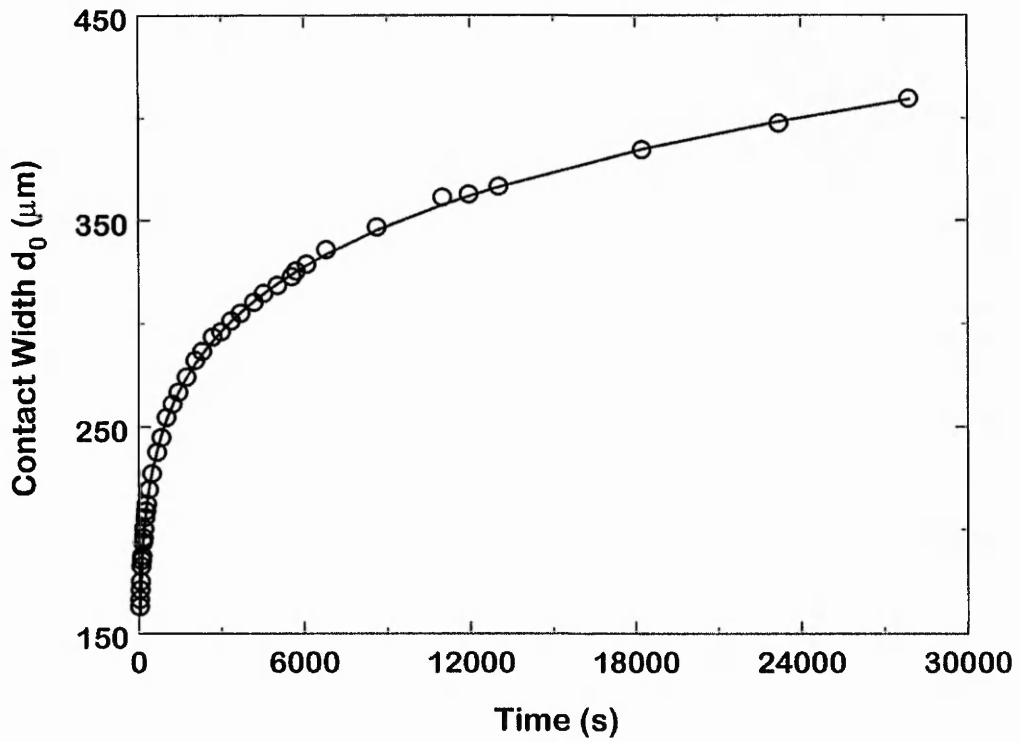


**Fig. A5** Contact width,  $d_0$ , (top chart) for experiment Figs. 4.16 (a) and 4.18 (b) using 41 stripe images (Table A1). Conversion of acoustic losses of the double transit measured in mV (mean value) into attenuation (dB), Table A2.

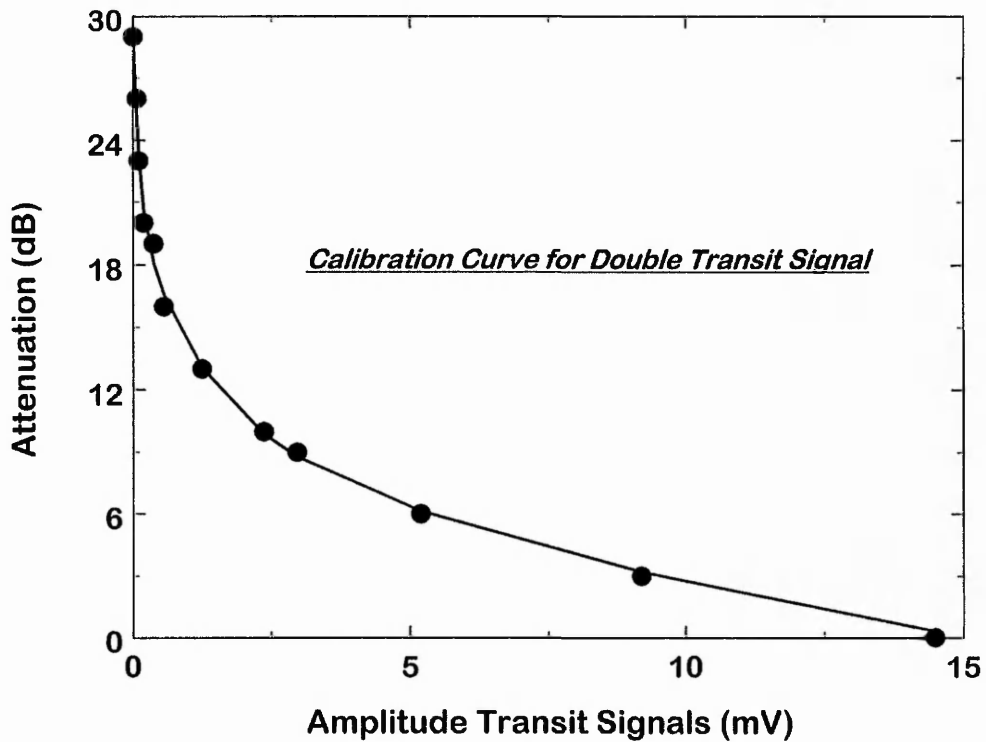
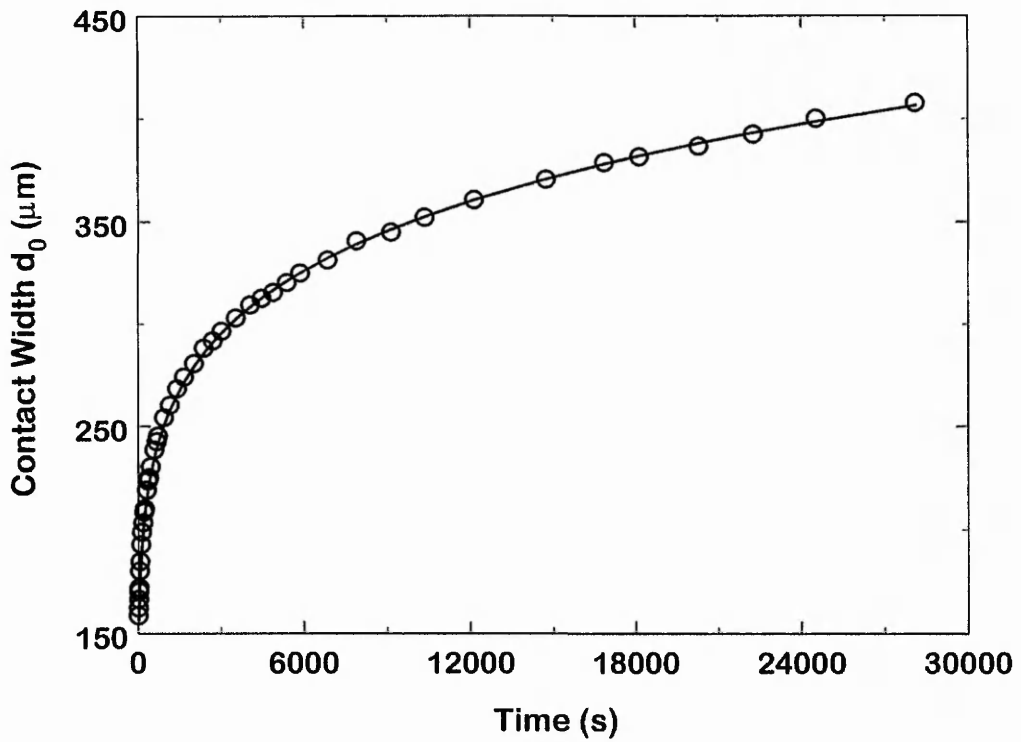


**Fig. A6** Contact width,  $d_0$ , (top chart) for experiment Figs. 4.16 (b) using 45 stripe images (Table A1). Conversion of acoustic losses of the double transit measured in mV (mean value) into attenuation (dB), Table A2.

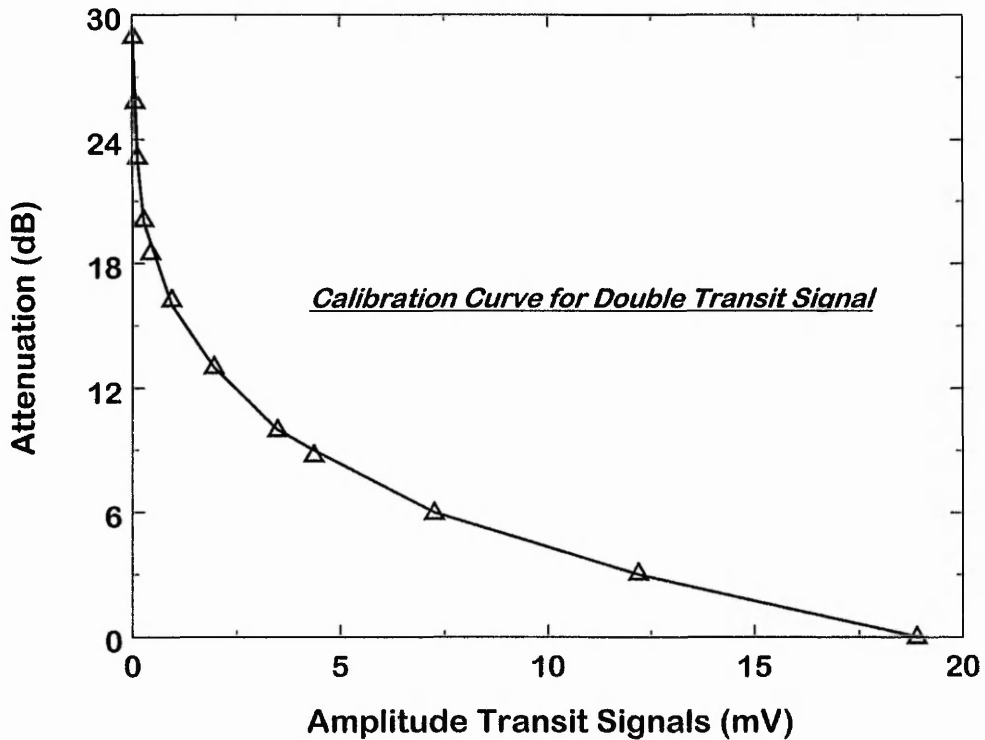
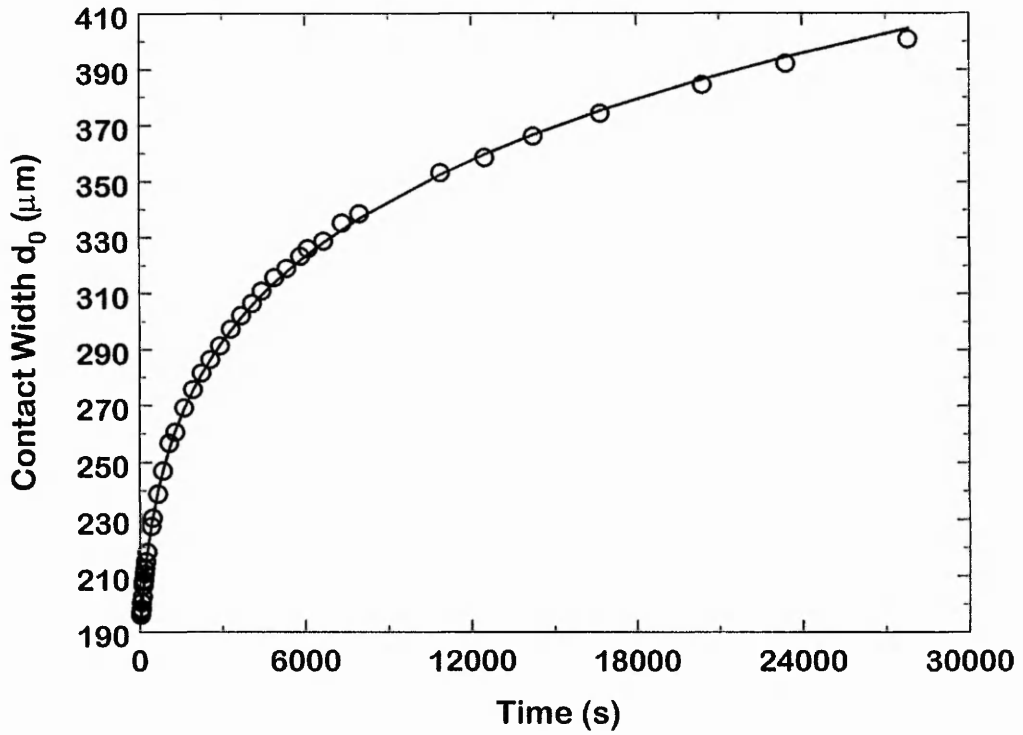


**Fig. A7** Contact width,  $d_0$ , (top chart) for experiment Figs. 4.18 (a) using 41 stripe images (Table A1). Conversion of acoustic losses of the double transit measured in mV (mean value) into attenuation (dB), Table A2.

# REFERENCES

- [1] L. Léger and J.F. Joanny, "Liquid spreading", *Reports on Progress in Physics*, **1992**, *55*, 431.
- [2] D. S. Ballantine, R. M. White, S. J. Martin, A. J. Ricco, E. T. Zellers, G. C. Frye, H. Wohltjen, *Acoustic Wave Sensors : Theory, Design, and Physico-Chemical Applications*, Academic Press: New York 1997.
- [3] H. Wohltjen, "Chemical microsensors and microinstrumentation", *Analytical Chemistry*, **1984**, *56*, 87A.
- [4] R. S. Muller, R. T. Howe, S. D. Senturia, R. L. Smith, R. M. White Eds., *Microsensors*, IEEE Press: New York 1990.
- [5] J. W. Grate, A. Snow, D. S. Ballantine, H. Wohltjen, M. H. Abraham, R. A. McGill and P. Sasson, "Determination of partition coefficients from surface acoustic wave vapor sensor responses and correlation with gas-liquid chromatographic partition coefficient", *Analytical Chemistry*, **1988**, *60*, 869.
- [6] D. S. Ballantine, H. Wohltjen, "Surface acoustic wave devices for chemical analysis (Report)", *Analytical Chemistry*, **1989**, *61*, 704A.
- [7] M. Madou and S. R. Morrison, *Chemical Sensing with Solid-State Devices*, Academic Press: New York 1989
- [8] J. W. Grate, S. J. Martin and R. M. White, "Acoustic TSM, SAW, FPW, APM wave microsensors; Part I (Report)", *Analytical Chemistry*, **1993**, *65*, 940A.
- [9] H. Kolsky, *Stress Waves in Solids*, Oxford University Press: London 1953.
- [10] W. P. Mason, Ed., *Physical Acoustics*, Academic Press: New York 1964.
- [11] D. Zhang, G. M. Crean, T. Flaherty and A. Shallow, "Development of interdigital acoustic wave transducers for biosensor applications", *Analyst*, **1993**, *118*, 429.
- [12] R. M. White, "Surface Elastic Waves", *Proceedings of the IEEE*, **1970**, *58*, 1238.
- [13] D. P. Morgan, *Surface-Wave Devices for Signal Processing*, Elsevier Science Publisher: Amsterdam 1985.
- [14] Lord Rayleigh, "On waves propagated along the plane surface of an elastic solid", *Proceeding London Mathematical Society*, **1885**, *17*, 4., in R. M. White, "Surface Elastic Waves", *Proceedings of the IEEE*, 1970, *58*, 1238.
- [15] A. A. Oliner, *Acoustic Surface Waves*, Springer-Verlag: Berlin 1978.
- [16] C. Caliendo, E. Verona and V. I. Anisimkin, "Surface acoustic wave humidity sensors: a comparison between different types of sensitive membrane", *Smart Material Structures*, **1997**, *6*, 707.
- [17] C. Caliendo, A. D' Amico, A. Furlani, G. Iucci, M. V. Russo and E. Verona, "Surface acoustic wave humidity sensor", *Sensors and Actuators B*, **1993**, *15/16*, 288.

- [18] C. Caliendo, A. D' Amico, A. Furlani, G. Iucci, M. V. Russo and E. Verona, "A new surface acoustic wave humidity sensor based on a polyethynylfurenol membrane", *Sensors and Actuators B*, **1994**, *18*, 82.
- [19] M. Tom-Moy, R. L. Baer, D. Spira-Solomon and T. P. Doherty, "Atrazine measurements using surface transverse wave devices", *Analytical Chemistry*, **1995**, *67*, 1510.
- [20] W. Welsch, C. Klein, R. M. Öksüzoglu and S. Hunklinger, "Immunosensing with surface acoustic wave sensors", *Sensors and Actuators A*, **1997**, *62*, 562.
- [21] W. Welsch, C. Klein, M. von Schickfus and S. Hunklinger, "Development of a surface acoustic wave immunosensor", *Analytical Chemistry*, **1996**, *68*, 2000.
- [22] E. Gizeli, M. Liley, C. R. Lowe and H. Vogel, "Antibody binding to a functionalized supported lipid layer: A direct acoustic immunosensor", *Analytical Chemistry*, **1997**, *69*, 4808.
- [23] T. Nomura and T. Yasuda, "Measurement of velocity and of liquid using surface acoustic wave delay line", *Japan Journal of Applied Physics*, **1990**, *29*, Suppl. 29-1, 140.
- [24] B. A. Auld, *Acoustic Fields and Waves in Solids*, John Wiley: New York 1973, vol. 2, Chap. 12, p. 283.
- [25] S. J. Martin, A. J. Ricco, T. M. Niemczyk and G. C. Frye, "Characterization of SH acoustic plate mode liquid sensors", *Sensors and Actuators*, **1989**, *20*, 253.
- [26] J. Kondoh and S. Shiokawa, "SH-SAW taste sensor based on acoustoelectric interaction", *IEEE - Ultrasonic Symposium*, **1993**, 421.
- [27] J. Kondoh, Y. Matsui and S. Shiokawa, "New biosensor using shear horizontal surface acoustic wave device", *Japan Journal of Applied Physics*, **1993**, *32*, 2376.
- [28] J. Kondoh and S. Shiokawa, "Liquid sensor using SH-SAW device", *Transaction IEICE C-II*, **1992**, *J75-C-II*, 224.
- [29] J. Kondoh, Y. Matsui and S. Shiokawa, "SH-SAW biosensor based on pH change", *IEEE - Ultrasonic Symposium*, **1993**, 337.
- [30] J. Kondoh, S. Shiokawa and Z. Georgiev, "A shear-horizontal SAW device as a pH monitor", *Sensors and Actuators B*, **1993**, *13-14*, 429.
- [31] G. McHale, M. I. Newton, S. M. Rowan and M. Banerjee, "The spreading of small viscous stripes of oil", *Journal of Physics D: Applied Physics*, **1995**, *28*, 1925.
- [32] H. Bouasse, *Capillarité et Phénomènes Superficiels*, Delagrave: Paris 1924.
- [33] J. S. Rowlinson and B. Widom, *Molecular Theory of Capillarity*, Oxford University Press: Oxford 1982.
- [34] T. Young, *Philos. Trans. R. Soc., London*, **1805**, *95*, 65. in L. Léger and J.F. Joanny, "Liquid spreading", *Reports on Progress in Physics*, **1992**, *55*, 431.
- [35] P. G. de Gennes, "Wetting: statics and dynamics", *Reviews of Modern Physics*, **1985**, *57*, 827.

- [36] D. Ausserré, A. M. Picard and L. Léger, "Existence and role of the precursor film in the spreading of polymer liquids", *Physical Review Letters*, **1986**, *57*, 2671.
- [37] C. O. Timmons and W. A. Zisman, "The effect of liquid structure on contact angle hysteresis", *Journal of Colloid and Interface Science*, **1966**, *22*, 165.
- [38] W. C. Bigelow, D. L. Pickett and W. A. Zisman, "Oleophobic monolayers. I. Films absorbed from solution in non-polar liquids", *Journal of Colloid Science*, **1946**, *1*, 513.
- [39] W. A. Neuman and R. J. Good, *Techniques of Measuring Contact Angles, Surface and Colloid Science*, Vol. II, in R. J. Good and R. R. Stromberg (Eds.), *Experimental Methods*, Plenum Press: New York 1979.
- [40] R. J. Good, "Contact angle, wetting, and adhesion: a critical review", *Journal of Adhesion Science and Technology*, **1992**, *6*, 1269.
- [41] J. K. Spelt, Y. Rotenberg, D. R. Absolom and W. Neumann, "Sessile-drop contact-angle measurements using axisymmetrical drop shape-analysis", *Colloids and Surfaces*, **1987**, *24*, 127.
- [42] W. C. Jones and M. C. Porter, "A method for measuring contact angles on fibers", *Journal of Colloid and Interface Science*, **1967**, *24*, 1.
- [43] C. Allain, D. Ausserré and F. Rondelez, "A new method for contact-angle measurements of sessile drops", *Journal of Colloid and Interface Science*, **1985**, *107*, 5.
- [44] H. Y. Erbil, "Surface Tension of Polymers", in *Handbook of Surface and Colloid Chemistry*, Chapter 9, pp 259-306, CRC Press LLC: New York: 1997.
- [45] A. W. Adamson, *Physical Chemistry of Surfaces*, John Wiley: New York 1982, Chapter II, Sec. 8, p25.
- [46] R. A. Hayes and J. Ralston, "The dynamics of wetting processes", *Colloids and Surfaces A-Physicochemical and Engineering Aspects*, **1994**, *93*, 15.
- [47] G. McHale, M. I. Newton, M. K. Banerjee and S. M. Rowan, "Interaction of surface acoustic waves with viscous liquids", *Faraday Discussion*, **1997**, *107*, 15.
- [48] L. H. Tanner, "The spreading of silicone oil drops on horizontal surfaces", *Journal of Physics D: Applied Physics*, **1979**, *12*, 1473.
- [49] H. Hervet and P. G. de Gennes, "The dynamics of wetting - precursor films in the wetting of dry solids", *Comptes Rendus de L Academie des Sciences Serie II*, **1984**, *299*, 499.
- [50] F. Brochard-Wyart, P. G. de Gennes, H. Hervet and C. Redon, "Wetting and slippage of polymer melts on semi-ideal surfaces", *Langmuir*, **1994**, *10*, 1566.
- [51] F. Tiberg and A. M. Cazabat, "Spreading of thin films of ordered nonionic surfactants. Origin of the stepped shape of the spreading precursor", *Langmuir*, **1994**, *10*, 2301.
- [52] P. Silberzan and L. Léger, "Evidence for a new spreading regime between partial wetting and total wetting", *Physical Review Letters*, **1991**, *66*, 185.

- [53] P. Carles and A. M. Cazabat, "The thickness of surface-tension-gradient-driven spreading films", *Journal of Colloid and Interface Science*, **1993**, 157, 196.
- [54] H. Schonhorn, H. L. Frisch and T. K. Kwei, "Kinetics of wetting of surfaces by polymer melts", *Journal of Applied Physics*, **1966**, 37, 4967.
- [55] J. D. Chen and N. Wada, "Wetting dynamics of the edge of a spreading drop", *Physical Review Letters*, **1989**, 62, 3050.
- [56] F. Brochard-Wyart and P. G. de Gennes, "Dynamics of partial wetting", *Advances in Colloid and interface Science*, **1992**, 39, 1.
- [57] F. Brochard and P. G. de Gennes, "Shear-dependent slippage at a polymer solid interface", *Langmuir*, **1992**, 8, 3033.
- [58] F. Brochard-Wyart, P. G. de Gennes, P. Pincus, "Suppression of sliding at the interface between incompatible polymer melts", *Comptes Rendus de L Academie des Sciences Serie II*, **1992**, 314, 873.
- [59] D. Li, P. Cheng and A. W. Neumann, "Contact-angle measurement by axisymmetrical drop shape-analysis (ADSA)", *Advances in Colloid and Interface Science*, **1992**, 39, 347.
- [60] Y. N. Lee and S. M. Chiao, "Visualization of dynamic contact angles on cylinder and fiber", *Journal of Colloid and Interface Science*, **1996**, 181, 378.
- [61] J. D. Chen, "Experiments on a spreading drop and its contact-angle on a solid" *Journal of Colloid and Interface Science*, **1988**, 122, 60, in J. D. Chen and N. Wada, "Wetting dynamics of the edge of a spreading drop", *Physical Review Letters*, **1989**, 62, 3050.
- [62] J. Daillant, J. J. Benattar, L. Bosio and L. Léger, "Final stages of spreading of polymer droplets of smooth solid surfaces", *Europhysics Letters*, **1988**, 6, 431.
- [63] J. Daillant, J. J. Benattar and L. Léger, "Ultrathin films in wetting evidenced by x-ray reflectivity", *Physical Review A*, **1990**, 41, 1963.
- [64] F. Heslot, A. M. Cazabat and P. Levinson, "Dynamics of wetting of tiny drops: Ellipsometric study of the late stages of spreading", *Physical Review Letters*, **1989**, 62, 1286.
- [65] M. I. Newton, G. McHale, S. M. Rowan and M. Banerjee, "A surface acoustic wave technique for the observation of dynamic wetting", *Journal of Physics D: Applied Physics*, **1995**, 28, 1930.
- [66] H. Ghiradella, W. Radigan and H. L. Frisch, "Electrical-resistivity changes in spreading liquid-films", *Journal of Colloid and Interface Science*, **1975**, 51, 522.
- [67] A. A. Oliner, *Acoustic Surface Waves: Topics in Applied Physics*, Springer: Berlin 1978
- [68] E. Benes, M. Gröschl, W. Burger and M. Schmid, "Sensors based on piezoelectric resonators", *Sensors and Actuators A*, **1995**, 48, 1.
- [69] W. G. Cady, *Piezoelectricity: An Introduction to the Theory and Applications of Electromechanical Phenomena in Crystals*, Dover, New York 2<sup>nd</sup> edn., 1964,
- [70] W. H. King, "Piezoelectric sorption detector", *Analytical Chemistry*, **1964**, 36, 1735.

- [71] K. Ema, M. Yokoyama, T. Nakamoto and T. Moriizumi, "Odor-sensing system using a quartz-resonator sensor array and neural network pattern recognition", *Sensors and Actuators*, **1989**, *18*, 291.
- [72] T. Nakamoto, A. Fukuda and T. Moriizumi, "Perfume and flavour identification by odour-sensing systems using quartz-resonator sensor array and neural-network pattern recognition", *Sensors and Actuators B*, **1993**, *10*, 85.
- [73] D. James, D. V. Thiel, G. R. Bushell, W. K. Busfield and A. Mackay-Sim, "Phase change and viscosity effects on a quartz crystal microbalance", *Analyst*, **1994**, *119*, 2005.
- [74] G. Sauerbrey, "Verwendung von Schwingquarzen zur Wägung dünner Schichten und zur Mikrowägung", *Zeitschrift für Physik*, **1959**, *155*, 206.
- [75] M. Thompson, G. K. Dhaliwal, C. L. Arthur and G. L. Calabrese, "The potential of the bulk acoustic wave device as a liquid-phase immunosensor", *IEEE Transactions on Ultrasonics, Ferroelectrics, and Frequency Control*, **1987**, *UFFC-34*, 127.
- [76] M. Yang and M. Thompson, "Multiple chemical information from the thickness shear mode acoustic wave sensor in the liquid phase", *Analytical Chemistry*, **1993**, *65*, 1158.
- [77] G. Sauerbrey, "Messung von Plattenschwingungen sehr kleiner Amplitude durch Lichtstrommodulation", *Zeitschrift für Physik*, **1964**, *178*, 457.
- [78] H. K. Pulker, E. Benes, D. Hammer and E. Solner, "Progress in monitoring thin film thickness with quartz crystal resonators", *Thin Solid Films*, **1976**, *32*, 27.
- [79] V. M. Mecca, "Loaded vibrating quartz sensors", *Sensors and Actuators A*, **1994**, *40*, 1.
- [80] V. M. Mecca, "A new method of measuring the mass sensitive area of quartz crystal resonators", *Journal of Physics E-Scientific Instruments*, **1989**, *22*, 59.
- [81] C. Mak and J. Crim, "Quartz crystal microbalance studies of disorder-induced lubrication", *Faraday Discussion*, **1997**, *107*, 389.
- [82] A. Dayo, W. Alnasrallah and J. Krim, "Superconductivity-dependent sliding friction", *Physical Review Letters*, **1998**, *80*, 1690.
- [83] V. Koutsos, E. W. van der Vegte, P. C. M. Grim and G. Hadziioannou, "Isolated polymer chains via mixed self-assembled monolayers: Morphology and friction studied by scanning force microscopy", *Macromolecules*, **1998**, *31*, 116.
- [84] P. L. Konash and G. J. Bastiaans, "Piezoelectrical crystals as detectors for liquid chromatography", *Analytical Chemistry*, **1980**, *52*, 1929.
- [85] A. P. M. Glassford, *Applications of Piezoelectric Quartz Crystal Microbalances*, in C. Lu and A. W. Czanderna, Eds., Vol. 7 of *Methods and Phenomena, Their Applications to Science and Technology*, Elsevier: New York 1984.
- [86] G. G. Guilbault, *Applications of Piezoelectric Quartz Crystal Microbalances*, in C. Lu and A. W. Czanderna, Eds., Vol. 7 of *Methods and Phenomena, Their Applications to Science and Technology*, Elsevier: New York 1984.

- [87] K. Kanazawa and J. G. Gordon, "Frequency of a quartz microbalance in contact with liquid", *Analytical Chemistry*, **1985**, *57*, 1770.
- [88] A. L. Kipling and M. Thompson, "Network analysis method applied to liquid-phase acoustic wave sensors", *Analytical Chemistry*, **1990**, *62*, 1514.
- [89] R. M. White, "Acoustic interactions from Faraday's crispations to MEMS" Introductory Lecture, *Faraday Discussion*, **1997**, *107*, 1.
- [90] S. Bruckenstein and M. Shay, "Experimental aspects of use of the quartz crystal microbalance in solution", *Electrochemistry Acta*, **1985**, *30*, 1295.
- [91] L. V. Rajakovic, B. A. Cavic-Vlasak, V. Ghaemmaghani, K. M. R. Kallury, A. L. Kipling and M. Thompson, "Mediation of acoustic energy transmission from acoustic wave sensors to the liquid phase by interfacial viscosity", *Analytical Chemistry*, **1991**, *63*, 615.
- [92] Z. Deng, D. C. Stone and M. Thompson, "Selective detection of aroma components by acoustic wave sensor coated with conducting polymer films", *Analyst*, **1996**, *121*, 671.
- [93] F. Josse, Z. A. Shana, D. E. Radtke, U. R. Kelkar, D. T. Haworth, "Quartz resonator as sensor for viscous/conductive liquids", *Electronics Letters*, **1989**, *25*, 1446.
- [94] Z. Lin, C. M. Yip, I. S. Joseph and M. D. Ward, "Operation of an ultrasensitive 30-MHz quartz crystal microbalance in liquids", *Analytical Chemistry*, **1993**, *65*, 1546.
- [95] H. E. Hager, "Fluid property evaluation by piezoelectric crystals operating in the thickness shear mode", *Chemical Engineering Communication*, **1986**, *43*, 25.
- [96] K. O. Wessendorf, "The lever oscillator for use in high resistance resonator applications", *Proceedings IEEE 1993 Frequency Control Symposium, Salt Lake City, UT, USA*, **1993**, 711.
- [97] E. M. Pater, S. Bruckenstein and A. R. Hillman, "Film mass and volume changes accompanying redox-driven solvent and salt transfer during redox switching of polyvinylferrocene film", *Journal of the Chemical Society, Faraday Transaction*, **1998**, *94*, 1097.
- [98] Z. A. Shana, H. Zong, F. Josse and D. C. Jeutter, "Analysis of electrical equivalent circuit of quartz crystal resonator loaded with viscous conductive liquids", *Journal of Electroanalytical Chemistry*, **1994**, *379*, 21.
- [99] H. Muramatsu, E. Tamiya and I. Karube, "Computation of equivalent circuit parameters of quartz crystals in contact with liquids and study of liquid properties", *Analytical Chemistry*, **1988**, *60*, 2142.
- [100] S. J. Martin, V. E. Granstaff and G. C. Frye, "Characterisation of quartz crystal microbalance with simultaneous mass and liquid loading", *Analytical Chemistry*, **1991**, *63*, 2272.
- [101] S. J. Martin, G. C. Frye, A. J. Ricco and S. D. Senturia, "Effect of surface roughness on the response of thickness-shear mode resonators in liquids", *Analytical Chemistry*, **1993**, *65*, 2910.
- [102] S. J. Martin, G. C. Frye and K. O. Wessendorf, "Sensing liquid properties with thickness-shear mode resonators", *Sensors and Actuators A*, **1994**, *44*, 209.

- [103] M. Yang and M. Thompson, "Surface-morphology and the response of the thickness-shear mode acoustic-wave sensor in liquids", *Langmuir*, **1993**, 9, 1990.
- [104] R. M. White and F. W. Voltmer, "Direct piezoelectric coupling to surface elastic waves", *Applied Physics Letters*, **1965**, 7, 314.
- [105] C. Campbell, *Surface Acoustic Wave Devices and their Signal Processing Applications*, Academic Press: Boston, 1989.
- [106] H. Wohltjen and R. Dessy, "Surface acoustic wave probe for chemical analysis. I. Introduction and instrument description", *Analytical Chemistry*, **1979**, 51, 1458.  
H. Wohltjen and R. Dessy, "Surface acoustic wave probes for chemical analysis. II. Gas chromatography detector", *Analytical Chemistry*, **1979**, 51, 1465.  
H. Wohltjen and R. Dessy, "Surface acoustic wave probes for chemical analysis. III. Thermomechanical polymer analyzer", *Analytical Chemistry*, **1979**, 51, 1470.
- [107] H. Wohltjen, "Mechanism of operation and design consideration for surface acoustic wave device vapour sensors", *Sensors and Actuators*, **1984**, 5, 307.
- [108] S. J. Martin, K. S. Schweizer, S. S. Schwarty and R. L. Gunshor, "Vapor sensing by means of a ZnO on Si surface acoustic wave resonator", *Proceedings IEEE Ultrasonics Symposium, Dallas, Texas*, **1984**, 207.
- [109] A. M. McGill, J. W. Grate and R. M. Anderson, "Surface and interfacial properties of surface acoustic wave gas sensors", *ACS Symposium*, **1994**, 561, 281.
- [110] A. J. Ricco and S. J. Martin, "Multiple frequency SAW devices for chemical sensing and material characterization", *Sensors and Actuators B*, **1993**, 10, 123.
- [111] P. D. Morgan, "Surface acoustic wave devices and applications", 1. Introductory review, *Ultrasonics*, **1973**, 11, 121.
- [112] D. P. Morgan, "Materials for surface-wave devices", Chapter 6.5, in D. P. Morgan *Surface-Wave Devices for Signal Processing*, Elsevier Science Publisher: Amsterdam 1985.
- [113] H. Matthews (ed.), *Surface Wave Filters, Design, Constructions, and Use*. John Wiley & Sons: New York, 1977
- [114] M. J. Vellekoop, "Acoustic wave sensors and their technology", *Ultrasonics*, **1998**, 36, 7.
- [115] S. G. Joshi, Y. Jin, "Characteristics and applications of quasi-shear-horizontal acoustic waves", *Ultrasonics*, **1996**, 34, 507.
- [116] K. Nakamura, M. Kazumi and H. Shimizu, "SH-type and Rayleigh-type surface waves on rotated Y-cut LiTaO<sub>3</sub>", *IEEE Symposium 1977*, **1977**, 819.
- [117] S. J. Martin and A. J. Ricco, "Monitoring photo-polymerization of thin films using SH-acoustic plate mode sensors", *Sensors and Actuators*, **1990**, A21-A23, 712.
- [118] R. C. Hughes, S. J. Martin, G. C. Frye and A. J. Ricco, "Liquid-solid phase transition detection with acoustic plate mode sensors: Application to icing of surfaces", *Sensors and Actuators*, **1990**, A21-A23, 693.

- [119] T. M. Niemczyk, S. J. Martin, G. C. Frye and A. J. Ricco, "Acoustoelectric interaction of plate modes with solution", *Journal of Applied Physics*, **1988**, 64, 5002.
- [120] F. Josse, Z. A. Shana, D. T. Haworth, S. Liew and M. Grunze, "On the use of ZX-LiNbO<sub>3</sub> acoustic plate mode devices as detectors for dilute electrolytes", *Sensors and Actuators B*, **1992**, 9, 97.
- [121] I. A. Victorov, *Rayleigh and Lamb Waves*, Plenum: New York, 1967.
- [122] S. G. Joshi and Y. Jin, "Excitation of ultrasonic Lamb waves in piezoelectric plates", *Journal of Applied Physics*, **1991**, 69, 8018.
- [123] S. G. Joshi and Y. Jin, "Propagation of ultrasonic Lamb waves in piezoelectric plates", *Journal of Applied Physics*, **1991**, 70, 4112.
- [124] S. G. Joshi and Y. Jin, "Calculation of electromechanical coupling coefficients of ultrasonic lamb waves", *Ultrasonics International 93 Conference Proceeding*, **1993**, 145.
- [125] M. J. Vellenkoop, G. W. Lubking, P. M. Sarro and A. Venema, "Evaluation of liquid properties using a silicon Lamb wave sensor", *Sensors and Actuators A*, **1994**, 43, 175.
- [126] B. Jakoby and M. J. Vellekoop, "Properties of Love waves: applications in sensors", *Smart Materials and Structures*, **1997**, 6, 668.
- [127] S. V. Biryukov, Y. V. Gulyaev, V. V. Krylov and V. P. Plessky, *Surface Acoustic Waves in Inhomogeneous Media*, Springer-verlag: Berlin Heidelberg, 1995.
- [128] J. Du, G. L. Harding, J. A. Ogilvy, P. R. Dencher and M. Lake, "A study of Love-wave acoustic sensors", *Sensors and Actuators A*, **1996**, 56, 211.
- [129] G. Kovacs and A. Venema, "Theoretical comparison of sensitivities of acoustic shear wave modes for (bio)chemical sensing in liquids", *Applied Physics Letters*, **1992**, 61, 639.
- [130] J. Enderlein, E. Chilla and H-J. Fröhlich, "Comparison of the mass sensitivity of Love and Rayleigh waves in a three-layer system", *Sensors and Actuators A*, **1994**, 41-42, 472.
- [131] Z. Wang, J. D. N. Cheeke and C. K. Jen, Sensitivity analysis for Love mode acoustic gravimetric sensors, *Applied Physics Letters*, **1994**, 64, 2940.
- [132] G. L. Harding and J. Du, "Design and properties of quartz-based Love wave acoustic sensors incorporating silicon dioxide and PMMA guiding layers", *Smart Materials and Structures*, **1997**, 6, 716.
- [133] E. Gizeli, "Design consideration for the acoustic waveguide biosensor", *Smart Materials and Structures*, **1997**, 6, 700.
- [134] G. S. Calabrese, H. Wohltjen and M. K. Roy, "Surface acoustic wave devices as chemical sensors in liquids. Evidence disputing the importance of rayleigh wave propagation", *Analytical Chemistry*, **1987**, 59, 833.
- [135] J. J. Campbell and W. R. Jones, "Propagation of surface waves at the boundary between a piezoelectric crystal and a fluid medium", *IEEE Transaction on Sonics and Ultrasonics*, **1970**, SU-17, 71.
- [136] H. Wohltjen and R. Dessy, "Surface acoustic wave probes for chemical analysis. III Themomechanical polymer analyzer", *Analytical Chemistry*, **1979**, 51, 1470.

- [137] J. E. Roederer and G. J. Bastiaans, "Microgravimetric immunoassay with piezoelectric crystals", *Analytical Chemistry*, **1983**, *55*, 2333.
- [138] P. Košťal, J. Machalíková and F. Cernobila, "Using an immersion surface acoustic wave sensor for liquid testing", *Journal of Physics III France*, **1993**, *3*, 355.
- [139] P. Košťal, "Surface acoustic wave measurements of evaporation rate", *Applied Acoustics*, **1996**, *47*, 121.
- [140] Z. X. Lin, R. M. Hill, H. T. Davis and M. D. Ward, "Determination of wetting velocities of surfactant superspreaders with the quartz-crystal microbalance", *Langmuir*, **1994**, *10*, 4060.
- [141] Z. X. Lin, T. Stoebe, R. M. Hill, H. T. Davis and M. D. Ward, "Improved accuracy in dynamic quartz-crystal microbalance measurements of surfactant enhanced spreading", *Langmuir*, **1996**, *12*, 345.
- [142] T. Stoebe, R. M. Hill, M. D. Ward and H. T. Davies, "Enhanced spreading of aqueous films containing ionic surfactants on solid substrates", *Langmuir*, **1997**, *13*, 7276.
- [143] Z. X. Lin and M. D. Ward, "Determination of contact angles and surface tensions with the quartz crystal microbalance", *Analytical Chemistry*, **1996**, *68*, 1285.
- [144] S. Shiokawa, T. Yamamoto, S. Yamakita and Y. Matsui, "Measurement of physical properties of liquid based on a droplet vibration excited by SAW streaming", *Proceedings of the World Congress in Ultrasonics*, **1997**, 90.
- [145] M. de Billy, "Influence of the wetting and the angle of immersion on the generation of a sholte wave: Experimental investigation", *Physics Letters*, **1983**, *96A*, 85.
- [146] M. de Billy and G. Quentin, "Experimental study of the Sholte wave propagation on a plane surface partially immersed in liquid", *Journal of Applied Physics*, **1983**, *54*, 4314.
- [147] M. I. Newton, G. McHale and M. K. Banerjee, "Reflection of surface acoustic waves by localized wetting liquids", *Applied Physics Letters*, **1997**, *71*, 3785.
- [148] G. McHale, M. K. Banerjee, M. I. Newton and V. V. Krylov, "Surface acoustic wave resonances in the spreading of viscous fluids", *Physical Review B*, **1999**, *59*, 8262.
- [149] G. McHale, M. I. Newton, M. K. Banerjee and S. M. Rowan, "An acoustic technique for the monitoring of dynamic wetting behaviour", accepted for publication in *Journal of Adhesion Science and Technology*, 1999.
- [150] J. Frenkel, "Viscous flow of crystalline bodies under the action of surface tension", *Journal of Physics*, **1945**, *IX*, 385.
- [151] G. McHale, S. M. Rowan and M. I. Newton, "Frenkel's method and the spreading of small spherical droplets", *Journal of Physics D: Applied Physics*, **1994**, *27*, 2619.
- [152] A. J. Ricco and S. J. Martin, "Acoustic-wave viscosity sensor", *Applied Physics*, **1987**, *50*, 1474.
- [153] J. F. Joanny and P. G. de Gennes, "Static structure of wetting films and contact lines", *Comptes Rendus des Seances de l' Academie des Science*, **1984**, *299*, 279.

---

REFERENCES

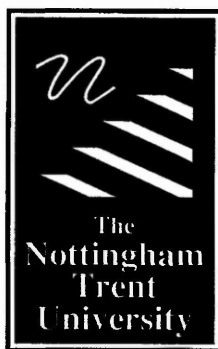
---

- [154] S. Strella, "Analysis of spreading of a viscous drop on a smooth surface", *Journal of Applied Physics*, **1970**, *41*, 4242.
- [155] R. B. Bird, W. E. Steward and E. N. Lightfoot, *Transport Phenomena*, John Wiley: New York, 1960.
- [156] S. Datta, *Surface Acoustic Wave Devices*, Prentice-Hall: Englewoods Cliffs, New Jersey, 1986.
- [157] B. A. Auld, *Acoustic Fields and Waves in Solids*, John Wiley: New York 1973.
- [158] L. Brekhovskikh and V. Goncharov, *Mechanics of Continua and Wave Dynamics*, Springer-Verlag: New York, 1982.
- [159] *IEEE Standard on Piezoelectricity 176-1987* in D. S. Ballantine, R. M. White, S. J. Martin, A. J. Ricco, E. T. Zellers, G. C. Frye, H. Wohltjen, *Acoustic Wave Sensors : Theory, Design, and Physico-Chemical Applications*, Academic Press: New York 1997.
- [160] M. Rodahl and B. Kasemo, "On the measurements of thin liquid overlayers with the quartz-crystal microbalance", *Sensors and Actuators A*, **1996**, *54*, 448.
- [161] R. B. Bird, R. C. Armstrong and O. Hassager, *Dynamics of Polymeric Liquids*, John Wiley & Sons: New York, 1977.
- [162] M. Rodahl and B. Kasemo, "On the measurements of thin liquid overlayers with the quartz-crystal microbalance", in G. McHale, M. K. Banerjee, M. I. Newton and V. V. Krylov, "Surface acoustic wave resonances in the spreading of viscous fluids", *Physical Review B*, **1999**, *59*, 8262.
- [163] J. D. Ferry, *Viscoelastic Properties of Polymers*, (3<sup>rd</sup> Edition), John Wiley & Sons: New York, 1980.
- [164] L. D. Landau and E. M. Lifshitz, *Fluid Mechanics*, (2<sup>nd</sup> Edition), Pergamon Press: Oxford, 1987.
- [165] TTI Thurlby Instruments, *TG 105 Pulse Generator Instruction Manual*, Huntington; Cambridgeshire: TTI Instruments LTD, 1991.
- [166] Marconi Instruments, *10 kHz - 1 GHz AM/FM Signal Generator 2022D; Operating Manual*, St. Albans; Hertfordshire: Marconi Instruments LTD, 1993.
- [167] Philips/Fluke, *Digital Storage Oscilloscope (DSO) PM 3365A User Manual*, Eindhoven: N. V. Philips Gloeilampen-fabrieken, 1989.
- [168] Mini-Circuits, *RF/IF Designer's Handbook*, Brooklyn; New York: Mini-Circuits division of Scientific Components, 1992.
- [169] M/A-COM, *RF-Microwave and Millimeter Wave, MMIC, hybrid and passive components*, Catalog No. M1013, Lowell; Massachusetts M/A-COM Inc, 1994.
- [170] A. J. Baden Fuller, *Microwaves*, 2<sup>nd</sup>. edition, Oxford: Pergamon Press, 1979.
- [171] HP Hewlett-Packard Company, *HP 8471D Coaxial RF & Microwave Detectors 100kHz - 2GHz*, Hewlett-Packard Company, Specification and Data Sheet, 1990.
- [172] YCC Crystal Technology Division, *LiNbO<sub>3</sub>-LiTAO<sub>3</sub> Single Crystal*, YCC Yamaju Ceramics Co. LTD, 1990.
- [173] S. P. Parker, *Optics Source Book*, 6<sup>th</sup>. edition, *Encyclopedia of Science and Technology*, New York: McGraw-Hill, 1988.

## REFERENCES

---

- [174] United Chemical Technologies, *Technical Articles - Introduction*, United Chemical Technologies, Inc., <http://www.unitedchem.com/intro.htm>, 1996.
- [175] E. Butkov, *Mathematical Physics*, Addison-Wiley Publishing: Reading, Massachusetts, 1968.



## **Libraries & Learning Resources**

**The Boots Library: 0115 848 6343  
Clifton Campus Library: 0115 848 6612  
Brackenhurst Library: 01636 817049**